Magnetic-field amplification in turbulent laser-plasmas

Archie F. A. Bott

Merton College

University of Oxford

Thesis submitted for the degree of

Doctor of Philosophy in Atomic and Laser Physics

Hilary, 2019

To my parents

Abstract

Understanding magnetic-field generation in turbulent plasma is essential for explaining the presence of dynamically significant magnetic fields in astrophysical environments such as the intracluster medium. Seemingly plausible theoretical frameworks attributing the origin and sustainment of these fields to amplification by the so-called fluctuation dynamo are somewhat hampered by conceptual uncertainties concerning the validity of the models in which these frameworks are formulated. A recent experiment on the OMEGA laser facility attempted to overcome some of these uncertainties by demonstrating the feasibility of magnetic-field amplification by stochastic motions up to dynamical strengths in actual turbulent plasma. In order to realise the scientific goals of this experiment, accurate measurements of stochastic magnetic fields arising in turbulent laser-plasmas were required. This thesis reports on the development of an analysis technique which meets this requirement by recovering the magnetic-energy spectrum from proton imaging data, as well as the mean magnetic-energy density and characteristic structure sizes. The general applicability and reliability of the technique is considered in depth. On application to data derived from the OMEGA experiment, the magnetic-energy density is found to increase over five hundred times in the experiment from its initial value; in addition, estimates of the maximum magnetic field strength indicate that the field is likely to be dynamically significant. The experiment therefore constitutes the first demonstration in the laboratory of the fluctuation dynamo. The results of a second experiment on the OMEGA laser facility – in which a remodelled variant of the previously employed experimental platform is used to provide a time-resolved characterisation of a plasma dynamo's evolution, measuring temperatures, densities, flow velocities and magnetic fields – are also described. It is shown that the initial growth of the dynamo-generated fields occurs exponentially at a rate which significantly exceeds the turnover rate of the driving-scale stochastic motions in the plasma. Both experiments validate the claim that the fluctuation dynamo is indeed capable of amplifying magnetic fields significantly.

Acknowledgements

There are many people I want to thank for helping me to write this thesis. First, I am very grateful to my supervisors Gianluca Gregori and Alex Sckekochihin for giving me the opportunity to study a fascinating series of experiments. I believe I am a much better physicist now than when I began my DPhil, and most of that is down to many enlightening conversations with both of you. I also want to thank Peter Norreys for his support and kindness over the last three years, and Steve Cowley for many enjoyable afternoons in front a blackboard thinking about microinstabilities (I'm afraid none of that ended up in this thesis, but watch this space...).

I appreciate the contributions of all my academic collaborators on the OMEGA experiments to my work, as well as the LLE staff who helped to make the experiments a reality. Special mentions go to Carlo Graziani, whose extensive knowledge and clever ideas were very helpful, and Petros Tzeferacos for providing support with simulations despite a consistently ludicrous schedule. My thanks to Don Lamb too for allowing me to take a key role in the OMEGA experiments.

To everyone in Gianluca's group and the Simon Room more generally (especially Alex R, Laura, Jena, Charlotte, Joseph, Alex S, Matthew, Paul, Brett, Tom P, Konstantin, Jacob and Tom W): thank you for advice, hard work on experiments, amusing coffee breaks, drinks and exceptional group Christmas meals. Thank you to my friends at Merton (particularly Kitty, Sam and Amy) and also the other wonderful people who have been here during my time in Oxford: Greg, Andrew, Damien, Lyndon, Scott, Logan, Lulu, Jenny and Dave. My thanks also to friends more distant, but no less valued: Ted, Will, Helen C, Zoe, Jess and Freddie. I am particularly grateful to Oli for always being there for me in difficult moments – even when on another continent – and also being superb company in happier ones!

As for my family, thank you to all my step-siblings, cousins and step-cousins for numerous excellent gatherings over the years – and also all my other relatives. I am particular indebted to my stepfather, JJ, for assiduously proof-reading this thesis and fixing my poor grammar. It's hard to know how to express my gratitude to my immediate family – Mum, Dad and Patrick – since I owe them all so much. Needless to say, I could never have written this thesis without their continued love and generosity. Finally, my deepest thanks to Dan: your unwavering support has kept me sane these last few months, and means the world to me.

Role of the Author

The results presented in this thesis are concerned with laboratory astrophysics experiments carried out on the OMEGA laser facility (USA). These experiments were not performed by the author in isolation, but were instead contributed to by a large collaboration. Here I clarify the contribution of the author to these experiments.

In Chapter 1, a brief review of fluctuation dynamo theory is given (Section 1.1); this material is derived from references interspersed throughout the text. Experiments investigating the fluctuation dynamo are then discussed (Section 1.2), culminating in a description of an experiment carried out at the OMEGA laser facility in August 2015 attempting to realise a fluctuation dynamo in the laboratory. The design of this experiment was conceived by Gianluca Gregori, Alexander Schekochihin, Petros Tzeferacos, Don Lamb, and others. FLASH simulations of the experiment were run and analysed by P. Tzeferacos. The set-up and design of the Thomson scattering diagnostic was undertaken by Dustin Froula and Joseph Katz; the associated Thomson scattering and Faraday-rotation analysis was carried out by Alex Rigby. Analysis for the X-ray images were initially done by Eugene Churazov (and subsequently performed by the author). The author began his DPhil two months after the experimental shot day, and was tasked with devising a technique for analysing the proton-imaging data which had been obtained from the OMEGA experiment. Section 1.3 reviews the proton-imaging diagnostic (derived from enclosed references), while Section 1.4 discusses why the proton-imaging data from the OMEGA experiment could not be analysed using previously established approaches. The physical processing of the CR-39 nuclear track detector for deriving digitised proton images was performed by Rich Petrasso's research group at MIT.

The author's original work begins in Chapter 2, and consists in the construction of an analytic theory for proton imaging of stochastic magnetic fields. The theoretical calculations and simulations were all carried out by the author, but were assisted by discussions with the author's supervisors (G. Gregori and A. Schekochihin), as well as other collaborators (Carlo Graziani, Thomas White, D. Lamb and P. Tzeferacos). An adapted form of this work has been published in the Journal of Plasma Physics.

Chapter 3 applies the techniques derived in Chapter 2 to the proton-imaging data from the OMEGA experiment. The analysis of both experimental and simulated proton-imaging data was carried out by the author; the creation of the simulated proton images was done by P. Tzeferacos. The author was a co-author on a paper (first author P. Tzeferacos) published in Nature Communications, which discussed the complete set of experiment results from the OMEGA experiment; the material in Chapters 1 and 3 is (mostly) adapted from that paper.

Chapter 4 outlines the results of a second OMEGA experiment (April 2017), which attempted to provide a time-resolved characterisation of fluctuation-dynamo-generated magnetic fields. The author contributed to the design of the experiment, and assisted with their implementation; the experimental lead for the shot day was Laura Chen. The analysis of the X-ray imaging diagnostic, the Thomson scattering diagnostic, and proton imaging diagnostic was carried out by the author. The results of the experiment are not yet published, but a manuscript (based on Chapter 4) is currently in preparation.

A glossary of frequently used notation and conventions employed in the thesis (Appendix A) and subsequent appendices are also the work of the author.

Publications

First author

- A.F.A. Bott, C. Graziani, T.G. White, P. Tzeferacos, D.Q. Lamb, G. Gregori, A.A. Schekochihin. *Proton imaging of stochastic magnetic fields*, J. Plasma Phys. 83 (2017)
- A.F.A. Bott, G. Gregori. *Thomson scattering cross section in a magnetized, high-density plasma*, Phys. Rev. E 99, 063204 (2019)
- A.F.A. Bott, S. Cowley, A. A. Schekochihin. *Kinetic stability of Chapman-Enskog plasmas*, (2019, in prep.)
- A.F.A. Bott et al. *Characterising the evolution of dynamo-generated magnetic fields in a turbulent laser plasma*, (2019, in prep.)

Other selected publications

- A. Rigby, J. Katz, A.F.A. Bott, T. G. White, P. Tzeferacos, D. Q. Lamb, D. H. Froula, G. Gregori. *Implementation of a Faraday Rotation Diagnostic at the OMEGA laser facility*, High Power Laser Science and Engineering 6 (2018)
- P. Tzeferacos et al. *Laboratory evidence of dynamo amplification of magnetic fields in a turbulent plasma*, Nat. Comm. 9, 591 (2018)
- P. Tzeferacos et al. *Numerical modelling of laser-driven experiments aiming to demonstrate magnetic field amplification via turbulent dynamo*, Phys. Plasmas 24, 041404 (2017)
- L. Chen et al. *Analogue of cosmic-ray transport in a laboratory turbulent plasma* (2018, submitted to PRL)

Contents

List of Figures

List of Tables

Chapter 1

The fluctuation dynamo

1.1 Introduction to fluctuation dynamo theory

1.1.1 Astrophysical context

The near universality of magnetic fields across many astrophysical environments has been well documented. For example, Faraday-rotation measurements show that in the intra-cluster medium (ICM) there exist stochastic magnetic fields with strengths which are typically $\sim$1-10 μG (Carilli and Taylor 2002). These field strengths are sufficiently large to imply that magnetic fields must be dynamically significant, with associated Lorentz forces acting on plasma bulk motions (Batchelor and Taylor 1950). Understanding how these fields attained such magnitudes is therefore a question at the heart of astrophysics (Kulsrud and Zweibel 2008).

There are many physical phenomena occuring in astrophysical contexts which are capable of generating magnetic fields in plasma. One such example is the Biermann battery mechanism, where mis-aligned electron temperature and density gradients combine to generate fields in initially unmagnetised plasma (Biermann and Schlüter 1951); another is the Weibel instability, which occurs in collisionless plasmas with temperature anisotropies (Weibel 1959, Huntington et al. 2015). However, most of these plasma processes tend to predict field magnitudes in the ICM which are far smaller than those observed (Kulsrud et al. 1997). This necessitates some alternative explanation for how fields are both amplified and maintained at such strength. Such a mechanism is the *fluctuation dynamo*, under which stochastic motions of plasma lead to rapid amplification of some small seed magnetic field (Subramanian et al. 2006, Ryu et al. 2008, Beresnyak 2012, Miniati and Beresnyak 2015).

1.1.2 Characterising stochastic flows and magnetic fields

Before discussing fluctuation dynamo theory, we begin with a brief overview of stochastic flows and magnetic fields and how they are characterised. For our purposes, a stochastic field is one which manifests essentially random behaviour and a wide range of values over both time and space. The exact values attained by a given stochastic field are very sensitive to the initial conditions of the underlying physical system; thus, subtle changes to the initial conditions lead to completely different instantiations of the field. Stochastic motions and magnetic fields are ubiquitous in plasma physics and are generated by a wide range of different mechanisms, including fluid instabilities and microinstabilities (Krall and Trivelpiece 1973, Davidson 1983). It is often the case in plasma that the velocity field $\mathbf{u}(\mathbf{x},t)$ and magnetic field $\mathbf{B}(\mathbf{x},t)$ at a given position $\mathbf{x}$ and time t have both mean and stochastic components (Davidson 2004):

$$\mathbf{u}(\mathbf{x},t) = \bar{\mathbf{u}}(\mathbf{x},t) + \delta\mathbf{u}(\mathbf{x},t) \ , \tag{1.1}$$

$$\mathbf{B}(\mathbf{x},t) = \bar{\mathbf{B}}(\mathbf{x},t) + \delta\mathbf{B}(\mathbf{x},t) \ , \tag{1.2}$$

where $\bar{\mathbf{u}}$ and $\bar{\mathbf{B}}$ are the non-stochastic mean components of the velocity and magnetic field respectively, and $\delta\mathbf{u}$ and $\delta\mathbf{B}$ are the stochastic, fluctuating components. The mean and fluctuating fields are distinguished by introducing an averaging operator $\langle\cdot\rangle$ with the property that $\langle\mathbf{u}\rangle = \bar{\mathbf{u}}$, and $\langle\delta\mathbf{u}\rangle = 0$ (and similarly for the magnetic field). This averaging operator can be interpreted as some type of ensemble average; alternatively, if the characteristic scale ℓ on which the fluctuating fields vary is much smaller than the scale $\bar{l}$ on which the mean fields vary, $\langle\cdot\rangle$ can be defined as being an average over some intermediate scale l which satisfies $\ell \ll l \ll \bar{l}$.

When considering stochastic flows (for example), the precise details of motions at a specific time or location typically provide little physical insight; instead, a statistical characterisation of such flows is more helpful. This is principally because stochastic flows often obey statistical symmetries, even if the exact velocity field of a stochastic flow does not. A particularly important statistical quantity characterising stochastic flows is the *kinetic-energy spectrum*, defined by

$$E(k) \equiv \frac{4\pi^3}{\mathcal{V}} \int \mathrm{d}\Omega\, k^2 \left\langle |\delta\hat{\mathbf{u}}(\mathbf{k})|^2 \right\rangle , \tag{1.3}$$

where $\mathcal{V} \sim l^3$ is the volume of averaging samples over which the spectrum is calculated, $\delta\hat{\mathbf{u}}(\mathbf{k})$ is the three-dimensional Fourier transform of the fluctuating velocity field, $\mathbf{k}$ is the wavevector, $k = |\mathbf{k}|$, and the integral is over solid angles Ω in $\mathbf{k}$ space. The kinetic-energy spectrum does not in general provide a complete description of a stochastic velocity field (see Adler 1981, for a discussion of this point for general stochastic fields). However, the kinetic-energy spectrum is a useful quantity to consider for three reasons. Firstly, it can be used to deduce both the root-mean-square (RMS) velocity field strength $u_{rms} \equiv \langle \delta\mathbf{u}^2 \rangle^{1/2}$ and velocity field correlation length ℓ_u via relations

$$u_{rms} = \left[2 \int_0^\infty \mathrm{d}k\, E(k) \right]^{1/2} , \tag{1.4}$$

$$\ell_u = \frac{\pi}{2} \frac{\int_0^\infty \mathrm{d}k\, k^{-1} E(k)}{\int_0^\infty \mathrm{d}k\, E(k)} . \tag{1.5}$$

Secondly, for the special case of isotropic, incompressible, non-helical Gaussian statistics the kinetic-energy spectrum is sufficient to provide a complete statistical characterisation of a stochastic velocity field (Adler 1981). Thirdly, even for non-Gaussian stochastic velocity fields (as physical fields often are), in many situations the kinetic-energy spectrum has a special significance. It describes energy distribution over wavenumber scales and so is often the focus of theoretical predictions (Gregori et al. 2015).

The equivalent quantity to the kinetic-energy spectrum for stochastic magnetic fields is known as the *magnetic-energy spectrum*; it is defined by

$$E_B(k) \equiv \frac{\pi}{\mathcal{V}} \int \mathrm{d}\Omega \, k^2 \left\langle \left| \delta\hat{\mathbf{B}}(\mathbf{k}) \right|^2 \right\rangle , \tag{1.6}$$

where $\delta\hat{\mathbf{B}}(\mathbf{k})$ is the three-dimensional Fourier transform of the fluctuating magnetic field. Analogously to equations (1.4) and (1.5), relations between the magnetic-energy spectrum and both the fluctuating RMS field strength $B_{rms} \equiv \langle \delta \mathbf{B}^2 \rangle^{1/2}$ and magnetic field correlation length ℓ_B can be written down:

$$B_{rms} = \left[8\pi \int_0^\infty \mathrm{d}k \, E_B(k) \right]^{1/2} , \tag{1.7}$$

$$\ell_B = \frac{\pi}{2} \frac{\int_0^\infty \mathrm{d}k \, k^{-1} E_B(k)}{\int_0^\infty \mathrm{d}k \, E_B(k)} . \tag{1.8}$$

1.1.3 Example: the kinetic-energy spectrum in incompressible hydrodynamic turbulence of a Newtonian fluid

Arguably the most famous example of a theoretical prediction for the kinetic-energy spectrum in a stochastic flow is Kolmogorov's five-thirds law arising for hydrodynamic, incompressible turbulence of a Newtonian fluid (Kolmogorov 1941a,b). Such motion is governed by the Navier-Stokes equations (Batchelor 1953):

$$\frac{\partial \mathbf{u}}{\partial t} + \mathbf{u} \cdot \nabla \mathbf{u} = -\nabla \left(\frac{p}{\rho} \right) + \nu \nabla^2 \mathbf{u} \, , \tag{1.9}$$

$$\nabla \cdot \mathbf{u} = 0 \, , \tag{1.10}$$

where p is the fluid pressure, ρ the (constant) fluid density, and ν the kinematic viscosity. Turbulence emerges in such a fluid if the *fluid Reynolds number* $\mathrm{Re} \equiv UL/\nu$ (for typical flow length scale L and characteristic velocity U) is sufficiently large. A precise mathematical characterisation of turbulence remains a notorious unsolved problem in classical physics.

Nevertheless, one phenomenological description of steady, homogeneous and isotropic turbulence – that is, turbulence whose statistical properties are independent of time, space and direction respectively – which has gained general acceptance is that of the energy cascade (Davidson 2004). First introduced by Richardson (1926), the turbulent velocity $\delta\mathbf{u}$ in a high-Reynolds number Newtonian fluid is described as consisting of a complicated arrangement of 'eddies' spanning many different length scales (for simplicity, we suppose that fluid has no mean flow: $\mathbf{u} = \delta\mathbf{u}$). The fluid Reynolds number associated with the largest eddies, whose scale L and characteristic velocity u_L are determined by the nature of system's external inputs, is by assumption large: $\mathrm{Re}_L = u_L L/\nu \gg 1$. Therefore, the action of viscous dissipation on these eddies is very weak. However, the eddies are also subject to inertial instabilities arising from the shearing motions of other eddies of similar size, which lead to the 'break-up' of the eddies into smaller eddies at the eddy turnover rate $\gamma_L \sim u_L/L$. The energy of the largest eddies is passed down to smaller-scale ones (hence the name 'energy cascade') at a rate γ_C which much be comparable to the eddy turnover rate; thus, the external energy flux Π per unit mass satisfies $\Pi \sim u_L^2 \gamma_C \sim u_L^3/L$. The break-up process also applies in turn to the smaller eddies, creating even smaller eddies. The cascade eventually ceases when eddies become sufficiently small that their viscous dissipation rate γ_ν becomes comparable to their turnover rate $\gamma_\ell \sim u_\ell/\ell$: $\gamma_\nu \sim \nu/\ell_\nu^2 \sim u_{\ell_\nu}/\ell_\nu$, where ℓ_ν is the so-called viscous dissipation scale, and u_{ℓ_ν} is the characteristic velocity of eddies at this scale. The energy cascade is represented pictorially in Figure 1.1. Since viscous dissipation is weak at all but the smallest scales, we conclude that the rate $\epsilon \equiv 2\nu|\nabla\mathbf{u}|^2 \sim \gamma_\nu u_{\ell_\nu}^2$ at which energy is dissipated at the viscous dissipation

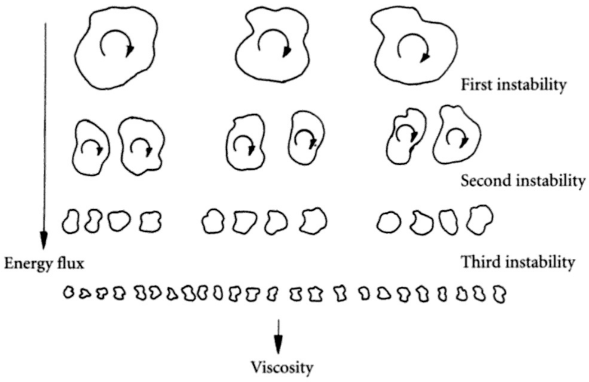

Figure 1.1: The energy-cascade model of hydrodynamic turbulence. Diagram illustrating the turbulent energy cascade towards small scales: the largest eddies are subject to inertial instabilities and break up into smaller eddies. This process repeats until eddies are sufficiently small for them to be subject to viscous dissipation. *Reproduced from Davidson (2004).*

scale must balance the external energy flux Π: this gives (Batchelor 1953)

$$\ell_\nu \sim L \left(\mathrm{Re}_L\right)^{-3/4} \ll L \,, \tag{1.11}$$

$$u_{\ell_\nu} \sim u_L \left(\mathrm{Re}_L\right)^{-1/4} \ll u_L \,, \tag{1.12}$$

$$\gamma_{\ell_\nu} \sim \gamma_L \left(\mathrm{Re}_L\right)^{1/2} \gg \gamma_L \,. \tag{1.13}$$

Building on this conception of turbulence, Kolmogorov (1941a) provides a theory of the statistics of the velocity field u_ℓ at scales ℓ intermediate between the scale of the largest eddies L and the viscous dissipation scale ℓ_ν by postulating that for $\ell \ll L$, eddies would only be affected by larger scales through a globally averaged energy flux, which is itself equal to the globally averaged dissipation $\bar{\epsilon} = 2\nu\langle|\nabla \mathbf{u}|^2\rangle$. He therefore concludes that in the so-called *universal equilibration range*, the velocity field u_ℓ would attain a universal form which on dimensional grounds must be

$$u_\ell = \left(\bar{\epsilon}\ell\right)^{1/3} F\left(\frac{\ell\bar{\epsilon}^{1/4}}{\nu^{3/4}}\right) \,, \tag{1.14}$$

where F is a function common to all hydrodynamic turbulent flows. This line of thinking can be extended further by supposing the length scale ℓ is much greater than the viscous dissipation microscale ℓ_ν: that is, $L \gg \ell \gg \ell_\nu$. In this interval (called the *inertial range*), the turbulent velocity of eddies at this scale cannot depend on the kinematic viscosity ν either, since viscous forces are effectively not acting on the flow. But the only dependence on ν in (1.14) is via the argument of F, which implies that it must be a constant for such ℓ. It follows that for $L \gg \ell \gg \ell_\nu$,

$$u_\ell \sim (\bar{\epsilon}\ell)^{1/3} \,. \tag{1.15}$$

This result can be related to the kinetic-energy spectrum (1.3) by noting that energy per unit mass associated with an eddy of size ℓ is approximately given by

$$u_\ell^2 \sim \int_{1/\ell}^{\infty} \mathrm{d}k \, E(k) \ , \tag{1.16}$$

where there is no contribution from eddies of size greater than ℓ to the integral since the associated velocities are essentially constant over length scales $\sim \ell$ (Batchelor 1953). Applying dimensional analysis to this relation yields *Kolmogorov's spectrum* for $L^{-1} \ll k \ll \ell_\nu^{-1}$:

$$E(k) \sim \bar{\epsilon}^{2/3} k^{-5/3} \,. \tag{1.17}$$

An indicative plot of the whole spectrum, with inertial and universal equilibrium ranges highlighted, is given in Figure 1.2. We note that for a kinetic-energy spectrum

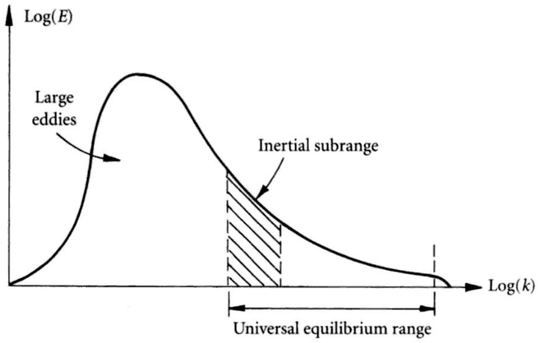

Figure 1.2: The kinetic-energy spectrum for hydrodynamic turbulence. A log-log plot of the characteristic shape of kinetic-energy spectrum $E(k)$ against wavenumber k for isotropic hydrodynamic turbulence. The locations in wavenumber space of the inertial subrange and the universal equilibration range are indicated. *Reproduced from Davidson (2004).*

of this shape, the integral relating the correlation scale ℓ_u defined in equation (1.1.2) to the kinetic-energy spectrum is dominated by wavenumbers k satisfying $k \sim 1/L$ and thus $\ell_u \sim L$.

Since Kolmogorov's theory was first put forward, there have been some important objections raised against his theory - not least Landau's objection that dissipation in a turbulent fluid is intermittent spatially (Landau and Lifshitz 1959). This has the consequence that the flux of energy between scales depends on the locally averaged dissipation rate rather than the globally averaged rate; it can subsequently be shown that this observation is incompatible with Kolmogorov's universality assumption. Nevertheless, in practice, intermittency only results in small corrections to Kolmogorov's theory: in experiments, significant evidence has been found for the existence of both the inertial and universal equilibrium ranges (see Figure 1.3)

1.1.4 Fluctuation dynamo theory in resistive magnetohydrodynamics (resistive MHD)

Having introduced the important concepts of the kinetic- and magnetic-energy spectra for stochastic flows and magnetic fields, we are now well placed to review theories of the fluctuation dynamo. The fluctuation dynamo is best understood in the context of resistive magnetohydrodynamics (resistive MHD), where plasmas are described as magnetised fluids with bulk velocity $\mathbf{u}$ (Cowling 1962, Tobias et al. 2013). Then, the magnetic field $\mathbf{B}$ satisfies the induction equation

$$\frac{\partial \mathbf{B}}{\partial t} = \nabla \times (\mathbf{u} \times \mathbf{B}) + \eta \nabla^2 \mathbf{B} \,, \tag{1.18}$$

for the plasma resistivity η. The relative importance of the inductive and diffusive terms on the right hand side of (1.18) at some characteristic length scale L is

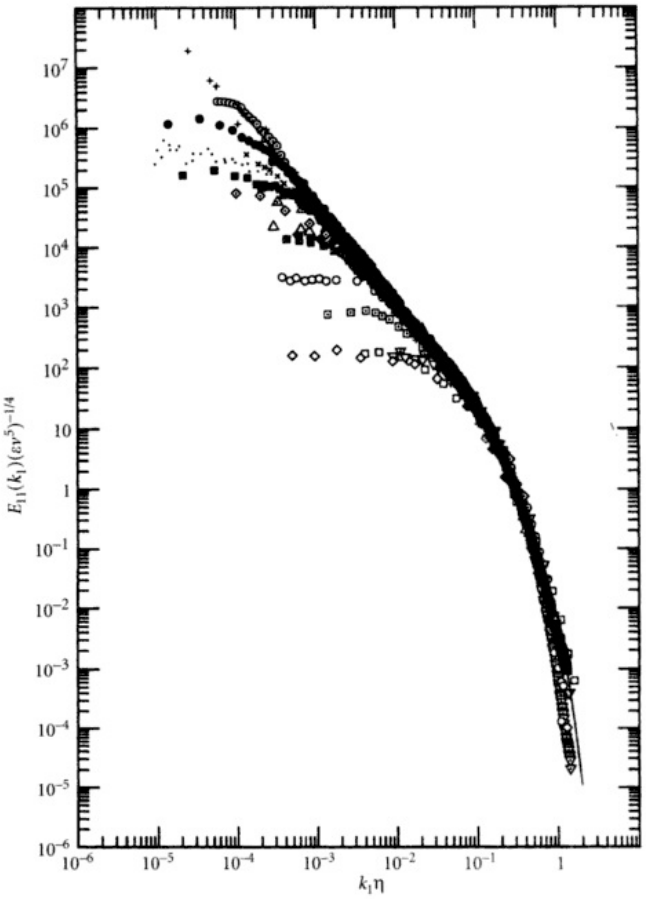

Figure 1.3: Experimental evidence for the Kolmogorov model of hydrodynamic turbulence. Plot of energy spectrum against wavenumber, normalised by the Kolmogorov scales, obtained from a range of experiments incorporating turbulent jets, wakes, boundary layers and grid turbulence. *Presented in Davidson (2004); here,* $\ell_\nu \mapsto \eta$.

determined by the magnitude of the *magnetic Reynolds number* Rm, defined by

$$\mathrm{Rm}_\ell \equiv \frac{UL}{\eta}\,, \tag{1.19}$$

where U is the characteristic velocity of the magnetised fluid. If $\mathrm{Rm} \ll 1$, field non-unformities are smoothed out diffusively. If on the other hand $\mathrm{Rm} \gg 1$, then the inductive term dominates and field lines move with the flow. As a result, field lines can be stretched, potentially leading to amplification.

The so-called kinematic MHD dynamo problem – that is, dynamos where the magnetic field is initially dynamically insignificant – has been studied comprehensively (see Schekochihin et al. 2002a, and references therein). Such studies have demonstrated that it is certainly not the case that all flows result in dynamo action: it can be proven analytically, for example, that two-dimensional flows or flows with spherical symmetry cannot sustain long-term dynamo action (Cowling 1933, Backus and Chandrasekhar 1956, Cowling 1957). It can also be shown that flows must have sufficiently large Rm for diffusive magnetic-field decay to be prevented (Childress and Gilbert 1995). Nevertheless, various MHD flows have been found to be capable of supporting dynamo action: for example, the Roberts (Roberts and Bullard 1972) or Ponomarenko dynamos (Ponomarenko 1973). Furthermore, it has also been proven that 'fast' dynamos – that is, dynamos which amplify fields at the rate U/L in the limit Rm $\to \infty$ — are only possible if the flow is chaotic (Vishik 1989, Galloway and Proctor 1992). This suggests that stochastic flows (including turbulent ones) are by definition prime candidates for effective dynamo action – a suggestion verified both analytically (Kazantsev 1968) and in numerical simulations (the first of which chronologically being Meneguzzi et al. 1981).

How stochastic motions interact with a magnetic field to produce net growth in field energy in the kinematic dynamo regime is most simply described heuristically via scaling arguments (Schekochihin et al. 2007). In Kolmogorov turbulence in the inertial range, it was argued in Section 1.1.2 that the velocity u_ℓ at scale ℓ satisfies scaling (1.15): $u_\ell \propto \ell^{1/3}$. This implies that the rate γ_ℓ at which field lines are stretched by motions with characteristic scale ℓ – which is equal to the eddy turnover rate γ_ℓ – satisfies $\gamma_\ell \propto \ell^{-2/3}$. Thus, field-line stretching happens most rapidly at small scales and at a much faster rate than the turnover rate u_{rms}/L of the largest-scale motions. Dominant field growth occurs first at the so-called *resistive scale* ℓ_η, which is defined as the length-scale at which $\ell \sim \eta/u_\ell$.

The scalings of the resistive scale and the magnetic-field growth rate depends on the magnetic Prandtl number of the flow, defined by

$$\mathrm{Pr} \equiv \frac{\nu}{\eta} = \frac{\mathrm{Rm}}{\mathrm{Re}} \, . \tag{1.20}$$

In the $\mathrm{Pr} \gg 1$ regime, the resistive scale is much smaller than the viscous dissipation scale: $l_\eta/l_\nu \sim \mathrm{Pr}^{-1/2} \ll 1$ (Schekochihin et al. 2004c). This is deep inside the viscous range; motions at such scale are still random, but spatially smooth (see Figure 1.4, left-hand panels). The dominant growth rate γ is simply the turnover rate of eddies at the viscous dissipation scale, which can be shown to be $\gamma \sim \mathrm{Re}^{1/2} u_{rms}/L$. The smooth nature of motions allows for analytical calculations of the magnetic-energy spectrum to be carried out in this limit: for $l_\nu^{-1} \ll k \ll l_\eta^{-1}$, the *Kazantsev spectrum* $E_B(k) \propto k^{3/2}$ is obtained (Kazantsev 1968, Kulsrud and Anderson 1992). The peak of the predicted spectrum is at the resistive scale. Numerical simulations

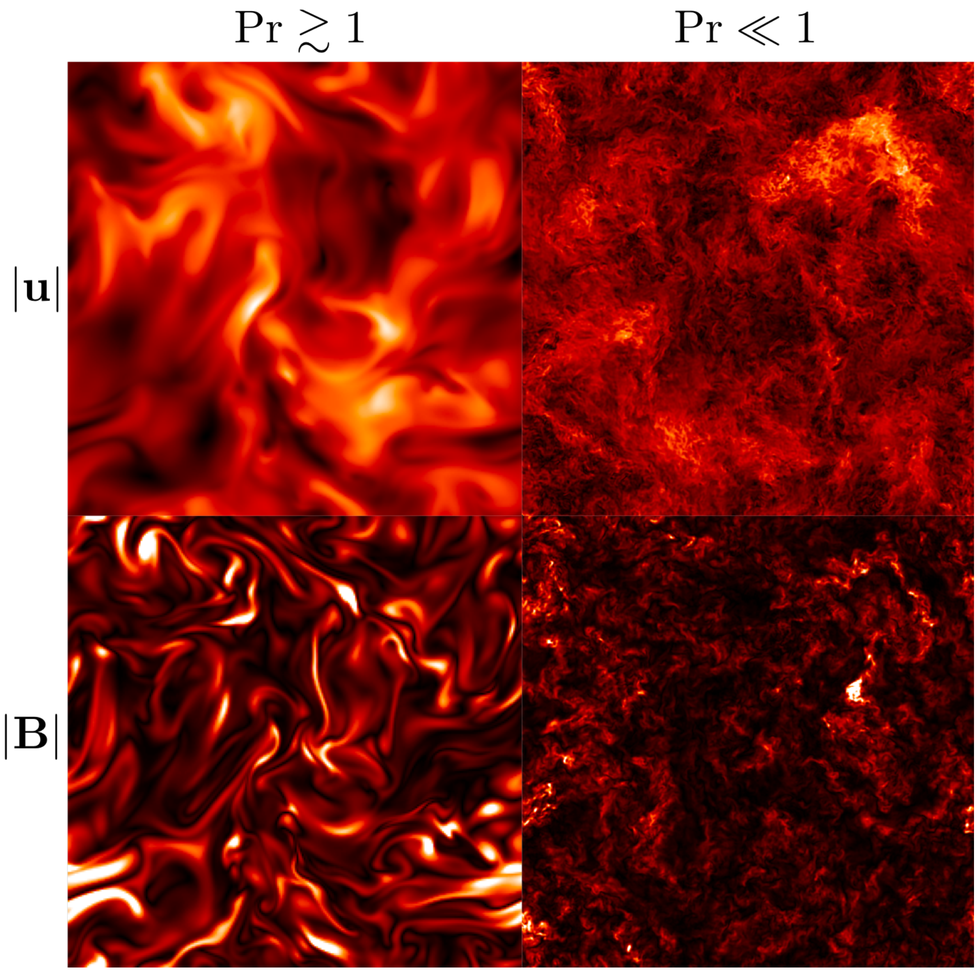

Figure 1.4: Numerical simulations of the fluctuation dynamo: high versus low magnetic Prandtl number. Cross-sections of the absolute values of the velocity (top) and the (growing) magnetic field (bottom) for two numerical MHD simulations of the fluctuation dynamo (resolution 512^3). Lighter/darker regions correspond to stronger/weaker fields respectively. The left column has $\mathrm{Re} = \mathrm{Rm} = 440$, and so $\mathrm{Pr} = 1$, while the right column has $\mathrm{Rm} = 430$, $\mathrm{Re} = 6200$ ($\mathrm{Pr} = 0.0694$). *Adapted from Schekochihin et al. (2007).*

of the kinematic dynamo in the Pr $\gg 1$ regime have demonstrated the feasibility of dynamo action due to stochastic motions, provided that Rm is larger than a critical value $\mathrm{Rm_c} \approx 50$; they have also verified the various theoretical predictions concerning scales, growth rates and spectra (Schekochihin et al. 2004c, Haugen et al. 2004). Simulations of the Pr $\gtrsim 1$ regime (which are typically easier to implement numerically) have also been performed and the results are similar to those of the Pr $\gg 1$ regime (Kida et al. 1991, Kleva and Drake 1995, Miller et al. 1996, Cho and Vishniac 2000, Haugen et al. 2003).

In the Pr $\ll 1$ regime (but with Rm $\gg 1$), the resistive scale $l_\eta/l_\nu \sim \mathrm{Pr}^{-3/4}$ is inside the turbulent inertial range (Moffatt 1961). Dominant stretching motions are therefore not smooth, but chaotic (see Figure 1.4, right-hand panels). Unlike the Pr $\gg 1$ regime, there does not exist a simple physical argument illustrating the existence (or not) of dynamo action in this case, for the simple reason that it is not clear *a priori* whether turbulent stretching of the field overcomes turbulent diffusion (Schekochihin et al. 2007). Analytical treatments of the regime are more challenging to perform, usually requiring invocation of some turbulent closure hypothesis (Kleeorin and Rogachevskii 1994, Kleeorin et al. 1996). Nonetheless, simulations have indicated that dynamo action is still possible in the Pr $\ll 1$ regime – but only if the more restrictive magnetic Reynolds number threshold $\mathrm{Rm_c} \approx 200$ is surpassed (Schekochihin et al. 2004a, 2005b). The magnetic-energy spectrum in this regime is found to have quite a different shape to that for the Pr $\gtrsim 1$ regime: as Pr decreases for fixed Rm, the peak of the magnetic-energy spectrum moves from the resistive scale to larger scales and the spectral slope around the resistive scale becomes negative (see Figure 1.5, left-hand panel). For wavenumbers satisfying $L^{-1} \ll k \ll l_\eta^{-1}$, there is some similarity to the power law $E_B(k) \propto k^{-1}$, which also emerges from considerations of turbulent induction of small-scale magnetic fields from a large-scale field (Ruzmaikin and Shukurov 1982, Kleeorin and Rogachevskii 1994, Kleeorin et al. 1996). For $k \gg l_\eta^{-1}$, the spectrum becomes much steeper, matching the Golitsyn spectrum: $E_B(k) \propto k^{-11/3}$ (Golitsyn 1960, Moffatt 1961).

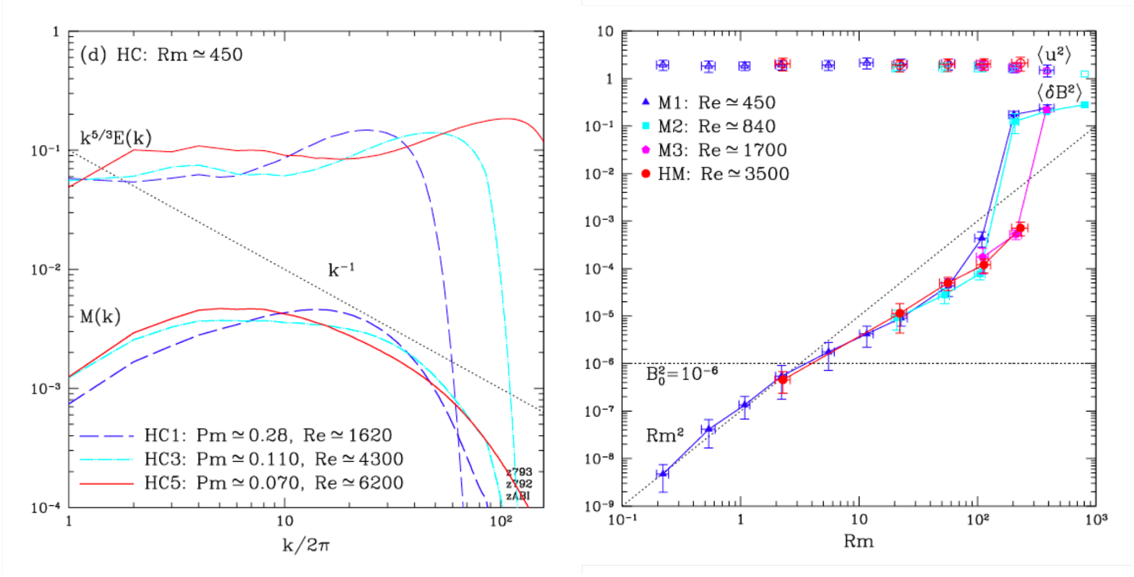

Figure 1.5: Key numerical results from MHD simulations of the fluctuation dynamo. Left: evolution of the magnetic-energy spectrum for decreasing Pr. Right: value of magnetic Reynolds number Rm against the RMS fluctuating magnetic-field strength (squared) $B_{rms}^2 = \langle \delta \mathbf{B}^2 \rangle$ at saturation. For $\mathrm{Rm} < \mathrm{Rm_c}$, the simulations include a uniform mean field, with initial (normalised) magnetic field strength $\bar{B} = 10^{-3}$. For $\mathrm{Rm} > \mathrm{Rm_c}$, runs with no mean field are assumed. The reference slope corresponds to predicted value of B_{rms}^2 arising in the limit $\mathrm{Rm} \ll 1$. *Adapted from Schekochihin et al. (2007); in their paper,* $E_B(k) \mapsto M(k)$, $\mathrm{Pr} \mapsto \mathrm{Pm}$ *and* $\bar{B} \mapsto B_0$.

The Golitsyn spectrum is also obtained when $\mathrm{Rm} \lesssim 1$.

For arbitrary Pr, amplification persists until field strengths come to approximate equipartition with the fluid kinetic energy if $\mathrm{Rm} > \mathrm{Rm_c}$ (Schekochihin et al. 2004c, Haugen et al. 2004) At this point, magnetic forces back-react on the flow via Lorentz forces; in MHD, the fluid momentum equation now includes a term dependent on the magnetic field (Tobias et al. 2013):

$$\frac{\partial \mathbf{u}}{\partial t} + \mathbf{u} \cdot \nabla \mathbf{u} = -\nabla \left(\frac{p}{\rho} \right) + \frac{(\nabla \times \mathbf{B}) \times \mathbf{B}}{4\pi\rho} + \nu \nabla^2 \mathbf{u} \,. \tag{1.21}$$

Simulations indicate that the magnetic field acts in such a way as to saturate growth at the resistive scale; then follows a period of slower field energy growth at increasingly large scales (resulting in a broad magnetic energy spectrum) until global (though non-uniform) energy equipartition is achieved (Schekochihin et al. 2004b). The precise saturated value of the magnetic field depends on how the system is physically driven, as well as Pr and Rm (Schekochihin et al. 2004c, Haugen et al. 2004); however, it is typically found that the magnetic energy is only a finite fraction of the kinetic energy. This is because the magnetic field is observed to be more intermittent than the velocity field. The resulting system is nonlinear even in incompressible MHD, rendering analytic characterisations of saturation extremely challenging. Nonetheless, there do exist a number of calculations supporting these numerical observations (Boldyrev 2001, Schekochihin et al. 2002b,c, Subramanian 2003, Cattaneo and Tobias 2009). If $\mathrm{Rm}_{\mathrm{c}} > \mathrm{Rm} \gg 1$, amplification of the magnetic field can still occur via stochastic tangling of the field; however, the saturated field strength depends on Rm and can be far below dynamical significance (see Figure 1.5, right panel). Thus, a key signature of genuine dynamo action is amplification to dynamical values.

1.1.5 Current theoretical debates in fluctuation dynamo theory

It is clear that within the framework of MHD, magnetic-field amplification via the fluctuation dynamo can account for fields with dynamical strengths. Furthermore, the magnetic Reynolds number of the ICM is thought to be exceptionally large and thus well above Rm_{c}: $\mathrm{Rm} \sim 10^{29}$ (Gregori et al. 2015). However, there remain serious theoretical questions concerning the viability of MHD dynamo theory as a satisfactory explanation for the origin of magnetic fields in the ICM. One such issue is the applicability of conventional MHD to actual astrophysical plasmas, which are typically only weakly collisional and composed of electrons and ions whose Larmor radii are many orders of magnitude smaller than their respective mean-free-paths (Schekochihin and Cowley 2006). This can alter the relevant plasma dynamics radically (Helander and Sigmar 2005, Schekochihin et al. 2005a, Kunz et al. 2014). For example, it is known that dynamo cannot be possible in plasma where the magnetic moment of particles is conserved, a corollary of which is that dynamo action is impossible in certain models sometimes invoked to describe weakly collisional plasma: kinetic magnetohydrodynamics, or the Chew-Goldberger-Low fluid equations (Helander et al. 2016).

That being said, there are still good reasons for believing that the fluctuation dynamo is a viable explanation for the presence of strong fields in the ICM – not least astrophysical observations showing that it is indeed turbulent (see, for example, Inogamov and Sunyaev 2003, Hitomi Collaboration 2016). There is also recent numerical evidence to indicate that the dynamo process can occur in both unmagnetised collisionless plasmas, albeit at a somewhat increased magnetic Reynolds number (Rincon et al. 2016), as well as magnetised collisionless plasma (St-Onge and Kunz 2018). However, a powerful way of supporting the theory would be direct evidence of the process in an actual plasma.

1.2 Experimental investigations of the fluctuation dynamo

1.2.1 Previous experiments

Dynamo processes have been investigated in the laboratory in various ways, including liquid metal experiments (Gailitis et al. 2000, 2001, Monchaux et al. 2007) and laser-plasma experiments (Meinecke et al. 2014, 2015). However, a bona fide fluctuation dynamo resulting in equipartition of magnetic and kinetic energy has not yet been replicated in the laboratory due to the difficulty of achieving the high magnetic Reynolds numbers required for the process to be possible. The aforementioned liquid metal experiments – which are inspired by known dynamo flows such as the Roberts or Pondarenko dynamos – typically have $\mathrm{Rm} \lesssim 100$, while previous attempts at a plasma dynamo at a laser facility reached $\mathrm{Rm} \sim 1$. Nevertheless, the latter approach has the advantage of scaling well with increasing laser energy, which results in both higher flow velocities and decreased resistivity (Gregori et al. 2015).

1.2.2 Experiment on the OMEGA laser facility: overview

A recent laser-plasma experiment demonstrated compelling evidence for the feasibility of the fluctuation dynamo in a turbulent plasma for the first time (Tzeferacos et al. 2018). The experiments were performed at the OMEGA laser facility at the Laboratory for Laser Energetics of the University of Rochester (Boehly et al. 1997) using a platform whose design was motivated by a previous laser-plasma experiment investigating turbulent amplification of magnetic fields on a smaller laser facility (Meinecke et al. 2015). In the experiment, ten long-pulse laser beams are applied to the backs of two opposing chlorine-doped plastic foils, creating supersonic plasma jets from their fronts. These jets then pass through asymmetric grids, before colliding at the target's centre. On collision, the jets coalesce, forming an 'interaction region' of plasma (demarcated by two shocks) whose density and temperature are significantly greater than that of either jet. The inhomogeneity and asymmetry of the initial plasma-jet density and flow profiles gives rise to significant shearing motion in the interaction region; this facilitates Kelvin-Helmholtz instabilities on a range of length scales (Hughes 1991), and thus significant stochasticity emerges in the velocity profile as the interaction region develops. In contrast to the initial jet motion, stochastic motions in the interaction region are subsonic, because of their reduced characteristic flow speeds and the interaction-region plasma's higher temperature. Further details on the experimental setup are given in Figure 1.6.

To aid the interpretation and design of the experiment (including the details of the targets and the grids), extensive two-dimensional and three-dimensional radiation-MHD simulations of the experimental set-up were carried out (see Figure 1.7) using the FLASH code (Fryxell et al. 2000, Dubey et al. 2013). The FLASH code is a parallel, adaptive-mesh-refinement (AMR), finite-volume Eulerian code with high-energy-density capabilities, including a three-temperature MHD solver (Lee 2013), non-ideal MHD effects such as magnetic resistivity (Tzeferacos et al. 2015), the Biermann battery (Fatenejad et al. 2013, Graziani et al. 2015), implicit thermal conduction and

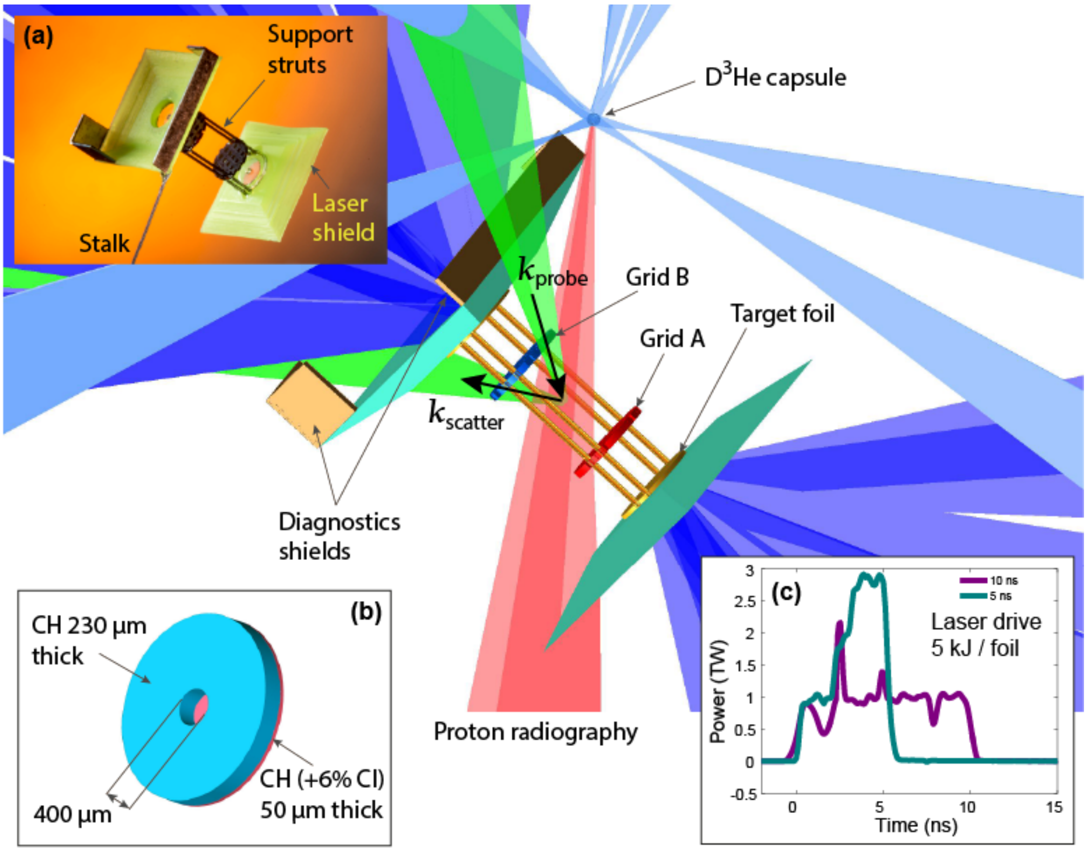

Figure 1.6: Laser, target and diagnostic configuration. The main target – see photo in sub-panel (a) – consists of two CH foils doped with 6% chlorine in atomic number – sub-panel (b) – that are separated by 8 mm. Each foil is illuminated by ten 500 J, 1 ns pulse length, frequency tripled (351 nm wavelength) laser beams with 800 μm spot diameter. The beams are stacked in time to achieve the two pulse profiles shown in sub-panel (c). An additional set of 17 beams, all fired simultaneously, are used to implode a proton backligher capsule (see Section 1.4 for more details). The two grids are placed 4 mm apart, with a 300 μm hole width and 300 μm hole spacing. Grid A has the central hole aligned on the center axis connecting the two foils, while grid B has the hole pattern shifted so that the central axis crosses the middle point between two holes. Thomson scattering uses a 30 J, 1 ns, frequency doubled (wavelength $\lambda = 526.5$ nm) laser beam to probe the plasma on the axis of the flow, 400 μm from the center and in a 50 μm focal spot, towards grid B. The scattered light is collected with 63° scattering angle and the geometry is such that the scattering wavenumber $\mathbf{k} = \mathbf{k}_{\text{scatter}} - \mathbf{k}_{\text{probe}}$, where $|\mathbf{k}_{\text{scatter}}| \approx |\mathbf{k}_{\text{probe}}| = 2\pi/\lambda$, is parallel to the axis of the flow. *Reproduced from Tzeferacos et al. (2018).*

radiation transport in the multi-group diffusion approximation, tabulated equations of state and material opacities and laser beams modelled with geometric-optics ray-tracing and inverse-Bremsstrahlung energy deposition. A detailed description of the numerical simulations carried out in conjunction with the experiment are described in Tzeferacos et al. (2017).

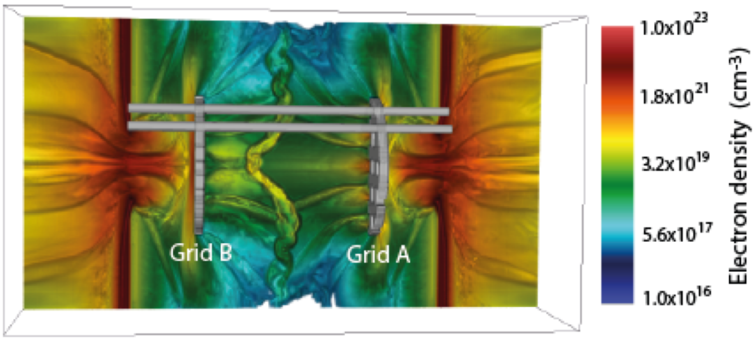

Figure 1.7: FLASH simulations of OMEGA experiment. Rendering of the electron density from three-dimensional FLASH simulations at $t = 35$ ns. The three-dimensional simulation of the experiment was performed on the Mira supercomputer at the Argonne National Laboratory (USA).

1.2.3 Experiment on the OMEGA laser facility: plasma characterisation

A set of diagnostics was fielded to measure the properties of the flow, its turbulence and the magnetic field generated by it (see Figures 1.8 and 1.9). Here, we provide a summary of the key results: full details of the experiment are give in the main text and Supplementary Information of Tzeferacos et al. (2018).

Self-emitted soft X-rays (< 2 keV) enhanced by the presence of a small amount of chlorine in the plasma were used to characterise the interaction of the colliding flow and assess properties of the resulting plasma inhomogeneities. X-ray images taken 35 ns after the drive-beam pulse's initiation (which is after the two laser-produced jets collide) indicated a broad non-uniform spatial distribution of emission over a region more than 1 mm across (see Figure 1.8a). In order to characterise the state of the turbulent plasma produced by the collision, power spectra of the X-ray intensity fluctuations were extracted from the experimental data using a two-dimensional fast Fourier transform (see Figure 1.8b). Under the assumption of isotropic statistics, fluctuations in the detected X-ray intensity can be directly related to density fluctuations (Churazov et al. 2012). The power spectrum of the density fluctuations extracted from the X-ray data was consistent with the peak of the spectrum being at

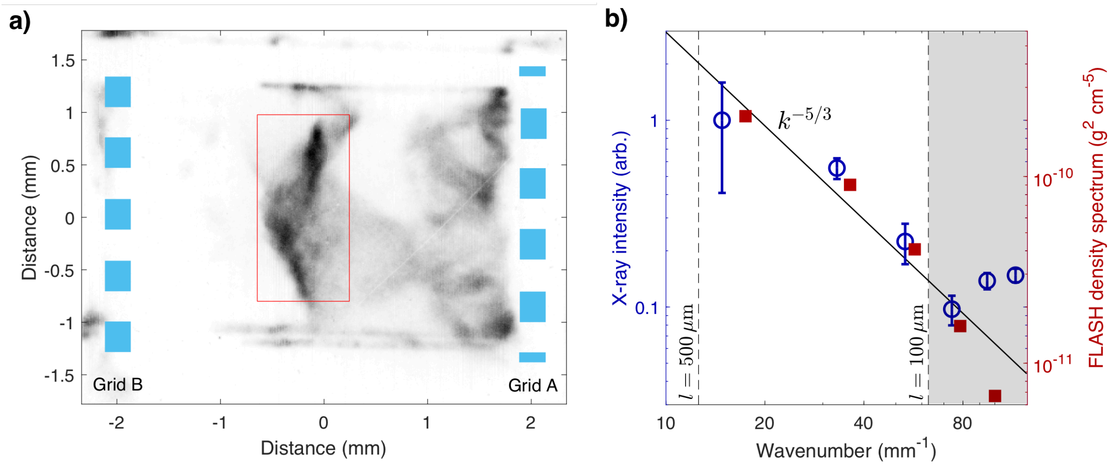

Figure 1.8: Characterisation of the plasma turbulence. **a)** X-ray pinhole image of the colliding flows 35 ns after the laser drive, using the 5 ns pulse profile. The image was recorded onto a framing camera with ~1 ns gate width and filtered with 0.5 μm C_2H_4 and 0.15 μm Al. The pinhole diameter is 50 μm. **b)** The open blue circles give the power spectrum of the X-ray emission from the collision region, defined by the rectangular region shown in panel a). The power spectrum has been filtered to remove edge effects and image defects. The error bars on the spectrum are calculated by dividing the rectangular region horizontally into three equally sized regions, and calculating the spectrum of each region; the standard error of the spectrum of the whole region is then determined assuming the three regions represent independent samples of the density fluctuations. More details of this procedure are given in Supplementary Method 2 of Tzeferacos et al. (2018). The shaded region at high wavenumbers is dominated by noise. The spectrum of the density fluctuations, as obtained from FLASH simulations in the turbulent region, is shown with red squares. *Adapted from Tzeferacos et al. (2018)*

wavenumber $k \approx 10\,\mathrm{mm}^{-1}$, with a Kolmogorov power law ($k^{-5/3}$ scaling) for larger wavenumbers. Experimental data from other diagnostics (see below) indicated that the plasma motions were indeed mainly subsonic (Mach number $\lesssim 1$ at the outer scale); as a result, density fluctuations injected at large scales behave as a passive scalar and the spectra of the density and velocity fluctuations should be the same (Zhuravleva et al. 2014). Given the uncertainty on the spectral measurement (depicted in Figure 1.8b), and the relatively narrow range of wavenumbers over which sub-driving scale fluctuations are resolved, the uncertainty on the spectral power law index in the inertial range of the turbulence is likely ~30%, which prohibits a firm conclusion (from the X-ray emission data alone) as to whether the stochastic motion in the interaction region can be characterised precisely as developed, subsonic, hydrodynamic turbulence. That being said, the uncertainty is sufficiently small to guarantee three things: first, that the wavelength associated with the peak of the spectrum is approximately the grid periodicity ($L \approx 600\,\mu\mathrm{m}$); second, that the majority of turbulent kinetic energy is concentrated near this (driving) scale; third, that plasma is certainly manifesting stochastic motions on a range of scales. These conclusions are also confirmed by FLASH simulations (Tzeferacos et al. 2017), which predicted subsonic motions of the plasma following the flow collision. Furthermore, the power spectrum of density fluctuations calculated directly from FLASH showed the same Kolmogorov power law scaling as the data (Figures 1.8b).

The Thomson scattering diagnostic (see Figure 1.6) allowed for the simultaneous measurement of three different velocities associated with the flow (Evans and Katzenstein 1969). First, the bulk plasma-flow velocity – composed of a mean flow velocity $\bar{u}$ and outer-scale turbulent velocity u_L – was obtained from the measurements of shifts (in frequency) of the scattered light resulting from the bulk plasma moving towards grid B. Second, the separation of the ion-acoustic waves is an accurate measure of the sound speed and thus of the electron temperature, T_e. Third, the FLASH prediction of equal ion and electron temperatures allowed for the inference from the broadening of the ion-acoustic features of the turbulent velocity u_ℓ on the scale $\ell = l_\mathrm{TS} \sim 50\ \mu\mathrm{m}$ (the Thomson scattering focal spot) (Inogamov and Sunyaev 2003, Meinecke et al. 2015).

Based on these measurements, it was found that, before collision, the two plasma flows move towards each other with axial mean velocity $\bar{u} \lesssim 200$ km/s in the laboratory rest-frame and have electron temperature $T_\mathrm{e} \approx 220$ eV. After the collision, the axial flow slows down to 20-40 km/s, with motions being converted into transverse components. The electron temperature increases considerably, reaching $T_\mathrm{e} \approx 450$ eV (Figure 1.9). The measured time-averaged (RMS) turbulent velocity at scale $\ell \sim l_\mathrm{TS}$ is $u_\ell \sim 55$ km/s. If u_ℓ has Kolmogorov scaling [c.f equation (1.15)], the turbulent velocity at the outer scale must therefore be $u_L \sim u_\ell (L/\ell)^{1/3} \approx 100$ km/s. Electron density estimates can be obtained from the measured total intensity of the Thomson scattered radiation, to give a value $n_\mathrm{e} \approx 10^{20}\,\mathrm{cm}^{-3}$, which is also consis-

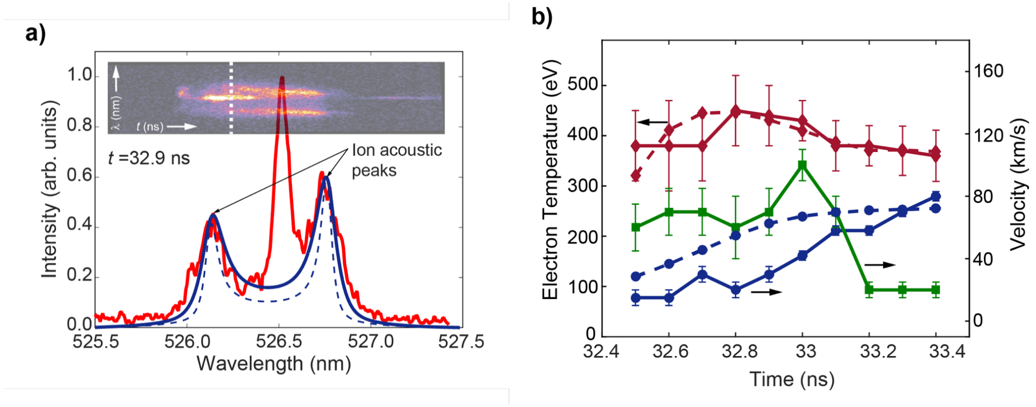

Figure 1.9: Thomson scattering measurements. Electron temperatures and flow velocities are obtained by fitting the experimental data with the frequency dependent Thomson scattering cross section (Evans and Katzenstein 1969). In the fitting procedure an electron density of $\lesssim 10^{20}$ cm^{-3} is assumed (as determined by an absolute calibration of the Thomson-scattered laser light and corroborated by FLASH simulations). At these electron densities, the frequency distribution of the scattered light does not depend on the electron density, which only provides an overall normalisation factor. **a)** Thomson scattering data (red solid line) at 32.9 ns obtained from a target driven with the 5 ns pulse profile. The blue dashed line corresponds to a plasma in thermodynamic equilibrium (assuming equal electron and ion temperatures). The central peak is due to stray light at the probe laser wavelength (and it is used to determine the instrumental resolution of the spectrometer). The blue solid line corresponds to the case in which additional broadening due to turbulence is included in the fitting procedure. The inset in the top panel shows the time-streaked image of the Thomson scattered light. The resolution of the streak camera is $\sim$ 50 ps and the Thomson scattering signal is fitted every 100 ps. **b)** Flow velocity towards grid B (full blue circles), turbulent velocity (full green squares), and electron temperature (full red diamonds) as measured by Thomson scattering for the case of a target driven with 5 ns laser profile. FLASH simulation results for the electron temperature and flow velocity in the probe volume are also reported in dashed lines. The error bars are estimated from the χ^2 fit of the data. *Adapted from Tzeferacos et al. (2018)*

tent with values predicted by FLASH simulations (Tzeferacos et al. 2017). A plasma with these parameters can be well described as being collisional, and in the resistive magneto-hydrodynamic (MHD) regime. For an MHD-type plasma, the characteristic fluid and magnetic Reynolds numbers attained in the experiment were estimated: $\mathrm{Re}_L \approx u_L L/\nu \sim 1200$ (ν is the viscosity) and $\mathrm{Rm}_L \approx 600$, using $L \approx 600$ μm, the characteristic driving scale determined by the average separation between grid openings. The experiment thus achieved conditions where Rm_L is comfortably larger than the expected critical magnetic Reynolds number required for the low-magnetic Prandtl number fluctuation dynamo (Schekochihin et al. 2007).

1.2.4 Experiment on the OMEGA laser facility: magnetic field evolution in FLASH simulations

The feasibility of dynamo action in the set-up is most simply illustrated by the FLASH simulation, in which the evolution of the magnetic field in a 500 μm control volume following the plasma jet and the interaction region can be tracked directly (see Figure 1.10a). The simulated time history of the RMS and maximum magnetic field strengths in this control volume is given in Figure 1.10b. In the FLASH simulation, the initial magnetic field present in the control volume – which is generated near the foil via the Biermann battery mechanism (Stamper et al. 1971) – decays as the jet propagates towards the centre of the target. This is due to the plasma's finite resistivity and also dilution of the magnetic field as the jet expands. The field strength just before collision is found to be $\sim$ 4 kG. Subsequent to collision, the magnetic field strength increases rapidly, before saturating around 5 ns subsequent to collision. RMS and peak field strengths are of the order of $\sim 60\,$kG and $\sim 300\,$kG respectively. Thus in the FLASH simulations, the magnetic field is amplified significantly. That growth is indeed due to motion of the plasma can be demonstrated by switching off the Biermann battery (the only other possible source of fields in the simulation) in the interaction region (shown in Figure 1.10a), for times $\geq$ 23 ns (corresponding to times after the jet collision). The resulting time histories (dashed lines in Figure 1.10b) do not show significant difference from those carried out including the Biermann battery at all times – solid lines in Figure 1.10b. This applies to both peak and RMS values of the magnetic field in the interaction region.

Examining the structure of the magnetic field in more detail, the magnetic-energy spectrum of the field in the control volume at a particular time can be calculated directly and compared to the kinetic energy spectrum (Figure 1.10c). The former is consistent with a k^{-1} power-law dependence for wavenumbers $\gtrsim 30\,\mathrm{mm}^{-1}$ (corresponding to structures with wavelengths $\lesssim 200\,\mu$m). This spectral slope, which is considerably shallower than the Kolmogorov-like spectrum found for the kinetic

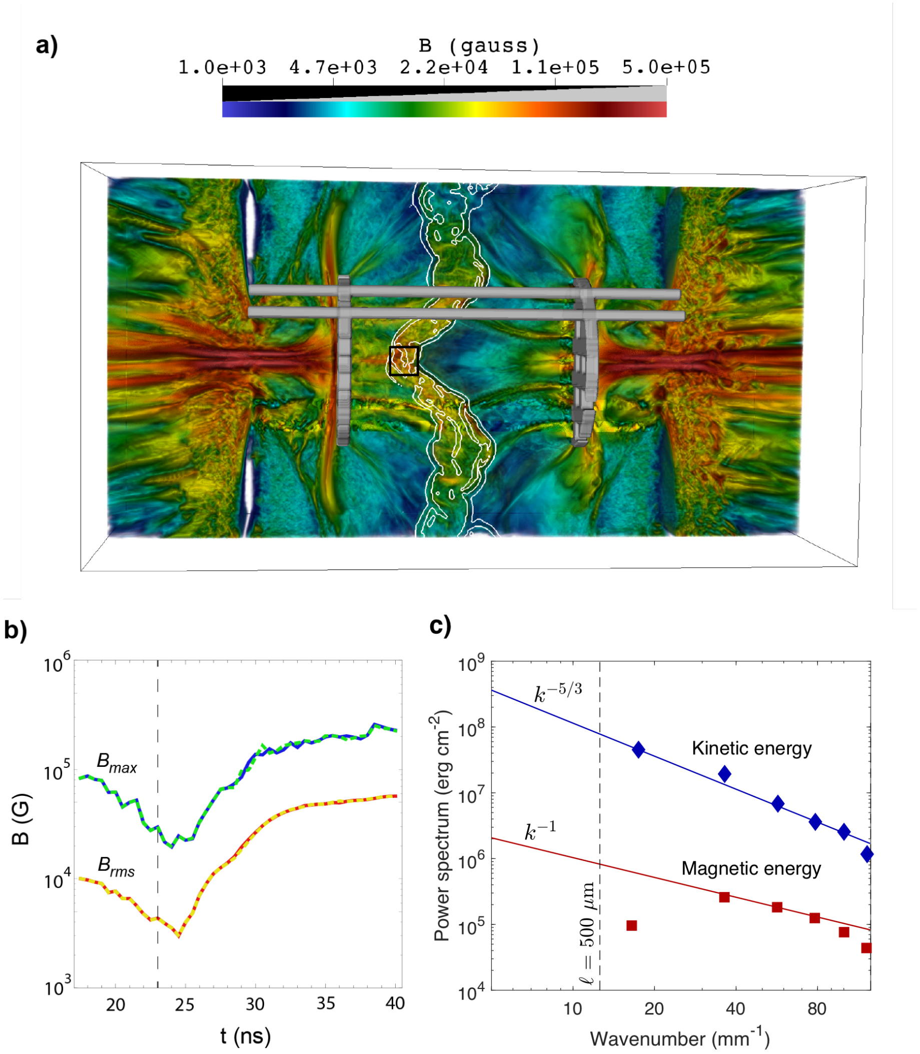

Figure 1.10: Magnetic-field generation in FLASH simulations. **a)** Rendering of the FLASH magnetic field strength 40 ns after drive-beam pulse initiation for the 5 ns pulse profile. The control volume is denoted in black and the region in which the Biermann battery is subsequently turned off is outlined by white boundaries. **b)** Evolution of maximum field strength, B_{max}, and the RMS field, B_{rms}, in the control volume indicated by a square box in panel a). The plot includes both the results of the full simulation (solid lines) and a simulation where the Biermann battery was switched off (dashed coloured lines) after jet collision (i.e. for times to the right of the vertical gray dashed line). **c)** Blue diamonds: power spectrum of the kinetic energy from FLASH simulations. Red squares: power spectrum of magnetic energy from FLASH simulations. *Adapted from Tzeferacos et al. (2018)*

energy, is similar to the spectra of tangled fields near and above the dynamo threshold discussed in Section 1.1.4 for the Pm $\ll$ 1 regime; it corresponds to significant magnetic energy at both smaller and larger scales.

1.2.5 Experiment on the OMEGA laser facility: Faraday-rotation measurements

To assess whether the fluctuation dynamo was indeed operating in the experiment, magnetic field measurements were performed using two techniques. The first of these was a Faraday-rotation set-up in which the rotation of the polarisation angle of Thomson scattered light provided an electron-density-weighted measure of the variation of the longitudinal component of the magnetic field integrated along the beam path (Segre 1999). The measured rotation angle for the time interval corresponding to the Thomson scattering measurements presented in Figure 1.9 is shown in Figure 1.11; it is found to fluctuate over a few degrees. A full description of the Faraday-rotation diagnostic as implemented in this experiment is provided by Rigby et al. (2018).

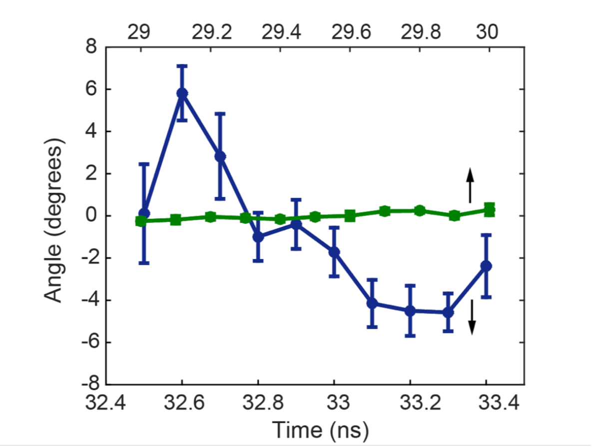

Figure 1.11: Faraday-rotation measurements. Estimated Faraday-rotation data from the Thomson scattering data. This was done by separating the scattered light into two orthogonal polarisations (see Supplementary Method 3 of Tzeferacos et al. (2018)). The blue line corresponds to the same conditions as for Figure 1.9b. The green line was obtained from an experiment involving a single-flow, single-grid experiment only, when the magnetic field was significantly smaller. The errors are determined by the standard deviation of the data within the shot. *Adapted from Tzeferacos et al. (2018)*

We can relate this measurement to the magnetic field by noting that when the Faraday-rotation angle $\Delta\vartheta$ is small, it is given (in Gaussian units) by (Ensslin and

Vogt 2003)

$$\Delta\vartheta = \frac{\lambda^2 e^3}{2\pi m_e^2 c^4} \int_0^{2l_{\rm path}} n_e(s)\, B_{\|}(s)\, {\rm d}s\,, \tag{1.22}$$

where λ is the probe laser beam's wavelength, e the elementary charge, m_e the electron mass, s the distance along the path, and $B_{\|}$ the component of the magnetic field parallel to the beam path. Twice the Thomson-scattering beam path-length $l_{\rm path}$ is used for the total path length of the integral, because the geometry of the interaction region was such that the Thomson scattering volume lies on the opposing side to that from which the probe beam originates. The incident laser's wavelength is $\lambda = 5.27 \times 10^{-5}\,$cm, implying that

$$\int_0^{2l_{\rm path}} n_{\rm e}(s)\, B_{\|}(s)\, {\rm d}s = 2.4 \times 10^{23} \Delta\vartheta \,{\rm G\ cm}^{-2}. \tag{1.23}$$

If the mean magnetic field is small or zero, the mean of the Faraday-rotation measure should vanish and so measured values of it correspond to the standard deviation of the line-of-sight integral in equation (1.23). This can be estimated by a random-walk argument: assuming that the magnetic structures with largest amplitudes have characteristic scale $\tilde{\ell}_B$, the typical deviation is equal to the deviation acquired across one correlated structure multiplied by the square root of the number of such structures encountered (as an aside, we note that $\tilde{\ell}_B$ and the correlation scale ℓ_B defined formally by equation (1.8) are technically distinct quantities, but they are usually the same order of magnitude). Equation (1.23) then implies

$$\sqrt{l_n \tilde{\ell}_B}\, n_{\rm e}\, B_{rms} \sim 1.7 \times 10^{23} \Delta\vartheta \ \,{\rm G\,cm}^{-2}, \tag{1.24}$$

where l_n is the interaction-region width. This estimate can be re-arranged to give $B_{rms} \approx 120\,(\Delta\vartheta/3^\circ)(n_{\rm e}/10^{20}\,{\rm cm}^{-3})^{-1}(l_n\tilde{\ell}_B/0.2\,{\rm mm}^2)^{-1/2}$ kG. A reasonable estimate for $\tilde{\ell}_B$ is the grid aperture: $\tilde{\ell}_B \sim 300\ \mu$m.

However, this particular measurement of the magnetic field has several issues when employed in isolation. First of these is the dependence of the Faraday-rotation measure on both the magnetic field and the plasma density. Since the plasma is in a turbulent state, assuming a uniform density along the path is questionable. This objection is particularly prescient if there exist correlations between the fluctuating density and the stochastic magnetic field: for example, a positive correlation between density and magnetic field would result in the field strength being systematically overestimated. The second issue is the lack of spatial information provided by the measurement. This prevents any inferences from the measurement about the structure of the magnetic field; in order to characterise typical field strengths, some value for the typical field scale must be assumed. The time-resolved nature of the measurement, which for previous laser-plasma experiments investigating turbulent amplification of magnetic fields has been used to infer spatial information about the field via the Taylor hypothesis (Meinecke et al. 2014), is of little use in this situation, because the stochastic nature of the motions in which the magnetic field is embedded means that there is not a well defined relationship applicable for a single measurement between the frequency dependence of the magnetic field evolution and its spatial structure. A corollary of both these issues is that the Faraday rotation measurement of the magnetic field for this experiment is only semi-quantitative at best in the absence of further interpretation by simulations. This state of affairs is unsatisfactory, because the key scientific goal of the experiment is only achieved if a robust measurement of the characteristic magnetic field strength can be obtained.

To overcome these issues, a second magnetic-field diagnostic was employed: *proton imaging.*

1.3 A (brief) review of proton imaging

Before discussing the proton-imaging data arising from the OMEGA experiment, we first provide a brief review of proton imaging. Proton imaging (also known as proton radiography) is an important electromagnetic-field diagnostic used in laser-plasma experiments, with applications spanning laboratory astrophysics and inertial

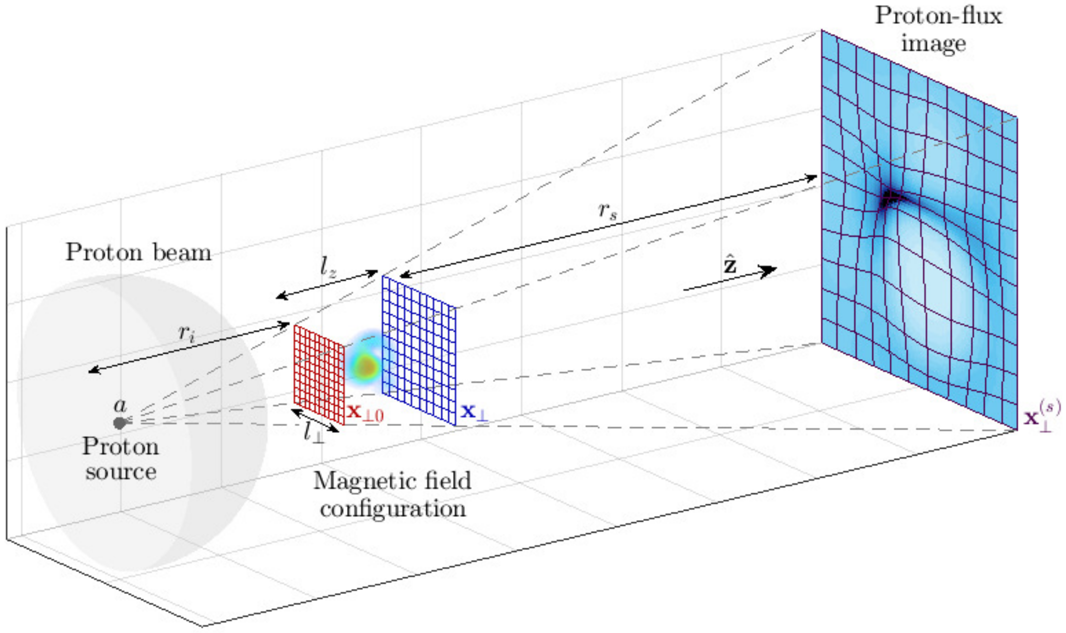

Figure 1.12: Set-up of proton-imaging diagnostic, with identified theoretical parameters. A particular magnetic field configuration is imaged by propagating an approximately planar proton beam through the structure. Spatially varying magnetic forces cause non-uniform deflection of protons, resulting in a particular proton-flux image. Here r_i is the distance from the proton source to the magnetic field configuration, a the proton source size, $l_\perp$ the perpendicular length scale of the configuration, l_z the parallel scale, r_s the distance from the configuration to the detector, $\mathbf{x}_{\perp 0}$ a perpendicular coordinate system for the imaging beam prior to interaction with the magnetic field, $\mathbf{x}_\perp$ a perpendicular coordinate system after the interaction, and $\mathbf{x}_\perp^{(s)}$ the image coordinate system.

fusion (Mackinnon et al. 2004, 2006, Li et al. 2006b). The diagnostic is implemented by passing an approximately uniform beam of imaging protons through a plasma onto a spatially resolved detector. Proton beams are typically generated in practice using one of two methods: the first is production of protons via the target normal sheath acceleration (TNSA) process using a high-intensity laser (Wilks et al. 2001, Borghesi et al. 2006). The second is the laser implosion of a capsule containing D_2 and D^3He gas that leads to creation of fusion protons (Séguin et al. 2004, Li et al. 2006b, Manuel et al. 2012). While inside the plasma, the imaging protons experience Lorentz forces arising from electromagnetic fields, which result in a non-uniform *image-flux distribution*. An idealised picture of a typical imaging set-up is shown in Figure 1.12.

When implemented successfully, proton imaging can help characterise electromagnetic structures, the measurement of which is crucial for understanding a wide range of plasma dynamics. However, as a two-dimensional diagnostic, a conventional proton-imaging set-up is unable to describe completely a full three-dimensional electromagnetic field configuration, instead yielding the two-dimensional image-flux distribution. Additionally, it is well known that the morphology and strength of image-flux structures do not correspond directly to the equivalent properties of the electromagnetic field (see Kugland et al. 2012). For proton imaging to provide useful measurements of electromagnetic fields, an interpretation of a proton-flux image in terms of the field creating it is therefore required.

Typically there are two ways in which the interpretation of proton-flux images is carried out. The first consists of simulating some artificial field, either by a bespoke electromagnetic-field generation method (see Levy et al. 2015), or with a more general plasma-simulation tool and then introducing a pre-defined proton beam: this is then propagated via a numerical scheme from source to detector. The resulting proton-flux image is compared to experimentally obtained images; similarities between the two are interpreted as evidence for the artificial field being similar to the experimental field (Borghesi et al. 2002, Huntington et al. 2015). Such a technique can be enhanced further by running optimisation schemes on proton ray-tracing codes applied to parametrised test fields to find the best possible fit between an electromagnetic-field structure and its associated proton-flux image (see Romagnani et al. 2005). This *forward-propagation* technique has been successfully used to describe electromagnetic fields produced in a range of laser-plasma experiments (for example, see Borghesi et al. 2007, Romagnani et al. 2008, Sarri et al. 2012).

An alternative approach is to perform a general analysis of the evolution of the proton beam analytically and so derive an analytical expression for the image-flux distribution in terms of the fields creating it (Kugland et al. 2012). The tractability of the relevant arguments is a result of the protons' large speed and low density relative to macroscopic plasma properties: this enables a range of physical processes to be neglected, leaving forces due to electromagnetic fields already present in the plasma solely responsible for alterations to the proton beam's dynamics (see Appendix B). In addition, a number of assumptions – such as that of a uniform mono-energetic beam from a point source, paraxiality, small proton deflection angles and point projection – allow for further simplifications. Typically, the image-flux distribution can be related to path-integrated fields (Graziani et al. 2017).

Analytic theory for regular electromagnetic structures is relatively well understood. Kugland et al. (2012) carried out analyses of various structures based on real-space conservation of proton flux and documented a wide range of features typically observed in proton-flux images. In particular, using simplifying assumptions (stated precisely in Section 2.4.1) they give an analytic relation – first derived, in fact, by Romagnani (2005) – between path-integrated fields experienced by an imaging beam and the resulting image-flux distribution (p. 5, equation (6) of Kugland et al. 2012), which from now on we will refer to as the *Romagnani-Kugland (RK) image-flux relation.* Kugland et al. (2012) then discussed the existence of a dimensionless parameter – the contrast parameter, μ – which effectively characterises image-flux phenomena (for magnetic fields, μ is defined precisely in Section 2.2.3). Physically, μ is a measure of the relative magnitude of proton displacements resulting from electromagnetic forces and the size of electromagnetic structures. For small constrasts, the image flux is related linearly to the path-integrated fields, with the consequence that the latter can in theory be directly reconstructed from proton-flux images (Graziani et al. 2017). However, as μ increases this relationship becomes highly nonlinear; beyond some critical value of μ some regions of proton flux overlap themselves, and intense structures (*caustics*) appear due to focusing of the proton beam (Kugland et al. 2012).

Both methods have strengths and weaknesses. Forward-propagation techniques require fewer assumptions than analytic theory and, in the case of a simple proton-flux image, finding the electromagnetic fields generating that image is usually tractable. However, if analytic theory is valid, it is useful for determining precisely what field statistics are retained in a proton-flux image. It can also lead to practical methods for extracting those statistics directly from an image.

1.4 Proton-imaging data from the OMEGA experiment

For the OMEGA experiment, the proton-imaging diagnostic was implemented by imploding a D^3He capsule (Li et al. 2006b), located 1 cm away from the centre of the target ($r_i = 1\,\mathrm{cm}$). The capsule (diameter 420 μm) was composed of 2 μm of SiO_2 and filled with 18 atm D^3He gas (6 atm D_2 and 12 atm ^3He); it was imploded using seventeen 500 J beams, each with a 1 ns pulse length and 1.82 mm defocus. This results in the generation of $\sim 10^8 - 10^9$ 3.0 MeV and 14.7 MeV fusion protons, from DD and D^3He fusion reactions respectively. The fusion reactions occur approximately 0.5 ns after the implosion is initiated, and the burst is released over 0.15 ns. Experimental measurements of the proton energy spectra emerging from such capsule implosions have previously demonstrated both energy broadening and an upshift in the mean energy (Manuel et al. 2012); this is believed to be due to strong time-varying electric fields arising during the capsule implosion. As a result, the mean energies W_{DD} and $W_{\mathrm{D^3He}}$ of the DD and D^3He fusion protons are found to be $W_{\mathrm{DD}} = 3.3\,\mathrm{MeV}$ and $W_{\mathrm{D^3He}} = 15.0\,\mathrm{MeV}$ respectively, with energy uncertainties $\sim 9\%$ and $\sim 4\%$.

The fusion protons rapidly travel outward from the centre of the backlighter; a finite fraction of those pass through the turbulent plasma generated by the colliding jets. The characteristic speeds of the DD and D^3He protons are $V_{\mathrm{DD}} = 2.51 \times 10^9\,\mathrm{cm/s}$ and $V_{\mathrm{D^3He}} = 5.31 \times 10^9\,\mathrm{cm/s}$ respectively; thus, we deduce that the transit time $\tau_{\mathrm{source,DD}}$ of the DD protons from the capsule to the experiment is $\tau_{\mathrm{source,DD}} = r_i/V_{\mathrm{DD}} \approx 400\,\mathrm{ps}$, while the transit time $\tau_{\mathrm{source,D^3He}}$ of the D^3He protons is $\tau_{\mathrm{source,D^3He}} \approx 190\,\mathrm{ps}$. Both these times are considerable shorter than the turnover time of the largest-scale plasma motions in the experiment ($\tau_L = L/u_L \approx 6\,\mathrm{ns}$); since the distance from the proton source to the target centre in the experiment is greater than the scale of the plasma ($l_z \lesssim 0.1\,\mathrm{cm}$) parallel to the proton beam's direction, both proton species experience (to a good approximation) the same static electromagnetic fields.

Subsequent to traversing the interaction-region plasma, the fusion protons reach a detector (positioned 27 cm away from the target centre – $r_s = 27$ cm) composed of $10\,\mathrm{cm} \times 10\,\mathrm{cm}$ interleaved metal sheets and solid-state nuclear track detector, CR-39 [chemical formula $C_{12}H_{18}O_7$; see Séguin et al. (2003)]. The specific design of the detector is as follows: 7.5 μm of tantalum, then 1.5 mm of CR-39, then 150 μm of aluminium, and finally another 1.5 mm of CR-39. The design is such that 3.3 MeV protons are stopped in the first layer of CR-39 and 15.0 MeV protons in the second; the tantalum filter minimises damage to the CR-39 resulting from X-rays. Highly charged ions deposit the majority of their energy close to where they are stopped completely, leaving small tracks of broken molecular bonds. The positions of these tracks is determined by etching the CR-39 for two to three hours in a 6N solution of sodium hydroxide, yielding tracks with diameters $\sim 10\,\mu$m. An automated microscope system records the location of tracks, before removing image defects and counting the number of protons in preset bin sizes: the output are proton (fluence) images. The robust design of the detector is such that protons reaching the detector are recorded with close to 100% efficiency.

A selection of 15.0 MeV and 3.3 MeV proton images obtained during the OMEGA experiment both during collision and subsequent to it are shown in Figure 1.13. Figure 1.13a and 1.13b, recorded at times corresponding to jet-collision with the 10 ns pulse profile, do not present significant variations in proton flux $\delta\Psi$ compared to the mean flux Ψ_0; this result is consistent with the absence of strong magnetic fields. However, at later times with the same pulse shape, significant flux structures emerge in the images. These structures are even more intense at the same time for the shortened 5 ns pulse profile.

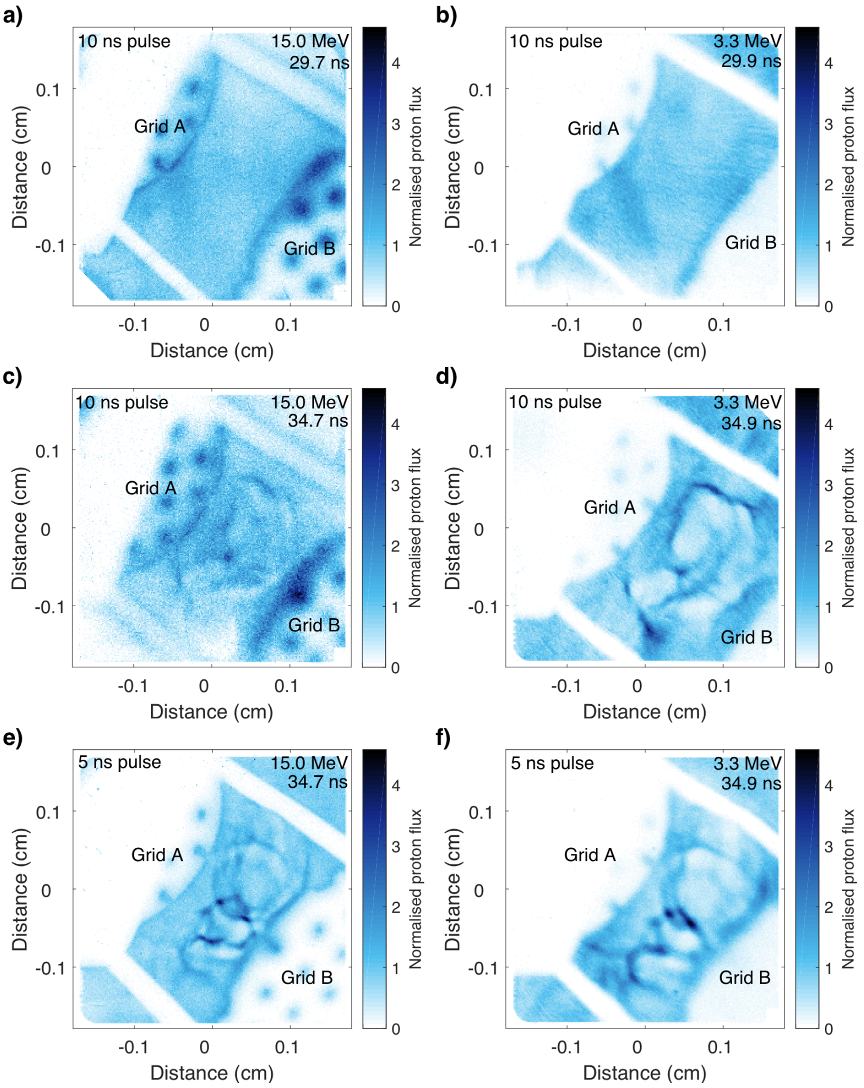

Figure 1.13: Proton images from the OMEGA experiment. a) Normalised number of 15.0 MeV protons detected on the second CR-39 plate in the detector pack, for a D^3He capsule implosion 29 ns after drive-beam pulse initiation. The normalisation is such that unity corresponds to the mean number Ψ_0 of protons per pixel on the detector; for this experimental shot, $\Psi_0 = 32$. The drive-beam pulse length used in this experiment was 10 ns. Due to the 0.5 ns second creation-delay and 0.2 ns transit time of the 15.0 MeV protons from capsule to target centre, the effective time of imaging is 29.7 ns. **b)** Normalised number of 3.3 MeV protons detected on the first CR-39 plate in the detector pack ($\Psi_0 = 101$) for the same experiment shot. The 0.4 ns transit time of the 3.3 MeV protons from the capsule to the experiment means that the effective time of imaging is 29.9 ns (0.2 ns later than the 15.0 MeV protons). **c)** Same as a), but for a D^3He capsule implosion 34 ns after drive-beam pulse initiation. In this shot, $\Psi_0 = 16$. **d)** Same as b), but for a D^3He capsule implosion 34 ns after drive-beam pulse initiation (same experimental shot as c); $\Psi_0 = 76$). **e)** Same as c), but with a 5 ns drive-beam pulse length ($\Psi_0 = 78$). **f)** Same as d), but with a 5 ns drive-beam pulse length (same experimental shot as e); $\Psi_0 = 118$).

In general laser-plasma experiments, such structure in proton images could be due to either electric or magnetic fields, whose simultaneous presence complicates systematic analysis. However, it can be argued in the OMEGA experiment that forces on the proton beam due to magnetic fields tend to dominate those due to electric fields. Such an argument goes as follows: in resistive MHD (including the Biermann battery term), the electric field is a known function of other plasma state variables (Gregori et al. 2015):

$$\mathbf{E} = -\frac{\mathbf{u} \times \mathbf{B}}{c} - \frac{\nabla p_e}{e n_e} + \frac{4\pi\eta}{c^2}\mathbf{j} \, , \tag{1.25}$$

where p_e is the electron pressure, n_e the electron density, and $\mathbf{j} \approx c\nabla \times \mathbf{B}/4\pi$ is the current. Thus, we can then estimate the relative magnitude of forces due to electric and magnetic fields on a given imaging proton using its equation of motion:

$$m_p \frac{\mathrm{d}\mathbf{V}}{\mathrm{d}t} = e\left[\mathbf{E} + \frac{\mathbf{V} \times \mathbf{B}}{c}\right] \, , \tag{1.26}$$

where $\mathbf{V}$ is the proton velocity (and V the proton speed), and m_p the proton mass. It follows that

$$\frac{|\mathbf{u} \times \mathbf{B}|/c}{|\mathbf{V} \times \mathbf{B}|/c} \sim \frac{U}{V} \, , \tag{1.27}$$

$$\frac{|\nabla p_e/e n_e|}{|\mathbf{V} \times \mathbf{B}|/c} \sim \beta^{1/2}\frac{d_i}{L}\frac{U}{V} \, , \tag{1.28}$$

$$\frac{|\eta\nabla \times \mathbf{B}/c|}{|\mathbf{V} \times \mathbf{B}|/c} \sim \mathrm{Rm}^{-1}\frac{U}{V} \, , \tag{1.29}$$

where U is again the characteristic fluid velocity, β the plasma beta, L the characteristic scale of the electric field fluctuation, and d_i the ion plasma skin depth, which is given by (Huba 1994)

$$d_i \equiv 3.1 \times 10^{-3} \left[\frac{Z}{3.5}\right]^{-1/2} \left[\frac{M}{6.5}\right]^{1/2} \left[\frac{n_e(\mathrm{cm}^{-3})}{10^{20}\mathrm{cm}^{-3}}\right]^{-1/2} \mathrm{cm}^{-3} \, . \tag{1.30}$$

Since in the OMEGA experiment $U \lesssim 2 \times 10^7\,\mathrm{cm/s}$, $L \approx 0.06\,\mathrm{cm}$, $\mathrm{Rm} \approx 600$, and the electron number density $n_e \sim 10^{20}\mathrm{cm}^{-3}$, we conclude that for the 3.3 MeV protons ($V \approx 2.5 \times 10^9\,\mathrm{cm/s}$) the electric force terms are all small compared to the magnetic forces provided $\beta \ll 6 \times 10^6$. In terms of characteristic field strengths, this condition is satisfied provided $B \gg 0.6\,\mathrm{kG}$. The bound is even stronger for the faster, 15.0 MeV protons.

There are then two reasons to believe this upper bound on β is indeed satisfied in the OMEGA experiment. First, the semi-quantitative field-strength estimate derived from the Faraday-rotation diagnostic implies that the value of B attained subsequent to the development of turbulence is of the order of one hundred kilogauss. Second, the FLASH simulations of the experiment involve stochastic magnetic fields of magnitudes $B_{rms} \sim 4 - 500\,\mathrm{kG}$; and although we shall see presently that the magnetic-field structure arising in the simulations should be regarded with significant skepticism, it seems unlikely that the FLASH code is producing fields larger than the physical ones by an order of magnitude or more. Even if these two arguments were to be seen inadequate, magnetic fields which do not satisfy the condition can in fact be shown to be very close to or below the threshold $B_{\mathrm{res}} \gtrsim 0.5\,\mathrm{kG}$ required for detecting those fields, given the geometry of the experiment and the nature of the proton source (see Section 3.3.1 for the derivation of the threshold). We conclude that all structures in these images are likely due to magnetic rather than electric fields (in Chapter 3, we will provide additional experimental evidence supporting this conclusion).

In spite of ruling out electric fields, systematic analysis of proton images derived from stochastic magnetic fields such as those shown in Figure 1.13 still presents a number of challenges. The complicated, seemingly random positioning of multiple structures in the proton images prohibits the attempted application of parameterised models for simple magnetic structures. One alternative forward-propagation technique involves simulating the proton-imaging set-up in the FLASH simulations and generating artificial proton images associated with the FLASH magnetic field at a particular time. The results of such a numerical calculation are shown in Figure

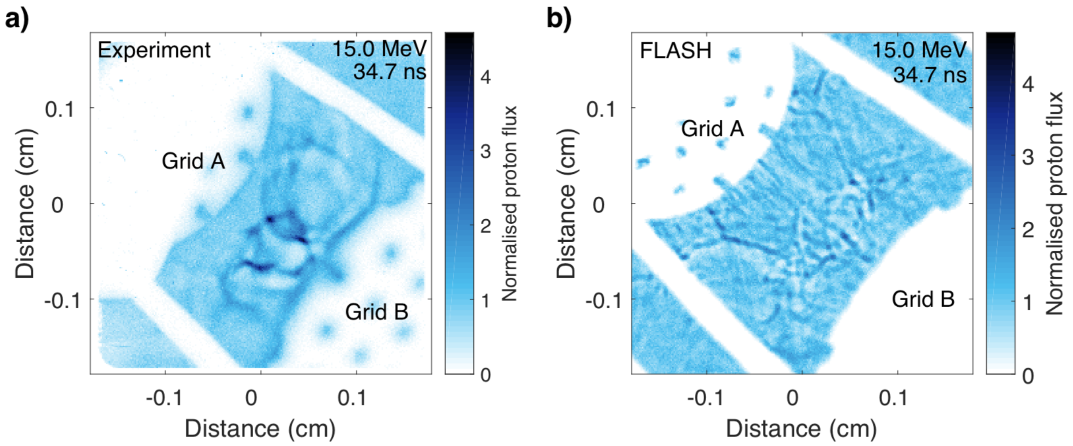

Figure 1.14: Comparison of experimental and FLASH-simulated proton images for the OMEGA experiment. a) Normalised number of 15.0 MeV protons detected on the second CR-39 plate in the detector pack, for a proton image corresponding to 34.7 ns after initiation of the 5 ns drive-beam pulse (c.f. Figure 1.13e). The normalisation is again such that unity corresponds to the mean number Ψ_0 of protons per pixel on the detector; for this experimental shot, $\Psi_0 = 78$. **b)** Normalised number of simulated 15.0 MeV protons detected on the (artificial) detector for a proton beam implemented for the FLASH-predicted magnetic fields at the equivalent simulation time to that in the experiment. The imaging parameters are chosen to be identical to those of the experiment.

1.14. It is unfortunately clear that the qualitative structure present in the FLASH-simulated proton images is quite distinct from that in the experimental data: the characteristic scale of flux variation is smaller in the FLASH simulation and magnetic structures evident in the FLASH simulation which extend beyond the edge of the interaction region are absent in the experimental data. We are forced to conclude that the magnetic-field morphology obtained in the FLASH simulations is unlikely to be consistent with that obtained in the experiment. This failure emphasises a fundamental difficulty associated with the application of forward-propagation techniques to proton images manifesting stochastic structure: in the event that numerical simulations do not adequately predict such structure, there is no self-evident systematic approach for modifying the simulations to fit better the data. Furthermore, we note that even if a simulation correctly reproduces in a statistical sense the stochastic structure of magnetic fields, the very nature of stochasticity implies that it is exceptionally unlikely that experimental images will be exactly the same as post-processed ones generated from the simulations.

It transpires that the analytic approach is more useful when using proton imaging to investigate stochastic magnetic field configurations. While dominant, magnetic forces experienced by the protons lead to small deflection angles, meaning that the approximations required for the use of analytic theory are often valid. This being the case, we can take advantage of analytic theory not requiring much prior knowledge of magnetic-field statistics (unlike forward-propagation techniques) without risking inaccurate results due to poor assumptions. To enable systematic analysis of the proton-imaging data obtained from the OMEGA experiment, we will therefore focus in the next chapter on constructing an analytic theory of proton imaging for stochastic magnetic fields.

Chapter 2

Proton imaging of stochastic magnetic fields

2.1 Introduction

A complete discussion of analytic theory of proton imaging for stochastic magnetic fields does not appear to exist in the literature. However, a few authors have considered various aspects of the general problem. Graziani et al. (2017) developed a linear, small-contrast-parameter-μ theory, applied it to multi-scale stochastic magnetic fields, and constructed a method for extracting the magnetic-energy spectrum from the autocorrelation function of the image-flux distribution assuming statistical isotropy and homogeneity of the field. There has also been extensive work modelling the diffusive evolution of a beam of charged particles through stochastic magnetic fields. Dolginov and Toptygin (1967) derived a governing equation for the ensemble-averaged distribution function of non-interacting, unmagnetised test particles using quasi-linear theory; this has been further developed by other authors (Hall and Sturrock 1967, Jokipii 1972). The result of such theories is typically a proton diffusion tensor, the form of which depends on the properties of both the beam and the field (Parker 1965).

In this chapter, we aim to determine the magnetic-energy spectrum from a proton image-flux distribution. If known, the magnetic-energy spectrum can in turn be used to deduce both typical magnetic-field strengths and spatial-correlation scales using equations (1.7) and (1.8) of Section 1.1.2. We address two areas not previously investigated systematically: first, the circumstances under which the extraction of the magnetic-energy spectrum is possible; second, how this extraction is done when it is feasible. Our approach to answering these questions will be to use the RK image-flux relation (introduced in Section 1.4) between the path-integrated magnetic field and the image-flux distribution. We explain in Section 2.2.2 that the path-integrated field is sufficient to characterise the magnetic-energy spectrum uniquely, provided magnetic fluctuations are assumed isotropic and homogeneous. Consequently, if it can be shown that the path-integrated field is extractable from a proton-flux image (or not), then the same is true for extracting the magnetic-energy spectrum for isotropic, stochastic magnetic fields.

Bearing this last statement in mind, we study the properties of the RK image-flux relation for the case of stochastic magnetic fields. Much as with regular electromagnetic structures, the types of image-flux features which manifest for stochastic magnetic fields are determined by μ. More specifically, we outline four regimes of distinctive image-flux phenomena in terms of μ. Of particular note in this context is the identification and characterisation of the large-μ (*diffusive*) regime, which in the context of proton imaging has not previously been discussed in much depth. For each regime, we investigate the possibility of the path-integrated magnetic field being reconstructed from an image-flux distribution, and if this reconstruction is possible, we provide a methodology for its practical implementation.

The text of the chapter is organised in the following manner. In Section 2.2, we discuss generally the interpretation of proton images resulting from stochastic magnetic fields. More specifically, in Section 2.2.1 we revise the description of stochastic magnetic fields given in Section 1.1.2 into a form appropriate for subsequent analysis. Section 2.2.2 introduces the RK image-flux relation mathematically, along with its correspondence to the magnetic-energy spectrum. By investigating the properties of the RK image-flux relation, Section 2.2.3 presents a general categorisation of image-flux features arising due to stochastic magnetic fields in terms of μ. In Section 2.3, we describe four distinct contrast regimes arising at different values of μ: linear (Section 2.3.1), nonlinear injective (Section 2.3.2), caustic (Section 2.3.3), and diffusive (Section 2.3.4). This description is combined with a numerical example illustrating key characteristics of each regime. We also describe possible methods for extracting the path-integrated field (and hence the magnetic-energy spectrum), as well as tests for identifying the likely contrast regime in which a given proton-flux image was formed. In Section 2.3.5, we illustrate the success (or failure) or the proposed methods for reconstructing the path-integrated field and magnetic-energy spectrum on the same numerical example used to characterise the contrast regimes.

In Section 2.4, we explore various technical issues and complications to the theory presented in Sections 2.2 and 2.3. Section 2.4.1 outlines the assumptions required for the RK image-flux relation to be valid. In Section 2.4.2, we discuss two theoretical complications to the contrast-regime classification of imaging set-ups applied to stochastic magnetic fields that are significant for multi-scale, or inhomogeneous, anisotropic stochastic fields. Both complications provide examples of situations in which the methods proposed for extracting the magnetic-energy spectrum from a proton-flux image are restricted. Finally, Section 2.4.3 describes three other limitations placed by current experimental capabilities on one's ability to determine the magnetic-energy spectrum using proton imaging.

Throughout this chapter, parameters and coordinate systems are defined as illustrated in Figure 1.12 of Chapter 1. We have in general deferred lengthy proofs of equations to either thesis appendices, or appendices of the published paper Bott et al. (2017). For reasons of brevity, we only include the most important appendices in the main text. Descriptions of all the numerical algorithms used in this chapter are presented in Appendix I.

2.2 Interpretation of proton-flux images generated by stochastic magnetic fields

2.2.1 Statistical characterisation of stochastic magnetic fields revisited

This chapter is concerned with recovering statistical properties of stochastic magnetic fields using a proton-imaging diagnostic – so we begin with a brief outline of the type of magnetic fields we will be considering. Recalling Section 1.1.2, we consider magnetic fields of the form

$$\mathbf{B}(\mathbf{x}) = \bar{\mathbf{B}}(\mathbf{x}) + \delta\mathbf{B}(\mathbf{x}) \ , \tag{2.1}$$

where $\bar{\mathbf{B}}$ is the non-stochastic mean field varying on the global scale of the plasma, constrained to be inside a cuboid region, dimensions $l_\perp \times l_\perp \times l_z$ (see Figure 1.12), and $\delta\mathbf{B}$ is the fluctuating field with correlation length $\ell_B \ll l_z, l_\perp$ (ℓ_B is defined precisely in Appendix C.2). The mean and fluctuating fields are again distinguished by introducing a spatial averaging operator $\langle \cdot \rangle$ with the property that $\left\langle \bar{\mathbf{B}} \right\rangle = \bar{\mathbf{B}}$, and $\langle \delta\mathbf{B} \rangle = 0$. In this case, the averaging operator is an average over intermediate scale l such that $\ell_B \ll l \ll l_z, l_\perp$. We restrict our focus to static fields only because with respect to the fast motion of the protons the evolution of magnetic fields is assumed slow (see Section 2.4.1 for a discussion of the validity of this assumption).

Throughout the rest of this chapter, we explore the question of whether a proton-imaging diagnostic can be used to extract the magnetic-energy spectrum. For convenience, we reproduce its definition here:

$$E_B(k) = \frac{\pi}{\mathcal{V}} \int \mathrm{d}\Omega \, k^2 \left\langle \left| \delta\hat{\mathbf{B}}(\mathbf{k}) \right|^2 \right\rangle \ . \tag{2.2}$$

We also reproduce the relations between the magnetic-energy spectrum, the characteristic magnetic field strength B_{rms}, and the correlation length ℓ_B:

$$B_{rms} = \left[8\pi \int_0^\infty \mathrm{d}k \, E_B(k)\right]^{1/2} , \tag{2.3}$$

$$\ell_B = \frac{\pi}{2} \frac{\int_0^\infty \mathrm{d}k \, k^{-1} E_B(k)}{\int_0^\infty \mathrm{d}k \, E_B(k)} . \tag{2.4}$$

A discussion of the mathematical characterisation of stochastic magnetic fields by an alternative mathematical object – the magnetic autocorrelation function – is given in Appendix C. This is an equivalent quantity to the magnetic-energy spectrum. It is sometimes useful to invoke it instead of the spectrum: the most physically intuitive definition of the magnetic-field correlation length is in terms of magnetic autocorrelation function, and for the derivations of spectral relations (2.11) and (2.35) presented in Appendices D and F respectively, the magnetic autocorrelation function enables a clearer characterisation of the accuracy of approximations made than does the magnetic-energy spectrum.

2.2.2 The plasma-image mapping

In the Introduction, we discussed the importance of the RK image-flux relation between the path-integrated magnetic field and image-flux distribution when seeking to determine the magnetic-energy spectrum; here we outline the form of this relation and its correspondence to the energy spectrum. The RK image-flux relation was originally derived from particle conservation in real space (Romagnani 2005, Kugland et al. 2012). In Appendix D of Bott et al. (2017), an alternative derivation from first principles using kinetic theory is presented.

Physically, magnetic forces experienced by the imaging protons lead to global restructuring of the imaging beam. For arbitrary magnetic-field configurations and imaging-beam parameters, characterising this restructuring is extremely complicated, particularly for a stochastic magnetic field. This is made clear by stating the general relationship between the proton beam distribution function and the final proton image [see Appendix D.1 of Bott et al. (2017)]. However, under some assumptions that are typically valid for proton-imaging set-ups, the complexity of such a relation is greatly reduced. We assume that a number of dimensionless parameters related to the dimensions of the imaging set-up (see Figure 1.12 of Chapter 1) are small: namely the size of the proton source relative to its distance from the plasma a/r_i, the paraxial parameter

$$\delta\alpha \equiv \frac{l_\perp}{r_i} \ll 1 \tag{2.5}$$

of the proton imaging set-up, the point-projection parameter

$$\delta\beta \equiv \frac{l_z}{r_s} \ll 1 \, , \tag{2.6}$$

and the magnitude of angular deflections $\delta\theta$ away from the initial proton trajectories [the magnitude of this for stochastic fields is shown subsequently in equation (2.13)]. We also assume $r_s \gtrsim r_i$. A full discussion of the validity of these assumptions and their significance in simplifying the general proton-imaging problem is given in Section 2.4.1.

In the limit where the above asymptotic parameters are indeed small, the form of the beam as a two-dimensional near-planar sheet [see Figure 1.12 and Appendix D.3 of Bott et al. (2017)] is retained following interaction with the magnetic field. Furthermore, internal re-distribution of proton flux within the sheet is entirely determined by velocity perturbations acquired inside the plasma. More specifically, it can be shown [p. 5, equations (3), (4) of Kugland et al. (2012); see p. 85, equations (2.7) of Romagnani (2005), and also Appendix D.4 of Bott et al. (2017)] that an imaging proton with initial perpendicular position $\mathbf{x}_{\perp 0}$ ends up with final perpendicular position on the detector

$$\mathbf{x}_\perp^{(s)}(\mathbf{x}_{\perp 0}) \approx \frac{r_s + r_i}{r_i}\mathbf{x}_{\perp 0} + \frac{r_s}{V}\,\mathbf{w}(\mathbf{x}_{\perp 0}) \, . \tag{2.7}$$

Here V is the initial speed of the proton beam, assumed mono-energetic, and the perpendicular velocity deflection $\mathbf{w}(\mathbf{x}_{\perp 0})$ caused by magnetic forces of an imaging proton with initial perpendicular position $\mathbf{x}_{\perp 0}$ is

$$\mathbf{w}(\mathbf{x}_{\perp 0}) \approx \frac{e}{m_p c}\hat{\mathbf{z}} \times \int_0^{l_z} \mathrm{d}s\, \mathbf{B}(\mathbf{x}(s)) \ , \tag{2.8}$$

where e is the proton charge, m_p the proton mass, and $\mathbf{x}(s)$ the proton trajectory. We can view $\mathbf{w}(\mathbf{x}_{\perp 0})$ as a function of the initial perpendicular position. We will call this function the *perpendicular-deflection field* for the remainder of this chapter. By conservation of proton flux within the imaging beam, the image-flux distribution $\Psi\left(\mathbf{x}_\perp^{(s)}\right)$ is then given by the RK image-flux relation (p. 5, equation (6) of Kugland et al. 2012):

$$\Psi\left(\mathbf{x}_\perp^{(s)}(\mathbf{x}_{\perp 0})\right) = \sum_{\mathbf{x}_\perp^{(s)} = \mathbf{x}_\perp^{(s)}(\mathbf{x}_{\perp 0})} \frac{\Psi_0}{\left|\det \nabla_{\perp 0}\left[\mathbf{x}_\perp^{(s)}(\mathbf{x}_{\perp 0})\right]\right|} \ , \tag{2.9}$$

where Ψ_0 is the initial flux distribution (assumed uniform), $\nabla_{\perp 0} \equiv \partial/\partial \mathbf{x}_{\perp 0}$ is a gradient operator with respect to the initial plasma coordinates, and the sum indicates that the total flux at any particular position on the detector can in general have contributions from protons with many different initial positions. A numerical illustration of the validity of equations (2.8) and (2.9) can be found in Appendix D.9 of Bott et al. (2017).

The *plasma-image mapping* (2.7) can be related to the magnetic-energy spectrum (2.2) via the perpendicular-deflection field (2.8). This is entirely equivalent to relating the path-integrated field to the magnetic-energy spectrum, because the former can be recovered from the perpendicular-deflection field directly by rearranging (2.8):

$$\int_0^{l_z} \mathrm{d}s\, \mathbf{B}_\perp(\mathbf{x}(s)) = -\frac{m_p c}{e}\hat{\mathbf{z}} \times \mathbf{w}(\mathbf{x}_{\perp 0}) \ . \tag{2.10}$$

If the stochastic magnetic field is assumed to be statistically isotropic and homogeneous (except for some global variation in RMS field strength magnitude), with an additional assumption of zero mean-magnetic field ($\bar{\mathbf{B}} = 0$, $\mathbf{B} = \delta\mathbf{B}$), it can then be shown (see Appendix D) that the deflection-field spectrum is related to the magnetic-energy spectrum by

$$E_B(k) = \frac{m_p^2 c^2}{4\pi^2 l_z e^2} k E_W(k) \ . \tag{2.11}$$

Here the deflection-field spectrum $E_W(k)$ is defined by

$$E_W(k_\perp) \equiv \frac{4\pi^2}{\mathcal{A}} \int \mathrm{d}\theta \, k_\perp \left\langle |\hat{\mathbf{w}}(\mathbf{k}_\perp)|^2 \right\rangle \ , \tag{2.12}$$

where $\mathcal{A}$ is the area of averaging samples over which the deflection-field spectrum is calculated, $\hat{\mathbf{w}}(\mathbf{k}_\perp)$ is the two-dimensional Fourier transform of the perpendicular-deflection field, $\mathbf{k}_\perp$ the perpendicular wavevector, and the integral is over the polar angle θ. Spectral relation (2.11) implies that if we can determine the perpendicular-deflection field from the image-flux distribution, then we can recover the magnetic-energy spectrum. It is important to note that the derivation of this result relies on the solenoidality of the magnetic field.

The deflection-field spectral relation (2.11) also allows for a simple calculation of the typical deflection angle $\delta\theta$ in terms of the magnetic field and initial proton speed. More specifically, integrating (2.11) over all wavenumbers (see Appendix D) gives, in the small-deflections limit,

$$\delta\theta \equiv \frac{w_{rms}}{V} = \frac{eB_{rms}}{m_p c V} \sqrt{l_z \ell_B} \, , \tag{2.13}$$

where $w_{rms} \equiv \left\langle \mathbf{w}^2 \right\rangle^{1/2}$ is the RMS of the perpendicular-deflection field, and ℓ_B is again the correlation length . We emphasize that both B_{rms} and ℓ_B can be calculated independently using (2.3) and (2.4) once the magnetic-energy spectrum has been derived from (2.11).

As noted by previous authors (Kugland et al. 2012, Graziani et al. 2017), the perpendicular-deflection field has the property of being irrotational, provided the typical deflection angle $\delta\theta \lesssim \ell_B/l_z$ (this assumption is potentially more restrictive than the small-angle approximation $\delta\theta \ll 1$ – as discussed in Section 2.4.1). Irrotationality of the perpendicular-deflection field follows from the solenoidality of the magnetic field:

$$\nabla_{\perp 0} \times \mathbf{w}(\mathbf{x}_{\perp 0}) = \hat{\mathbf{z}} \frac{e}{m_p c} \int_0^{l_z} \mathrm{d}z' \left(\frac{\partial \mathbf{x}_\perp(z')}{\partial \mathbf{x}_{\perp 0}} \cdot \nabla_\perp \right) \cdot \mathbf{B} \approx \hat{\mathbf{z}} \frac{e}{m_p c} \int_0^{l_z} \mathrm{d}z' \, \nabla \cdot \mathbf{B} = 0 \, , \quad (2.14)$$

where $\nabla \equiv \partial / \partial \mathbf{x}$ denotes the gradient operator with respect to the beam-proton position $\mathbf{x}(s)$. The approximation $\partial \mathbf{x}_\perp(z') \, / \partial \mathbf{x}_{\perp 0} \approx \underline{\underline{\mathbf{I}}}$ holds if the proton trajectories do not cross inside the plasma [for a more detailed discussion of this result, see Appendix D.8 of Bott et al. (2017)]. As a consequence, the perpendicular-deflection field can always be written as the gradient of the *deflection-field potential*, defined by

$$\varphi(\mathbf{x}_{\perp 0}) \equiv \int_C \mathrm{d}\mathbf{l} \cdot \mathbf{w}(\tilde{\mathbf{x}}_{\perp 0}) \, , \quad (2.15)$$

where C is any path from the origin to the perpendicular coordinate $\mathbf{x}_{\perp 0}$ and $\mathrm{d}\mathbf{l}$ is an infinitesimal line element along this path. Under the same assumption, the perpendicular-deflection field is given by the magnetic field integrated along the *unperturbed trajectories*:

$$\mathbf{w}(\mathbf{x}_{\perp 0}) \approx \frac{e}{m_p c} \hat{\mathbf{z}} \times \int_0^{l_z} \mathrm{d}z' \, \mathbf{B}\left(\mathbf{x}_{\perp 0} \left(1 + \frac{z'}{r_i} \right), z' \right) . \quad (2.16)$$

We observe that introducing the vector potential $\mathbf{A}$ satisfying $\mathbf{B} = \nabla \times \mathbf{A}$ into (2.16) recovers equations (78) of Kugland et al. (2012). As we discuss in Sections 2.3.1 and 2.3.2, the irrotationality property of the perpendicular-deflection field is essential for attempts for reconstructing the path-integrated field from the image-flux distribution.

2.2.3 The contrast parameter μ

Equation (2.9) is the desired RK image-flux relation between the image-flux distribution and the path-integrated magnetic field, via plasma-image mapping (2.7); we now explore the properties of the RK image-flux relation. As is clear from the appearance of the Jacobian determinant of the plasma-image mapping in (2.9), the size of Jacobian-matrix elements of the plasma-image mapping will be of significance for characterising image-flux features. These elements have physical meaning, describing the relative size of initial gradients in perpendicular velocities of protons compared to gradients resulting from deflections due to magnetic forces. Mathematically, their size is quantified by the *constrast parameter* μ, which we define for a proton imaging set-up applied to a stochastic magnetic field with correlation length ℓ_B by

$$\mu \equiv \frac{d_s}{\mathcal{M}\ell_B} = \frac{r_s \delta\theta}{\ell_B^*} = \frac{\delta\theta}{\delta\alpha} \frac{r_s}{r_s + r_i} \frac{l_\perp}{\ell_B} , \tag{2.17}$$

where $d_s \equiv r_s \delta\theta$ is the typical perpendicular displacement of a proton from its undeflected position on the detector,

$$\mathcal{M} = \frac{r_i + r_s}{r_i} \tag{2.18}$$

the image magnification, and $\ell_B^* = \mathcal{M}\ell_B$ is the magnified correlation length. If $r_s \gg r_i$, (2.17) reduces to the definition of μ given in previous literature (see equation (11) of Kugland et al. 2012, Graziani et al. 2017): $\mu = r_i \delta\theta/\ell_B$.

The universal dependence of image-flux features on μ – irrespective of the particular magnetic field structure – enables a systematic approach to the heuristic interpretation of proton-flux images. Since μ is a function of field strength via the typical proton deflection angle $\delta\theta$, its identification for a particular image-flux distribution is a useful way to estimate magnetic field strengths attained in experiments. Substituting definitions (2.5) and (2.13) for $\delta\alpha$ and $\delta\theta$ respectively into (2.17) gives

$$\mu = \frac{r_s r_i}{r_s + r_i} \frac{e B_{rms}}{m_p c V} \sqrt{\frac{l_z}{\ell_B}} . \tag{2.19}$$

This shows that $\mu \propto B_{rms}/V$, the same as the RMS proton deflection angle $\delta\theta_{rms}$. By substituting appropriate values of physical constants into (2.19) we can explicitly write the field strength associated with a particular μ as

$$B_{rms}(\mathrm{kG}) \approx 250 \left(\frac{\mathcal{M}}{\mathcal{M}-1}\right) \mu \left[\frac{W(\mathrm{MeV})}{3.3\,\mathrm{MeV}}\right]^{1/2} \left[\frac{r_i(\mathrm{cm})}{1\,\mathrm{cm}}\right]^{-1} \left[\frac{\ell_B(\mathrm{cm})}{l_z(\mathrm{cm})}\right]^{1/2} \mathrm{kG}\,, \quad (2.20)$$

where W is the energy of the beam protons). When using (2.20) to make a quick order-of-magnitude estimate, an educated guess for the correlation length could be reasonably used (though the typical field strength and correlation length can be determined independently if the magnetic-energy spectrum is known). We discuss how to estimate μ from a proton image in Section 2.3. Comparing (2.13) and (2.19), it is clear that $\delta\theta_{rms}$ and μ have different dependences on the correlation scale of the field: $\delta\theta_{rms} \propto \ell_B^{1/2}$, while $\mu \propto \ell_B^{-1/2}$. Thus a field with smaller-scale structures will give larger values for μ, despite the typical deflection angle being reduced [a numerical example of this is given in Appendix G of Bott et al. (2017)].

Beyond qualitative estimates, whether the path-integrated field (and hence magnetic-energy spectrum for isotropic stochastic magnetic fields) can be directly extracted from experimental data – and if so, how this extraction is carried out – changes depending on μ. This change is best elucidated for stochastic magnetic fields in terms of four contrast regimes: *linear* ($\mu \ll 1$), *nonlinear injective* (μ below some critical value $\mu_c \sim 1$), *caustic* ($\mu \geq \mu_c$) and *diffusive* ($\mu \gtrsim r_s/(r_s + r_i)\,\delta\alpha$, where $\delta\alpha$ is again the paraxial parameter). Here, μ_c is defined to be the smallest value of μ associated with the imaging of a particular stochastic magnetic field such that the plasma-image mapping (2.7) is not injective (one-to-one). These four contrast regimes are discussed in the next section.

2.3 Contrast regimes

We begin by providing a general characterisation of the linear (Section 2.3.1), nonlinear injective (Section 2.3.2), caustic (Section 2.3.3) and diffusive (Section 2.3.4) regimes respectively.

To help with this illustration we consider proton images associated with a particular stochastic magnetic-field configuration. These images are simulated numerically using the technique presented in Appendix I.1. Multi-scale fields possessing a power-law spectrum are of interest when studying the fluctuation dynamo (Schekochihin et al. 2004c, Gregori et al. 2015) so, using methods described in Appendix I.2, we generate an artificial Gaussian stochastic field with a magnetic-energy spectrum $E_B(k)$ of the form

$$E_B(k) = \frac{B_{rms}^2}{8\pi} \left(p-1\right) \frac{k^{-p}}{{k_l}^{-p+1} - {k_u}^{-p+1}} \, , \quad k \in [k_l, k_u] \, , \tag{2.21}$$

where k_l and k_u represent the lower and upper wavenumber cutoffs and p is the spectral index. Calculations of key quantities for this spectrum, such as correlation scale ℓ_B, are given in Appendix G.1. For this section, we set $p = -11/3$, corresponding to a Golitsyn spectrum (Golitsyn 1960). We make this choice for two reasons. Firstly, as mentioned in Section 1.1.4 the magnetic-energy spectrum is thought to follow such a power law in a turbulent magnetised flow with a low Reynolds number (c.f. Section 1.1.4, and also Moffatt (1961), Schekochihin et al. (2007), Gregori et al. (2015)). Secondly, a rapidly decaying power law of this form has the useful property that both the dominant magnetic and image-flux structures have similar spatial scales, avoiding certain complications important for more shallow power laws (discussed in Section 2.4.2).

To imitate configurations realistic to actual experiments, we also introduce an overall Gaussian envelope

$$\tilde{\mathbf{B}} = \mathbf{B} \, \exp\left[-4\sigma\left(\mathbf{x} - l_z \hat{\mathbf{z}}/2\right)^2/l_z^2\right] , \tag{2.22}$$

where σ is an adjustable constant. While this does introduce a range of local field strengths, and hence effective contrasts regimes, due to the slowly varying inhomogeneity of the magnetic field RMS relative to the field-structure size, the central part

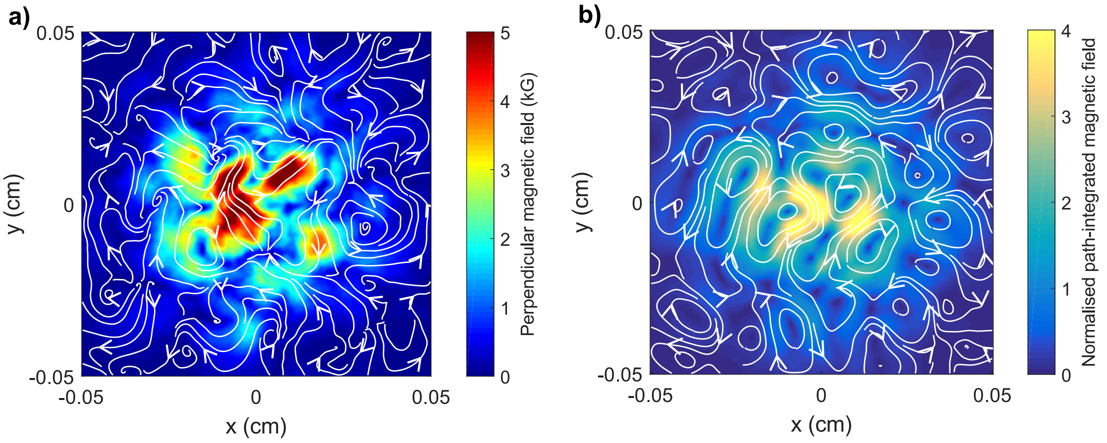

Figure 2.1: Sample of Gaussian compact stochastic magnetic field configuration for use in illustration of contrast regimes (Section 2.3). The field sample is taken to have length scales $l_i = l_z = l_\perp = 0.1\,\mathrm{cm}$, and is specified on a 201^3 array (grid spacing $\delta x = l_i/201$). The sample is generated using the methods described in Appendix I.2. The magnetic-energy spectrum is set to be a Golitsyn power law of the form (2.21), with index $p = -11/3$, spectral cutoffs $k_l = 6\pi/l_i$, $k_u = 120\pi/l_i$, $B_{rms} = 1\,\mathrm{kG}$, and $\ell_B = 80\,\mu\mathrm{m}$. A Gaussian envelope of the form (2.22) is applied, with $\sigma = 3$, giving $B_{rms,0} \approx 3\,\mathrm{kG}$. In all plots of two-dimensional vector fields, colour variations denote the value of the labelled quantity, while the white lines with directional arrows are streamlines of the plotted vector field. **a)** Slice of perpendicular magnetic field taken along central perpendicular plane in configuration. **b)** Path-integrated perpendicular magnetic field experienced by 3.3 MeV protons originating from a point source located at a distance $r_i = 1\,\mathrm{cm}$ from the magnetic field configuration. This field was calculated numerically using test protons (see Appendix I.3 for a description of this technique).

of the proton-flux image still manifests a single contrast regime. For the particular Gaussian shape used, the effective RMS magnetic field strength $B_{rms,0}$ experienced by protons with trajectories close to the perpendicular origin can be analytically related to the global RMS values (see Appendix I.2):

$$B_{rms,0} = B_{rms}\left[\frac{\pi}{8\sigma}\mathrm{erf}\left(\sqrt{2\sigma}\right)\right]^{-1/2} . \qquad (2.23)$$

Plots of such a synthetic field are shown in Figure 2.1. The contrast parameter μ, defined by (2.17), is linear in the field strength, so the same field configuration can be used to explore all possible regimes. For each regime, we calculate the normalised image flux, shown in Figure 2.2, with fixed scales for the sake of comparison. We also show the perturbed image-coordinate grid associated with the plasma-image mapping (2.7). Throughout Sections 2.3.1, 2.3.2, 2.3.3 and 2.3.4, we will refer back to Figure 2.2 as a visual aid for typical features of proton images in each contrast regime.

2.3.1 Linear regime of proton imaging - $\mu \ll 1$

If μ is small, relating the magnetic field and the image flux becomes a much simpler problem. This follows from the result [re-derived in Appendix E - see also (Romagnani 2005, Graziani et al. 2017)] that if $\mu \ll 1$, the plasma-image mapping (2.7) becomes, to leading order in μ,

$$\mathbf{x}_{\perp}^{(s)} = \frac{r_s + r_i}{r_i}\mathbf{x}_{\perp 0}\left[1 + \mathcal{O}(\mu)\right] , \tag{2.24}$$

while the RK image-flux relation (2.9) can be rewritten as

$$\frac{\delta\Psi\left(\mathbf{x}_{\perp}^{(s)}\right)}{\Psi_0^{(s)}} = \frac{r_s r_i}{r_s + r_i}\frac{4\pi e}{m_p c^2 V}\int_0^{l_z} j_z\left(\mathbf{x}_{\perp 0}\left(1 + \frac{z'}{r_i}\right), z'\right) \mathrm{d}z' , \tag{2.25}$$

where we remind the reader that $\mathbf{j} \approx c\nabla \times \mathbf{B}/4\pi$ is the (MHD) current, and $\delta\Psi\left(\mathbf{x}_{\perp}^{(s)}\right) \equiv \Psi\left(\mathbf{x}_{\perp}^{(s)}\right) - \Psi_0^{(s)}$ is the image-flux deviation from the initial mean image flux, which in turn is related to the initial flux Ψ_0 by the image-magnification factor $\mathcal{M}$, viz., $\Psi_0^{(s)} = \Psi_0/\mathcal{M}^2$. It follows from (2.25) that proton-flux images in the linear regime have a simple physical interpretation: they display the undeflected path integrated z component j_z of the MHD current (Romagnani 2005, Graziani et al. 2017). The linear regime is therefore so called, because the magnitude of image-flux deviations is linear in the magnetic field.

Linear-regime image-flux relation (2.25) has another consequence: estimating the magnitude of the image-flux deviations compared to the mean image flux, we see that $\delta\Psi \sim \mu\Psi_0^{(s)} \ll \Psi_0^{(s)}$. The linear regime is therefore characterised by small relative image-flux deviations, providing a useful observational tool for recognising proton-flux images of stochastic magnetic fields in the linear regime. An example of this phenomenon is shown in Figure 2.2a, a flux image of a Golitsyn field with

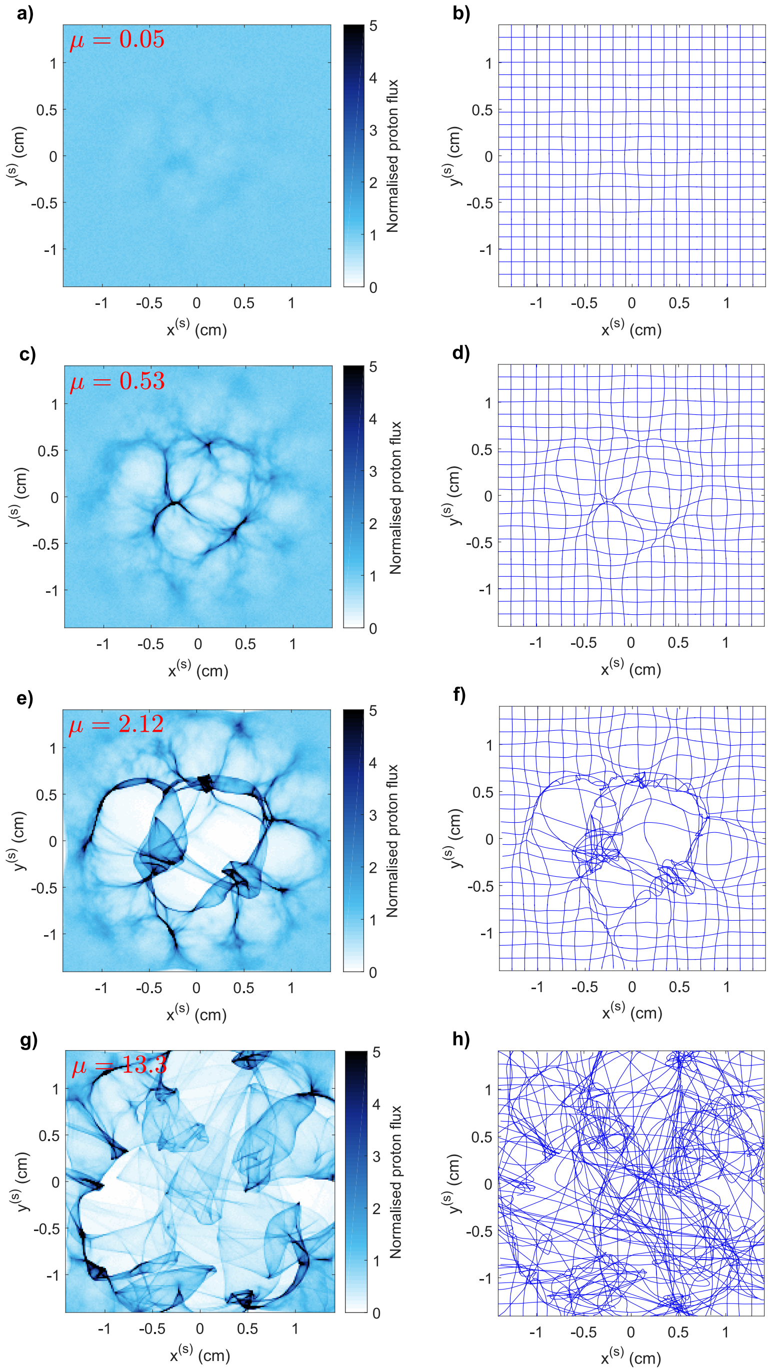

Figure 2.2: Characterisation of proton-flux images of stochastic magnetic fields by contrast regime. 3.3-MeV-proton flux images generated on an artificial detector at a distance $r_s = 30\,\mathrm{cm}$ from magnetic field configuration described in Figure 2.1, for a range of magnetic field strengths [and hence values of μ (2.17)]. The general arrangement of the imaging is the same as shown in Figure 1.12. The proton point-source was located at a distance $r_i = 1\,\mathrm{cm}$ on the opposing side of the configuration to the detector, and 3×10^7 protons were used per image. The procedure used to generate these images is described in Appendix I.1. **a)** Normalised proton-flux image in the linear regime, with $\mu \ll 1$ ($B_{rms,0} \approx 3\,\mathrm{kG}$). **b)** Effective image-coordinate grid arising from magnetic perturbations to initial Cartesian grid in the linear regime. **c)** Normalised proton-flux image in the nonlinear injective regime, with $\mu < \mu_c \sim 1$ ($B_{rms,0} \approx 30\,\mathrm{kG}$). **d)** Image-coordinate grid in the nonlinear injective regime. **e)** Normalised proton-flux image in the caustic regime, with $\mu \geq \mu_c$ ($B_{rms,0} \approx 120\,\mathrm{kG}$). **f)** Image-coordinate grid in the caustic regime. **g)** Normalised proton-flux image in the diffusive regime, with $\mu \gtrsim 1/\delta\alpha$ ($B_{rms,0} = 750\,\mathrm{MG}$). **h)** Image-coordinate system in a diffusive regime.

parameters tuned to have small μ: relative image-flux deviations indeed appear faint. The smallness of coordinate-grid perturbations relative to a Cartesian grid implied by (2.24) is demonstrated in Figure 2.2b for a Golitsyn field with $\mu \ll 1$.

More quantitatively, the RMS of relative image-flux variations is small in the linear regime. Linear-regime image-flux relation (2.25) enables the following relation between μ and the relative image-flux RMS to be derived analytically under the assumption of homogeneous and isotropic magnetic field statistics (see Appendix F):

$$\left(\frac{\delta\Psi}{\Psi_0}\right)_{rms} \equiv \left\langle \left(\frac{\delta\Psi}{\Psi_0^{(s)}}\right)^2 \right\rangle^{1/2} = \sqrt{\frac{\pi}{2}} \frac{r_i r_s}{r_s + r_i} \frac{eB_{rms}}{mcV} \sqrt{\frac{l_z}{l_\Psi}} = \sqrt{\frac{\pi}{2}\frac{\ell_B}{l_\Psi}}\mu \,, \tag{2.26}$$

where l_Ψ is the relative image-flux correlation length (defined in Appendix F). This can be rearranged to give a formula for μ in terms of the RMS of relative image-flux deviations:

$$\mu = \mu_0 \left(\frac{\delta\Psi}{\Psi_0}\right)_{rms} \,, \tag{2.27}$$

where $\mu_0 \equiv \sqrt{2l_\Psi/\ell_B\pi}$ depends on the particular stochastic field configuration, but it can be shown analytically that for any isotropic, homogeneous stochastic magnetic field, $\mu_0 \leq 2/\pi$ (Appendix F). The estimate (2.27) of μ combined with RMS magnetic field strength estimate (2.20) leads to a simple formula for the RMS field strength in terms of the RMS of the relative image-flux:

$$\begin{aligned} B_{rms}(\mathrm{kG}) \approx\ & 40 \left[\frac{W(\mathrm{MeV})}{3.3\,\mathrm{MeV}}\right]^{1/2} \left[\frac{r_i(\mathrm{cm})}{1\,\mathrm{cm}}\right]^{-1} \\ & \times \left[\frac{l_z(\mathrm{mm})}{1\,\mathrm{mm}}\right]^{-1/2} \left[\frac{\ell_B(\mathrm{mm})}{0.08\,\mathrm{mm}}\right]^{1/2} \left(\frac{\delta\Psi}{\Psi_0}\right)_{rms} \mathrm{kG}\,. \end{aligned} \tag{2.28}$$

As mentioned in the discussion accompanying (2.20), a reasonable approximate value for the correlation length ℓ_B may be taken for the purpose of using this estimate of the magnetic field strength. ℓ_B can be evaluated precisely using the quantitative techniques described in the subsequent paragraphs. We note expression (2.28) only applies for small μ; once μ approaches unity, the RMS of the relative image-flux begins to increase nonlinearly with μ (see Appendix F).

In the linear regime, the path-integrated field can always be reconstructed uniquely from the image-flux distribution. This follows from the result (2.15) that the perpendicular-deflection field can be written as the gradient of the deflection-field potential φ provided $\delta\theta \lesssim \ell_B/l_z$:

$$\mathbf{w}(\mathbf{x}_{\perp 0}) \approx \nabla_{\perp 0}\varphi(\mathbf{x}_{\perp 0}) \ . \tag{2.29}$$

The assumption $\delta\theta \lesssim \ell_B/l_z$ is indeed valid in the linear regime, because $\delta\theta \, l_z/\ell_B \sim \mu \, \delta\alpha \left(r_s + r_i\right)/r_s \ll 1$. It can then be shown (Appendix E) that the image-flux deviation $\delta\Psi$ and the deflection-field potential φ are related by a Poisson equation

$$\nabla_{\perp 0}^2\varphi(\mathbf{x}_{\perp 0}) = -\Xi(\mathbf{x}_{\perp 0}) \ , \tag{2.30}$$

where the source function $\Xi(\mathbf{x}_\perp)$ is proportional to relative image-flux deviations:

$$\Xi(\mathbf{x}_{\perp 0}) = \mathcal{M}\frac{V}{r_s}\frac{\delta\Psi\left(\mathbf{x}_\perp^{(s)}\right)}{\Psi_0^{(s)}} \ . \tag{2.31}$$

If suitable boundary conditions are applied, for example

$$\hat{\mathbf{n}} \cdot \nabla_{\perp 0}\varphi(\mathbf{x}_{\perp 0}) = 0 \, , \tag{2.32}$$

equation (2.30) is well posed with a unique solution for $\nabla_{\perp 0}\varphi$, and so is invertible (see Kugland et al. 2012, section VB for a more detailed discussion of this). For example, the standard two-dimensional (2D) solution to the Poisson equation (2.30) with vanishing boundary conditions at infinity is

$$\varphi(\mathbf{x}_{\perp 0}) = \frac{1}{2\pi}\int \mathrm{d}^2\tilde{\mathbf{x}}_\perp \log\left(\frac{l_\perp}{|\mathbf{x}_\perp - \tilde{\mathbf{x}}_{\perp 0}|}\right)\Xi(\tilde{\mathbf{x}}_\perp) \ . \tag{2.33}$$

The use of $l_\perp$ in this expression is arbitrary, since the integral of $\Xi(\mathbf{x}_\perp)$ over the image vanishes by conservation of particles. The perpendicular-deflection field is then given by (2.29); for the case of infinite boundary conditions, we find

$$\mathbf{w}(\mathbf{x}_{\perp 0}) = -\frac{1}{2\pi}\int \mathrm{d}^2\tilde{\mathbf{x}}_{\perp} \frac{\mathbf{x}_{\perp 0} - \tilde{\mathbf{x}}_{\perp}}{\left|\mathbf{x}_{\perp 0} - \tilde{\mathbf{x}}_{\perp}\right|^2} \Xi(\tilde{\mathbf{x}}_{\perp}) \ . \tag{2.34}$$

The path-integrated magnetic field follows from (2.10). For finite regions, Poisson equation (2.30) can in principle be inverted numerically. However, Graziani et al. (2017) report that such an approach when applied to reconstructing path-integrated fields from proton images quickly becomes unsuccessful for non-asymptotically small μ. For this reason, we suggest using the field reconstruction algorithm described in Section 2.3.2 to reconstruct the path-integrated field instead.

If the perpendicular-deflection field (and hence the path-integrated field) has been reconstructed, the magnetic-energy spectrum can be predicted using spectral relation (2.11). However, the simple form of the relation (2.26) between image flux and magnetic field in the linear regime allows for the application of statistical methods directly to proton-flux images to obtain properties of the fields creating that image. In particular, for homogeneous and isotropic magnetic-field statistics satisfying $\ell_B \ll l_z$ (Appendix F, and Graziani et al. 2017), the 1D magnetic-energy spectrum (2.2) is related to the 2D spectrum of image-flux deviations $\hat{\eta}(k)$ by

$$E_B(k) = \frac{1}{2\pi}\frac{m_p^2 c^2 V^2}{e^2 r_s^2 l_z}\hat{\eta}\left(\frac{r_i}{r_s + r_i}k\right) \ . \tag{2.35}$$

Here, $\hat{\eta}(k)$ is defined by

$$\hat{\eta}(k_{\perp}) \equiv \frac{1}{2\pi\mathcal{A}}\int \mathrm{d}\theta \, \frac{\mathcal{M}^4}{\Psi_0^2}\left\langle \left|\widehat{\delta\Psi}(\mathbf{k}_{\perp})\right|^2 \right\rangle \ , \tag{2.36}$$

where $\widehat{\delta\Psi}(\mathbf{k}_{\perp})$ is the Fourier transform of the relative image-flux deviation.

To summarise, if a stochastic magnetic field with isotropic and locally homogeneous statistics is imaged in the linear regime, the path-integrated field and magnetic-energy spectrum can be reconstructed. However, we caution that unless μ is very small, distortions to results obtained using linear analysis manifest themselves, both in reconstructing perpendicular-deflection fields, and in the magnetic-energy spectrum using linear-regime flux spectral relation (2.35) (see Section 2.3.5 for an example).

A detailed discussion of proton imaging of stochastic magnetic fields in the linear regime – including an alternative field-reconstruction algorithm to cope with weakly nonlinear effects – is presented in Graziani et al. (2017).

2.3.2 Nonlinear injective regime: $\mu < \mu_c \sim 1$

In the nonlinear injective regime, μ is sufficiently large that beam-focusing effects associated with the nonlinear term resulting from magnetic deflections in plasma-image mapping (2.7) have a non-trivial effect on the image-flux distribution. However, μ is not so great as to lead to the proton beam intersecting itself, and hence loss of injectivity of the plasma-image mapping, which first occurs at some critical $\mu = \mu_c$ [shown in Appendix L of Bott et al. (2017)]. The importance of nonlinearity for moderate μ and preservation of injectivity for $\mu < \mu_c$ are illustrated by the plasma-image coordinate mapping for the test Golitsyn field shown in Figure 2.2d: the image-coordinate grid is visually distorted, but coordinate curves do not cross each other. The nonlinear injective regime can be distinguished from the linear regime simply by the presence of image-flux structures whose deviation from the mean image flux is similar in magnitude to the mean (see Figure 2.2c).

When injective, the plasma-image mapping tends to preserve the morphology of the proton-flux image obtained for the same magnetic field, but with small μ – so image-flux structures can still be qualitatively interpreted in terms of path-integrated MHD current structure. However, structures with positive relative image-flux tend to be narrow due to beam focusing, and those with negative relative image-flux enlarged. This phenomenon is evident in the nonlinear injective proton-flux image of the Golitsyn field, Figure 2.2c.

Nonlinear effects mean that a different approach for reconstructing path-integrated fields must be adopted to that expounded for the linear regime. One such approach can be found by noting that since the plasma-image mapping (2.7) is injective, the sum in RK image-flux relation (2.9) disappears, leaving

$$\Psi\left(\mathbf{x}_{\perp}^{(s)}(\mathbf{x}_{\perp 0})\right) = \frac{\Psi_0}{\det \nabla_{\perp 0}\left[\mathbf{x}_{\perp}^{(s)}(\mathbf{x}_{\perp 0})\right]} \,. \tag{2.37}$$

Our goal is to solve (2.37) for $\mathbf{x}_{\perp}^{(s)}(\mathbf{x}_{\perp 0})$ given an image-flux distribution $\Psi\left(\mathbf{x}_{\perp}^{(s)}(\mathbf{x}_{\perp 0})\right)$. We proceed by noting that the plasma-image mapping (2.7) can be rewritten in terms of a potential field $\phi(\mathbf{x}_{\perp 0})$:

$$\mathbf{x}_{\perp}^{(s)} \approx \nabla_{\perp 0}\phi(\mathbf{x}_{\perp 0}) \approx \nabla_{\perp 0}\left[\frac{r_s + r_i}{2r_i}\mathbf{x}_{\perp 0}^2 + \frac{r_s}{V}\,\varphi(\mathbf{x}_{\perp 0})\right] \,. \tag{2.38}$$

The existence of $\phi(\mathbf{x}_{\perp 0})$ follows from that of the deflection-field potential, which is defined in Section 2.3.1, equation (2.15). Equation (2.37) can then be restated as an equation for $\phi(\mathbf{x}_{\perp 0})$:

$$\Psi(\nabla_{\perp 0}\phi(\mathbf{x}_{\perp 0})) = \frac{\Psi_0}{\det \nabla_{\perp 0}\nabla_{\perp 0}\phi(\mathbf{x}_{\perp 0})} \,. \tag{2.39}$$

Equation (2.39) is an example of an Monge-Ampère equation, which appear in numerous mathematical and physical contexts (Gangbo and McCann 1996). Despite its nonlinearity, it can be shown (Brenier 1991) that there is a unique (up to a constant) solution for ϕ with Neumann boundary conditions

$$\hat{\mathbf{n}} \cdot \nabla_{\perp 0}\phi(\mathbf{x}_{\perp 0}) = \hat{\mathbf{n}} \cdot \mathbf{x}_{\perp 0} \,. \tag{2.40}$$

One approach for establishing this result comes from the observation that the solution of the Monge-Ampère equation also solves the L_2 *Monge-Kantorovich problem* (Villani 2008). This correspondence is explained in Appendix H. This means that with an appropriate *field-reconstruction algorithm*, $\nabla_{\perp 0}\phi$ can be reconstructed from a given proton-flux image, which can then be used to calculate the perpendicular-deflection field

$$\mathbf{w}(\mathbf{x}_{\perp 0}) = \frac{V}{r_s}\nabla_{\perp 0}\left(\phi - \frac{r_s + r_i}{2r_i}\mathbf{x}_{\perp 0}^2\right) . \qquad (2.41)$$

The path-integrated magnetic field can then be calculated using (2.10). There exist a number of possible algorithms for solving the Monge-Ampère equation (2.39) (Dean and Glowinski 2006), and some have recently been applied to the problem of recovering path-integrated magnetic fields from proton-flux images (Kasim et al. 2017). In Appendix I.4, we outline one such field-reconstruction algorithm, which is both simple to implement and computationally efficient (Sulman et al. 2011). Furthermore, we have recently made available an open-source PYTHON code ('PROton-imaged B-field nonLinear Extraction Module', or PROBLEM) which solves the inversion problem numerically using this approach. As explained in Section 2.2.2, the reconstructed path-integrated magnetic field can be combined with deflection-field spectral relation (2.11) to deduce the magnetic-energy spectrum.

To summarise, like the linear regime the path-integrated magnetic field and magnetic-energy spectrum are always recoverable from an individual proton-flux image in the nonlinear injective regime. This perhaps counter-intuitive result essentially holds because of the irrotationality of the perpendicular-deflection field, discussed in Section 2.2.2. Furthermore, the techniques used to achieve this are more widely applicable than those derivable from linear theory. However, care must be taken when applying the field-reconstruction algorithm to arbitrary proton-flux images, because the results can be misleading if the plasma-image mapping is not injective. This is described in the next section.

2.3.3 Caustic regime: $\mu \geq \mu_c$

For μ greater than μ_c, gradients in the perpendicular-deflection field are sufficiently large that the plasma-image mapping (2.7) becomes multi-valued in places (see Figure 2.2f) – a phenomenon sometimes referred to as *mesh-twisting* (Kugland et al. 2012). Physically, in this regime some of the paths of imaging protons cross before reaching the detector, and hence there exist regions of image flux whose constituent protons originate from spatially-disconnected initial positions. That multi-valuedness of the plasma-image mapping only occurs at $\mu \geq \mu_c$ follows from the observation that such crossing requires that the determinant of the plasma-image mapping change sign. For this to happen, the magnitude of gradients of the perpendicular-deflection field must be comparable to gradients in the undeflected mapping – which by the definition of μ (2.17) is precisely the criterion of μ sufficiently large. This alone does not guarantee the existence of μ_c; however, the conditions required for the absence of mesh-twisting at all values of μ are typically incompatible with stochasticity [see Appendix L of Bott et al. (2017)]. The particular value of μ_c depends on the particular stochastic field, but typically is order unity [although heuristic arguments can be given implying that it likely decreases logarithmically with the field scale ℓ_B; see Appendix L of Bott et al. (2017)].

The multi-valuedness of the plasma-image mapping is closely associated with caustics, defined as curves on which the determinant of the plasma-image mapping (2.7) vanishes (equation (14) of Kugland et al. 2012):

$$\det \nabla_{\perp 0}\left[\mathbf{x}_{\perp}^{(s)}(\mathbf{x}_{\perp 0})\right] = 0\,. \tag{2.42}$$

This is (trivially) because a sign reversal of the determinant for a continuous mapping cannot occur without the value of that determinant passing through zero. If the determinant does indeed vanish, the denominator in RK image-flux relation (2.9) also does, yielding a formally infinite local image-flux. In practice the local image-flux value is limited by finite resolution of proton images (Kugland et al. 2012) – however, the morphology of proton-flux images is still dominated by caustics if there are present. This is evident in the caustic-regime proton-flux image of the test Golitsyn field, shown in Figure 2.2e.

The relationship between caustics and magnetic fields creating them has been studied in great depth elsewhere (see section IV of Kugland et al. 2012); for our purposes, we simply note that the width, strength and distance between caustics do not necessarily reflect equivalent properties of the magnetic field, implying that great care must be taken when qualitatively assessing magnetic structures from proton-flux images containing caustics.

Similar care must be taken when attempting quantitative analysis. In the caustic regime the reconstruction of the path-integrated field from a proton-flux image is no longer a well-posed problem: for a given proton image, there exists a number of path-integrated fields (and hence plasma-image mappings) which give the same flux distribution via the RK image-flux relation (2.9). Intuitively this seems reasonable, because without the injectivity constraint, the RK image-flux relation insufficiently determines the path-integrated field. An explicit example of many different path-integrated fields corresponding to a simple image-flux distribution is given in Appendix M of (Bott et al. 2017). In addition to this simple analytical example, the impossibility of solving the RK image-flux relation (2.9) for non-injective plasma-image mappings can be demonstrated numerically (and is done so in Section 2.3.5). Attempts to reconstruct the magnetic-energy spectrum in the caustic regime are also prone to failure. In short, we emphasise that the caustic regime is much less amenable to direct analysis than either the linear, or the nonlinear injective regime.

This being the case, identifying the presence of caustics in a proton image is essential for a sensible interpretation of that image. In principle, caustics should typically be identifiable in proton-flux images from narrow curves of high proton flux. In practice, proton-flux images have a finite spatial resolution which can disguise these, making distinguishing between the nonlinear injective regime and caustic regime a non-trivial problem. The issue, and possible ways around it, is explored in Section 2.4.3.

For a systematic review of caustic theory in the context of proton imaging for electromagnetic structures, see Kugland et al. (2012).

2.3.4 Diffusive regime: $\mu \gtrsim r_s/(r_i + r_s)\, \delta\alpha \gg 1$

For large μ, the characteristic nature of the plasma-image mapping changes yet again. The position of protons in any given local region on the detector is dominated by the perpendicular-deflection field, rather than the projected position in the absence of magnetic fields. More specifically, if $\mu \gtrsim r_s/(r_i + r_s)\, \delta\alpha$, then proton trajectories have already crossed as they leave the plasma. This follows because the perpendicular displacement inside the plasma due to magnetic deflections $l_z\, \delta\theta$ is comparable to the typical size of magnetic structures ℓ_B: $l_z\, \delta\theta \sim \mu\, \delta\alpha\, (r_s + r_i)/r_s \ell_B \gtrsim \ell_B$. As a consequence, the perpendicular-deflection field can no longer be written as the gradient of the deflection-field potential, and the magnetic field integrated along the actual proton trajectories is not equivalent to the magnetic field integrated along undeflected trajectories (in other words, equations (2.15) and (2.16) do not apply in the diffusive regime).

The diffusive regime is incompatible with the small-deflection assumption for regular fields with $\ell_B \sim l_z$, since then the deflection angle $\delta\theta \gtrsim 1$. Furthermore, successful imaging in such a parameter space is practically unfeasible, because it would require a prohibitively large detector. However, the diffusive regime can be reached without violating the small-angle approximation for sufficiently small-scale fields due to the opposite scalings of μ and the typical deflection angle $\delta\theta$ with correlation length ℓ_B: $\mu \propto \ell_B^{-1/2}$, while $\delta\theta \propto \ell_B^{1/2}$.

In the diffusive regime, image-flux variations are typically much less pronounced in magnitude than seen in the caustic regime (Figure 2.2g, central part of image). Qualitatively, this is due to chaotic tangling of proton trajectories from spatially uncorrelated regions of the imaged field (Figure 2.2h). In a technical sense, a proton-flux image in the diffusive regime is still filled with caustics, the outlines of which are still visible in the central part of Figure 2.2g; however, since even pairs of protons with close initial positions often end up at disparate spatial locations, the proportion of image flux concentrated into an individual caustic drops as μ increases.

An alternative interpretation of the proton-flux image in the diffusive regime can be given in terms of diffusive-type models. As first shown by Dolginov and Toptygin (1967), the diffusion of a fast proton beam through compact, isotropic stochastic magnetic fields with correlation length $\ell_B \ll l_z, l_\perp$ can be described by perpendicular velocity diffusion coefficient

$$D_w = \frac{V e^2 B_{rms}^2 \ell_B}{4 m_p^2 c^2} \,. \tag{2.43}$$

The result is valid in the small-deflections limit $\delta\theta \ll 1$, which in turn necessitates that the proton Larmor radius ρ_p associated with the typical RMS magnetic field strength B_{rms} satisfy $\rho_p \gg \ell_B$:

$$\frac{\rho_p}{\ell_B} = \frac{mcV}{eB\ell_B} \sim \delta\theta^{-1} \sqrt{\frac{l_i}{\ell_B}} \gg 1 \,. \tag{2.44}$$

For the reader's convenience, Appendix O.1 of Bott et al. (2017) presents an alternative derivation of diffusion coefficient (2.43).

The uncertainty in perpendicular velocity Δw acquired due to diffusion leads to a 'smearing effect': under a diffusive model with coefficient D_w given by (2.43), the image-flux distribution is related to the (here non-uniform) initial distribution by convolution

$$\Psi\left(\mathbf{x}_\perp^{(s)}\right) = \frac{1}{\pi\delta^2} \int \mathrm{d}^2\tilde{\mathbf{x}}_\perp^{(s)} \, \Psi_0^{(s)}\left(\tilde{\mathbf{x}}_\perp^{(s)}\right) \exp\left[-\left(\frac{\mathbf{x}_\perp^{(s)} - \tilde{\mathbf{x}}_\perp^{(s)}}{\delta}\right)^2\right] , \tag{2.45}$$

where

$$\delta = r_s \frac{\Delta w}{V} = \frac{e B_{rms} r_s}{m_p c V} \sqrt{l_z \ell_B} \,. \tag{2.46}$$

This result is derived in Appendix O.2 of Bott et al. (2017). We see that a diffusive model of proton-flux images predicts that an initially uniform flux distribution will not display relative image-flux deviations if the stochastic magnetic field being imaged has a uniform envelope. For a magnetic field with a spatially varying envelope,

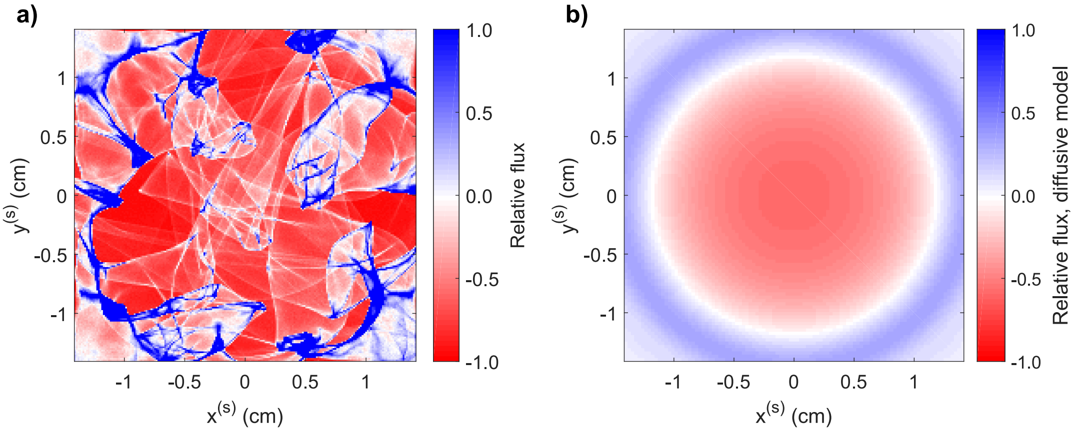

Figure 2.3: Comparison of relative flux image predicted by diffusive model compared with actual result in diffusive regime. a) 3.3 MeV proton image-flux distribution associated with magnetic field described in figure 2, with $B_{rms,0} = 750\,\mathrm{kG}$. Here, relative flux refers to $\delta\Psi\left(\mathbf{x}_\perp^{(s)}\right)/\Psi_0^{(s)}$, where $\delta\Psi\left(\mathbf{x}_\perp^{(s)}\right) \equiv \Psi\left(\mathbf{x}_\perp^{(s)}\right) - \Psi_0^{(s)}$ is the flux deviation, and $\Psi_0^{(s)}$ the mean image flux. The same imaging parameters as those described in figure 4 are used (see figure 4g for normalised proton-flux image). **b)** Predicted relative proton-flux image assuming uniform initial flux, and diffusive model of imaging beam evolution (2.45), with $\delta = \delta(\mathbf{x}_\perp) = \delta_0 \exp\left[-4\sigma \mathbf{x}_\perp^2/l_i^2\right]$. Here, δ_0 is given by (2.46), with $B_{rms} = 750\,\mathrm{kG}$, and $l_i = l_z = l_\perp = 0.1\,\mathrm{cm}$.

such as the Golitsyn field shown in Figure 2.1, (2.45) instead indicates that different sections of the initial flux distribution will be subject to different diffusion rates. For the Gaussian envelope used to create the stochastic field shown in Figure 2.1, this results in the central region of the proton image having a reduced image flux when compared to the mean initial image flux; the central region is surrounded by a ring of greater-than-average image flux (illustrated in Figure 2.3b). Comparing the diffusive prediction of the relative image-flux distribution to the actual relative image-flux distribution shown in Figure 2.3a, we see that the diffusive model fails to capture many features of the true proton-flux image: in particular, caustic structures. However, for stochastic fields with smaller-scale structures than the Golitsyn field, the diffusive model is more accurate, and caustic structures are suppressed [two examples are provided in Appendix O.3 of Bott et al. (2017)].

The observation of decreased intensity of image-flux deviations relative to the mean image flux is not sufficient to identify uniquely the diffusive regime – the same observation also holds for the linear regime (as discussed in Section 2.3.1). Operationally, the diffusive regime can usually be distinguished by noting that unless fields have an extremely small spatial correlation scale ℓ_B, deflections of protons will be large enough to result in net loss of proton flux from an image. This loss of flux can be measured if the initial flux is known. Another, more conclusive test identifying the diffusive regime – requiring practical modification to experimental platforms – is to introduce a partial obstruction into the path of the imaging proton beam. This could include a sharp edge, a pinhole, or some type of grid. In the diffusive regime, the edges associated with any of these features will appear blurred by diffusive scattering of protons due to the stochastic fields.

Quantitative analysis of proton images in the diffusive regime is much more restricted in scope that in other regimes. Whilst the plasma-image mapping (2.7) is still formally valid, in the diffusive regime, the perpendicular-deflection field is an extremely complicated object, and is not recoverable from an individual proton-flux image (for the same reason as described for the caustic regime for Section 2.3.3). That being said, statistical information pertaining to the magnetic field can often be extracted from proton-flux images. More specifically, for sufficiently small-scale fields the diffusion coefficient D_w (2.43) can be measured, which is turn gives an estimate of $B_{rms}^2 \ell_B$. This is most simply done by using one of the partial-obstruction methods mentioned above, and calculating the extent of blurring effects. It is also conceivable that numerical extraction of D_w could be undertaken, assuming a model for the image-flux distribution of the form (2.45), and suitable boundary conditions. How this is done more precisely – and when this is a well-posed mathematical problem – are open questions which we do not answer here.

There is an extensive literature discussing diffusion due to stochastic magnetic fields in the context of cosmic rays (Dolginov and Toptygin 1967, Jokipii 1972, Hall and Sturrock 1967, Parker 1965, Blandford and Eichler 1987); however, the author of this chapter is not aware of any discussion directly concerned with the diffusive scattering of a proton imaging beam. The key positive result of this section, then, is to have derived a relation (2.45) between the image-flux distribution and the diffusive scattering of the proton beam by a stochastic magnetic field.

2.3.5 Numerical demonstration of field-reconstruction algorithm

To conclude this characterisation of the four contrast regimes, we illustrate the efficacy (or lack thereof) of the proposed field-reconstruction algorithm for recovering the path-integrated field numerically in each contrast regime. More specifically, we apply the field-reconstruction algorithm outlined in Appendix I.4 (the PROBLEM code) to the proton images presented in Figure 2.2. The reconstructed path-integrated fields normalised to the RMS of the actual magnetic field in each case are shown in Figure 2.4; these are compared with the true path-integrated field, shown in Figure 2.1b. Figure 2.4 also presents a calculation of magnetic-energy spectrum determined using spectral relation (2.11) (blue circles) applied to the reconstructed perpendicular-deflection field in each case. For comparison, the true spectra (red line) of the Golitsyn fields are shown, along with the results of linear-regime flux spectral relation (2.35) applied directly to each image-flux distribution (purple circles).

The possibility of successful reconstruction of the path-integrated field in the linear regime (from the proton image shown in Figure 2.2a) is illustrated in Figure 2.4a; we see strong agreement with Figure 2.1b in terms of both field morphology and strength in the central region. The recovery of the magnetic-energy spectrum from the same proton-flux image is illustrated in Figure 2.4b: both the linear-regime flux spectral relation (2.35) and deflection-field spectral relation (2.11) recover the correct power law at the energetically dominant wavenumbers. However, at higher wavenumbers, a flattening of both predicted spectra is observed. This effect is likely due to Poisson noise, and is discussed further in Section 2.4.3.

The result of the field-reconstruction algorithm in the nonlinear injective regime

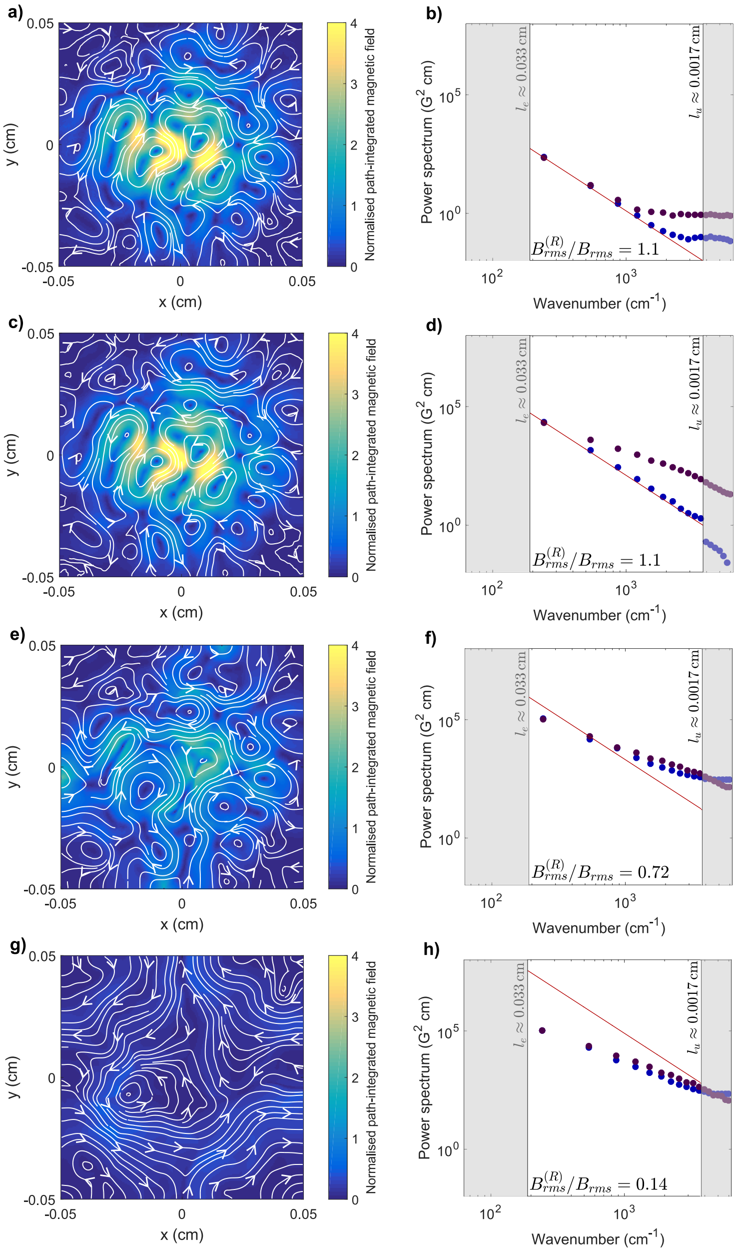

Figure 2.4: Efficacy of techniques for reconstructing magnetic field statistics directly from proton-flux images across contrast regimes. For each proton-flux image shown in figure 2.2, a reconstructed path-integrated magnetic field was produced by applying the field-reconstruction algorithm (see Appendix I.4) appropriate for inverting the Monge-Ampère equation (2.39) with boundary conditions (2.40), before recovering the perpendicular-deflection field using (2.41), and finally the path-integrated field by (2.10). The true field is shown in figure 2.1b. The magnetic-energy spectrum (true result shown in red) was predicted in two ways: using spectral relation (2.11) applied to the reconstructed perpendicular-deflection field (blue), and linear-regime spectral relation (2.35) applied directly to the proton-flux images (purple). **a)** Path-integrated magnetic field reconstructed from linear-regime proton-flux image ($\mu \ll 1$), figure 2.2a. **b)** Predicted magnetic energy spectra, derived from figures 2.2a and 2.4a. **c)** Same as **a)**, but for nonlinear-injective-regime proton-flux image ($\mu < \mu_c$), figure 2.2c. **d)** Same as **b)**, but spectra derived from Figures 2.2c and 2.4c. **e)** Same as **a)**, but for caustic-regime proton-flux image ($\mu \geq \mu_c$), figure 2.2e. **f)** Same as **b)**, but for figures 2.2e and 2.4e. **g)** Same as **a)**, but for diffusive-regime proton-flux image ($\mu \gtrsim 1/\delta\alpha \gg 1$), figure 2.2f. **h)** Same as **b)**, but for figures 2.2f and 2.4f.

– that is, the algorithm is applied to the image-flux distribution shown in Figure 2.2c – is shown in Figure 2.4b. Similarly to the results for the linear regime, the predicted path-integrated magnetic field is a close match to the true field in terms of both its field strength and direction. Figure 2.4d shows the predicted magnetic-energy spectrum using deflection-field spectral relation (2.11); the true spectrum is recovered over a wide range of wavenumbers. We note that despite the Poisson noise being the same in proton-flux images Figure 2.2a and 2.2c, the spectrum predicted from the latter is less distorted at high wavenumbers. This is because the magnitude of deviations in the image flux due to magnetic fields are larger in the latter case, so the relative effect of Poisson noise is reduced.

In contrast, the predicted magnetic-energy spectrum from linear-regime flux spectral relation (2.35) does not follow the expected $k^{-11/3}$ power law, instead moving towards a k^{-2} law. This distorted power law is obtained because the strong, narrow image-flux structures that appear irrespective of the underlying magnetic-energy spectrum have a characteristic 'sharp-edge' spectrum (Arévalo et al. 2012). We conclude that direct application to images involving order-unity relative image-flux variations of linear-regime flux spectral relation (2.35) can lead to misleading results.

Figure 2.4e shows the results of the field-reconstruction algorithm described in Section 2.3.2 applied to the proton-flux image Figure 2.2e (an image containing caustics). While the streamlines of the path-integrated perpendicular magnetic field retain a reasonable agreement, the field strength distribution does not: the typical magnitude is reduced. The mapping recovered by the field-reconstruction algorithm is instead the unique injective mapping satisfying Monge-Ampère equation (2.39) given the image-flux distribution shown in Figure 2.2e.

Figure 2.4f demonstrates that the magnetic-energy spectrum predicted by spectral relation (2.11) applied to the reconstructed perpendicular-deflection field is distorted to a k^{-2} spectrum, much as the magnetic-energy spectrum predicted by linear-regime flux spectral relation (2.35) is distorted as nonlinearity of the plasma-image mapping becomes important.

Finally, attempts to reconstruct the path-integrated field in the diffusive regime lead to extremely inaccurate results. This failure is illustrated by the path-integrated field Figure 2.4g reconstructed from the image-flux distribution shown in Figure 2.4f. Predicted field strengths are orders of magnitude lower than the true values, and the recovered field's morphology resembles that of a regular field rather than of the actual stochastic one. This inaccuracy is also replicated in the predicted magnetic-energy spectrum shown in Figure 2.2h: the Golitsyn spectrum is again distorted to a k^{-2} power law due to the caustic ring-like structure seen in Figure 2.2g, and the predicted spectrum at the energetically dominant wavenumbers is strongly suppressed.

A simple quantitative way to compare the quality of the predicted reconstructions for different contrast regimes is to calculate the predicted RMS magnetic field strength from the recovered magnetic-energy spectra using (2.3). The results are shown in Table 2.1. It is clear that the predicted values for B_{rms} are close to the actual ones in the linear and nonlinear injective regimes, but B_{rms} is under-predicted in the caustic and diffusive regimes. That the typical field strengths predicted by the field-reconstruction algorithm are reduced is a manifestation of the general analytical result that the reconstructed perpendicular-deflection field will always provide a lower bound on the RMS deflection-field strength (Gangbo and McCann 1996), which can in turn be used to provide a lower bound on the RMS magnetic field strength. Explicitly, it can be shown (see Appendix H) that

Contrast regime	μ	$B_{rms}^{(R)}$ (kG)	B_{rms} (kG)
Linear	0.05	1.10	1.00
Nonlinear injective	0.53	10.5	10.0
Caustic	2.12	29.0	40.0
Diffusive	13.1	36.1	250

Table 2.1: Comparison with true result of RMS magnetic field strength predicted using magnetic-energy spectrum derived from (2.11) in different contrast regimes.

$$B_{rms}^2 \geq \frac{m_p^2 c^2}{e^2 l_z^2} \left\langle (\nabla_{\perp 0} \varphi)^2 \right\rangle , \tag{2.47}$$

where $\nabla_{\perp 0}\varphi$ is the deflection-field potential recovered from the solution to Monge-Ampère equation (2.39). Furthermore, in Appendix H, it is demonstrated for the Golitsyn test field outlined in Figure 2.1 that this lower bound property becomes very weak as μ increases further.

In short, this numerical example validates the claim that for proton-flux images of stochastic magnetic fields created in the linear and nonlinear injective regimes, the true path-integrated field is extractable using an appropriate field-reconstruction algorithm. Furthermore, the predicted magnetic-energy spectrum agrees well with the true result. Neither of these results are true in the caustic and diffusive regimes.

2.4 Technicalities and complications

2.4.1 Assumptions

As mentioned in Section 2.2.2, the applicability of plasma-image mapping (2.7) and RK image-flux relation (2.9) to the proton imaging set-up depends on various assumptions: a mono-energetic, instantaneous, uniform beam from a point source, paraxialilty, point projection, and small deflections. Here, we state each of these precisely, and explore their validity. In addition to the effects stated below, in deriving the stated plasma-image mapping, a range of physical processes are neglected in line with previous work on analytic models of proton imaging (Kugland et al. 2012). These are discussed in Appendix B.

Mono-energetic, instantaneous uniform proton beam from point source

There exist several comprehensive reviews of the generation of proton beams to be used for imaging via both high-intensity lasers (Wilks et al. 2001, Borghesi et al. 2006, Kar et al. 2008, Daido et al. 2012), and the proton capsule backlighters (Li et al. 2006a, Manuel et al. 2012); the interested reader is referred to the enclosed references. In this chapter, we only discuss briefly those properties which justify our assumption that a proton beam used for imaging can be well modelled as mono-energetic, instantaneous, uniform, and as originating from a point source.

Mono-energetic

An imaging beam can often be approximated as mono-energetic for two reasons. First, for the case of capsule implosions, the fusion-generated protons have a characteristic energy determined by the nuclear reaction creating them, a value which is retained to $3-9\%$ accuracy in the imaging beam. This is not the case for protons generated using high-intensity laser sources, which typically have a thermal spectrum. Secondly, proton detectors are typically designed to image different proton energies separately, by taking advantage of the short distance over which protons of a given energy typically deposit their energy (Ziegler 1999). Most relevantly for this thesis, a detector based on sheets of CR-39 interleaved with metal filters has an effective energy resolution of $\sim 0.1\,\mathrm{MeV}$ (Séguin et al. 2003). That being said, it is still not the case in general that the protons creating any particular experimental proton-flux image are mono-energetic, irrespective of the energy distribution of the source. For example, calibrated radiographic film (RCF) in a stack configuration is often used in proton imaging set-ups; and whilst the distribution of deposited energy per proton in a given layer of the stack is sharply peaked ($\sim 0.2\,\mathrm{MeV}$ full-half-width-maximum) around some critical value of proton energy, the contribution of protons with significantly higher energies can be non-negligible (Nürnberg et al. 2009). Nevertheless, for the OMEGA experiment, the mono-energetic assumption is a sound one.

If this assumption were violated, plasma-image mapping (2.7) would still be valid individually for a given proton with initial speed V – but RK image-flux relation (2.9) would have to be modified to take into account that protons at different initial speeds have distinct plasma-image mappings. Doing so leads to a significantly more complicated image-flux relation.

Instantaneous

The instanteneity of the imaging process is the result of the temporal pulse length of proton sources τ_{pulse} and the transit time of protons across the plasma τ_{path} being small compared to the evolution time of the magnetic-field configuration of interest. For fusion-produced protons, $\tau_{\text{pulse}} \sim 100\,\text{ps}$ (Séguin et al. 2004), while for TNSA-produced protons, $\tau_{\text{pulse}} \sim 10\,\text{ps}$ (Wilks et al. 2001). For both, the transit time across the plasma can be estimated as

$$\tau_{\text{path}} \sim 40 \left[\frac{l_z(\text{cm})}{0.1\,\text{cm}}\right] \left[\frac{W(\text{MeV})}{3.3\,\text{MeV}}\right] \text{ps}\,. \tag{2.48}$$

Thus, provided the plasma dynamics to be studied is on nano-second timescales, this approximation of instantaneity is a good one. This is indeed the case for many relevant experiments involving stochastic magnetic fields (Tzeferacos et al. 2017, 2018), though by no means all (for example, see Mondal et al. 2012). For time-varying fields, the effect of inductive electric fields is likely significant – which in turn leads to the invalidation of expression (2.8) for the perpendicular-deflection field. In addition, magnetic fields varying on timescales shorter than τ_{pulse} would lead to the front part of the proton beam seeing different magnetic fields to the back part of the beam; the resulting proton image would then be the superposition of the proton images for both fields.

Point source

The point source approximation is the natural consequence of the size of the proton source a being much smaller than the distance r_i from the source to the plasma. For fusion protons, $a \approx 40 - 50\,\mu\text{m}$ (Li et al. 2006b), while for TNSA protons this is even smaller: $a \approx 10\,\mu\text{m}$ (Wilks et al. 2001). To prevent the diagnostic interfering with experiment, one typically chooses $r_i \geq 1\,\text{cm}$, so $r_i \gg a$. However, the source's finite size prevents imaging of magnetic structures on scales smaller than the size of the source; the consequences of this for the extraction of magnetic field statistics are discussed in Section 2.4.3.

Initially uniform proton flux

Finally, the uniformity of initial proton flux is a consequence of approximately isotropic emission of protons from the source across the solid angle encapsulating the experiment. In practice, this assumption is not always satisfied. Experimental characterisation of proton-flux images produced by a capsule implosion in the absence of imaging fields show RMS relative flux deviations of $16 \pm 7\,\%$ for 3.3 MeV fusion protons and $26 \pm 10\,\%$ for 15.0 MeV protons; possible deviations of up to $50\,\%$ across the detector have been measured (Manuel et al. 2012). Naive application of field-reconstruction algorithms which presume a uniform initial flux to proton images created using a capsule implosion can therefore result in the accidental recovery of non-physical path-integrated magnetic fields. This problem is illustrated explicitly and discussed further in Section 2.4.3. However, such variations are typically limited to longer length scales: for variations in initial flux with correlation length ℓ^* on the detector satisfying $\ell^* \lesssim \ell_c^* \equiv 0.02(r_i + r_s)$, the relative amplitude of the variations compared to the mean flux is typically $\sim 3\%$ (Manuel et al. 2012). This allows for the application of high-pass filters to isolate flux features resulting from stochastic magnetic fields from those due to variations in the initial flux (see Section 2.4.3). The problem is more acute for TNSA protons, whose initial distribution can display perpendicular spatial structuring (Nürnberg et al. 2009).

Paraxiality

If the distance from the proton source to the plasma is much greater than the dimensions of the plasma, $r_i \gg l_\perp, l_z$, we can approximate the section of the beam passing through the plasma as planar, despite the fact that proton beams generated by fusion reactions in a D_2 capsule implosion generally take the form of a uniformly expanding spherical shell (Li et al. 2006b). For a given proton, this paraxial approximation is effectively an expansion of the position and velocity of the proton in terms of half of the paraxial parameter

$$\frac{\delta\alpha}{2} = \frac{l_\perp}{2r_i} \ll 1\,, \tag{2.49}$$

the ratio of the size of the region being imaged to the radius of curvature of the beam. The factor of two appears, because the approximating plane is chosen to be exact at the centre of the beam. For typical experimental set-ups, $\delta\alpha \approx 0.05 - 0.2 \ll 1$ (Kugland et al. 2012).

Increasing the paraxial parameter $\delta\alpha$ does not significantly change the nature of the four contrast regimes described in Section 2.3 qualitatively, although for sufficiently large values a slight decay in proton flux towards the edges of images may be detectable. For quantitative analysis, higher-order corrections in $\delta\alpha$ to the plasma-image mapping (2.7) can be introduced (Kugland et al. 2012).

Point projection

The point-projection assumption requires that the distance r_s from the plasma to the detector be much greater than l_z. This means that displacements of protons from their undeflected trajectories acquired inside the plasma due to magnetic forces are negligible compared to those displacements of protons resulting from their free-streaming motion beyond the plasma with an altered deflection velocity. Mathematically, the plasma-image mapping (2.7) is effectively an expansion in

$$\delta\beta \equiv \frac{l_z}{r_s} \ll 1\,, \tag{2.50}$$

retaining only the leading order term in $\delta\beta$. In actual proton-imaging set-ups as typically implemented, $l_z \ll r_i \ll r_s$, so $\delta\beta \ll 1$.

Small proton-deflection angles

To derive the expression (2.8) for the perpendicular-deflection field, the size of typical proton-velocity deflections are assumed small compared to the initial proton velocity. Since (2.8) shows that deflection velocities are perpendicular to the initial direction

– that is, that $\mathbf{w} \cdot \mathbf{V}_0 \approx \mathbf{w} \cdot \hat{\mathbf{z}} \approx 0$ (where $\mathbf{V}_0$ is the undeflected velocity of an imaging proton) – the deflection angle of the proton due to magnetic forces must therefore be small:

$$\delta\theta \equiv \cos^{-1}\left[\frac{\mathbf{V}_0 \cdot (\mathbf{V}_0 + \mathbf{w})}{|\mathbf{V}_0|\,|\mathbf{V}_0 + \mathbf{w}|}\right] \approx \frac{|\mathbf{w}|}{V} \ll 1\,. \tag{2.51}$$

The magnitude of this parameter can be practically estimated for stochastic fields imaged by protons with energy W using deflection angle RMS (2.13):

$$\delta\theta \sim \frac{eB}{m_p c V}\sqrt{l_z \ell_B} \approx \left[\frac{B(\mathrm{MG})}{2.6\,\mathrm{MG}}\right]\left[\frac{W(\mathrm{MeV})}{3.3\,\mathrm{MeV}}\right]^{-1/2}\left[\frac{l_z(\mathrm{cm})\,\ell_B(\mathrm{cm})}{0.01\,\mathrm{cm}^2}\right]^{1/2}. \tag{2.52}$$

The same estimate can also be used to determine whether $\delta\theta \lesssim \ell_B/l_z$, and hence whether the perpendicular-deflection field is irrotational. Since $\ell_B < l_z$, this condition is typically more stringent than $\delta\theta \ll 1$.

It is clear that if deflections are not small, $\delta\theta \sim 1$ inevitably implies that the system is in the diffusive regime $\mu \sim r_i/\ell_B \gg 1$. This has the consequence that, despite the technical lack of validity of the derivation of plasma-image mapping (2.7) in this case, proton-flux images in the large-deflection regime are likely to have many qualitatively similar features to diffusive proton-flux images – albeit combined with a significant loss of total flux from the detector.

2.4.2 Theoretical complications

We have claimed in the previous sections that the imaging of stochastic magnetic fields can be classified into four general regimes depending on μ, and that in two of these regimes (linear and nonlinear injective), the path-integrated field can be extracted directly from proton-flux images; under the further assumption of isotropy, this is sufficient to determine the magnetic-energy spectrum of the stochastic field. Whilst these statements are true for many stochastic fields, there are others for which the efficacy of the proposed analysis techniques must be re-considered: these are discussed in this section. Note that we distinguish between inherent constraints on the technique, which are unavoidable, and constraints due to experimental effects, which can in principle be overcome with advances in diagnostic implementation. The former are discussed in this section, the latter in Section 2.4.3.

Spatially inhomogeneous and anisotropic fields

The classification into four contrast regimes that can be distinguished simply by particular characteristics of proton-flux images holds for locally homogeneous stochastic fields. However, this classification is not strictly valid for more general fields with inhomogeneous or anisotropic statistics. In particular, for an arbitrary proton-flux image, the contrast regime associated with that image cannot be uniquely identified. This is related to the non-uniqueness of the inversion problem associated with recovering path-integrated magnetic fields associated with a particular proton-flux image – introduced in Section 2.2.3 and discussed in Sections 2.3.3 and 2.3.4. We further illustrate this phenomenon with an example consisting of two strikingly distinct path-integrated fields (incorporating different contrast regimes) giving near-identical image-flux distributions (Figure 2.5). Despite the mathematical impossibility of distinguishing between the path-integrated fields in Figures 2.5a and 2.5b without additional information, in practice there are various qualitative tests that could in principle be employed. For example, if there are multiple species of imaging protons, and the transit time and pulse length of all these species are much smaller than the evolution timescales of the system, the multiple-beam energy comparison technique described in Section 2.4.3 to find caustics could also be used to distinguish between these path-integrated magnetic fields. More specifically, the path-integrated field could be reconstructed from a 3.3 MeV proton image (such as Figure 2.5c), before predicting what a 15.0 MeV proton image would look like. This could be compared to the actual 15.0 MeV proton image to test the veracity of the reconstructed path-integrated field.

Even in the situation when the path-integrated field is uniquely extractable from its associated proton-flux image (implying that the contrast regime of the imaging

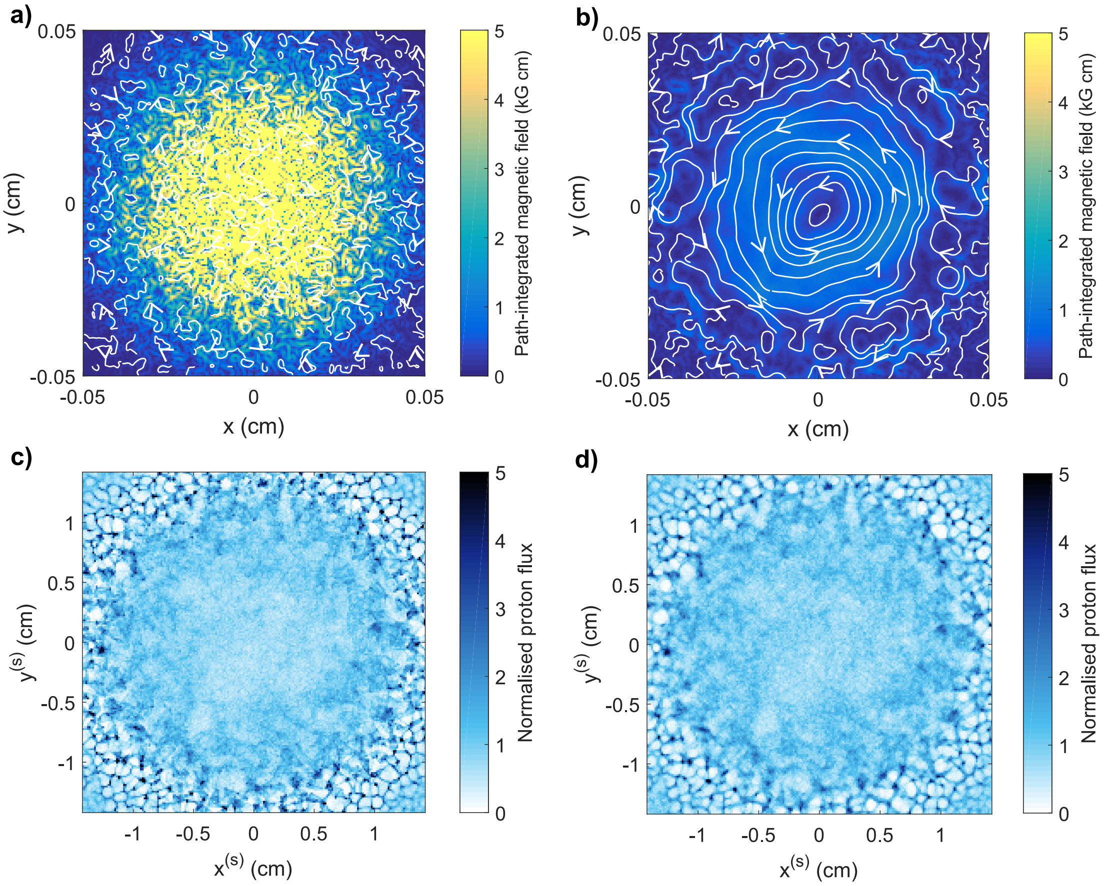

Figure 2.5: Illustration of ill-posedness of reconstruction for spatially inhomogeneous stochastic magnetic fields. a) Path-integrated perpendicular magnetic field associated with small-scale magnetic cocoon configuration (see Appendix G.3) with correlation scale $\ell_B = 0.8\,\mu$m. A Gaussian envelope of the form (2.22) is applied to the magnetic field, with $\sigma = 3$ and $B_{rms,0} = 2.2\,$MG. **b)** Path-integrated magnetic field associated with perpendicular-deflection field reconstructed from proton-flux image c) generated from magnetic field described in a), assuming an injective mapping. Typical proton deflection velocities in the central region are reduced by a factor ~ 25. **c)** 3.3-MeV proton-flux image created by imaging field configuration a) with 3×10^6 15.0 MeV protons from point source located at $r_i = 1\,$cm from the field configuration, and detector located on the opposing side, with $r_s = 30\,$cm. **d)** Predicted 3.3-MeV proton-flux image, assuming proton beam with same imaging parameters as c) experienced path-integrated magnetic field b) while traversing the plasma.

diagnostic must be linear, or nonlinear injective), for a spatially-inhomogeneous field, the magnetic-energy spectrum of the stochastic field is not necessarily extractable from the path-integrated field. More specifically, the derivations of equations for the magnetic-energy spectrum [deflection-field spectral relation (2.11), or linear-regime flux spectral relation (2.35)] given in Appendices D and F rely on both the assumption that magnetic field statistics do not vary along the path of the proton beam, and that the statistics are the same perpendicular and parallel to the direction of proton motion. These assumptions can likely be relaxed to include the case when the field is statistically inhomogenenous, and anisotropic in the perpendicular direction (Ensslin and Vogt (2003) demonstrate this in the context of calculating magnetic energy spectra from Faraday rotation measurements).

Variable μ across scales

It is clear from its definition (2.17) that μ is scale-dependent, increasing as the scale ℓ_B of magnetic structures decreases relative to the path length of the imaging protons. Magnetic structures imaged in a proton-imaging set-up are, therefore, in a potentially different contrast regime depending on their strength and size. For multi-scale stochastic fields, such as those with power law spectra of the form $E_B(k) \propto k^{-p}$, we can estimate μ at a particular scale ℓ_B. The field strength at this scale for such a power law goes as

$$B \sim B_0 \left(\frac{\ell_B}{l_z}\right)^{(p-1)/2} , \tag{2.53}$$

and so μ is given by

$$\mu \sim \mu_0 \left(\frac{\ell_B}{l_z}\right)^{p/2-1} . \tag{2.54}$$

We see that for $p > 2$, μ decreases with scale, whereas the opposite is true for $p < 2$. We discuss the consequences of both possibilities in turn.

The case of sufficiently steep power spectra ($p > 2$) – of which the Golitsyn spectrum (2.21) with $p = -11/3$ is an example – is generally much easier to investigate. The largest μ is at largest scales, which coincides with both the strongest magnetic and path-integrated structures. Whether the path-integrated field and magnetic-energy spectrum can be extracted successfully is therefore not altered by the presence of smaller-scale fields.

On the contrary, for shallow spectra ($p < 2$), small-scale fields become extremely important for a proper understanding of proton-flux images, as well as their analysis. Firstly, the fact that μ increases with decreasing scale (in opposition to the path-

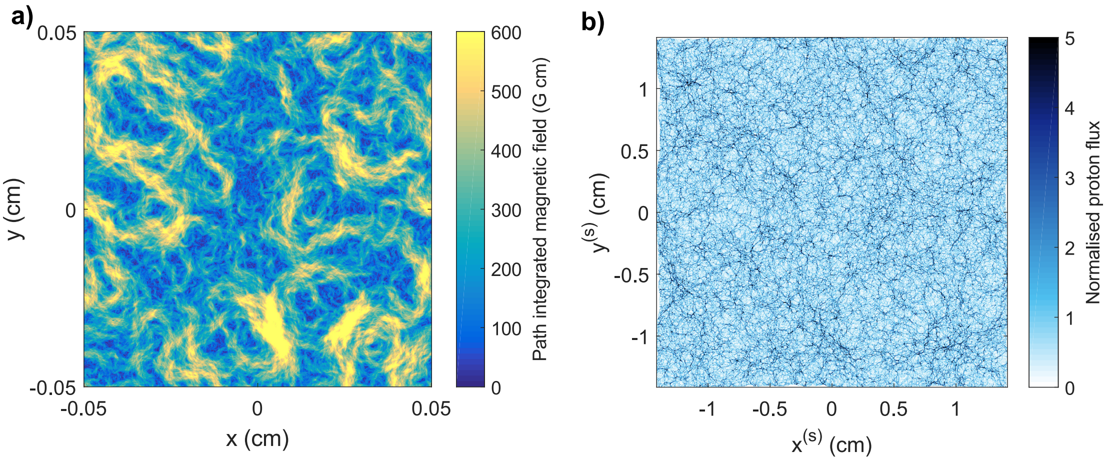

Figure 2.6: Illustration of variation in μ across scales, with consequent discrepancy in structure size between path-integrated magnetic field, and proton-flux image. a) Predicted path-integrated field for periodic stochastic Gaussian magnetic field specified on 1001^2 array of spatial extent $l_i = l_\perp = l_z = 0.1\,\mathrm{cm}$, with power law spectrum of the form (2.55), spectral cutoffs $k_l = 4\pi/l_i$, $k_u = 800\pi/l_i$, and field RMS $B_{rms} = 10\,\mathrm{kG}$. **b)** Proton-flux image generated with 3.3 MeV protons from a point source at distance $r_i = 1\,\mathrm{cm}$ from the array, with imaging detector at distance $r_s = 30\,\mathrm{cm}$ on the opposite side.

integrated field) means that the dominant features in a proton image may be at much smaller scales than the dominant features in the path-integrated field. We illustrate this with an example. Figure 2.6 shows a typical path-integrated magnetic field resulting from a k^{-1} spectrum with a wavenumber range of a few decades. Creating a proton-flux image from this path-integrated field using the plasma-image mapping (as described in Appendix I.3), we see that the strongest features are at the smallest scales, in contrast to the path-integrated magnetic field, where larger coherent structures are evident. This can be explained physically with recourse to an interpretation of proton-flux images as projections of path-integrated MHD current structures: for shallow enough spectra, the dominant MHD current structures are at the smallest scales. For actual proton-flux images, this fine structure would typically be masked by finite-resolution effects; that being said, for stochastic field configurations, Figure 2.6 provides another example of the inadequacy of using image-flux structure as a proxy for magnetic field structure.

More quantitatively, the ability to reconstruct both path-integrated fields and magnetic energy spectra is limited by diffusive scattering at small scales. If $\mu(\ell_B) <$

μ_c at all scales, for μ_c the critical value of μ at which the plasma-image mapping (2.7) loses injectivity, both can be recovered. However, this inequality being reversed at small scales can prevent successful reconstruction not only at those scales, but those at which injectivity is technically preserved. This is because large-scale structures are distorted by small-scale ones.

The phenomenon of smaller-scale fields preventing successful reconstruction of larger-scale ones is best illustrated by considering an example. Figure 2.7a shows a stochastic magnetic field with a magnetic-energy spectrum of the form

$$E_B(k) = \frac{B_{rms}^2}{8\pi} \frac{\log k_u/k_l}{k} \,, \quad k \in [k_l, k_u] \,, \tag{2.55}$$

combined with a Gaussian envelope of the form (2.22). The wavenumber-range is chosen to be large – that is, $k_l \ll k_u$ – and field strength such that the proton imaging set-up applied to the largest structures has $\mu < \mu_c$. The proton-flux image (Figure 2.7b) has strong image-flux structures on many scales, with larger image-flux structures somewhat dispersed by smaller, caustic ones. Figure 2.7c, shows the same field, but with high wavenumbers filtered out at a scale k_c. The resulting proton-flux image (Figure 2.7d) now falls into the nonlinear injective regime, indicating that μ at larger length-scales is indeed below the critical value. Figure 2.7e shows the path-integrated magnetic field reconstructed from Figure 2.7b using the field reconstruction algorithm described in Section 2.3.2. While the reconstruction still captures the global morphology of the field, its fine structure is altered. This difference is shown more clearly by calculating the magnetic-energy spectra, shown in Figure 2.7f. The magnetic-energy spectrum resulting from spectral relation (2.11) applied to the reconstructed field is suppressed at high wavenumbers. Indeed, the effect is sufficiently strong to lead to spectral distortion at wavenumbers which would otherwise be correctly reconstructed if wavenumbers $k > k_c$ were removed. In contrast to the reconstruction of steeper power spectra, the magnetic-energy spectrum calculated from linear theory using formula (2.35) applied to the proton image shown in Figure 2.7b is closer to the true result, although the associated spectral curve is still distorted.

In short, for shallow magnetic-energy spectra, the presence of small-scale fields leads to the suppression of small-scale image-flux structures, which in turn hides high wavenumber modes when attempting to reconstruct both path-integrated fields and magnetic-energy spectra.

2.4.3 Experimental complications

In addition to the theoretical restrictions placed on the use of a proton imaging diagnostic to assess magnetic field statistics, additional constraints arise from limitations to the implementation of the diagnostic. These are discussed more generally elsewhere, but here we outline three effects which are particularly important when attempting to extract accurately path-integrated magnetic fields and energy spectra directly from proton images: Poisson noise, initial inhomogeneities in the initial flux distribution, and finite image resolution effects imposed by a finite source size.

Poisson noise

Poisson noise is an unavoidable effect associated with proton-flux images involving a finite number of imaging protons, and leads to spectral distortion. The finite number of protons in the imaging beam mean that locally the initial flux distribution is noisy. Since the sample is very large, these deviations are well described by Poisson statistics. Thus, if the mean flux per pixel is N_Ψ, then the standard deviation of fluctuations is $\sqrt{N_\Psi}$, giving signal-to-noise ratio $1/\sqrt{N_\Psi}$.

Since such noise is uncorrelated, its contribution to the two-dimensional relative image-flux spectrum is uniform. More specifically, the requirement that the integrated power spectrum of Poisson noise has variance $1/N_\Psi$ leads to

$$\hat{\eta}^{(PN)} \approx \left(\frac{\delta x}{2\pi}\right)^2 \frac{1}{N_\Psi} \,, \tag{2.56}$$

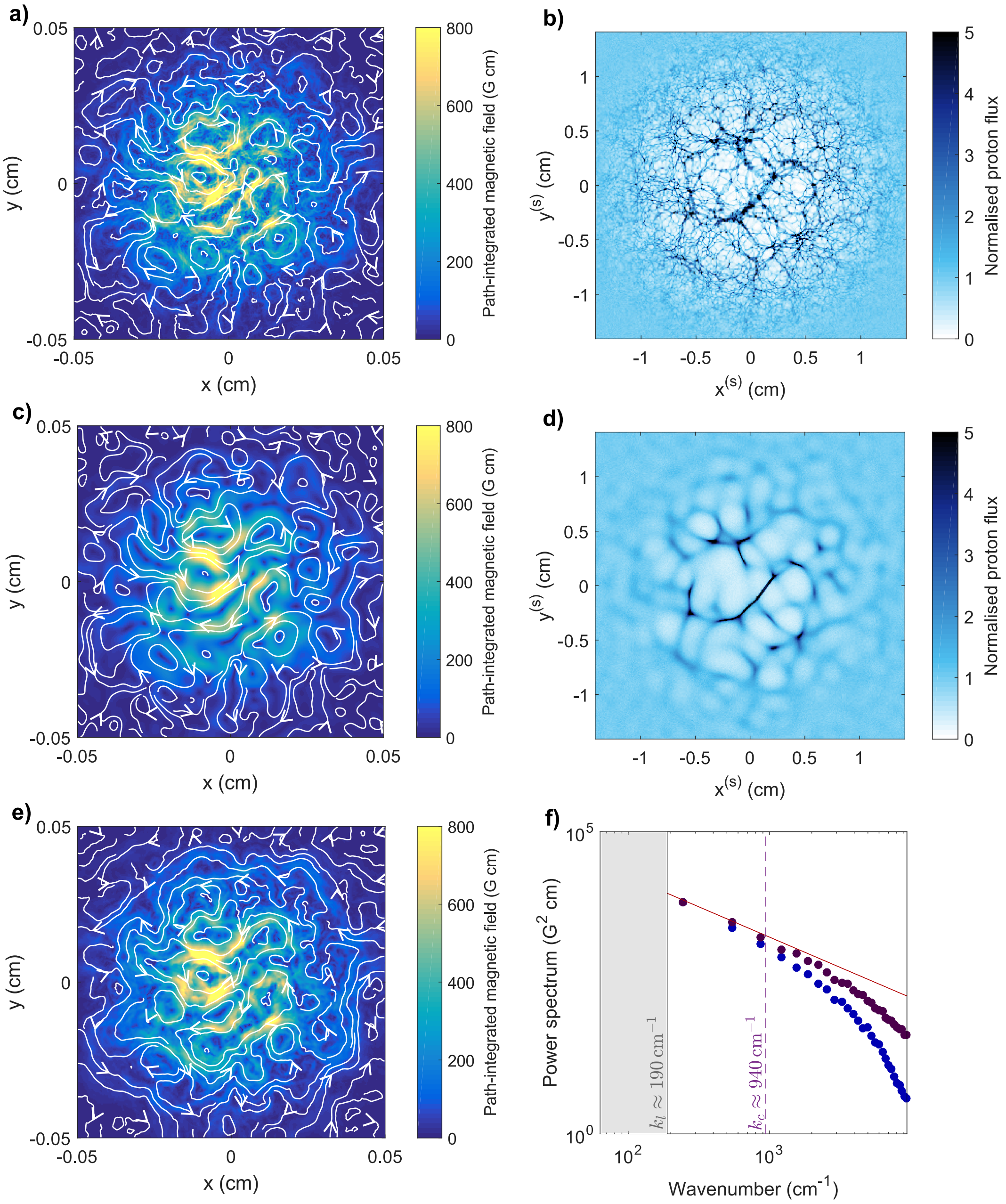

Figure 2.7: Analysing proton-flux images of stochastic magnetic fields with broad magnetic energy spectra. A stochastic magnetic field sample, with magnetic-energy spectrum of the form (2.55), is generated in a region, with dimensions $l_i = l_z = l_\perp = 0.1\,\mathrm{cm}$. Field values are specified on a 301^3 array (grid spacing $\delta x = l_i/301$). The spectral cut-offs were set to be $k_l = 6\pi/l_i$, $k_u = 2\pi/\delta x$, and $B_{rms,0} = 40\,\mathrm{kG}$. A Gaussian envelope of the form (2.22) is again applied to the magnetic field, with $\sigma = 3$. Imaging of the field is then implemented using the parameters given in Figure 4. **a)** Path-integrated perpendicular magnetic field as experienced by imaging 3.3 MeV protons. **b)** 3.3-MeV proton-flux image. **c)** Path-integrated perpendicular magnetic field, with magnetic field wavemodes whose wavenumber exceeds $k_c = 30\pi/l_i$ removed. **d)** 3.3-MeV proton-flux image of filtered magnetic field. **e)** Predicted path-integrated magnetic field found by applying field reconstruction algorithm. **f)** Magnetic energy spectra: true result (red), plotted with prediction using deflection-field spectral relation (2.11) (blue) and linear-regime spectral relation (2.35) (purple).

for δx the pixel size in length units. This in turn gives predicted magnetic-energy spectrum

$$E_B^{(PN)}(k) \approx \frac{1}{(2\pi)^3} \frac{m_p^2 c^2 V^2}{e^2 r_s^2 l_z} \delta x^2 \frac{1}{N_\Psi} \,. \tag{2.57}$$

Thus for a multi-scale spectrum, values of the true spectrum will be dominated by the Poisson contribution if too small. This presents a potential difficulty for analysing proton-flux images in the linear regime if either the mean image-flux is low, or the physical signal is weak. The problem is evident for the predicted spectra shown in Figure 2.4b (purple markers): the shallowing of the spectrum as predicted by linear-regime flux spectral relation (2.35) is due to Poisson noise.

However, in practice the Poisson noise does not usually prevent successful analysis of proton-flux images. The effect on Poisson noise on the spectrum can be anticipated using (2.57), and subsequently removed (Churazov et al. 2012). Furthermore, nonlinear field reconstruction algorithms tend to reduce spectral distortion (Figure 2.4b, blue markers). Thirdly, the restrictions on pixel size required to manage Poisson noise are usually less stringent that those already in place due to other factors limiting resolution (Séguin et al. 2004). That being said, if possible it is preferable to design proton-imaging set-ups in such a way that the magnitude of Poisson noise be significantly less than image-flux features due to magnetic fields.

Inhomogeneity of initial flux distribution

The methods used to reconstruct magnetic field statistics directly from proton-flux images described in Sections 2.3.1 and 2.3.2 rely on prior knowledge of the initial flux distribution. For experimental implementations of proton imaging, this initial distribution is usually assumed to be uniform. However, as discussed in in Section 2.4.1, at the present time it is difficult in practice to achieve a completely uniform initial flux distribution. In the absence of alternative methods for determining the initial flux, there is consequently significant uncertainty over this quantity.

Unfortunately, the ramifications of an unknown initial flux distribution for successful extraction of magnetic field statistics cannot be disregarded: in general, path-integrated fields are no longer uniquely determined by the proton-flux image alone. Conceptually this is because it becomes impossible to distinguish between variations in the image flux resulting from magnetic deflections, and those due to variations in the initial flux. We illustrate this phenomenon with a numerical example – Figure 2.8. Taking two distinct path-integrated fields (Figures 2.8c and 2.8d), but also choosing two distinct initial flux distributions (Figures 2.8a and 2.8b), it can be seen that it is possible to produce a near identical image-flux distribution (Figures 2.8e and 2.8f). Naive assumption of a uniform initial flux distribution when applying a field reconstruction algorithm can therefore lead to prediction of non-physical field structures: a far from satisfactory outcome.

The problem is accentuated further by the fact (first stated in Section 2.4.1) that initial variations in flux are typically concentrated on larger length-scales, and so associated non-physical path-integrated fields recovered by any field-reconstruction algorithm can have a significant magnitude compared to physical fields. More specifically, we can use equation (2.28) to estimate the uncertainty in RMS magnetic field magnitude ΔB_{rms} introduced by uncertainities in the initial proton flux with typical RMS magnitude $(\delta\Psi/\Psi_0)_{rms,S}$ and correlation length ℓ^* on the detector:

$$\begin{aligned}\Delta B_{rms}(\mathrm{kG}) \;\approx\; & 21\left[\frac{W(\mathrm{MeV})}{3.3\,\mathrm{MeV}}\right]^{1/2}\left[\frac{r_i(\mathrm{cm})}{1\,\mathrm{cm}}\right]^{-1} \\ & \times\left[\frac{l_z(\mathrm{mm})}{1\,\mathrm{mm}}\right]^{-1/2}\left[\frac{\ell(\mathrm{mm})}{0.83\,\mathrm{mm}}\right]^{1/2}\left[\frac{(\delta\Psi/\Psi_0)_{rms,S}}{0.16}\right]\mathrm{kG}\,, \qquad (2.58)\end{aligned}$$

where $\ell \equiv \ell^*/\mathcal{M}$ (and $\ell^* = 2.5\,\mathrm{cm}$, corresponding to the correlation length of the largest periodic structure which can appear on a 10 cm by 10 cm detector such as the one relevant to this thesis), and we have used the value for $(\delta\Psi/\Psi_0)_{rms,S}$ typically found for 3.3 MeV protons derived from a fusion-capsule source (Manuel et al. 2012). We conclude that the relative error induced by uncertainities in the initial proton

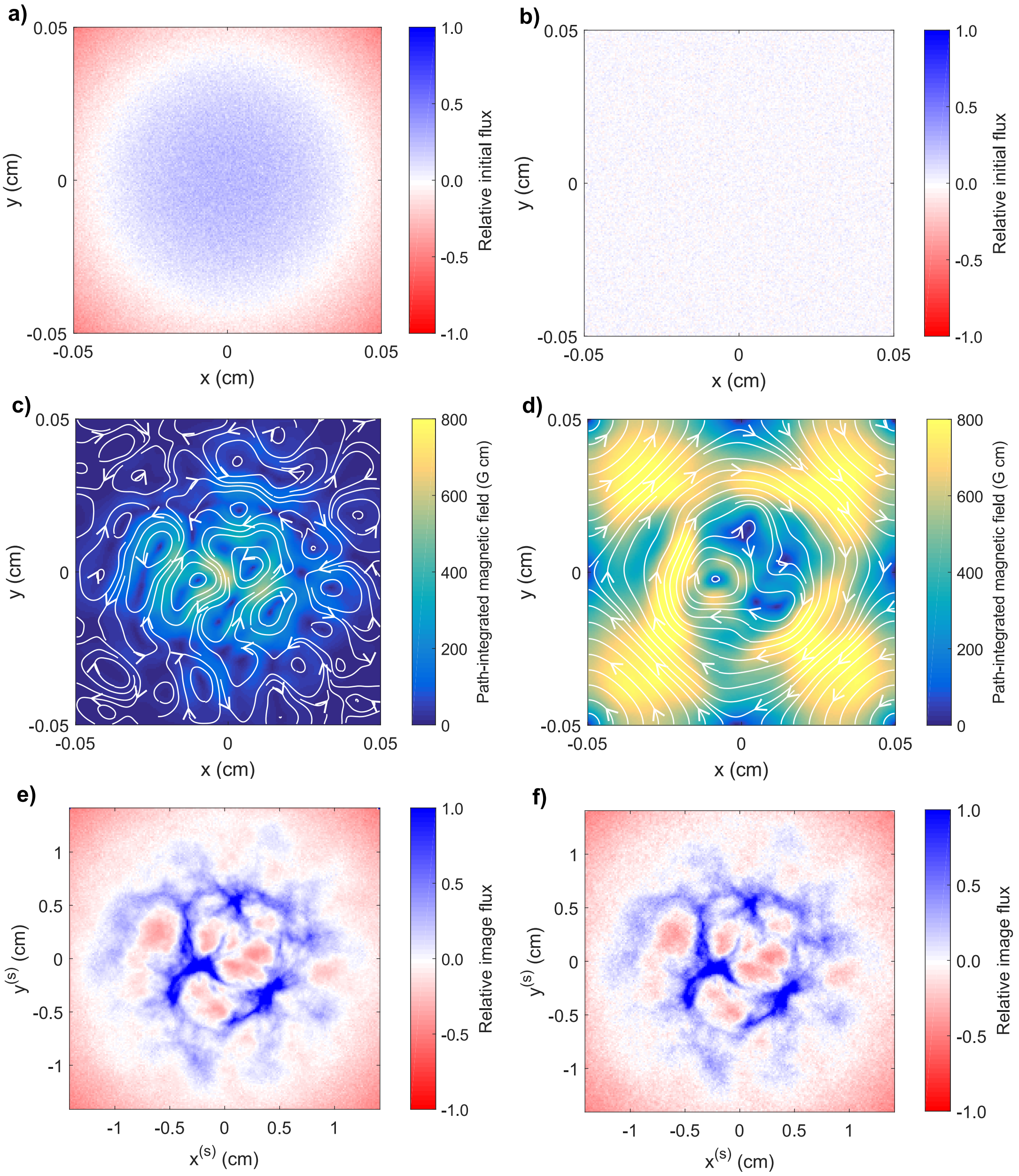

Figure 2.8: Effect of initial flux inhomogeneity on well-posedness of field reconstruction algorithms. a) Non-uniform initial 3.3-MeV proton image-flux distribution, with $\Psi_0(\mathbf{x}_{\perp 0}) = \Psi_0/4\left(5 - 6x_{\perp 0}^2/l_i^2\right)$. Imaging parameters of the set-up are the same as those described in Figure 4. **b)** Uniform initial flux distribution. **c)** Path-integrated perpendicular magnetic field experienced by beam with initial flux distribution shown in a). The magnetic field is the same as that described in Figure 2, with $B_{rms,0} = 15\,\mathrm{kG}$. **d)** Path-integrated perpendicular magnetic field experienced by initial flux distribution shown in b). The magnetic field is constructed by applying the field reconstruction algorithm to proton-flux image c). **e)** 3.3-MeV proton-flux image resulting from initial flux distribution a) experiencing path-integrated field c). **f)** 3.3-MeV proton-flux image resulting from initial flux distribution b) experiencing path-integrated field d).

flux distribution is significant:

$$\begin{aligned}\frac{\Delta B_{rms}}{B_{rms}} &\approx 0.52\left[\frac{\ell(\mathrm{mm})}{0.83\,\mathrm{mm}}\right]^{1/2}\left[\frac{\ell_B(\mathrm{mm})}{0.08\,\mathrm{mm}}\right]^{-1/2} \\ &\quad\times\left[\frac{(\delta\Psi/\Psi_0)_{rms,S}}{0.16}\right]\left[\frac{(\delta\Psi/\Psi_0)_{rms,S}}{1}\right]^{-1} . \qquad (2.59)\end{aligned}$$

This finding is reflected in the significant difference in magnitude of the path-integrated fields shown in Figures 2.8c and 2.8d, which nonetheless give rise to the near-identical proton images.

The distorting effect of initial flux inhomogeneities, however, can to a certain extent be countered. As was noted in Section 2.4.1, variations in initial flux are typically much smaller than the mean flux for sufficiently small structures. As a result, short-scale image-flux deviations due to deflections, particularly strong deviations from nonlinear focusing, are distinguishable from potential initial flux structures. Difficulties then only arise when considering weaker, long-scale flux variation (strong long-scale variation is inevitably associated with the appearance of focused narrow image-flux features). Therefore, to isolate flux structures associated with genuine path-integrated magnetic field structures, we propose applying a high-pass filter to the image-flux distribution to remove long-scale variation. In the best-case scenario – in which all flux structures of interest have correlation lengths below the scale ℓ_c^* defined in Section 2.4.1 – the typical magnitude $(\delta\Psi/\Psi_0)_{rms,S}$ of variations in the initial proton flux satisfies $(\delta\Psi/\Psi_0)_{rms,S} \approx 0.03$. Assuming a characteristic scale length $l_{\mathrm{filt}}^* = 0.8\,\mathrm{mm}$ for the applied low-pass filter, it follows that $\ell^* \approx 0.25 l_{\mathrm{filt}}^*$, and so (2.58) gives $\Delta B_{rms} \approx 1.9\,\mathrm{kG}$. The relative uncertainity in the RMS field strength is then approximately given by $\Delta B_{rms}/B_{rms} \approx 0.05$ for the same parameter values as presented in equation (2.59). Thus, provided the RMS of flux variations is not too small, field reconstruction algorithms applied to a high-pass filtered image give a reasonable estimate of fields below the scale of the filtering. Neverthless, we emphasize that the uncertainty ΔB_{rms} could be greater than this estimate if flux structures of interest have correlation lengths larger than ℓ_c^*, on account of the typical magnitude of initial flux variations increasing above this scale (Manuel et al. 2012).

We also note that long-scale path-integrated magnetic fields – if present – could in principle alter the positioning of short-scale image-flux structures, giving rise to the possibility that path-integrated fields reconstructed from filtered images are distorted compared to the true fields at that scale. The importance of this effect can be tested by comparing the results of the field reconstruction algorithm applied to the filtered image with the reconstructed path-integrated field deduced from the unfiltered image, but with filtering applied directly post-reconstruction. In any case, since long-scale variations in flux are typically not large, intuitively this effect should not be significant in practice.

Smearing effects due to finite source size

As mentioned in Section 2.4.1, proton-imaging set-ups usually have a small but finite source size, placing a lower limit on the size of magnetic structures which can be imaged. This statement can be made more precise by calculating the effect of the finite source of the perpendicular velocity distribution of the beam. It can then be shown using kinetic theory [Appendix D.7 of Bott et al. (2017)] that when a magnetic field configuration is imaged with a proton beam generated by a finite source, the resulting image-flux distribution $\tilde{\Psi}\left(\mathbf{x}_\perp^{(s)}\right)$ is equal to the image-flux distribution generated by a point source (the 'unsmeared flux' Ψ), but convolved with a point-spread function:

$$\tilde{\Psi}\left(\mathbf{x}_\perp^{(s)}\right) = \int \mathrm{d}^2\tilde{\mathbf{x}}_\perp^{(s)}\, \Psi\left(\tilde{\mathbf{x}}_\perp^{(s)}\right) S\left(\mathbf{x}_\perp^{(s)} - \tilde{\mathbf{x}}_\perp^{(s)}\right) , \tag{2.60}$$

where S is given by

$$S\left(\mathbf{x}_\perp^{(s)} - \tilde{\mathbf{x}}_\perp^{(s)}\right) = \frac{V^2}{r_s^2} P\left(\frac{\tilde{\mathbf{x}}_\perp^{(s)} - \mathbf{x}_\perp^{(s)}}{r_s} V\right) . \tag{2.61}$$

Here, $P = P(\delta \mathbf{V}_{\perp 0})$ is the distribution function of perpendicular velocities associated with the source's finite size; it is a function of

$$\delta \mathbf{V}_{\perp 0} = \mathbf{V}_{\perp 0} - \frac{\mathbf{x}_{\perp 0}}{r_i} V \,, \tag{2.62}$$

which quantifies the degree of deviation from the paraxial approximation for the initial beam-proton velocity. The form of P depends on three-dimensional emission profile of the proton source.

The limitation of image resolution by a finite source size places a number of constraints on the possibility of reconstructing the magnetic-energy spectrum. Firstly, as mentioned in Section 2.3.3, smearing of fine image-flux structure can make the differentiation of the nonlinear injective and caustic regimes difficult. This is illustrated in Figure 2.9. Figures 2.9a and 2.9b show point-source proton-flux images of the same artificial test stochastic magnetic field introduced in Figure 2.1 (with $B_{rms,0} \approx 60\,\mathrm{kG}$), but created using two imaging proton species with different speeds: 3.3 MeV (Figure 2.9a) and 15.0 MeV (Figure 2.9b). Since μ is inversely proportional to the initial imaging proton speed, μ for the 15.0-MeV proton-flux image is lower – with the consequence that its plasma-image mapping is injective, unlike the 3.3-MeV proton plasma-image mapping. The two point-source proton-flux images are qualitatively distinct – pairs of caustics are evident in Figure 2.9a – and hence can be identified as belonging to the caustic and nonlinear injective regimes respectively. Figures 2.9c and 2.9d show the same fields imaged with protons generated from a finite spherical source. This reduces the spatial resolution of the image – and consequently, the sharp caustic structures disappear.

To distinguish between the nonlinear injective and caustic regimes, we need more information than can be provided by a single proton image. Fortunately, typical experimental methods for generating imaging proton beams produce at least two beam energies simultaneously, which can be imaged independently (Wilks et al. 2001, Li et al. 2006b). If the transit and beam duration times of all proton beams

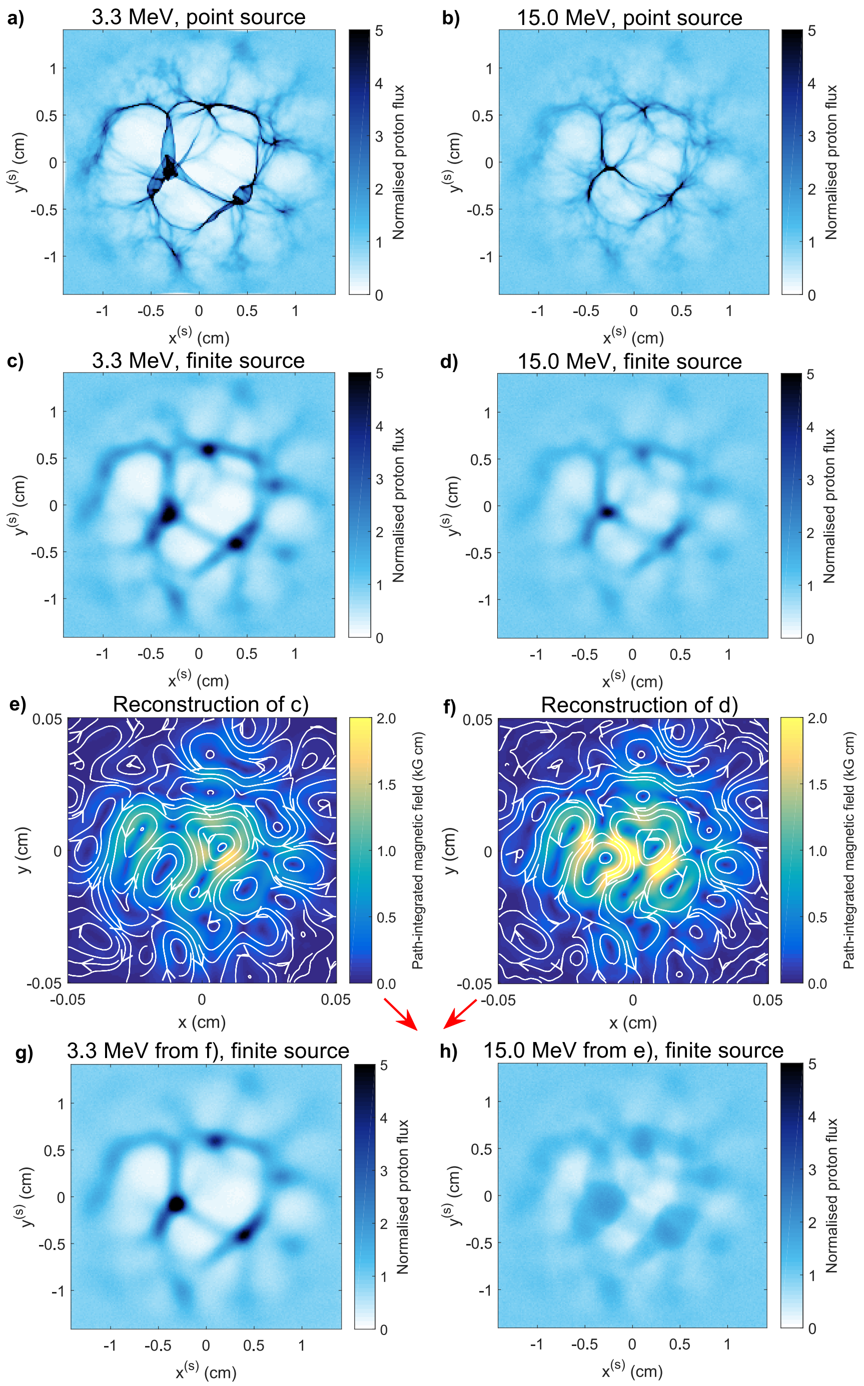

Figure 2.9: Distinguishing the nonlinear injective and caustic contrast regimes using nonlinear field-reconstruction algorithms and multiple beam energies. a) 3.3 MeV proton-flux image of magnetic field described in figure 2, with $B_{rms,0} = 64\,\mathrm{kG}$, and same imaging parameters as those described in figure 3. **b)** Same as a), but with imaging beam composed of 15.0 MeV protons. **c)** Same as a), but now imaging implemented using a finite uniform spherical proton source with diameter $a = 50\,\mu\mathrm{m}$. **d)** Same as c), but with imaging beam composed of 15.0 MeV protons. **e)** Reconstructed path-integrated magnetic field obtained by applying the field-reconstruction algorithm (described in Section 2.3.2) to c). **f)** Same as e), but algorithm applied to d). **g)** Predicted 3.3 MeV proton-flux image, assuming imaging proton beam experienced reconstructed path-integrated field shown in f) as a result of traversing magnetic field (the implementation is discussed in Appendix I.3). Under the caustic detection scheme outlined in the main text, this image is to be compared with c). **h)** Predicted 15.0 MeV proton-flux image, assuming imaging proton beam experienced path-integrated field shown in e). This image is to be compared with d).

are much shorter than the timescales on which dynamical evolution of the magnetic field occurs, then the proton-flux images from all beams will be of approximately the same magnetic field (see Section 2.4.1 for a discussion of this).

Comparing proton images of the same magnetic field at different imaging beam energies is a useful technique for identifying caustics. Most simply, if proton images contain caustics, irrespective of the beam energy, then the width of strong, positive image-flux structures will typically increase with lowered beam-energy; in contrast, if all images fall into the nonlinear injective regime, then the narrowest structures will occur at the lowest energies. This principle is illustrated in Figures 2.9c and 2.9d, where strong, positive relative image-flux features are broader for the 3.3 MeV protons than the 15.0 MeV ones – suggesting that the former contains smeared caustics.

A more robust caustic detection scheme comes from application of the field-reconstruction algorithm outlined for $\mu < \mu_c$ in Section 2.3.2 on the different beam-energy proton-flux images of the same magnetic structures. If a path-integrated field reconstructed from one proton species is close to the true path-integrated field, then all imaging protons species should have seen that reconstructed field: thus the proton-flux images generated using the plasma-image mapping combined with the predicted path-integrated field should be consistent with the actual proton-flux images (this procedure is discussed in Appendix I.3). Figures 2.9g and 2.9h show the 3.3-MeV and 15.0-MeV proton-flux images predicted using the reconstructed perpendicular-deflection fields for 15.0 MeV (Figure 2.9f) and 3.3 MeV (Figure 2.9e) protons respectively, followed by artificial smearing with a point-spread function appropriate for a uniform finite spherical source [see Appendix E of Bott et al. (2017)]. Figure 2.9g is very similar to Figure 2.9c, verifying the validity of the reconstructed perpendicular-deflection field shown in Figure 2.9. However, Figure 2.9h disagrees substantially with Figure 2.9d: for example, the width of positive image-flux structures in 2.9h is much greater than the true widths in Figure 2.9d. We conclude that the field-reconstruction algorithm provides an effective method for detecting the presence of caustics.

Smearing also has important consequences for accurately reconstructing both path-integrated fields and magnetic energy spectra. More specifically, smearing reduces the strength of path-integrated fields reconstructed directly from proton-flux images by reducing the sharpness of nonlinearly focused image-flux features. It also introduces a upper wavenumber cut-off on predicted magnetic energy spectra. Both these effects are illustrated in Figure 2.10 with a numerical example. Figure 2.10a shows a proton-flux image generated by imaging the Golitsyn field described in Figure 2.1, along with the (near-accurate) reconstructed field (Figure 2.10b). Figure 2.10c shows the equivalent image-flux distribution generated by a finite source. The reconstructed morphology, while similar, is reduced in strength. The effect on spectral reconstruction in this example is more pronouced (Figure 2.10g): wavenumbers close to and beyond the smearing scale are suppressed in the spectrum derived from Figure 2.10d.

The impact of smearing on successful extraction of field statistics from proton-flux images can be somewhat reduced by use of a deconvolution algorithm. In particular, for a known point-spread function S, there exist algorithms (such as the Richardson-Lucy algorithm) for recovering the maximum likelihood solution for the unsmeared image-flux distribution given the smeared image-flux distribution (Richardson 1972, Lucy 1974). The procedure is illustrated in Figure 2.10e, with associated reconstructed path-integrated field in Figure 2.10f. It is clear that the maximum likelihood solution for the de-smeared image-flux distribution recovered by the Richardson-Lucy algorithm does not have identical morphology to the actual unsmeared image-flux distribution. However, the morphology and strength of the reconstructed path-integrated field is much more similar; furthermore, the magnetic-energy spectrum recovered from the path-integrated field (see Figure 2.10g, orange markers) is a much closer match to the true result (Figure 2.10g, blue markers).

More quantitatively, Figure 2.10h gives the ratio of the predicted RMS magnetic field strength to the actual value for a range of field strengths, as calculated by in-

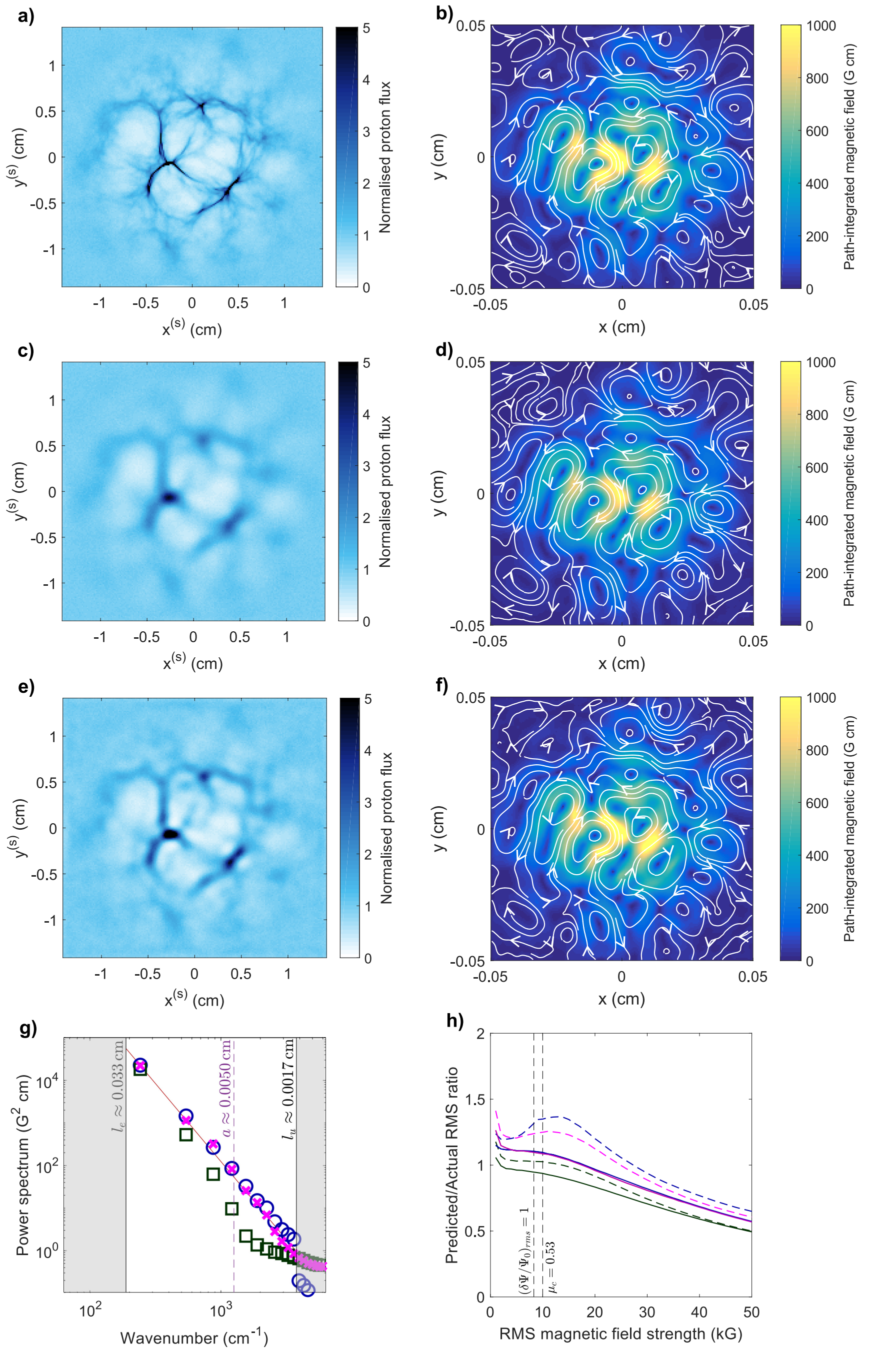

Figure 2.10: Effect of finite source size on successful extraction of magnetic field statistics. **a)** ‘Unsmeared’ 3.3-MeV proton-flux image created by imaging Golitsyn field, $B_{rms,0} = 30\,\mathrm{kG}$ (reproduction of figure 4c for convenience of reference). **b)** Predicted path-integrated magnetic field resulting from application of field reconstruction algorithm to figure a). **c)** ‘Smeared’ 3.3-MeV proton-flux image created by imaging same field as a), but with a finite proton source, with diameter $a = 50\,\mu\mathrm{m}$. **d)** Same as b), but with field reconstruction algorithm applied to c). **e)** ‘De-smeared’ 3.3-MeV proton image subsequent to application of Richardson-Lucy algorithm for ten iterations. **f)** Same as b), but with field reconstruction algorithm applied to e). **g)** Magnetic energy spectra: true result (red), plotted with predictions using deflection-field spectral relation (2.11) applied to b) (blue circles), d) (dark green squares) and f) (magenta crosses). **h)** Ratio of predicted to actual RMS magnetic field strength for a range of field strengths using both linear-regime flux spectral relation (2.35) (dashed) and reconstructed deflection-field spectral relation (2.11) (solid), applied to unsmeared (blue), smeared (dark green) and de-smeared (magenta).

tegrating predictions of the magnetic-energy spectrum. The results from using both linear-regime flux spectral relation (2.35) and reconstructed deflection-field spectral relation (2.11) applied to unsmeared (blue), smeared (green), and de-smeared (orange) proton-flux images are shown. It is clear that for both approaches, the smeared proton-flux image leads to reductions in predictions of field strength of 10-20 % – but that these can be removed quite effectively using a deconvolution algorithm. We also note that beyond the appearance of caustics, all methods increasingly under-estimate the predicted RMS field strength; this is related to the lower-bound property of the reconstructed perpendicular-deflection fields discussed in Section 2.3.3.

For experimental analysis with a somewhat limited resolution range, we conclude that deconvolution algorithms are helpful for deducing magnetic-energy spectra over a reasonable range of wavenumbers.

2.5 Conclusions

In this chapter, we have shown that the magnetic-energy spectrum of a wide range of isotropic stochastic magnetic fields can be determined using a proton imaging diagnostic, but only provided the parameters of the imaging are appropriately tuned. More specifically, we have used an analytic theory of proton imaging established under a set of simplifying assumptions typically valid when carrying out proton imaging to show that proton-flux images of stochastic magnetic fields can be classified into four regimes – linear, nonlinear injective, caustic and diffusive – dependent on μ (which quantities the relative size of magnetic structures and proton displacements due to magnetic deflections). In the linear and nonlinear injective regimes, the magnetic energy is extractable from the image-flux distribution provided the stochastic fluctuations are homogeneous and isotropic: and we have described a procedure for achieving this (the PROBLEM code). In the caustic and diffusive regimes, we have shown that the problem is not well posed – at least, not without additional assumptions about the structure of the stochastic magnetic field – in that stochastic magnetic fields with different magnetic energy spectra can give proton image-flux distributions with identical statistics. We have investigated several complications to this description placed by particular types of stochastic fields, in particular showing that shallow power law spectra are often unreproducable using the proposed (or any other) proton imaging techniques. In addition, three limitations on the utility of the diagnostic due to experimental constraints have been described, as well as techniques for minimising their impact.

Chapter 3

Analysing proton images from the OMEGA fluctuation dynamo experiment

3.1 Analysis of 15.0 MeV proton images

3.1.1 Reconstruction of path-integrated fields

The results of the previous chapter are now applied to the experimental data obtained for the fluctuation-dynamo OMEGA experiment discussed in Chapter 1. The experimental 15.0 MeV proton images first introduced in Figures 1.13a, 1.13c, and 1.13e of Chapter 1 are reproduced in Figure 3.1; we also present the magnitude of the path-integrated perpendicular magnetic field extracted using the field-reconstruction algorithm described in Chapter 2 (i.e. the PROBLEM code). In more detail, the method for applying the field-reconstruction algorithm to the data is as follows. We first select a region of the proton image to analyse; this region is chosen to be as large as possible, within the parameters of staying inside the region of high proton flux between the grids, maintaining an approximately rectangular shape, avoiding large long-scale variations in flux and choosing a boundary which does not intersect

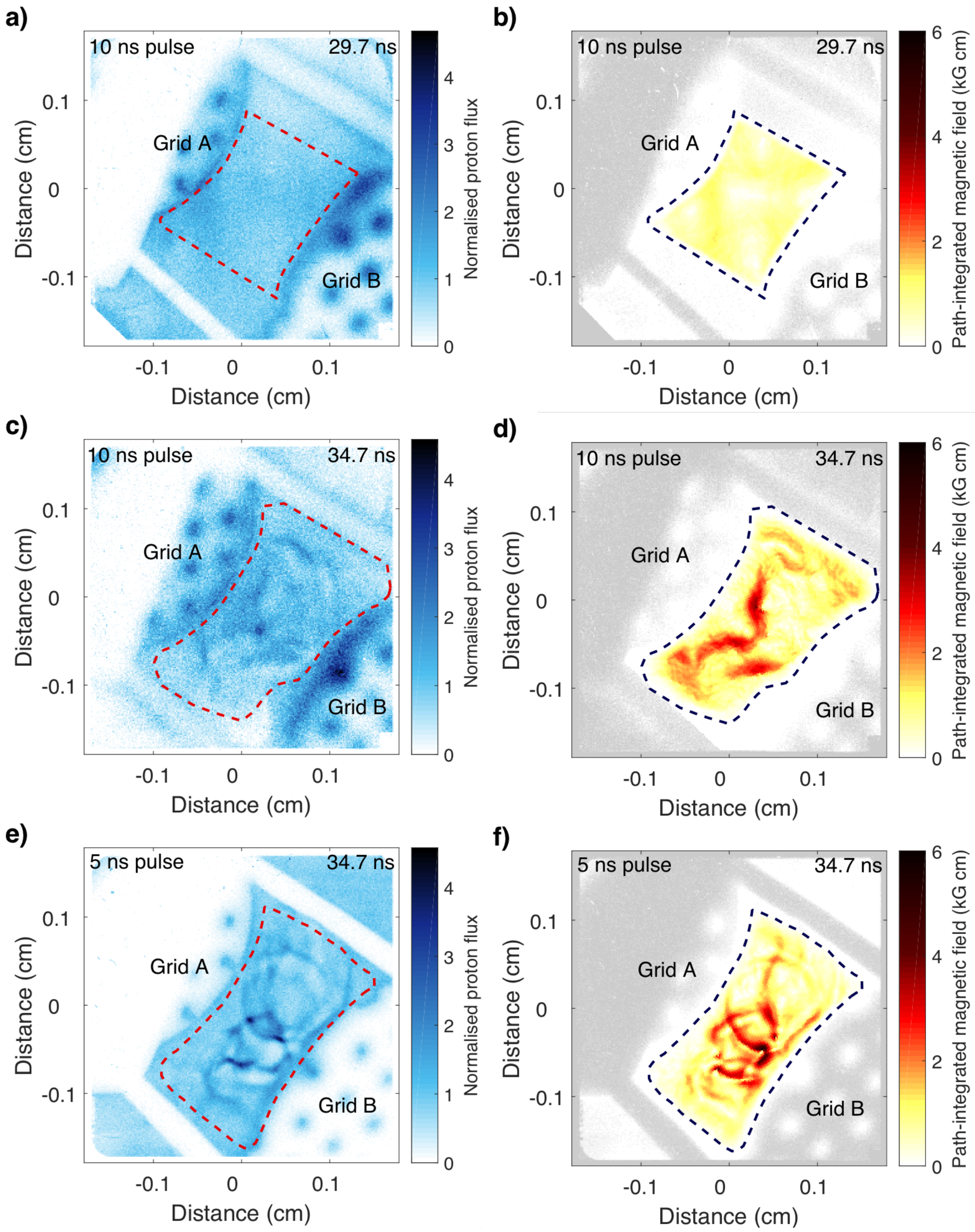

Figure 3.1: 15.0-MeV proton-image analysis. **a)** 15.0 MeV proton image corresponding to 29.7 ns after a 10 ns drive-beam pulse initiation (c.f. Figure 1.13a) The dashed line denotes the boundary of the region to which the reconstruction algorithm is applied. **b)** Magnitude of path-integrated perpendicular magnetic field recovered from a) using field-reconstruction algorithm (for details, see main text). **c)** 15.0 MeV proton image corresponding to 34.7 ns after a 10 ns drive-beam pulse initiation (c.f. Figure 1.13c). **d)** Magnitude of path-integrated perpendicular magnetic field recovered from c) using field-reconstruction algorithm. **e)** 15.0 MeV proton image corresponding to 34.7 ns after a 5 ns drive-beam pulse initiation (c.f. Figure 1.13e). **f)** Magnitude of path-integrated perpendicular magnetic field recovered from e) using field-reconstruction algorithm.

regions with high levels of proton flux. We then embed the cropped region of proton flux inside a larger rectangular region, whose size is chosen to be as small as possible while still containing the cropped region. Values of proton flux are then systematically assigned to pixels outside the cropped region: these values are calculated by linearly interpolating between the nearest actual pixel value and the mean flux of the cropped region of protons.

At this point, two filtering procedures were employed. First, the Lucy-Richardson deconvolution algorithm (Richardson 1972, Lucy 1974) discussed in Section 2.4.3 of Chapter 2 was applied to the rectangular flux samples, in order to mitigate the effect of the finite proton source size on the field reconstruction algorithm (that is, the 'smearing' effect described in the aforementioned section). In the case of a D^{3}He capsule, the proton source profile has been shown experimentally to be Gaussian, with full-width-half-maximum (FWHM) of 50 μm (Séguin et al. 2004, Li et al. 2006b). The point-spread function affecting the proton image is therefore also Gaussian with the same FWHM and so the Lucy-Richardson deconvolution scheme was implemented accordingly. For the particular flux images shown in Figure 3.1, ten iterations of the algorithm were found to balance optimally the recovery of the flux distribution with the undesired side effect of Poisson noise enhancement introduced by the deconvolution process. The efficacy of the deconvolution scheme is further enhanced by the general robustness of the non-linear reconstruction algorithm to small-scale noise (see Chapter 2, Section 2.4.3). An illustration of successful application of Lucy-Richardson deconvolution for simulated FLASH proton images is given later (Figure 3.8). In addition to the deconvolution algorithm, a Gaussian high-pass filter (FWHM $1.5 l_{\mathrm{i}} \approx 0.22\,\mathrm{cm}$) was applied to a selected flux region in order to remove long-scale variation in the flux distribution. Since the dominant structures remaining in the reconstructed path-integrated field are of the order $\tilde{\ell}_B \sim 300\,\mu\mathrm{m}$ and order-unity flux features are still retained in the filtered flux image, we conclude that our field-reconstruction algorithm captures the energetically dominant magnetic structures.

Subsequent to the filtering, we calculated path-integrated fields from the the rectangular region by assuming that the image-flux distribution Ψ is related to the path-integrated field by the Monge-Ampère equation (2.39) of Section 2.3.2 – that is,

$$\Psi(\nabla\phi(\mathbf{x}_{\perp 0})) = \frac{\Psi_0}{|\det \nabla\nabla\phi(\mathbf{x}_{\perp 0})|} \, , \tag{3.1}$$

where we remind the reader that the potential $\phi(\mathbf{x}_{\perp 0})$ is related to the perpendicular-deflection field $\mathbf{w}(\mathbf{x}_{\perp 0})$ via equation (2.41):

$$\mathbf{w}(\mathbf{x}_{\perp 0}) = \frac{V}{r_s}\nabla_{\perp 0}\left(\phi - \frac{r_s + r_i}{2r_i}\mathbf{x}_{\perp 0}^2\right) \, . \tag{3.2}$$

The initial flux is chosen to be entirely uniform, with mean value set equal to that of the rectangular flux region. The flux relation (3.1) was inverted numerically using the finite-difference scheme described in Appendix I.4. Subsequent to convergence of the algorithm, the perpendicular-deflection field is only retained for pixels inside the original cropped region, with other values removed via a Gaussian window function, and is re-oriented to the original position of its associated flux region. The perpendicular path-integrated field is calculated using equation (2.10) of Section 2.2.2:

$$\int_0^{l_z} \mathrm{d}s \, \mathbf{B}_\perp(\mathbf{x}(s)) = -\frac{m_p c}{e}\hat{\mathbf{z}} \times \mathbf{w}(\mathbf{x}_{\perp 0}) \, . \tag{3.3}$$

In each image, the magnitude of the path-integrated perpendicular magnetic field is shown; we emphasise that the output of the field-reconstruction algorithm is in fact two-dimensional.

It is clear that the peak path-integrated perpendicular magnetic fields recovered from the 15.0 MeV proton image just prior to collision (Figure 3.1b) are weaker ($\sim 1\,\mathrm{kG}$ cm) than those subsequent to collision for both the 10 ns pulse ($\sim 4\,\mathrm{kG}$ cm – Figure 3.1d) and the 5 ns pulse ($\sim 6\,\mathrm{kG}$ cm – Figure 3.1f). The morphology of the fields is also quite different: smooth, regular field structures prior to collision ($\ell_B \sim 0.1 - 0.2\,\mathrm{cm}$) give way to much smaller structures ($\ell_B \lesssim 0.03\,\mathrm{cm}$). When considered with respect to the contrast-regime framework outlined in Chapter 2, these results are consistent with the absence of strong, sharp features in the proton image recorded at collision (i.e. Figure 3.1a) and their presence subsequent to collision (Figures 3.1c and 3.1e): the contrast parameter μ is proportional to B_{rms} and also increases for smaller magnetic structures. In other words, proton images at collision are in the linear contrast regime ($\mu \ll 1$), while those subsequent to it satisfy $\mu \sim 1$. Whether the path-integrated magnetic structures at these later times are in the non-linear injective or caustic regimes is a subtle question; we will temporarily defer discussion of this until Section 3.2.

3.1.2 Calculating the magnetic energy spectrum and characteristic field strengths

Assuming for now that the reconstructed path-integrated perpendicular magnetic fields are accurate, we can make quantitative estimates of the magnetic field strength both prior to and after collision. Just prior to the jet collision, the path length l_z of the protons through the plasma is of the order of the grid's lateral dimensions $l_z \sim l_n \gtrsim 0.2-0.3\,\mathrm{cm}$; since $|\int \mathbf{B}_\perp \mathrm{d}s| \approx 1\,\mathrm{kG\ cm}$, we therefore estimate $B \lesssim 3-5\,\mathrm{kG}$. This is consistent with the initial 4 kG magnetic field strengths obtained in the FLASH simulation.

Subsequent to collision and the emergence of stochastic magnetic field structures, the spectrum of magnetic field energy $E_B(k)$ can be calculated directly from the path-integrated perpendicular magnetic field using equation (3.3) combined with deflection-field spectral relation (2.11) of Section 2.2.2:

$$E_B(k) = \frac{1}{4\pi^2 l_z} k E_{\mathrm{path}}(k) \ , \tag{3.4}$$

where $E_{\mathrm{path}}(k) = m_p^2 c^2 E_W(k)/e^2$ is the one-dimensional spectrum of the path-integrated magnetic field under normalisation condition

$$\int \mathrm{d}k\, k E_{\mathrm{path}}(k) = \left(\int \mathrm{d}^2\mathbf{x}\, \mathbf{B}_\perp \right)^2_{rms} . \tag{3.5}$$

The RMS value of the magnetic field can then be evaluated by integrating over all wavenumbers to give (c.f. equation (2.3) of Chapter 2)

$$B_{rms} = \left[8\pi \int_0^\infty E_B(k)\, \mathrm{d}k \right]^{1/2} . \tag{3.6}$$

In practice, the values of the RMS field strength are best calculated by summing over pixel values of a Fourier-transformed sample of (zero-mean) path-integrated perpendicular magnetic fields. As the collision occurs, and the interaction region of shocked turbulent plasma coalesces, FLASH simulations indicate that the proton path-length scale l_z decreases to $l_z \approx 0.6\,\mathrm{mm}$. Assuming this value of l_z to be correct, we calculate the magnetic-energy spectrum from the centre of the interaction region arising for the 5 ns pulse shape (Figure 3.2a); the result is shown in Figure 3.2b. The peak of this spectrum occurs at wavenumbers consistent with the claim that energetically dominant magnetic structures have a size $\tilde{\ell}_B \sim 300 - 400\ \mu\mathrm{m}$. For wavenumbers $\gtrsim 2\pi\tilde{\ell}_B^{-1}$, the uncertainty on the spectral measurement is sufficiently large that it is not possible to conclude whether the data is more consistent with a shallow k^{-1} spectrum (as predicted by the FLASH simulations), or with a spectrum characteristed by a larger (negative) power-law index (such as a $k^{-5/3}$ Kolmogorov spectrum). Intriguingly, it is certaintly the case that any power-law fit for the derived spectrum at wavenumbers $\gg 2\pi\tilde{\ell}_B^{-1}$ requires a much larger power-law index than that obtained in the FLASH simulations. For the RMS field strength, we obtain $B_{rms} \approx 100$ kG.

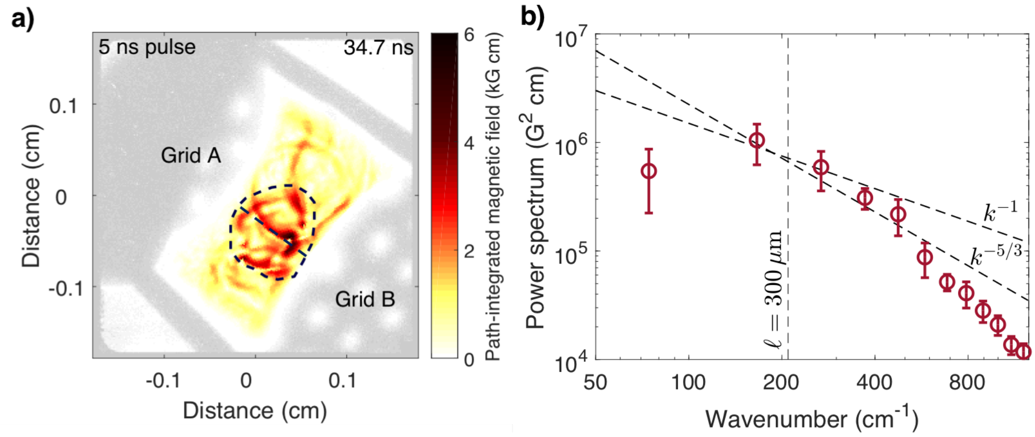

Figure 3.2: Reconstructed magnetic-energy spectrum. **a)** Magnitude of path-integrated perpendicular magnetic field recovered from a proton image 34.7 ns after drive-beam pulse initiation using field-reconstruction algorithm (c.f. Figure 3.1f), plotted with region to be used for spectral analysis. **b)** Magnetic-energy spectrum derived using equation (3.4) applied to the region(s) illustrated in panel a). The calculation is performed as follows: an appropriate Gaussian window function is applied to the chosen sample (which is embedded in a larger rectangular region), which is subsequently Fourier-transformed. Equally-spaced annular wavenumber bins ($\Delta k = 3.5\pi/l_i$, $l_i = 0.1$ cm) are then employed with an unbiased estimator for the central bin position used in each case. The relative height of the spectrum is then re-normalised using the ratio of the total rectangular region's area to the sample area. The error bars on the spectral slope are determined by calculating the spectra separately for the two marked regions, and then assuming those spectra constitute independent samples of the path-integrated field.

3.2 Initial discussions

On first inspection, the techniques developed in Chapter 2 for analysing proton images of stochastic magnetic fields seem to have been at least moderately successful: we have been able to derive measurements of characteristic magnetic field strengths from the proton images recorded both at the point of collision and subsequent to it; in the latter case we have also been able to derive the magnetic-energy spectrum. The values of the RMS field strength subsequent to collision are relatively similar to those obtained from the Faraday-rotation diagnostic, providing some initial confidence in the measurement. The approach also reveals quantitatively how the magnetic fields present in the experiment differ from those in the FLASH simulation: in particular, there exist significant magnetic fluctuations at scales somewhat larger than the largest fluctuations predicted by FLASH (for which $\tilde{\ell}_B \sim 150 - 200\,\mu$m).

However, there remain reasonable grounds to treat these initial results with some caution. Firstly, it is not immediately clear whether the contrast regime of the imaging set-up for the largest-scale stochastic magnetic structures is the nonlinear injective regime or the caustic regime; given the resolution of the set-up, distinguishing between the two requires additional analysis of the form suggested in Section 2.4.3. This issue is further complicated by the possible presence of shallow power-law magnetic-energy spectra – for example, the k^{-1} spectral slope found in the FLASH simulations. As discussed in Section 2.4.2 of Chapter 2, the injectivity assumption required for the field-reconstruction algorithm to be applicable is scale-dependent. Small-scale magnetic structures are more likely to lead to the crossing of trajectories of neighbouring protons than larger structures of the same field strength, even though the deflections associated with the small structures are smaller. For multi-scale stochastic magnetic fields, this means that the field-reconstruction algorithm applied to small-scale flux structures with sufficiently large μ will produce an underestimate of small-scale path-integrated fields – which in turns leads to the suppression of small wavelengths in the magnetic energy spectrum (see Section 2.4.2). Secondly, the theory presupposes that all flux structures are due to magnetic fields already present in the plasma prior to the arrival of the imaging proton beam; although the argument presented in Section 1.4 of Chapter 1 suggests this is reasonable, an experimental verification of this assumption would be of some value.

Bearing these issues in mind, we now perform a series of additional tests to validate the approach.

3.3 Validating path-integrated field reconstruction analysis

3.3.1 Simplifying assumptions

The applicability of the field-reconstruction algorithm to our particular imaging set-up depends on the various assumptions outlined in Section 2.4.1 of Chapter 2: paraxiality, point-projection, and small deflections. We remind the reader that the paraxial approximation – that is, approximating the proton beam as it passes through the plasma as a planar sheet – is effectively an expansion of the position and velocity of the particle in terms of half of the paraxial parameter [c.f. equation (2.49)]:

$$\frac{\delta\alpha}{2} \equiv \frac{l_\perp}{2r_\mathrm{i}} \ll 1\,. \tag{3.7}$$

For all times in our experiment, we have $l_\perp \lesssim 0.3\,\mathrm{cm}$, $r_\mathrm{i} = 1\,\mathrm{cm}$, giving $\delta\alpha/2 \approx 0.15 \ll 1$, as required. The point-projection assumption – that is, the assumption that the distance r_s from the plasma to the screen is much greater than l_z, meaning that displacements from undeflected proton trajectories acquired inside the plasma due to magnetic forces are negligible compared to the displacements resulting from the free motion of particles after they have exited the plasma – also holds, since $r_s = 27\,\mathrm{cm} \gg l_z \lesssim 0.3\,\mathrm{cm}$ at all times in the experiment.

Next, we check that typical proton-velocity deflections are assumed small compared to the initial proton velocity; this is equivalent to confirming that $\delta\theta = |\mathbf{w}|/V$ is indeed a small parameter. The perpendicular-deflection field $\mathbf{w}(\mathbf{x}_{\perp 0})$ due to magnetic forces of a proton with initial position $\mathbf{x}_0$ and velocity $\mathbf{V}$ is given by equation (2.8) – that is,

$$\mathbf{w}(\mathbf{x}_{\perp 0}) \approx \frac{e}{mc}\hat{\mathbf{z}} \times \int_0^{l_\mathrm{i}} \mathrm{d}s\, \mathbf{B}(\mathbf{x}(s))\ , \tag{3.8}$$

where $\hat{\mathbf{z}} = \mathbf{V}/V$ is the direction of travel of the proton. The deflection angle of the proton is then

$$\delta\theta = \frac{e}{mcV}\left|\int_0^{l_\mathrm{i}} \mathrm{d}s\, \mathbf{B}(\mathbf{x}(s))\right|\ . \tag{3.9}$$

For our experiment, Figure 3.1 shows that the maximum predicted path-integrated magnetic field takes a value of $\sim 6\,\mathrm{kG\,cm}$, which in turn gives maximum predicted deflection velocity $|\mathbf{w}| \approx 5.7 \times 10^7\,\mathrm{cm/s}$. For the slowest species of proton used for imaging (3.3 MeV), we have $V \approx 2.5 \times 10^9\,\mathrm{cm/s}$, so $\delta\theta \leq 0.02$ for all imaging protons.

Finally, it was claimed in Section 1.4 that structure arising in proton images from the OMEGA experiment is due to magnetic fields only, rather than both electric and magnetic fields; we now validate this claim in two ways. First, we show that the threshold value B_{res} below which magnetic field strengths cannot be measured reliably by our proton-imaging set-up satisfies $B_{\mathrm{res}} \gtrsim 0.5\,\mathrm{kG}$: this threshold was used in Section 1.4 to support a theoretical argument ruling out electric fields. In Section 2.4.3, it was shown that the uncertainity ΔB_{rms} in the RMS magnitude of the stochastic magnetic fields is given by equation (2.58). Substituting the maximum possible experimental value for the path length ($l_z \approx 0.3\,\mathrm{cm}$), and setting the correlation scale ℓ of initial flux variations equal to the image resolution $a \approx 50\,\mu\mathrm{m}$ (which in our experiment is determined by the proton source size) then gives the required lower bound:

$$\begin{aligned} B_{\mathrm{res}}(\mathrm{kG}) \quad &\gtrsim \quad 0.5 \left[\frac{W(\mathrm{MeV})}{3.3\,\mathrm{MeV}}\right]^{1/2} \left[\frac{r_i(\mathrm{cm})}{1\,\mathrm{cm}}\right]^{-1} \\ &\times \left[\frac{l_z(\mathrm{cm})}{0.3\,\mathrm{cm}}\right]^{-1/2} \left[\frac{a(\mu\mathrm{m})}{50\,\mu\mathrm{m}}\right]^{1/2} \mathrm{kG}\,. \end{aligned} \tag{3.10}$$

Second, we demonstrate that the magnitude of the electric fields necessary for causing the structures seen in proton images from the OMEGA experiment is much larger than would be expected physically. The perpendicular-deflection field $\mathbf{w}(\mathbf{x}_{\perp 0})$ imparted by an electric field $\mathbf{E}$ is given by (Kugland et al. 2012)

$$\mathbf{w}(\mathbf{x}_{\perp 0}) \approx \frac{e}{m_p V} \int_0^{l_{\mathrm{i}}} \mathrm{d}s\, \mathbf{E}(\mathbf{x}(s)) \ . \tag{3.11}$$

By analogy to equation (2.13) (or equivalently, a random-walk argument), the RMS magnitude E_{rms} of a stochastic electric field can then be related to the typical deflection angle $\delta\theta$ by $E_{rms} \sim m_p V^2 \delta\theta / e\sqrt{\tilde{\ell}_E l_z}$, or equivalently,

$$E_{rms} \approx 160 \left[\frac{W(\mathrm{MeV})}{3.3\,\mathrm{MeV}}\right] \left[\frac{l_z(\mathrm{cm})}{0.06\,\mathrm{cm}}\right]^{-1/2} \left[\frac{\tilde{\ell}_E(\mathrm{cm})}{0.03\,\mathrm{cm}}\right]^{-1/2} \left[\frac{\delta\theta}{0.01}\right] \mathrm{MV/m}\,, \tag{3.12}$$

where $\tilde{\ell}_E$ is the characteristic length scale associated with electric-field structures.

Comparing this estimate to the characteristic field strength which would arise (for example) from electron pressure gradients on the same length scale (Gregori et al. 2015), we find that $E \sim k_B T_e / e\tilde{\ell}_E$, or

$$E \approx 1.5 \left[\frac{T_e(\mathrm{eV})}{450\,\mathrm{eV}}\right] \left[\frac{\tilde{\ell}_E(\mathrm{cm})}{0.03\,\mathrm{cm}}\right]^{-1} \, \mathrm{MV/m}\,. \tag{3.13}$$

The stated conclusion follows.

3.3.2 Early-time proton images

One simple test of the field-reconstruction algorithm is provided by the 15.0 and 3.3 MeV proton images recorded just prior to collision (see Figures 3.3a and Figures 3.3b respectively). The contrast regime of both images is linear (that is, variations in flux are small compared to the mean flux); thus, in theory the field-reconstruction algorithm should be applicable to both images. Furthermore, as discussed in Section 1.4 of Chapter 1, the evolution of the plasma jets is slow ($\sim 3\,\mathrm{ns}$) compared to the difference in transit times associated with the two proton species ($\leq 0.2\,\mathrm{ns}$). We conclude that the field-reconstruction algorithm should recover approximately the same field morphology when applied to separately to both images. The results of the field-reconstruction algorithm are shown in Figures 3.3c and 3.3d; we have indicated the direction of the path-integrated perpendicular field as well as the strength. There is both qualitatively and quantitatively good agreement in terms of both field strength and morphology, validating our approach.

3.3.3 Predicted proton images

Another reality check for the field-reconstruction algorithm can be performed by generating artificial proton flux images, with the deflections of simulated protons determined by the reconstructed path-integrated field combined with equation (3.8) and the RK image-flux relation (see also Appendix I.4). The test consists in com-

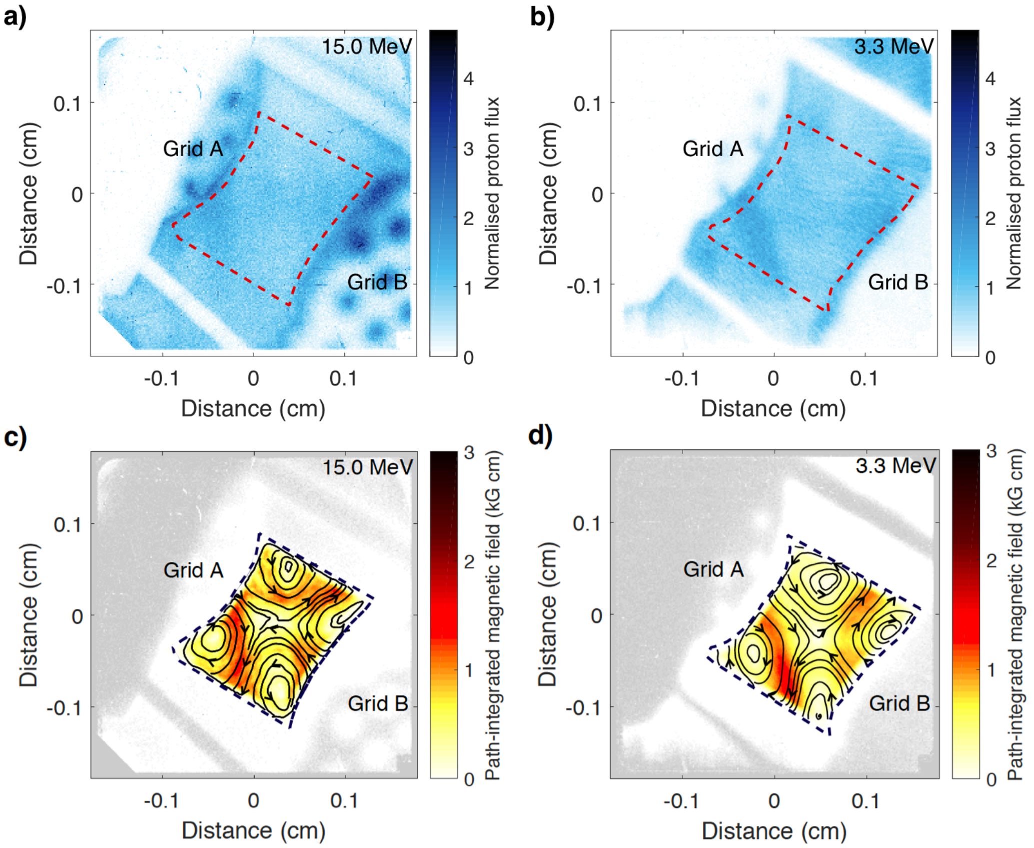

Figure 3.3: Comparison of 15.0 MeV and 3.3 MeV reconstructed path-integrated magnetic field at collision. **a)** 15.0 MeV proton image corresponding to 29.7 ns after a 10 ns drive-beam pulse initiation (c.f. Figure 1.13a). **b)** 3.3 MeV proton image corresponding to 29.9 ns after a 10 ns drive-beam pulse initiation (c.f. Figure 1.13b). **c)** Perpendicular path-integrated magnetic field recovered from a) using field-reconstruction algorithm. Colour variations denote the magnitude of the path-integrated magnetic field while the black lines with directional arrows are 2D streamlines of the perpendicular path-integrated magnetic field. **d)** Same as c) but using path-integrated field recovered from b), not a).

paring these synthetic images to the experimental ones; by the very construction of the field-reconstruction algorithm, the results should be the same. To incorporate the effect of the finite-source size, we apply to the predicted images the same point-spread function assumed when employing the Lucy-Richardson deconvolution algorithm in Section 2.4.3. The predicted flux image (Figure 3.4a) derived from the path-integrated field shown in Figure 3.1f agrees fairly well with Figure 3.1e, although the strength of the strong, narrow flux features in the predicted flux image is reduced compared to the experimental one. Enhancing the path-integrated field by 20% recovers the observed strength of the flux features (see Figure 3.4b), sug-

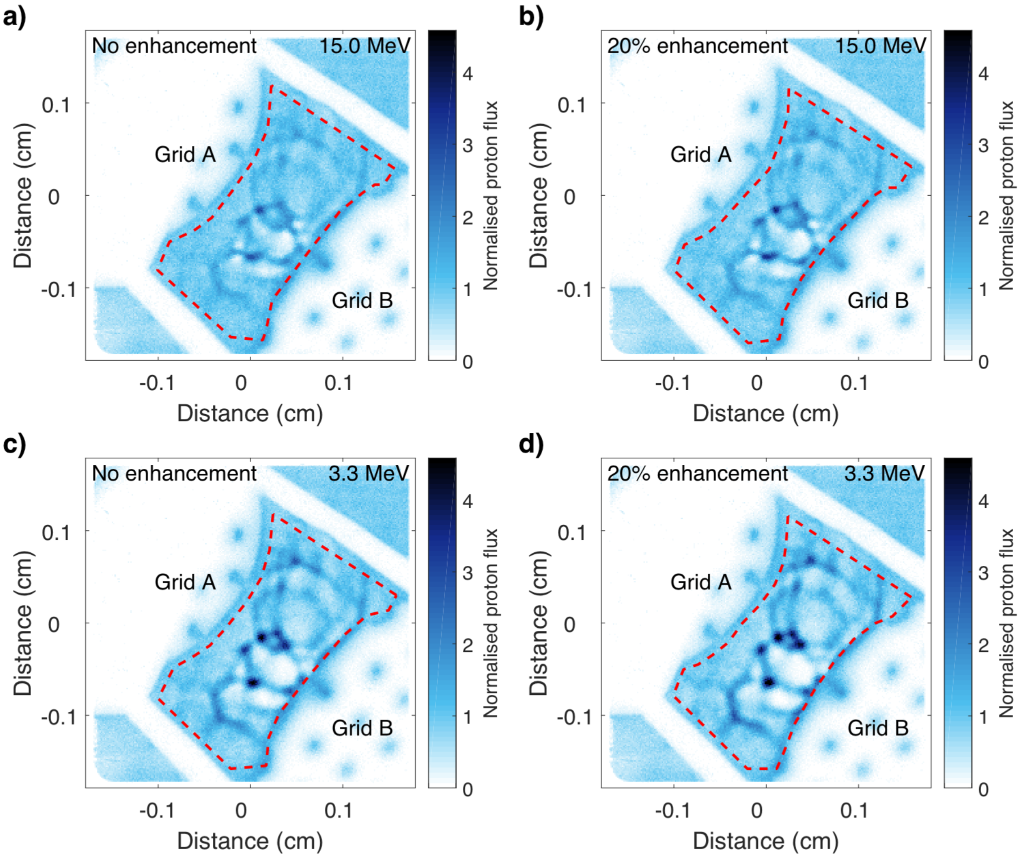

Figure 3.4: Validation of field-reconstruction algorithm via predicted proton images. **a)** 15.0 MeV flux image predicted using reconstructed path-integrated magnetic field shown in Figure 3.1f. The image is created by seeding test protons uniformly in the region over which the path-integrated field is defined (marked by a dashed red line), before assigning velocities to those particles. These velocities are given by the combination of a particle's initial velocity before interacting with fields and velocity perturbation (equation 3.8) due to magnetic fields. The particles are then allowed to propagate to the screen, with dimensions set equal to those in the experiment. The mean flux in each region is set equal to the mean flux of the experimental image. To account for finite source size, a Gaussian point spread function with FWHM 50 μm $\approx 0.14\,$cm is subsequently applied to the images. **b)** Same as a) but with the strength of the path-integrated field increased by 20%. **c)** 3.3-MeV flux image predicted using reconstructed path-integrated magnetic field shown in Figure 3.1f. The equivalent experimental image is shown in Figure 1.13f (and Figure 3.5b). The path-integrated field experienced by the slower proton species is the same assuming magnetically dominated deflections, but their initial perpendicular velocity is reduced. **d)** Same as c) but with the strength of the path-integrated field increased by 20%.

gesting that the reconstructed path-integrated field shown in Figure 3.1e is in fact marginally underestimated. This is most likely due to insufficient application of the Lucy-Richardson deconvolution algorithm.

When considered simultaneously with the 3.3 MeV images, predicted proton images can also be used to verify the assumption of injectivity of the 15.0 MeV images. As was explained in Section 1.4, to a good approximation the 3.3 MeV and 15.0 MeV protons are also deflected by the same magnetic fields. As a result, any path-integrated perpendicular magnetic field reconstructed from the flux image of one proton species should be consistent with flux images obtained for the other species. This can be tested by predicting an image using the perpendicular-deflection field reconstructed from proton images of one species combined with the RK image-flux relation, but varying the initial proton speed to match that of the other proton species. When such a test is carried out for the 15.0 MeV proton reconstructions, the morphology of predicted 3.3 MeV proton images agrees well with the actual 3.3 MeV proton images – see Figure 3.4c compared to Figure 3.5b for an example. Furthermore, the numerical experiments in Section 2.4.3 investigating the use of the field-reconstruction algorithm in the regime where caustic appearance cannot be detected by the test given above suggest that the predicted path-integrated field morphology remains relatively robust, though field strength can be somewhat underestimated. This is consistent with the observation (see Figures 3.4b and 3.4d) that a 20% increase in field strength still leads to similar flux features.

As well as verifying the injectivity assumption, the agreement between actual 3.3 MeV proton images and those predicted using the RK image-flux relation provides an additional demonstration that the flux structures in the proton images are due to magnetic rather than electric fields. This is because the perpendicular-deflection field $\mathbf{w}(\mathbf{x}_{\perp 0})$ imparted by an electric field $\mathbf{E}$ is inversely proportional to the initial proton speed in the small-deflections limit [see equation (3.11)]. Thus, if electric fields were responsible for the structures seen in both the 15.0 MeV and 3.3 MeV images, the 3.3 MeV proton image predicted assuming magnetically dominated deflections would be inconsistent with the experimental data. No such inconsistency is observed.

3.3.4 Reconstruction analysis of 3.3 MeV proton images

Given the marginality of the injectivity assumption for the faster 15.0 MeV proton species, the inverse velocity dependence of the contrast parameter implies that caustics are likely to be present in the 3.3 MeV images, shown in Figure 3.5. Qualitatively, the increased thickness of the intense flux-structures in Figure 3.5b compared to those in the equivalent 15.0 MeV flux image (Figure 3.1f) is consistent with the existence of caustics in the former (as explained in Section 2.3.3 of Chapter 2). However, the characteristic structure of branched caustics is disguised by finite resolution effects. To demonstrate their presence, we instead employ the technique described in Section 2.4.3 of Chapter 2: apply the field-reconstruction algorithm to the 3.3 MeV images to determine a path-integrated perpendicular magnetic field, predict 15.0 MeV images, and then compare them to the experimental 15.0 MeV images. Applying the field-reconstruction algorithm to the 3.3 MeV images shown in Figures 3.5a and 3.5b gives the path-integrated perpendicular magnetic fields shown in Figures 3.5c and 3.5d respectively. It is clear that the latter underestimate field strengths compared to those recovered from the 15.0 MeV images, which is a characteristic sign of caustic structure. The 15.0 MeV images predicted using the RK image-flux relation (Figures 3.5e and 3.5f) are qualitatively quite distinct to the true images: the predicted high-intensity structures are much broader than the true ones. We conclude that caustics are indeed present in the 3.3 MeV images.

3.3.5 Energy images

A different approach for assessing whether magnetic forces are indeed the dominant mechanism acting on the beam is to consider the so-called ‘mean-energy map’ recorded on the CR-39 plates for the 15.0 MeV protons (Li and Petrasso 1993, Li et al. 2016). The mean-energy map is calculated by measuring the diameters of etched CR-39 tracks; in a given slice, smaller track diameters correspond to higher-energy protons. If stochastic electric fields (as opposed to magnetic fields) caused proton

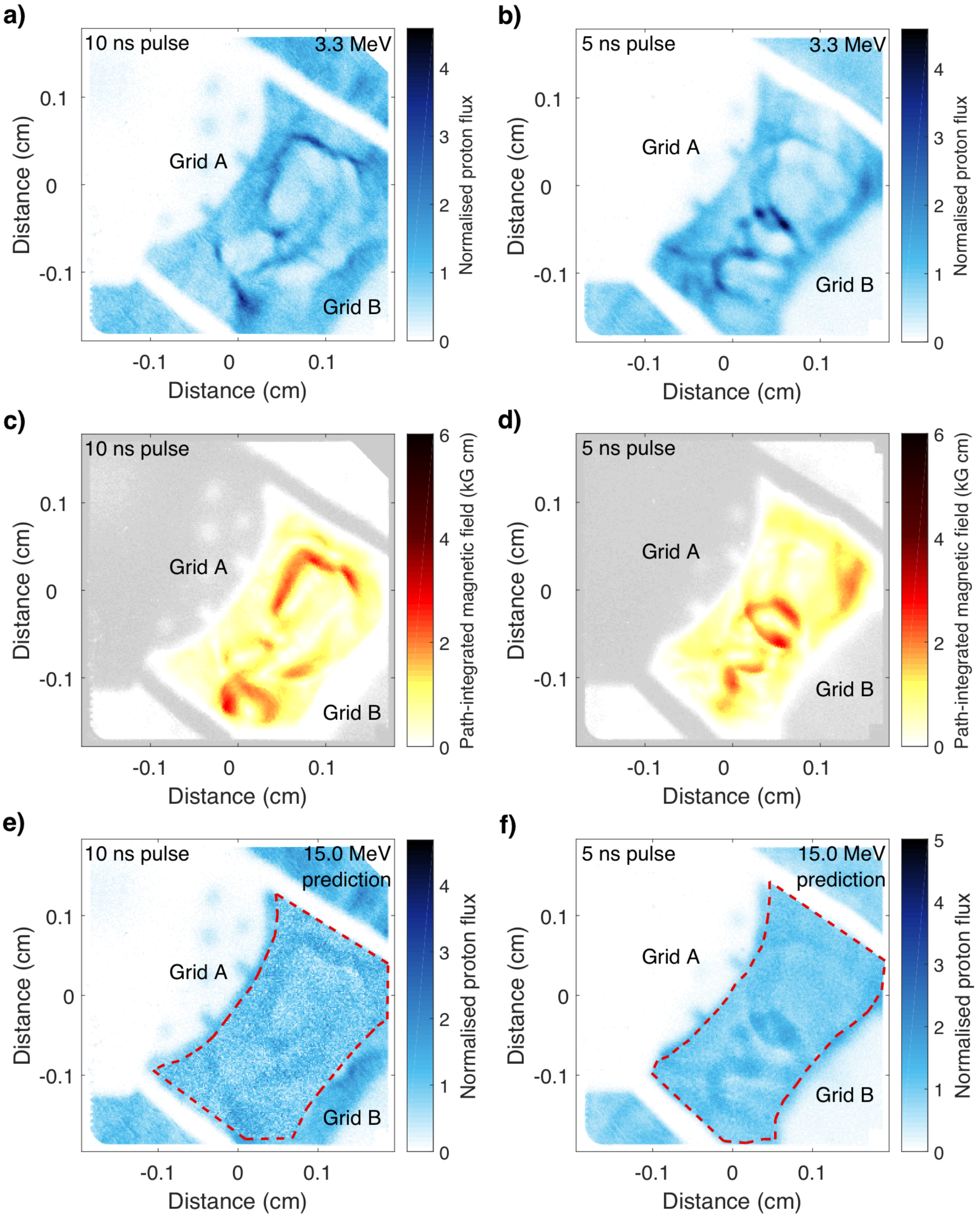

Figure 3.5: Identifying caustics in the 3.3 MeV proton images. **a)** 3.3 MeV proton image corresponding to 34.9 ns after a 10 ns drive-beam pulse initiation (c.f. Figure 1.13d). **b)** Same as a) but with a 5 ns drive-beam pulse initiation (c.f. Figure 1.13f). **c)** Path-integrated magnitude of path-integrated perpendicular magnetic field recovered from a) using field-reconstruction algorithm, under the assumption that no caustics are present i.e. that equation (3.1) is valid. **d)** Same as c) but with the field-reconstruction algorithm applied to b) rather than a). **e)** 15.0 MeV flux image predicted using (reconstructed) path-integrated perpendicular magnetic field shown in c). The method for generating the predicted image is described in the caption of Figure 3.4. The equivalent experimental proton image is shown in Figure 3.1c. **f)** 15.0 MeV flux image predicted using (reconstructed) path-integrated perpendicular magnetic field shown in d). The equivalent experimental proton image is shown in Figure 3.1e.

deflections, the resulting changes in proton energy would in principle lead to inhomogeneities in the mean-energy map. Figure 3.6 shows that, on the contrary, the mean proton energy has a uniform distribution without pronounced structures in the interaction region. This seems to supports the claim that the structures seen in the flux images shown in Figures 3.1a and Figures 3.1b are due to deflections of protons by magnetic, rather than electric fields. That being said, this result should be regarded with some skepticism. The energy resolution of the plates is $\sim 0.1\,\mathrm{MeV}$ (Séguin et al. 2003); since the maximum deflection angle $\delta\theta_{\max}$ associated with the 15.0 MeV protons satisfies $\delta\theta_{\max} \approx 0.01$, we conclude that the maximum energy change δW which any proton could experience is $\delta W \approx W\delta\theta_{\max} = 0.15\,\mathrm{MeV}$, which is marginally above the diagnostic's resolution. It is therefore debatable the extent to which the technique on its own provides conclusive evidence for the absence of electric fields in this experiment.

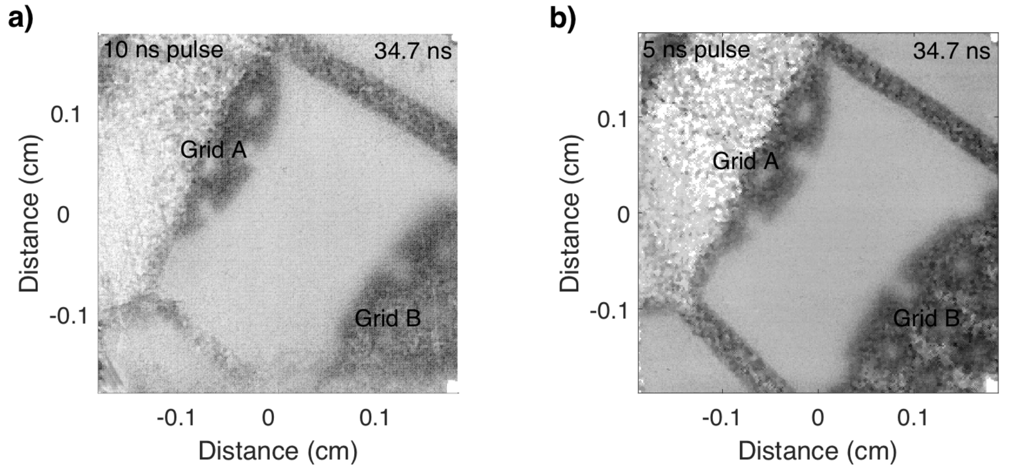

Figure 3.6: Mean proton energy images. Mean proton energy versus position for the 15.0 MeV protons recorded on the second CR-39 plate. **a)** Target with both grids and with the two chlorinated plastic foils driven with the 10 ns pulse shape. The D^{3}He capsule was imploded at $t = 34$ ns. **b)** same as a) but with a 5 ns driver pulse length.

3.4 Validating spectral analysis

3.4.1 Suppression of small-scale structures for shallow power spectra

In spite of likely discrepancies between the actual magnetic fields and those simulated by the FLASH code, the simulated fields still offer a useful testbed for the spectral analysis techniques employed to deduce the magnetic-energy spectrum in Section 3.1.2. In particular, the possibility of first calculating the precise magnetic-energy spectrum from the three-dimensional fields in the simulation and then comparing the result with spectra recovered using the field-reconstruction algorithm enables the efficacy of the latter to be observed directly. Furthermore, the geometry of the colliding plasma jets with respect to the simulated proton-imaging diagnostic provides a more realistic example than the simple test fields described in Chapter 2.

Firstly, the FLASH magnetic fields can be used to illustrate the phenomenon, described in Section 2.4.2, of suppression of small-wavelength structures when reconstructing magnetic-energy spectra from proton images. Figure 3.7a shows the exact path-integrated perpendicular magnetic field experienced by the imaging proton beam (generated from a point source) resulting in the proton image given in Figure 3.7b. The field-reconstruction algorithm applied to this image results in the path-integrated perpendicular magnetic field shown in Figure 3.7c. Qualitatively, we see that, while the largest path-integrated magnetic-field structures in the reconstructed image are similar, small-scale structure is absent. More quantitatively, Figure 3.7d shows three magnetic-energy spectra: the spectrum derived from the 500 μm control volume placed at the centre of the interaction region, the spectrum of the exact path-integrated field [calculated using equation (3.4) applied to Figure 3.7a], and the spectrum from the reconstructed path-integrated magnetic field. While the spectrum calculated from the exact path-integrated field is barely distinguishable from the spectrum derived from the control volume (given the uncertainity on the

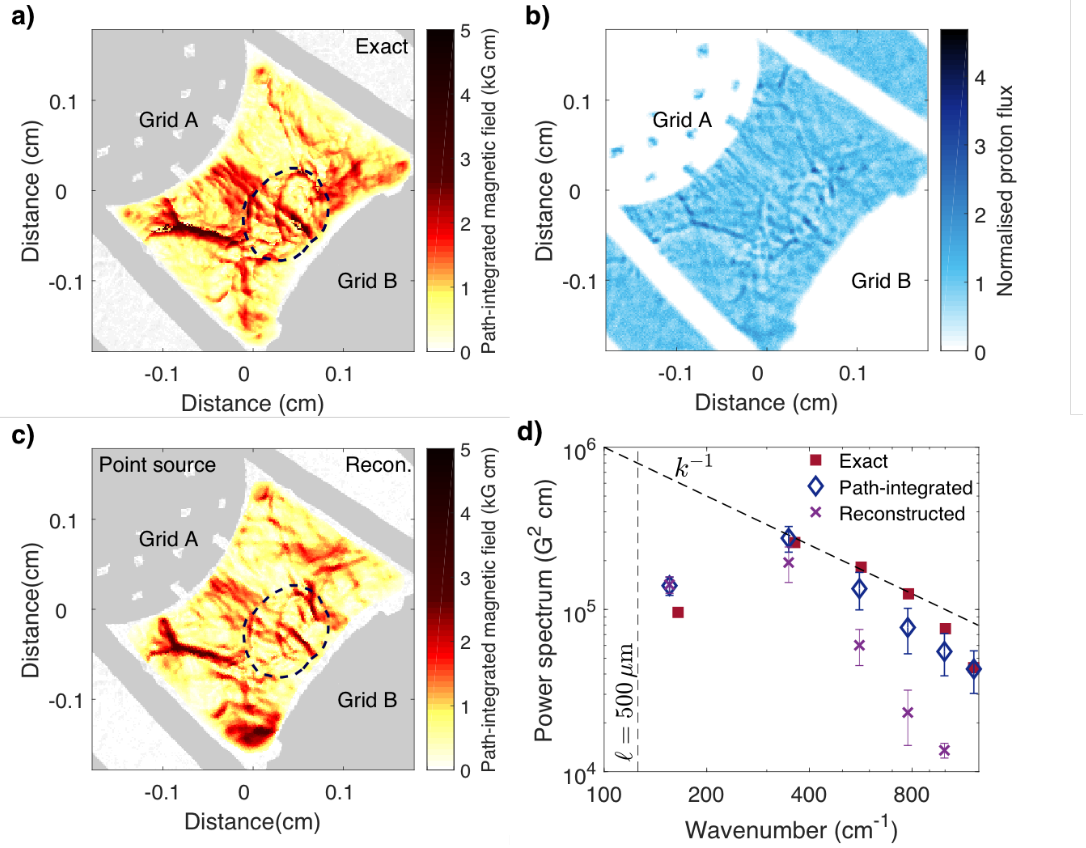

Figure 3.7: Suppression of magnetic-energy spectrum's high-wavenumber tail due to small-scale caustic structure. **a)** Magnitude of exact perpendicular path-integrated magnetic field experienced by artificial proton beam as it passes through the FLASH-simulated magnetic fields (at 34.7 ns after drive-beam pulse initiation). The spatially resolved two-dimensional map is recorded by calculating the average perpendicular path-integrated field experienced by all protons arriving in a given pixel. The region subsequently used for spectral analysis is demarcated by the dashed line. **b)** Simulated proton image associated with beam described in a) (c.f. Figure 1.14b). **c)** Magnitude of perpendicular path-integrated magnetic field recovered using the field-reconstruction algorithm applied to b). **d)** Magnetic-energy spectrum calculated inside the interaction region using three methods: using FLASH magnetic field values in the 500 μm control volume (red squares, see also Figure 1.10c of Chapter 1); the exact path-integrated field shown in a) experienced by the proton beam (blue diamonds); and the path-integrated magnetic field shown in c) reconstructed from FLASH synthetic proton images (purple crosses). The error bars on the latter two spectra are calculated using the same approach as was used for the error bars on Figure 3.2b.

former), the spectrum calculated from the reconstructed path-integrated field has a much steeper tail (which is statistically significant). We conclude (again) that the power-law behaviour of shallow magnetic-energy spectra is not recoverable if the contrast parameter of outer-scale magnetic structures is of order unity. The effect of high-wavenumber spectral suppression on the predicted value $B_{rms}^{(R)}$ of the RMS magnetic-field strength is less pronounced than the change to the spectral slope but is still significant: $B_{rms}^{(R)}/B_{rms} \approx 0.78$ for the FLASH simulations.

3.4.2 Finite proton source size

Next, we test the Lucy-Richardson deconvolution algorithm used to correct the field-reconstruction algorithm for a finite proton source size and the calculation of B_{rms}. Synthetic proton images are generated using the FLASH simulation with both a point source and a more realistic finite $40\,\mu$m source. This allows the reconstructed path-integrated field from the point source (Figure 3.8a) to be compared with the reconstructed field from the finite source, both without (Figure 3.8b) and with (Figure 3.8c) the use of the deconvolution algorithm. Figure 3.8b shows that without the deconvolution algorithm, the reconstruction process leads to lower field strengths; quantitatively, we find the RMS magnetic-field strength $B_{rms,f}^{(R)}$ is only 80% of the field strength $B_{rms,p}^{(R)}$ derived from the point-source reconstruction. However, with the deconvolution algorithm a much closer match is achieved: the RMS field strength $B_{rms,d}^{(R)}$ in this case satisfies $B_{rms,d}^{(R)}/B_{rms,p}^{(R)} \approx 0.96$. Both these results are reflected in the magnetic-field spectra (Figure 3.8d) predicted from the proton imaging using equation (3.4); the magnetic-energy spectrum derived from the path-integrated field shown in Figure 3.8b is suppressed across all wavenumbers as compared to the other reconstructed spectra. We note that all reconstructed spectra are suppressed compared to the spectrum derived from the exact path-integrated field, particularly at high wavenumbers.

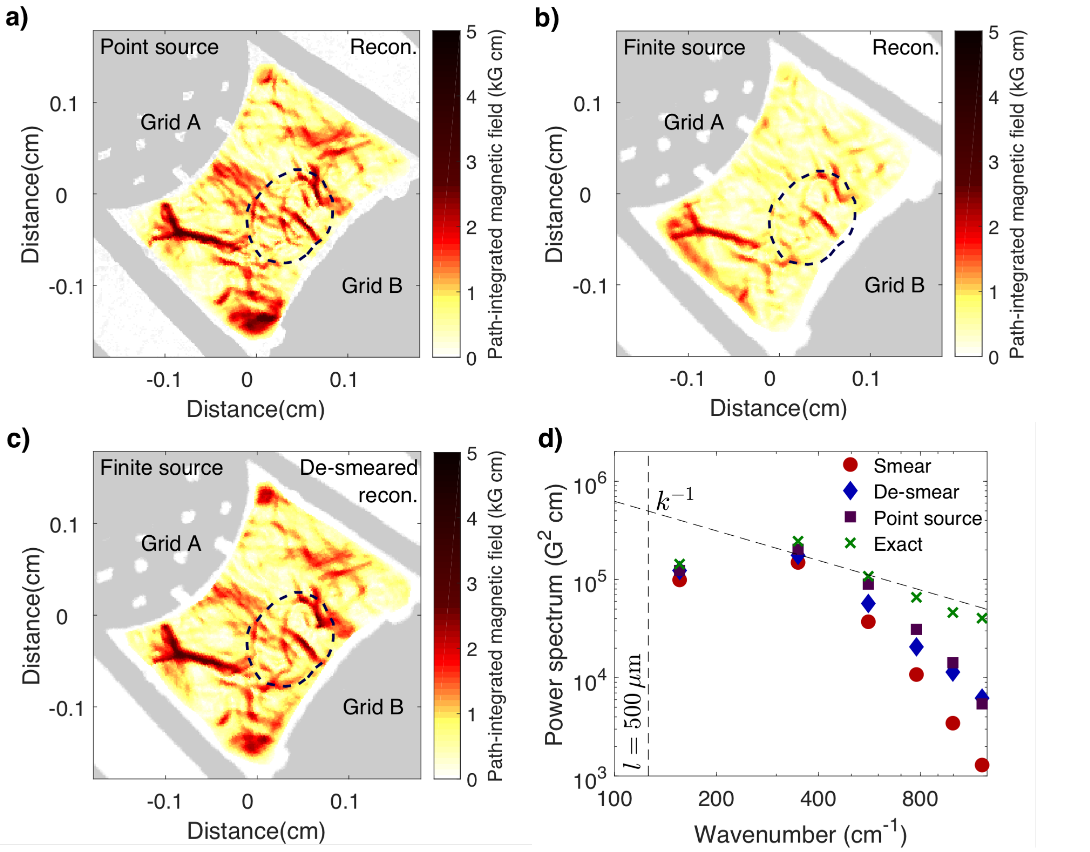

Figure 3.8: Effect of finite proton source size on field-reconstruction algorithm. **a)** Path-integrated magnetic field recovered from simulated proton images created using a quasi-point source of 2×10^{-6} μm diameter using field-reconstruction algorithm. **b)** Same as a) but with a finite-size proton source of diameter 40 μm. **c)** Same as b) but with the Lucy-Richardson deconvolution algorithm included in the reconstruction algorithm. **d)** Extracted magnetic-energy spectra for the three previous cases, as well as the magnetic-energy spectra derived from the exact path-integrated field.

3.5 Implications for the OMEGA fluctuation dynamo experiment

The results of our validation of the field-reconstruction algorithm and associated prediction for the magnetic-energy spectrum are mostly positive but with several provisos. We have demonstrated that the assumptions required for the analysis technique to be valid are satisfied and the self-consistency of the field-reconstruction algorithm has been illustrated. It has subsequently been shown that most likely source of the intense flux-structures seen after jet collision are indeed stochastic magnetic fields and that the values for the path-integrated field obtained from the 15.0 MeV reconstructions are consistent with the 3.3 MeV images. Less favourably for the technique, we have found that two effects inhibit the accuracy of the reconstructed path-integrated field: the finite proton source size and the potential suppression of small-wavelength path-integrated structures due to the presence of small-scale caustics. The former can mostly be rectified using the Lucy-Richardson deconvolution algorithm, but the latter is a fundamental limitation of the set-up. Considering these two effects concurrently, we conclude that the $\sim 100\,\mathrm{kG}$ values of the reconstructed RMS magnetic-field strength is likely to represent a reasonable estimate of the true RMS magnetic-field strength (or perhaps a slight underestimate); however, the predicted magnetic-energy spectrum is not necessarily a reasonable reflection of the true spectrum.

The implications of these results for the physics underlying the OMEGA experiment are as follows. We have been able to verify that the initial seed magnetic fields are indeed energetically subdominant: $B \approx 4\,\mathrm{kG}$. In the absence of any strong turbulence in the flows, the explanation that these fields are generated by the Biermann battery mechanism produced at the laser spots and then advected by the flow – an explanation supported by the FLASH simulations – seems reasonable. We have then shown that, as the two plasma flows collide, the magnetic-field morphology becomes stochastic and characteristic strengths grows from their small initial values to $\sim 100 - 120$ kG. We assume this to be near the saturated value of the field strength, because the Faraday rotation measurement begins over 2 ns (comparable to dynamical times) before the proton-imaging diagnostic and we infer similar magnetic field strengths from both. We note that the expected timescale for saturation to be reached is of the order of an outer-scale eddy-turnover time, $\tau_L = L/u_L \sim 6$ ns (Tobias et al. 2013), a period that is comparable to the time that has elapsed between the initial flow collision and the magnetic field measurements. Since the jet-collision results in a turbulent plasma with a magnetic Reynolds number above the threshold for dynamo action, a plausible candidate for the measured amplification is the fluctuation dynamo.

We claim that the increase of the magnetic field during the collision cannot be simply explained by the compression of the field lines due to the formation of shocks due to the quasi-parallel nature of the initial seed fields. Additional Biermann battery field generation is not a plausible explanation either; this is because the turbulent Peclet number Pe_L – which can be calculated for a multi-species collisional plasma with a known electron temperature T_e, electron density n_e and turbulent velocity u_L at scale L using

$$\begin{aligned}\mathrm{Pe}_L &\equiv \frac{u_L L}{\chi} \\ &\approx 0.14\left[\frac{Z_{\mathrm{eff}}}{7.3}\right]\left[\frac{\log\Lambda}{7}\right]\left[\frac{u_L\,(\mathrm{cm/s})}{10^7\,\mathrm{cm/s}}\right] \\ &\qquad\times\left[\frac{n_e\,(\mathrm{cm}^{-3})}{10^{20}\,\mathrm{cm}^{-3}}\right]\left[\frac{T_e\,(\mathrm{eV})}{450\,\mathrm{eV}}\right]^{-5/2}\left[\frac{L\,(\mathrm{cm})}{0.06\,\mathrm{cm}}\right],\end{aligned} \tag{3.14}$$

where $\chi = 5.1\times10^{21}\,T_e^{5/2}/n_e Z_{\mathrm{eff}}\log\Lambda\,\mathrm{cm}^2/\mathrm{s}$ is the thermal diffusivity, $Z_{\mathrm{eff}} \equiv \sum_j Z_j^2 n_j/n_e$ is the effective ion charge experienced by the electrons when interacting with the multiple ion species (each with charge Z_j, number density n_j), and $\log\Lambda$ is the Coulomb logarithm (Simakov and Molvig 2014) – is small for our experiment, assuming experimentally measured parameters in the interaction region. As a consequence, the plasma is close to isothermal, and temperature gradients in the interaction region are not strong enough for the Biermann battery to be efficient. Both these claims are supported by FLASH simulations.

Collisionless (magnetic-field-generating) plasma processes such as the ion Weibel instability (Huntington et al. 2015) cannot be responsible for the amplification of the magnetic field either, on account of the plasma's high collisionality. More specifically, during the formation of the interaction region ($\sim$ 29 ns), we estimate the characteristic linear growth rate of the ion Weibel instability associated with the counter-propagating jets as being (Ryutov et al. 2014)

$$\gamma_{\rm W} \sim \frac{U_{\rm jet}}{c}\omega_{{\rm p}i} \approx 9.3\times10^{8}\alpha_{\rm W}\left[\frac{Z_{\rm C}}{6}\right]\left[\frac{M}{12}\right]^{-1/2}\left[\frac{U_{\rm jet}\,({\rm cm/s})}{2\times10^{7}\,{\rm cm/s}}\right]\left[\frac{n_e\,({\rm cm}^{-3})}{1\times10^{19}\,{\rm cm}^{-3}}\right]^{1/2}\,{\rm s}^{-1}, \tag{3.15}$$

at wavenumber $k \sim d_i^{-1} \equiv \omega_{{\rm p}i}/c$ (for $\omega_{{\rm p}i}$ the plasma frequency). Here, $\alpha_{\rm W}$ is a growth-rate reduction factor associated with the stabilising effects of intra-jet collisions on the Weibel instability. By comparison, the collisional slowing rate $\nu_{\rm S}^{\rm C|C'}$ – which is also approximately equal to the collisional perpendicular relaxation rate $\nu_{\perp}^{\rm C|C'}$ – is given by

$$\nu_{\rm S}^{\rm C|C'} \sim 8.1\times10^{8}\left[\frac{Z_{\rm C}}{6}\right]^{3}\left[\frac{M}{12}\right]^{-1/2}\left[\frac{U_{\rm jet}\,({\rm cm/s})}{2\times10^{7}\,{\rm cm/s}}\right]^{-3}\left[\frac{n_e\,({\rm cm}^{-3})}{1\times10^{19}\,{\rm cm}^{-3}}\right]\,{\rm s}^{-1}, \tag{3.16}$$

where we have used the fact that, with respect to the carbon-ion population in one jet, the distribution of carbon ions in the other jet is effectively a beam travelling with velocity $2U_{\rm jet}$ (Huba 1994). Assuming $\alpha_{\rm W} \lesssim 0.5$ (in fact, a conservative choice of upper bound – see Ryutov et al. (2014)), we conclude that collisional relaxation prevents the Weibel instability from being present. Once the interaction region has coalesced, the collisional slowing rate of carbon ions subsequently arriving into the interaction region increases approximately eightfold, on account of the interaction region itself being approximately stationary in the laboratory frame; thus, the ion Weibel instability is inhibited in this experiment.

One simple test of the fluctuation-dynamo hypothesis is the following: if saturation of the fluctuation dynamo is reached, the magnetic field energy should become comparable to the turbulent kinetic energy at the outer scale. We find $B_{rms}^2/4\pi\rho u_L^2 \approx 0.03 - 0.04$ (where ρ is the plasma's mass density and we have assumed that $B_{rms} \approx 100 - 120$ kG). Although this mean magnetic-energy-density is only a small finite fraction of the kinetic energy-density, there are a number of arguments suggesting that such an energy ratio is indeed indicative of dynamo saturation. First, in simulations of the fluctuation dynamo conducted for magnetic Reynolds numbers Rm not much larger than the critical threshold Rm_c, the dissipation rate of the magnetic field is found to be greater than the dissipation rate of kinetic energy; when combined with the observation that the field distribution is found to be quite intermittent, this typically results in small energy ratios (Schekochihin et al. 2004c, Beresnyak 2012). Second, since for the low-Pr number MHD dynamo it is anticipated that magnetic energy will be concentrated equally across all scales between the outer scale and the resistive scale, the inability of the proton-imaging diagnostic to measure structures with characteristic wavelengths $\lesssim 100\,\mu$m implies that a significant fraction of the magnetic energy is not detected by the proton-imaging diagnostic. Since the energy ratio depends on the square of the magnetic field, including this fraction would result in a significantly higher magnetic-kinetic energy ratio.

Another good indication that the magnetic field has reached a dynamically saturated state is its attainment of dynamical strengths in the most intense structures, which are not necessarily volume filling. To find an upper experimental bound on the maximum field, B_{max}, we assume that the deflections acquired by the imaging protons across the plasma come from an interaction with a single structure. The strongest individual structure in the reconstructed path-integrated image has scale $\sim 140\,\mu$m with a path-integrated field of 6 kG cm. This gives $B_{\mathrm{max}} \lesssim 430\,\mathrm{kG}$, which leads to $B_{\mathrm{max}}^2/(4\pi\rho u_L^2) \lesssim 0.5$, consistent with dynamical strength.

3.6 Conclusions

In summary, the results of the experiment appear to provide a consistent picture of magnetic field amplification by turbulent motions, in agreement with the longstanding theoretical expectation that the fluctuation dynamo is responsible for dynamical equipartition between kinetic and magnetic energies in high magnetic Reynolds number plasmas – and in particular found in many astrophysical environments. A crucial step in arriving at these results was the theory of proton imaging for stochastic magnetic fields derived in Chapter 2, which allowed for quantitative measurements of both the initial and final magnetic field strengths. This being said, it is reasonable to maintain a degree of skepticism about the robustness of these conclusions. More specifically, for this particular experiment the proton imaging diagnostic was not employed on every laser shot: and thus, only two shots for this experiment employed the proton imaging diagnostic successfully subsequent to the development of stochastic motion in the interaction region (and hence possible formation of stochastic magnetic fields). We are therefore unable to confirm the consistency (or not) of the final RMS field strengths attained in the plasma, which must be regarded as a limitation of this work.

Chapter 4

Characterising the evolution of dynamo-generated magnetic fields in turbulent laser-plasma

4.1 Introduction

In this chapter, we report on a second experiment carried out at the OMEGA laser facility which attempted to create a $\mathrm{Pr} \sim 1$ fluctuation dynamo. We provide a time-resolved characterisation of the plasma dynamo's evolution, measuring spatially averaged electron and ion temperatures, densities, flow velocities, and magnetic fields. Most significantly, we experimentally determine a lower bound on the fluctuation dynamo's growth rate, finding that growth occurs much more rapidly than the turnover rate of driving-scale stochastic motions in the plasma. The second experiment also demonstrates that the key result of the first experiment – amplification of magnetic fields to dynamical strengths – can be replicated robustly.

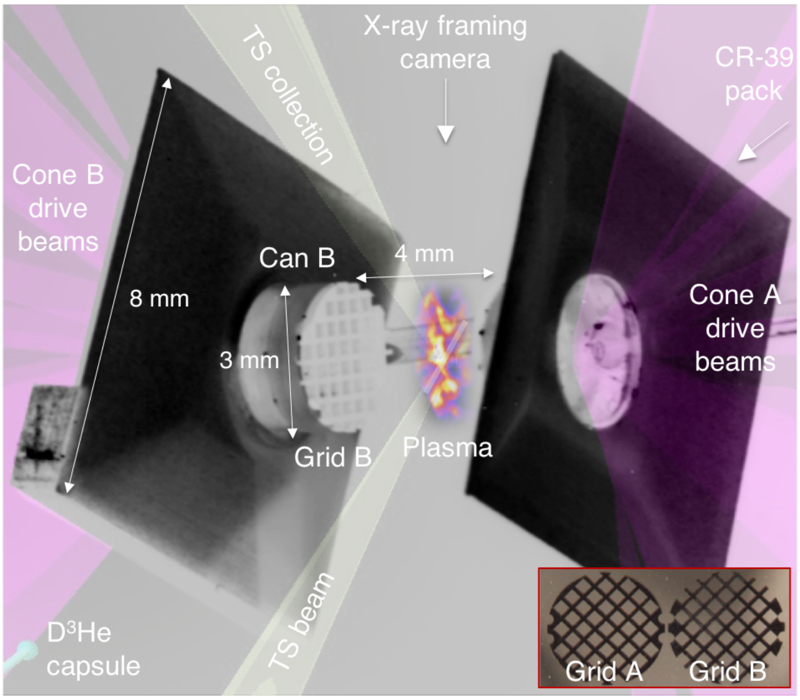

Figure 4.1: Experimental set-up of modified platform. An annotated photograph of a target used in our experiment. The laser-beam-driven foils are composed of CH plastic and are 3 mm in diameter and 50 μm in thickness; attached to the front sides of each foil are 230 μm thick, 3 mm diameter annular 'washers', also composed of CH plastic, with a 400 μm central hole. The separation between the two opposing foils is 8 mm. The shields (which prevent direct interaction between the front- and rear-side blow-off plasmas) are also CH plastic. CH plastic cans attach polyamide grids to the foils; the grids themselves are 250 μm thick, with a 3 mm diameter, 300 μm holes and 100 μm wires. The holes in the opposing grids are chosen to be offset (see bottom right); grid A has a hole located at its centre, while grid B has crossing rods. Ten 500 J drive beams (individual pulse length 1 ns) with 351 nm wavelength and 800 μm focal spot size were applied to each foil, configured to deliver a 10 ns staggered flat pulse shape with a total energy per foil of 5 kJ. The orientation of the Thomson scattering (TS) beam is denoted, as well as the cylindrical scattering volume and collection direction. A D^3He capsule is attached to the target for the proton imaging diagnostic (see Section 4.5 for technical details): fusion protons generated by the capsule's implosion which pass between the target grids are detected via a CR-39 pack positioned as shown.

4.2 Experimental design

The platform employed for the experiment was quite similar to that described in Section 1.2.2 (see Figure 4.1 for a schematic of the experimental target): a region of turbulent plasma was created by colliding two laser-plasma jets, whose flow profiles were pre-modified by two asymmetric grids. At a given instant, the plasma was characterised using various experimental diagnostics: X-ray imaging for investigating the interaction-region plasma's evolution (Section 4.3), Thomson scattering for measuring the physical state of the plasma (Section 4.4), and proton imaging for quantifying magnetic fields (Section 4.5).

In spite of the many similarities with the first OMEGA experiment, the target utilised in the new experiment was distinct in a few key regards. The thickness of the grid wires was decreased to 100 μm, whilst the hole width was maintained at 300 μm (see Figure 4.1, bottom right). This change was implemented in order to reduce inhomogeneity of the interaction region's global morphology arising from the asymmetry of the grids. Chlorine dopants previously introduced into the CH foils in order to enhance X-ray emissivity of the plasma were removed; their presence in even moderate quantities was subsequently found to affect the interaction-region plasma's dynamics significantly and in particular to reduce the magnetic Prandtl number. Finally, rod supports connecting the grids to the CH foils were removed and the grids instead attached via CH 'cans' (see caption of Figure 4.1). This modification increased the field of view of both the X-ray framing camera and proton imaging diagnostics; recent improvements in target fabrication procedures mitigated the risk of target warping, which previously prohibited such a modification from being introduced.

We also somewhat altered our methodology for diagnosing the plasma state. In place of a polarimetry set-up, we instead measured the Thomson scattering spectra of high-frequency fluctuations – the electron-plasma-wave (EPW) feature – as well as low-frequency fluctuations – the ion-acoustic-wave (IAW) feature – concurrently. Furthermore, in place of the previous measurements resolving the scattering spectrum from a small volume during a 1 ns time window, we instead employed a spatially resolved, 1 ns time-integrated set-up, measuring plasma parameters in a cylindrical region passing through the grids' midpoint, with length 1.5 mm and a 50 $\mu\mathrm{m}^2$ cross-sectional area (see Figure 4.1). This allowed for the simultaneous measurement of a range of fundamental plasma parameters indicative of characteristic values of the interaction-region plasma: mean electron number density $\bar{n}_e$, fluctuation electron number density Δn_e, electron temperature T_e, ion temperature T_i, in-flow velocity $\bar{u}_{\rm in}$ and small-scale stochastic velocity ΔV. Because of the prior validation for our set-up of the accuracy of magnetic-field measurements as derived from proton imaging (Rigby et al. 2018), the absence of polarimetry did not prevent the measurement of any significant physical quantities.

In order to obtain a time-resolved characterisation of our experiment, we advanced the application of our diagnostics from shot-to-shot, beginning prior to collision and then proceeding in 1.5 ns intervals. The specifications of the X-ray framing camera diagnostic, the Thomson scattering diagnostic and the proton imaging diagnostics, as well as the results obtained for our experiment, are given in Sections 4.3, 4.4 and 4.5 respectively.

4.3 X-ray framing camera

Images of self-emitted soft X-rays (around $\sim 0.1 - 1.5$ keV) from the interaction-region plasma were recorded using a framing camera (Kilkenny et al. 1988, Bradley et al. 1995) configured with a two-strip microchannel plate (MCP) (Rochau et al. 2006) and a 50 μm pinhole array. The pinhole array was situated 9.14 cm away from the centre of the target and the main detector at 27.4 cm, giving rise to a 2× image magnification. A thin filter composed of 0.5 μm polypropene and 150 nm of aluminium was placed in front of the MCP, removing radiation with photon energy $\lesssim 100\,\mathrm{eV}$. The MCP itself was operated with a 1 ns pulse-forming module at a constant 400 V bias, and the two strips sequentially gated: this allowed for two images (time-integrated over a 1 ns interval) of the plasma at pre-specified times to be detected for each experimental shot. Electrons exiting the MCP struck a phosphor plate, producing an optical image which was recorded using a 4096 × 4096 9-μm pixel charge-coupled device (CCD) camera. The chosen voltage bias was such that the response of the CCD camera was linear and thus the relative counts of two given pixels provides a measure of the relative (optical) intensity incident on the CCD.

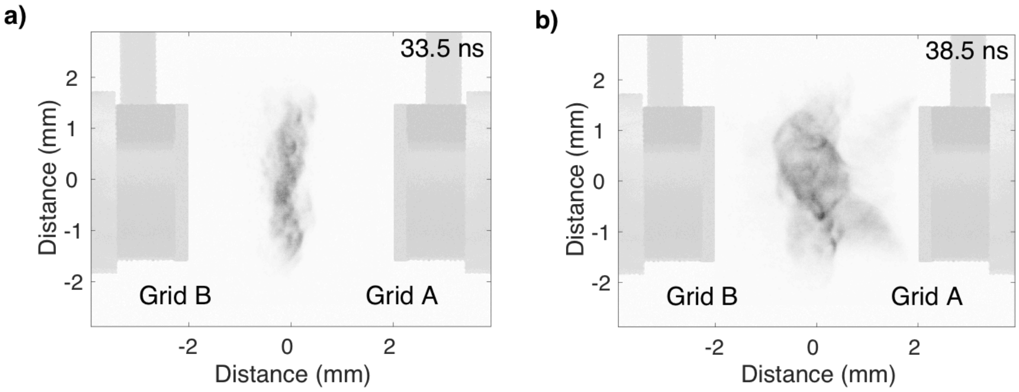

Figure 4.2: Imaging of self-emitted X-rays for each experimental shot. Characteristic output images from X-ray framing camera diagnostic on one experimental shot. In both images, the colour map is linear and adjusted such that the maximum displayed pixel value is 1,050 (corresponding to the maximum pixel count of all our experimental images). The images shown have been cropped and are both 870 × 641 pixels. To aid interpretation of the images, an outline of the target has been superimposed onto both images. The respective designs of grid A and B are shown in Figure 4.1, bottom right. **a)** X-ray image, recorded with the first MCP strip 33.5 ns after the drive-beams are initiated. On this experimental shot, the Thomson scattering probe beam was initiated 1 ns after the first MCP strip was gated and the proton backlighter capsule irradiated 1.5 ns later again; thus, self-emitted X-rays detected in the image are purely due to the interaction-region plasma's dynamics. **b)** X-ray image, recorded with the second MCP strip 38.5 ns after the drive-beams are initiated. This image was recorded after both the Thomson scattering probe beam and the proton backlighter were employed.

To allow comparison between the X-ray images of the interaction-region plasma at different stages of its evolution, the framing-camera bias was fixed throughout the experiment and its value optimised for probing the interaction-region plasma at peak emission. Given this normalisation and the measured signal-to-noise ratio, the effective dynamic range of the camera was ∼100.

Two X-ray images arising from one particular experimental shot are shown in Figure 4.2. Of the two X-ray imaging times recorded for a given experimental shot, the earlier time (see Figure 4.2a) was chosen to fall before the application of the other diagnostics, in order to measure the X-ray emissivity of the interaction-region plasma in the absence of any additional perturbing effects associated with those diagnostics (in particular, probe heating from the Thomson scattering beam, or X-ray heating from the proton capsule backlighter); the latter time (Figure 4.2b) was chosen to be after the application of the other diagnostics, for determining whether such heating effects were indeed significant. Comparing Figure 4.2a and Figure 4.2b, we see that, in addition to the dynamical evolution of the interaction region, increased emission is observed in the latter image from plasma between grid A and the central interaction-region plasma. This effect is most likely due to the aforementioned heating; the diagonal feature corresponds to the projected trajectory of the Thomson scattering beam and only plasma between grid A and the target centre is visible to the proton backlighter capsule. We henceforth refer to the earlier time images as ‘unperturbed’ self-emission X-ray images and the latter as ‘perturbed’ images; the various consequences of the perturbative heating effects of the other diagnostics will be discussed subsequently.

Given the (previously mentioned) fixed X-ray framing camera bias, we find that for times $\lesssim 25\,\mathrm{ns}$, self-emitted X-rays from the individual plasma jets are barely detectable in the absence of the diagnostic perturbative heating effects (see Figure 4.3a and Figure 4.3b). However, around 26 ns after the onset of the driving laser pulses, a region of emission situated approximately halfway between the grids emerges (Figure 4.3c). 1.5 ns later, the total intensity of the region is significantly higher (Figure 4.3d). We conclude that the interaction-region plasma coalesces at around 26 ns.

Subsequent to the formation of the interaction-region plasma, the size of the region of bright emission increases in both the direction parallel to the ‘line-of-centres’ – that is, the line connecting the midpoints of grid A and grid B – and perpendicular to it (see Figure 4.4). Emission peaks 3 ns after the interaction-region’s coalescence, before decaying away at later times (first column of Figure 4.4). Concurrently to the peak emission being reached, random fluctuations in the detected X-ray intensity across the emitting region appear (second column, Figure 4.4) and subsequently become clearly visible by eye. The X-ray images shown in Figure 4.4 are all unperturbed images; the equivalent perturbed images are shown in Figure 4.5. Aside from the previously discussed characteristic differences between unperturbed and perturbed images, the qualitative evolution of the perturbed images over time

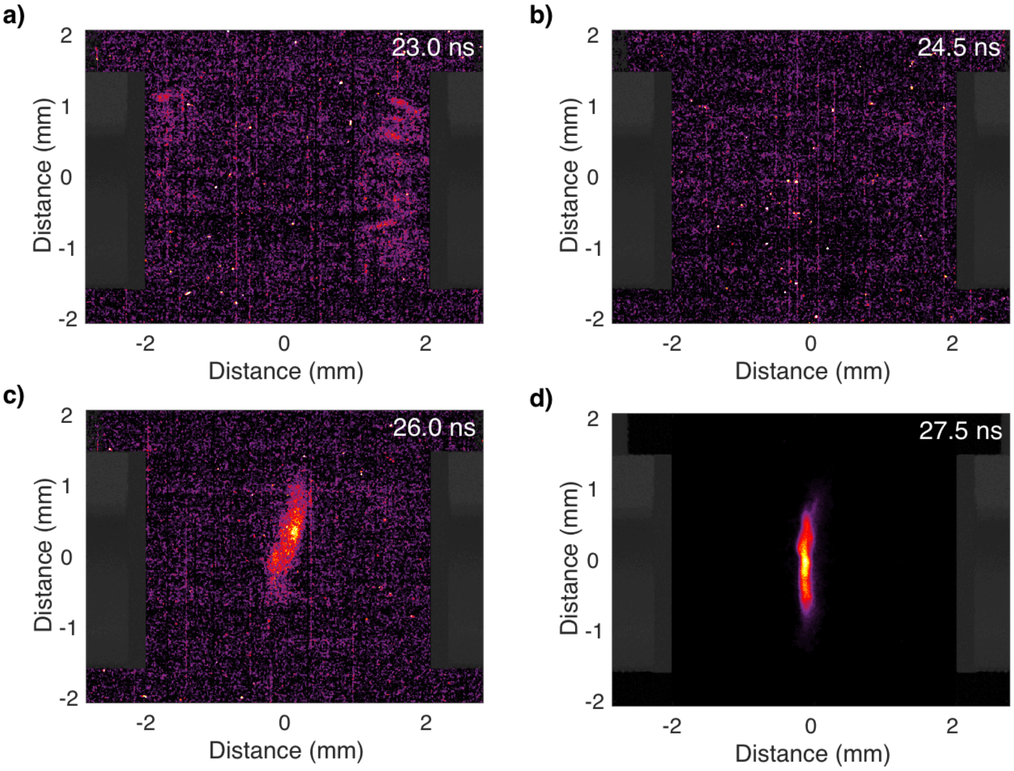

Figure 4.3: X-ray self-emission prior to and at interaction-region coalescence. The featured sequence of X-ray images are taken on different experimental shots. For clarity's sake, we only compare unperturbed images from the first MCP strip i.e. images unaffected by diagnostic heating. The first three images are adjusted to have the same colour map, normalised to the maximum pixel count (56 counts) of c); the final image is normalised to its own maximum pixel count. We note that the absence of noise in d) is due to the much higher signal-to-noise ratio. To aid interpretation of the images, a projection of the target is superimposed in grey on each image. The respective timings (in ns) of the images after drive-beam laser-pulse initiation are **a)** 23.0 ns, **b)** 24.5 ns, **c)** 26.0 ns, and **d)** 27.5 ns.

is broadly similar.

In order to distinguish fluctuations in emission from global inhomogeneities in total self-emission from the interaction-region plasma, we determine relative X-ray intensity maps based on empirically derived mean-emission profiles. The mean-emission profiles are calculated via the direct application to the images of a 57 × 57 pixel smoothing mean-filter. With a pixel size of $9\,\mu$m, this corresponds to assuming that the mean-emission profile varies smoothly on scales $\gtrsim 500\,\mu$m; the largest relative fluctuations inside the interaction region have typical size $L \lesssim 200-400\,\mu$m, providing a modest scale separation. However, applying only a smoothing mean-filter to the images is inadequate for determining reasonable mean-emission

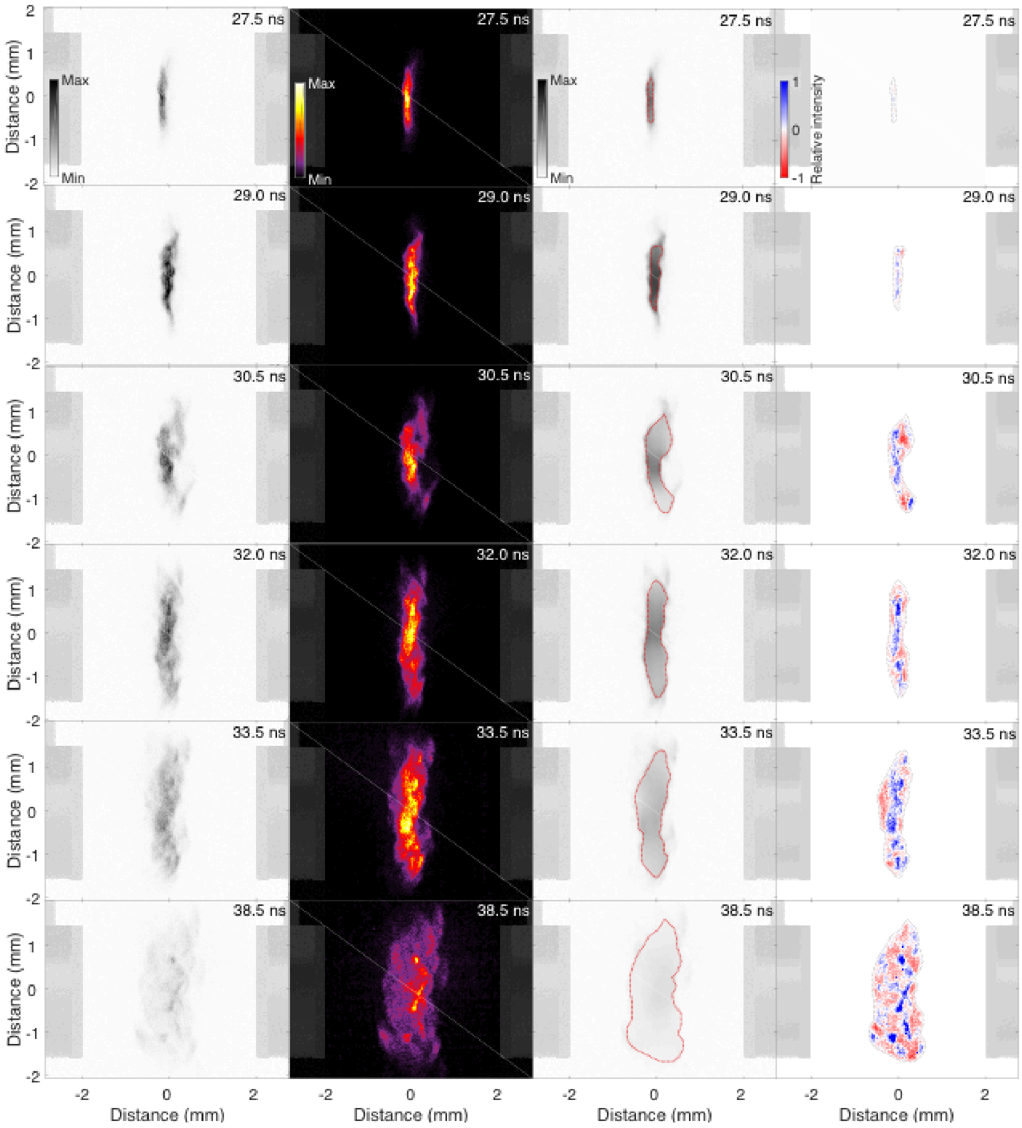

Figure 4.4: The interaction-region plasma's evolution. Unperturbed self-emission X-ray images of the interaction-region plasma. Each image was recorded at the indicated time on a different experimental shot. Far-left column: absolute X-ray intensity images, normalised to a maximum count value of 1,050. Mid-left: X-ray intensity images normalised by the maximum pixel value in the image. Mid-right: mean-emission profiles calculated from the far-left column; the boundary denoted in red in each image is that used to calculate the two-dimensional Gaussian window function discussed in the main text and the colour map is the same as the far-left images. Far-right: relative X-ray intensity map calculated from the mean-emission profile. Fluctuations with a positive value with respect to the mean intensity are denoted in blue, negative in red, with maximum and minimum values set at ±100% of the mean value.

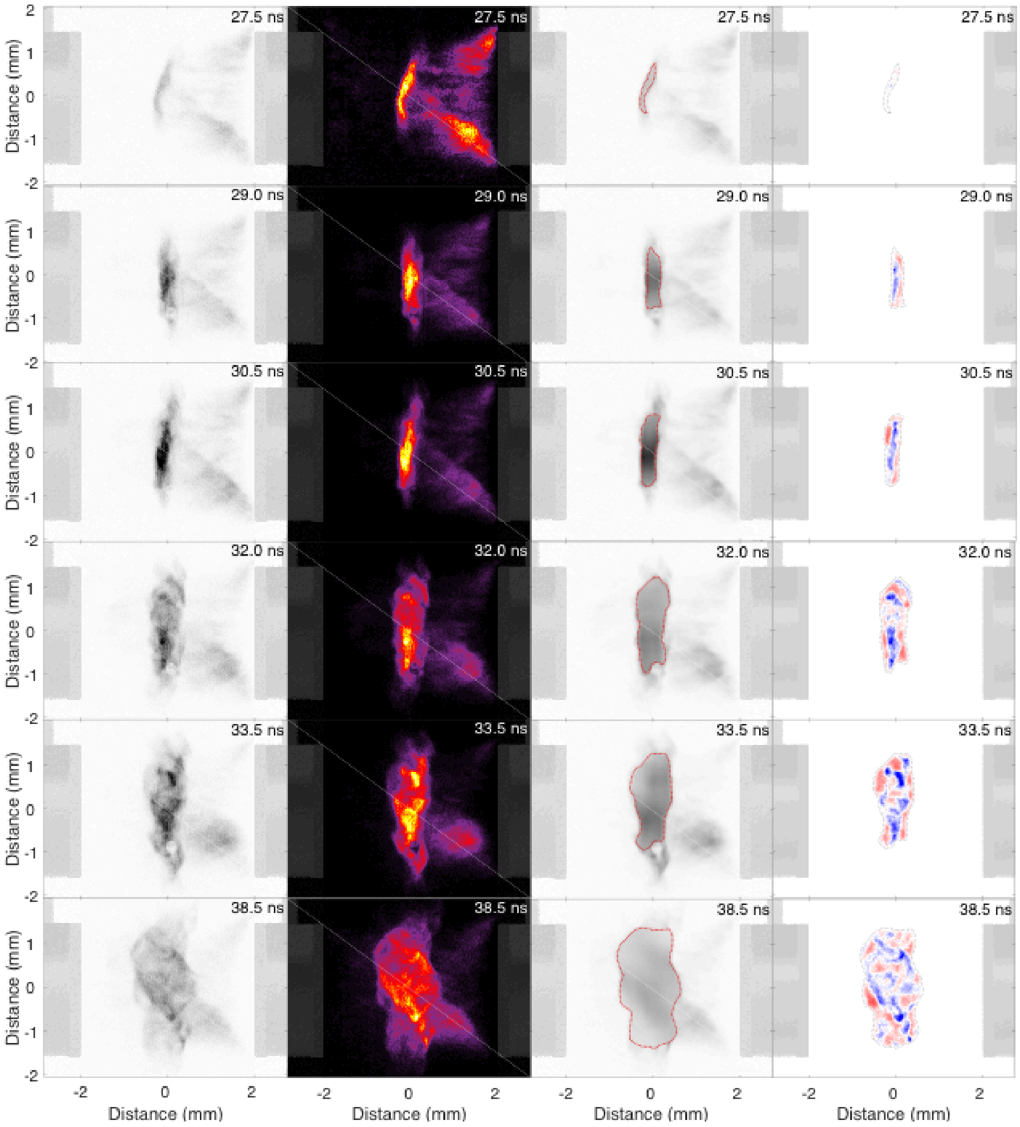

Figure 4.5: The interaction-region plasma's evolution in the presence of perturbative diagnostic heating. Perturbed self-emission X-ray images of the interaction-region plasma. The parameters of each column are identical to those of Figure 4.4. We note that the CCD camera used to record this sequence of images was damaged in a small localised region, slightly below the centre of each image; we therefore chose our window functions so that this region was excluded from subsequent analysis.

profiles; the presence of shocks on either side of the interaction-region plasma implies that the global emission profile would in reality have sharp boundaries (on scales $\lesssim 500\,\mu$m), a feature not adequately picked up by a linear filter. This phenomenon is evident in Figure 4.4, where the X-ray emission is observed to drop rapidly over $\sim 10-20$ pixels ($\sim 100-200\,\mu$m). To account for this, a two-dimensional Gaussian window function on the scale of the boundary is combined with the mean-emission profile to prevent the boundary region from distorting the calculated relative X-ray intensity map (similar techniques are also applied when spectrally analysing data with gaps (Arévalo et al. 2012)). The mean-emission profiles calculated for the unperturbed and perturbed X-ray images shown in the far-left columns of Figure 4.4 and Figure 4.5 respectively are given in the third columns of the same figures and the corresponding relative intensity images are presented in the far-right columns.

Quantitative analysis of the X-ray images can be carried out by noting that the plasma jets are fully ionised even prior to collision ($T_e \sim 200\,\mathrm{eV}$) and so X-ray emission from the plasma during the interaction is dominated by Bremsstrahlung radiation. Assuming a thermal distribution of particles, the Bremsstrahlung emission spectral density $\epsilon_\omega^{\mathrm{ff}}$ for a CH plasma is given by

$$\epsilon_\omega^{\mathrm{ff}} = 1.2 \times 10^{-36} Z_{\mathrm{eff}} n_e^2 T_e^{-1/2} \exp\left(-\frac{\hbar\omega}{k_B T_e}\right) \bar{g}_{\mathrm{ff}} \,, \tag{4.1}$$

where $Z_{\mathrm{eff}} = (Z_{\mathrm{C}}^2 + Z_{\mathrm{H}}^2)/(Z_{\mathrm{C}} + Z_{\mathrm{H}})$ is the effective ion charge experienced by electrons (Z_{H} and Z_{C} being the charges of hydrogen and carbon ions respectively), ω the frequency of radiation, k_B Boltzmann's constant, and $\bar{g}_{\mathrm{ff}}$ the velocity averaged Gaunt factor (Rybicki and Lightman 1979). Since the interaction-region plasma is optically thin to X-rays detected by the framing camera, the measured (optical) intensity I on the CCD camera satisfies $I \propto \int \mathrm{d}s \int \mathrm{d}\omega \, \epsilon_\omega^{\mathrm{ff}} \hat{R}(\omega)$, where the integral is performed along the line-of-sight, and $\hat{R}(\omega)$ is a function incorporating the (relative) frequency-dependent responses of both the X-ray camera filter and the MCP (see Figure 4.6a). Substituting equation (4.1), this proportionality relation becomes $I = I(n_e, T_e) \propto \int \mathrm{d}s \, n_e^2 \hat{f}(T_e)$, where $\hat{f}(T_e)$ is a temperature-dependent function given by

$$\hat{f}(T_e) = \frac{\hat{\mathcal{A}}}{T_e^{-1/2}} \int \mathrm{d}\omega \, \hat{R}(\omega) \exp\left(-\frac{\hbar\omega}{k_B T_e}\right) , \tag{4.2}$$

for $\hat{\mathcal{A}}$ a normalisation constant. The function $\hat{f}(T_e)$ is plotted in Figure 4.6b; we see that for temperatures $\sim 300 - 500$ eV (the characteristic temperature of the

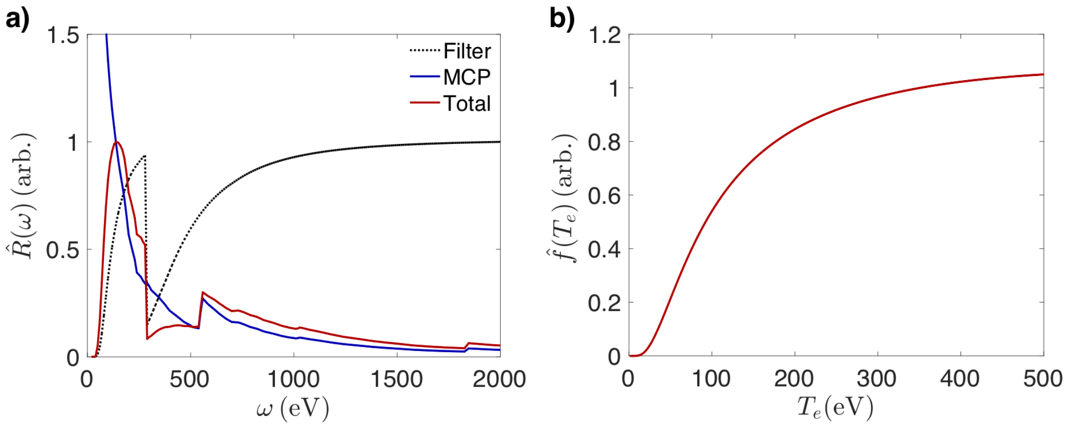

Figure 4.6: Response of the X-ray framing camera. a) Response functions $\hat{R}(\omega)$ associated with X-ray framing camera filter alone (black, dotted), the microchannel plate alone (blue), and the combined response (red). The total response and filter response are normalised to their maximum values respectively; the MCP response was normalised to its value at the frequency at which the total response is maximised. **b)** Relative temperature dependence of the measured optical intensity on the CCD camera. The curve is normalised to its value at $T_e \approx 350\,\text{eV}$.

plasma just after interaction-region coalescence– see Section 4.4), the measured X-ray intensity is only weakly dependent on temperature. However, the X-ray intensity is a sensitive function of electron number density.

The relationship is significant for several reasons. First, the FHWM of the emitting region can be used as a reasonable measure of the width l_n of the interaction region, on account of its increased density compared to either jet. Determining this width is essential for extracting magnetic field estimates from the proton imaging (see Section 4.5). Figure 4.7a illustrates how this measurement is carried out in practice: we consider three vertically averaged lineouts of the mean-emission profile, calculate the FWHMs of these lineouts, and then estimate the error on the measurement from the standard error of the FWHMs. The mean-emission profile is marginally more robust than the original X-ray image for calculating l_n, because fluctuations distort the measured maximum value of the vertically averaged profile. The resulting values of l_n are shown in Figure 4.7c, in blue. Following an initial decrease in value subsequent to the interaction region's coalescence, l_n increases steadily over time.

Second, relative fluctuations δI in X-ray intensity (such as those shown in Figure 4.7b) are closely correlated with fluctuations δn_e in density; indeed, for small

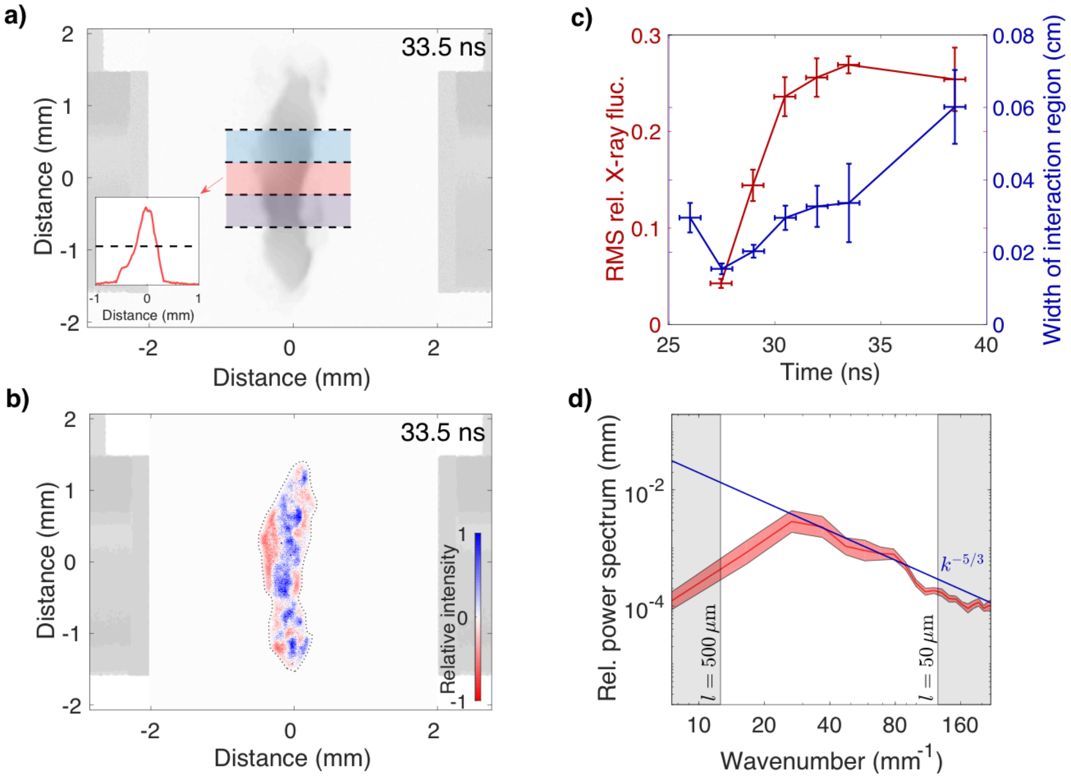

Figure 4.7: Characterising the interaction-region plasma using X-ray imaging. **a)** Mean-emission profile of unperturbed X-ray image, recorded 33.5 ns after drive-beam pulse initiation, shown with regions used to calculate average one-dimensional parallel profiles. One such profile, along with the half-maximum value, is also depicted. **b)** Relative X-ray intensity map associated with mean-emission profile given in a). **c)** Root-mean-square (RMS) of relative X-ray fluctuations (in red) and width of the interaction region l_n over time (in blue). To determine an error on the RMS fluctuation measurement, the RMS values of fluctuations in unperturbed and perturbed images recorded at the same time are employed, under the assumption that the statistics of the density fluctuations (and hence the intensity fluctuations) are negligibly affected by diagnostic perturbative heating effects. **d)** One-dimensional power spectrum of relative density fluctuations (red line), calculated from the relative X-ray intensity map given in b). The error on the spectrum (pink patch) is determined using the power spectrum of b) and the power spectrum of the relative X-ray intensity map derived from the perturbed X-ray image at 33.5 ns equivalent to b).

intensity fluctuations compared to the mean intensity $\bar{I}$, $\delta I/\bar{I} \approx 2\int \mathrm{d}s\, \delta n_e/\bar{n}_e$ (assuming that $\delta T_e/\bar{T}_e \lesssim \delta n_e/\bar{n}_e$, an assumption which will be validated later – see Section 4.6). The root-mean-square (RMS) of the relative X-ray fluctuations therefore provides a simple measure of the onset of stochasticity in the interaction region. The increase in relative X-ray fluctuation magnitude $(\delta I/\bar{I})_{rms}$ shown in Figure 4.7c (in red) illustrates that significant fluctuations develop in a 5 ns interval following interaction-region coalescence, after which their magnitude saturates at a finite fraction of the mean X-ray intensity of the region: $\delta I \lesssim 0.3\bar{I}$. Under the additional assumption that density fluctuations contribute to the line-of-sight integral as a random walk, we find $\delta n_e/\bar{n}_e \lesssim (l_{n\perp}/L)^{1/2}\delta I/2\bar{I}$, where $l_{n\perp}$ is the perpendicular extent of the interaction region and L the characteristic scale of dominant density fluctuations in the plasma. Taking $l_{n\perp} \lesssim 0.3$ cm and $L \approx 0.04$ cm (corresponding to the grid periodicity), we deduce that $\delta n_e/\bar{n}_e \lesssim 0.5$. Thus, it follows that density fluctuations are not too large compared to the mean density and thus the stochastic motions of the plasma are subsonic.

Third, under the assumption of isotropic fluctuation statistics, the power spectrum of path-integrated density fluctuations derived from the X-ray fluctuations can be directly related to the power spectrum of density fluctuations. Since in a subsonic plasma density behaves as a passive scalar (Zhuravleva et al. 2014), this in turn allows for the measurement of the velocity power spectrum (as was described in Section 1.2.3 for the first OMEGA experiment). The results of such a calculation applied to Figure 4.7b are shown in Figure 4.7d: the spectrum is extended across the full range of resolved wavenumbers and for characteristic wavenumbers $2\pi/L \lesssim k < k_{\mathrm{res}} = 127\,\mathrm{mm}^{-1}$, the spectral slope is consistent with a Kolmogorov power law. Such a power law would be anticipated theoretically for turbulent, subsonic plasma.

Finally, we explore differences between unperturbed and perturbed X-ray images recorded at the same time, in order to characterise the perturbative heating effects associated with the Thomson scattering and proton imaging diagnostics. Figure 4.8a and Figure 4.8b document such a comparison $\sim 3\,\mathrm{ns}$ after collision (at $\sim 26\,\mathrm{ns}$) while the equivalent comparison $\sim 12.5\,\mathrm{ns}$ after collision is given by Figure 4.8c and Figure 4.8d. Qualitatively, we note that emission from the interaction-region plasma itself in the former case is not obviously different in the perturbed and unperturbed images: the absolute value of the emission is similar, as is the morphology of the region. However, at later times, emission from the perturbed X-ray images is noticeably higher. More quantitatively, we use the maximum pixel values of the one-

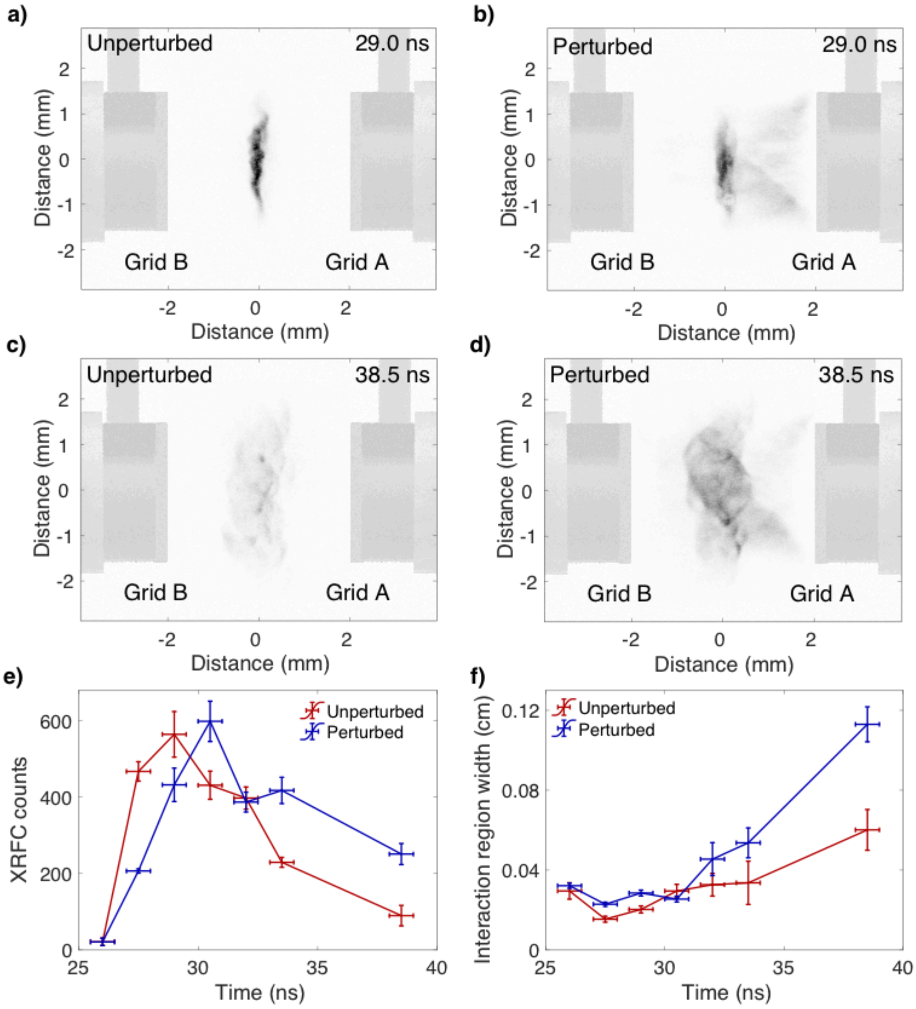

Figure 4.8: Perturbed versus unperturbed self-emission X-ray images. a) Self-emission X-ray image at 29.0 ns after the initiation of the drive-beam pulse, in the absence of perturbative diagnostics. The colour map of the image is the same as Figure 4.2. **b)** Same as a), except in the presence of perturbative diagnostics. **c)** Unperturbed X-ray image at 38.5 ns. **d)** Perturbed X-ray image at 38.5 ns. **e)** Evolution of mean maximum value of one-dimensional mean-emission profiles over time for unperturbed (red) and perturbed (blue) X-ray images. The error on each measurement is calculated using the error arising from the three distinct lineouts calculated from different perpendicular positions in the interaction-region plasma – see Figure 4.7a. **f)** Mean-interaction width over time for unperturbed and perturbed X-ray images. The width and errors are calculated in the same manner as described in the caption of Figure 4.7.

dimensional mean-emission profiles used to calculate the interaction region width (c.f. Figure 4.7a) to compare the relative emission levels associated with the unperturbed and perturbed cases respectively (Figure 4.8e). Somewhat unexpectedly, we find that immediately subsequent to interaction-region coalescence, emission from the unperturbed cases is greater. This trend is most likely to be explained by thermal expansion of interaction-region plasma induced by the additional diagnostic heating: although hotter temperatures would result in slightly increased emission, this trend would be counteracted by lower mean densities in the expanded interaction region, particularly since the measured X-ray intensity is much more strongly dependent on density than temperature for $T_e \sim 300 - 500\,\mathrm{eV}$. This argument derives some weight from the observation that the measured interaction-region width in the perturbed images is slightly larger (Figure 4.8f) immediately subsequent to collision. At later times, Figure 4.8e illustrates the (expected) trend of significantly reduced X-ray intensity in the unperturbed images as compared to the perturbed ones. The most likely explanation of this observation is a reduced interaction-region plasma temperature in the unperturbed case ($T_e \sim 50 - 100$ eV); we will quantify this effect in Section 4.4.

4.4 Thomson scattering diagnostic

The Thomson scattering diagnostic employed a 30 J, frequency-doubled (526.5 nm) laser, which probed the plasma in a cylindrical volume with cross-sectional area 50 $\mu\mathrm{m}^2$ and length 1.5 mm centred on the target's centre, which is coincident with the target chamber centre (TCC). The orientation of the scattering volume is shown in Figure 4.1. The scattered light was collected with scattering angle 63°. As mentioned in Section 4.2, the Thomson scattering signal was resolved spatially along the cylindrical scattering volume and integrated over the 1 ns duration of the laser pulse. The high and low-frequency components of the spectrum are recorded separately using two distinct spectrometers; the separation is performed using a beam splitter. For experimental times approximately coincidental with interaction-region coalescence, clear scattering spectra at both low at high frequencies were obtained. The unprocessed IAW and EPW features for four times close to interaction-region coalescence are shown in Figure 4.9 (Figure 4.9a to Figure 4.9d are the IAW features and Figure 4.9e to Figure 4.9h the EPW features).

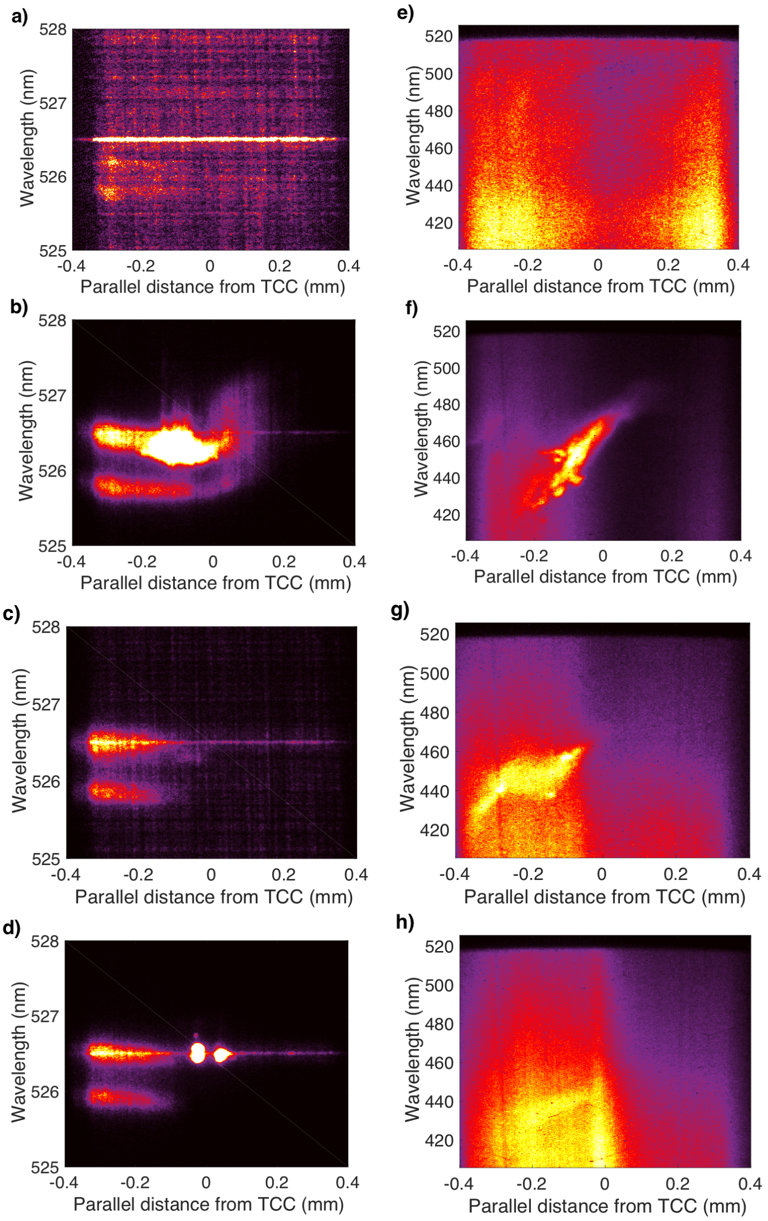

Figure 4.9: Experimental Thomson scattering spectra at interaction-region coalescence. The low-frequency spectra (IAW features) are shown in the left column (a-d) and the high-frequency spectra (EPW features) in the right column (e-h). The scattering volume is oriented at a 63° angle to the direction parallel to the line-of-centres; for convenience of reference (particular in relation to the X-ray images), we report distances projected onto the line-of-centres. The timings of the images are as follows: **a)**, **e)**, 24.0 ns; **e)**, **f)** 25.5 ns; **c)**, **g)** 27.0 ns; **d)**, **h)** 28.5 ns.

To interpret these IAW and EPW features, a theory relating the scattered laser -light detected at a particular wavelength – or, equivalently, frequency – to fundamental properties of the plasma is needed. For a given scattering vector **k**, it can be shown that the spectrum $I(\mathbf{k},\omega)$ of the laser light scattered by the plasma at frequency ω is given by (Evans and Katzenstein 1969)

$$I(\mathbf{k},\omega) = N_e I_0 \sigma_{\mathrm{T}} S(\mathbf{k},\omega)\,, \tag{4.3}$$

where N_e is the total number of scattering electrons, I_0 the intensity of the incident laser, $\sigma_T \equiv (e^2/m_e c^2)^2 \sin^2\vartheta_{\mathrm{T}}$ the Thomson cross-section for scattering by a free electron (e is the elementary charge, m_e the electron mass, c the speed of light, and ϑ_{T} the angle between the wavevector of scattered light and the electric field direction vector of the incident light), and

$$S(\mathbf{k},\omega) \equiv \frac{1}{2\pi N_e}\int \mathrm{d}t\, \exp\left[\mathrm{i}(\omega-\omega_0)t\right]\langle n_e(\mathbf{k},0)n_e(\mathbf{k},t)^*\rangle \tag{4.4}$$

the dynamic form factor (for ω_0 the frequency of the incident light). Assuming the distribution functions of the plasma are close to shifted Maxwellian distributions, with electron number density n_e, electron temperature T_e, temperature T_j of ion species j, and bulk fluid velocity $\mathbf{u}$, and also that the plasma Debye length $\lambda_{\mathrm{D}} \lesssim 10^{-6}\,\mathrm{cm}$ (assumptions which will be justified a priori), we find that $\alpha \equiv 1/k\lambda_{\mathrm{D}} \gtrsim 8 > 1$; thus, we can employ the Salpeter approximation for the dynamic form factor (Evans and Katzenstein 1969):

$$S(\mathbf{k},\omega) \approx \frac{1}{kv_{\mathrm{th}e}}\Gamma_\alpha\left(\frac{\tilde{\omega}-\omega_0}{kv_{\mathrm{th}e}}\right) + \sum_j \frac{Z_j}{kv_{\mathrm{th}j}}\left(\frac{\alpha^2}{1+\alpha^2}\right)^2 \Gamma_{\bar{\alpha}_j}\left(\frac{\tilde{\omega}-\omega_0}{kv_{\mathrm{th}j}}\right), \tag{4.5}$$

where $\tilde{\omega} \equiv \omega - \mathbf{k}\cdot\mathbf{u}$ is the Doppler-shifted frequency, the sum is over all ion species in the plasma, Z_j is the charge of ion species j,

$$\Gamma_\alpha(x) \equiv \frac{\exp\left(-x^2\right)}{\sqrt{\pi}\left|1+\alpha^2 W(x)\right|^2}\,, \tag{4.6}$$

and $\bar{\alpha}_j = Z_j \alpha^2 T_e/T_j(1+\alpha^2)$. Here, the complex function $W(x)$ can be defined in terms of the plasma dispersion function $Z(x)$ via $W(x) \equiv 1 + xZ(x)$ (Fried and Conte 1961). For low-frequency fluctuations (in particular, ion-acoustic waves), $\omega -$

$\omega_0 \sim k v_{\mathrm{th}j}$ and so the first term on the right hand side of (4.5) is small by an $\mathcal{O}[Z_i (m_e T_i)^{1/2}/(m_i T_e)^{1/2}] \ll 1$ factor when compared to the second (this factor is indeed small provided the ion temperature T_i – assumed equal for all ion species – is comparable to the electron temperature); thus the shape of the low-frequency spectrum is dominated by the second term. On the other hand, for high-frequency fluctuations (electron-plasma waves) satisfying $\omega - \omega_0 \sim k v_{\mathrm{the}}$, the second term is smaller than the first by an exponential factor $\mathcal{O}[\exp{(-m_e T_i/m_i T_e)}] \ll 1$; thus the shape of the high-frequency spectrum is dominated by the first term. We conclude that we can relate physical properties of the plasma to the measured EPW and IAW features using fits given by the first and second terms of (4.5) respectively.

However, for our experiment, there is a complication: the presence of stochastic motions and density fluctuations. The presence of such fluctuations mean that the bulk fluid velocity $\mathbf{u}$ and electron density n_e are not necessarily fixed parameters inside the Thomson scattering volume during the time-integrated spectrum, but instead possess a range of values. To account for this range, we assume that fluctuations of velocity and density are isotropic and normally distributed in the time-integrated Thomson scattering volume, with means $\bar{\mathbf{u}}$ and $\bar{n}_e$, and standard deviations Δu and Δn_e respectively. Under this assumption, the appropriate fit for the IAW feature is

$$\begin{aligned} S_{\mathrm{IAW}}(\mathbf{k},\omega) &\approx \frac{\sqrt{3}}{\sqrt{\pi}\Delta u} \int \mathrm{d}\tilde{U}_{\|} \, \exp\left[-\frac{3(\tilde{U}_{\|}-\bar{u}_{\|})^2}{\Delta u^2}\right] \\ &\qquad \times \sum_j \frac{Z_j}{k v_{\mathrm{th}j}} \left(\frac{\alpha^2}{1+\alpha^2}\right)^2 \Gamma_{\bar{\alpha}_j}\left(\frac{\omega - k\bar{U}_{\|} - \omega_0}{k v_{\mathrm{th}j}}\right), \end{aligned} \tag{4.7}$$

where $\bar{u}_{\|} \equiv \hat{\mathbf{k}} \cdot \mathbf{u}$, while for the EPW feature, we use

$$S_{\mathrm{EPW}}(\mathbf{k},\omega) \approx \frac{1}{\sqrt{\pi}\Delta n_e} \int \mathrm{d}\tilde{n}_e \, \exp\left[-\frac{(\tilde{n}_e - \bar{n}_e)^2}{\Delta n_e^2}\right] \frac{1}{k v_{\mathrm{the}}} \Gamma_\alpha\left(\frac{\omega - \omega_0}{k v_{\mathrm{the}}}\right). \tag{4.8}$$

In spite of the seeming complexity of their defining equations, for a fully ionised CH plasma the spectral shapes implied by (4.7) and (4.8) are quite simple: a double peak structure, where the position and width of the peaks depends on plasma parameters. For the IAW feature, the distance between the peaks provides a measure of T_e; the shift in the position of the double-peaked spectrum with respect to the incident probe beam frequency gives a measurement of the bulk velocity $\bar{u}_{\|}$; the width of both peaks is a function of both T_i and of small-scale stochastic motion Δu. The effect of the density on the shape of the IAW feature is negligible. For the EPW feature, the opposite holds: the position of the peak is determined by n_e. The width of the peak is in general determined by a range of factors – Landau damping, collisions and the range of densities Δn_e. For our experiment, both collisional broadening and that by Landau damping are small, but the spread of densities can be significant.

We illustrate the fitting procedure with two examples. Figure 4.10a shows the IAW feature at 27.0 ns after the laser pulse. To fit the experiment spectrum at a given position, we first average the spectrum over a 100 μm interval centred at that position. We then calculate a fit using equation (4.7), substituting $\omega = kc$, and varying T_e, T_i, $\bar{u}_{\|}$ and Δu. In the chosen geometry of the diagnostic, the bulk velocity parallel to $\hat{\mathbf{k}}$ is equal to the in-flow velocity $\bar{u}_{\rm in}$ parallel to the target's line of centres i.e. $\bar{u}_{\|} = \bar{u}_{\rm in}$. We do not use an absolute calibration of the spectrum for the fit; we instead normalise the height of the theoretical spectrum to the lower-wavelength experimental peak (the higher-wavelength experimental peak is typically distorted by a stray-light feature). Once a best fit is obtained, we then vary each parameter individually to assess the sensitivity of the fit. Figure 4.10b and Figure 4.10c demonstrate this process for the electron temperature T_e and velocity Δu respectively: we find sensitivities of ±30% for T_e and ±15% for $\bar{u}_{\rm in}$. Fitting T_i and Δu is more subtle, because both quantities have a similar effect on the spectrum. We therefore instead choose to fit an effective ion temperature, $T_{i,\rm eff}$ including both broadening from ion temperatures and small-scale stochastic motions; we will subsequently outline a method for determining separately T_i and Δu. The sensitivity of the fit for $T_{i,\rm eff}$ is found to be ±40%. While it is in general true that the sensitivity of a fit can

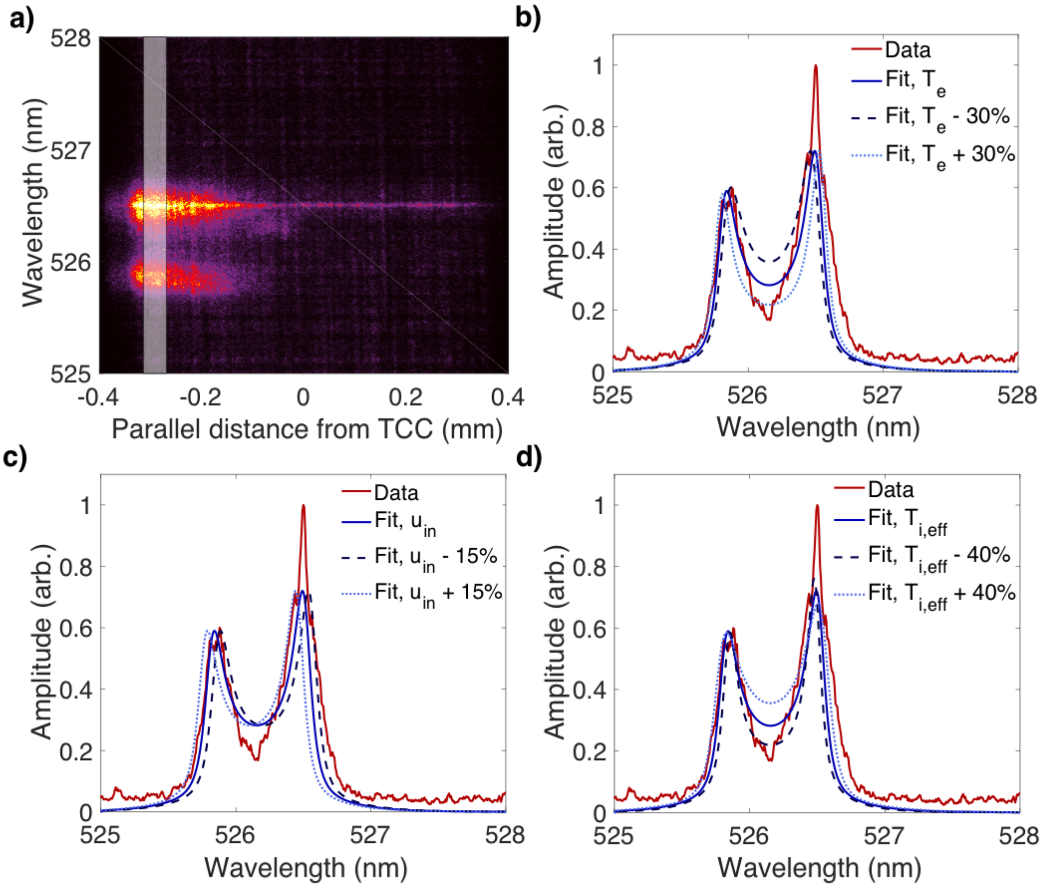

Figure 4.10: Fitting the IAW feature. a) IAW spectrum from 27.0 ns after drive-beam pulse initiation. In subsequent plots, the experimental 1D spectrum (in red) is calculated by averaging the full spectrum horizontally over the region denoted by the translucent rectangle. **b)** Experimental spectrum, plotted with best-fit spectrum ($T_e = 470\,\text{eV}$, $T_{i,\text{eff}} = 620\,\text{eV}$, $\bar{u}_{\text{in}} = 230\,\text{km/s}$, $n_e = 1.2 \times 10^{20}\,\text{cm}^{-3}$) in solid blue, as well as fits parametrised by T_e sensitivity bounds (-30% dashed, +30% dotted). All fits are convolved with the (experimentally measured) instrument function, which has a characteristic width of 0.025 nm. The sharp peak seen at the probe beam wavelength (526.5 nm) is a so-called 'stray-light' feature, and is not part of the plasma's Thomson scattering spectrum; it is disregarded for the purposes of fitting. **c)** Same as b) but plotted with fits parametrised by $\bar{u}_{\text{in}}$ sensitivity bounds. **d)** Same as b) but plotted with fits parametrised by $T_{i,\text{eff}}$ sensitivity bounds.

be underestimated systematically using our chosen methodology – that is, fixing all physical parameters for the fits save one, and then varying the chosen parameter to determine the sensitivity – on account of couplings between parameters, such considerations do not apply to the IAW fits. This is because the parameters Δu, T_e, and $T_{i,\text{eff}}$ each only influence one characteristic of the fit: the average peak position, peak separation and peak width respectively.

Figure 4.11a shows the EPW feature for the same experimental shot. We again

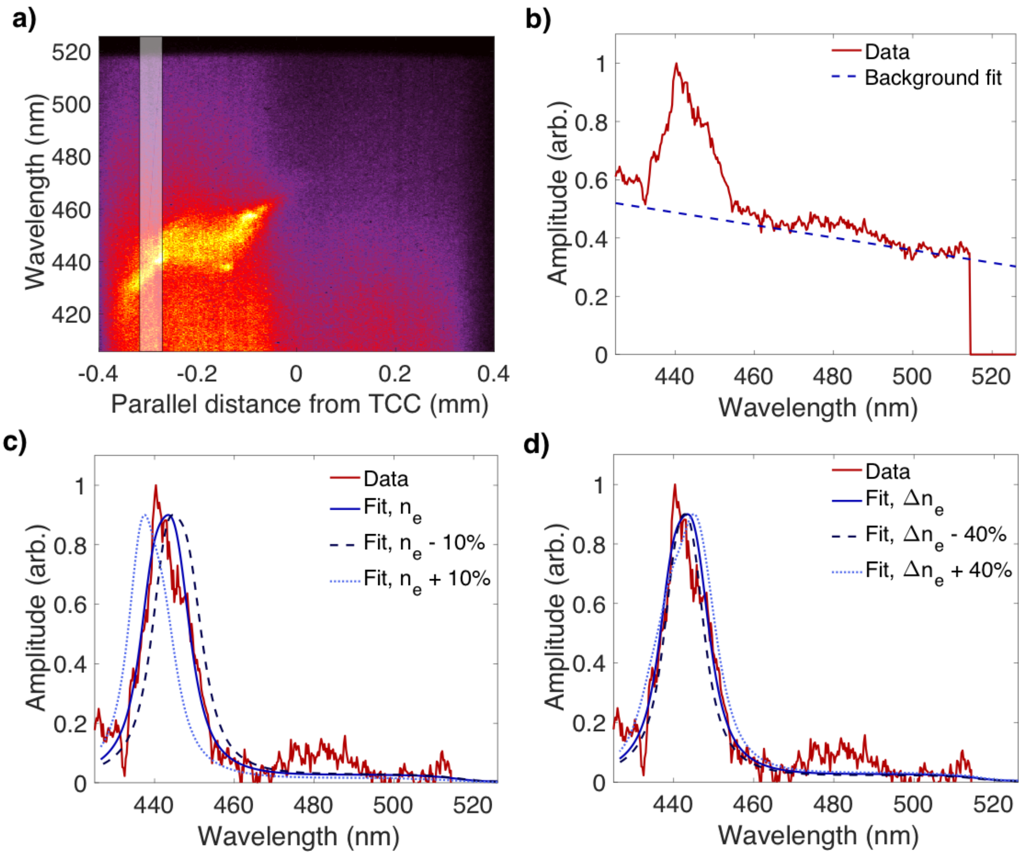

Figure 4.11: Fitting the EPW feature. a) EPW spectrum from 27.0 ns after drive-beam pulse initiation. In subsequent plots, the experimental 1D spectrum (in red) is calculated by averaging the full spectrum horizontally over the region denoted by the translucent rectangle. **b)** Raw experimental spectrum, plotted with linear background fit. **c)** Background-subtracted experimental spectrum plotted with best-fit spectrum ($T_e = 470\,\text{eV}$, $T_{i,\text{eff}} = 620\,\text{eV}$, $\bar{u}_{\text{in}} = 230\,\text{km/s}$, $\bar{n}_e = 1.2 \times 10^{20}\,\text{cm}^{-3}$, $\Delta n_e = 0.35 \times 10^{20}\,\text{cm}^{-3}$) in solid blue, as well as fits parametrised by $\bar{n}_e$ sensitivity bounds (-10% dashed, +10% dotted). All fits are convolved with the (experimentally measured) instrument function, which has a characteristic width of 0.025 nm. **d)** Same as b) but plotted with fits parametrised by Δn_e sensitivity bounds.

determine the experimental EPW spectrum at a given position by averaging over a $100\,\mu$m interval. Before attempting to fit the EPW spectrum, we must first subtract the background signal: this is more significant for the EPW spectrum than the IAW spectrum – on account of the former's reduced magnitude – and is most likely to be associated with radiative emission from the plasma. We find that the background signal for our data is well characterised by a linear fit (see Figure 4.11b). We then fit the experimental spectrum (4.8) by varying $\bar{n}_e$ and Δn_e, before determining the sensitivity of the fits to variations in these quantities: we find ±10% for $\bar{n}_e$ (Figure 4.11c) and ±40% for Δn_e (Figure 4.11d). As with the IAW fits, $\bar{n}_e$ and Δn_e affect different characteristics of the EPW fit, and so our methodology for assessing the fit sensitivity is appropriate. However, we note that the peak position of the EPW feature can be weakly sensitive to the assumed electron temperature as well as $\bar{n}_e$; since the electron temperature is held constant when fitting the EPW feature, using the value determined from the IAW feature, the quoted ±10% sensitivity for $\bar{n}_e$ could in practice be a slight underestimate. Nonetheless, we do not believe it worthwhile carrying out a multivariate sensitivity fit, because the dependence of the peak position on electron temperature is anticipated theoretically to be $\mathcal{O}(\alpha^{-2}) \ll 1$ when compared to the dependence on the mean electron density. Since the uncertainty in T_e from the IAW fit is ±30%, we conclude that corrections to the sensitivity in $\bar{n}_e$ due to the uncertainty in T_e will be no more than a few percent.

In order to arrive at measurements of the parameters indicative of the interaction-region plasma, we average the parameters obtained from fits at each position over the complete spatial extent of the observed IAW and EPW features. The time evolution of physical parameters is obtained by repeating the experiment, but applying the Thomson scattering diagnostic at a different time with respect to the drive beams. To determine independently T_i and Δu, we use the fact that motions are subsonic and thus estimate $\Delta u \approx c_{\mathrm{s}} \Delta n_e / \bar{n}_e$, where c_{s} is the sound speed; this leaves T_i as the only free parameter determining $T_{i,\mathrm{eff}}$ in the fits.

The evolution of temperatures in plasma present in the Thomson scattering volume is shown in Figure 4.12a, densities in Figure 4.12b, and velocities in Figure 4.12c. At 24 ns, the characteristic electron and ion temperature is given by $T_e \approx T_i \approx 180\,\mathrm{eV}$, the characteristic flow speed $\bar{u}_{\mathrm{in}} \approx 260\,\mathrm{km/s}$, and mean electron number density $\bar{n}_e \approx 2.5 \times 10^{19}\,\mathrm{cm}^{-3}$. Such parameters are similar to those previously obtained for a single plasma jet (see Section 1.2.3), and thus suggest that the interaction-region plasma has not yet coalesced. By contrast, 1.5 ns later, both electron and ion temperature were found to be much larger than their jet pre-collision values: $T_e \approx T_i \approx 450\,\mathrm{eV}$. The measured mean electron number density

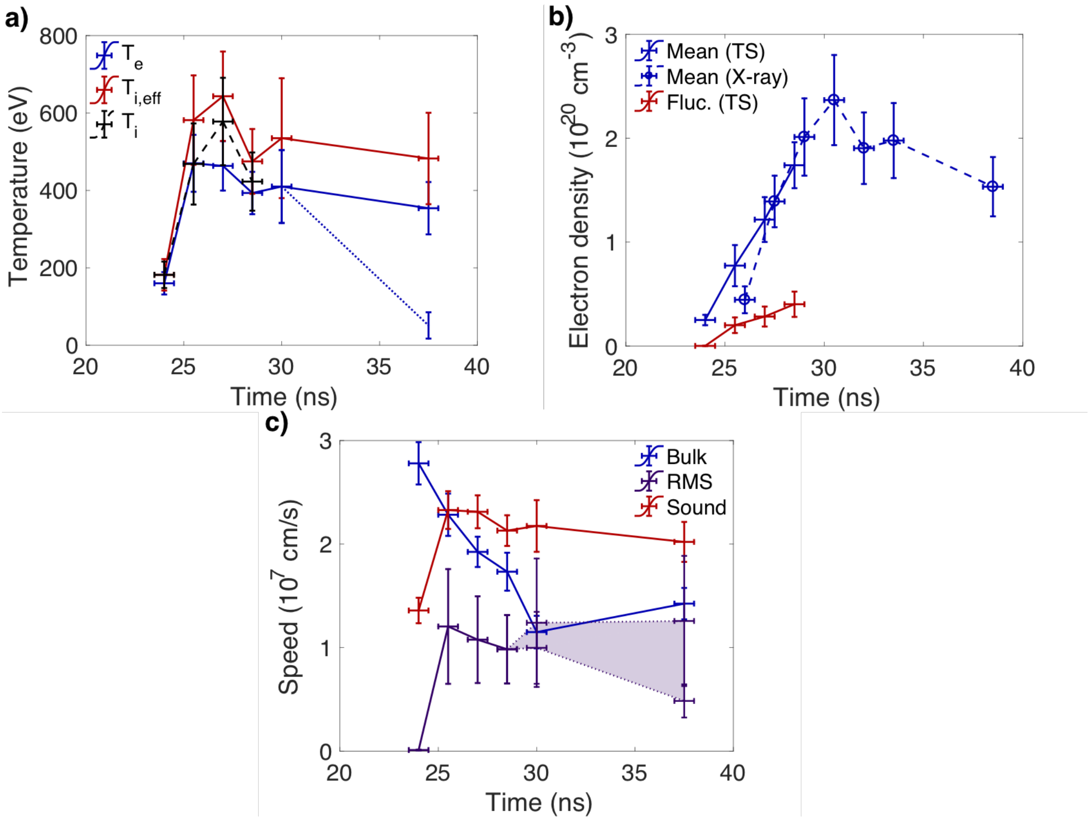

Figure 4.12: Time-evolution of interaction-region plasma state. a) Evolution of electron temperature (blue), effective ion temperature (red) and ion temperature (black, dashed) over time. All values are determined as described in the main text; errors are determined by combining in quadrature the fit sensitivity and the variability of parameters as measured across the Thomson scattering volume for each time. The alternative electron temperature history at later times (blue, dotted) is a projected lower bound calculated from the difference in mean self-emitted X-ray intensities in the presence and absence of the Thomson scattering diagnostic. **b)** Evolution of mean electron density $\bar{n}_e$ (blue) and Δn_e (red) over time. Errors are calculated in the same manner as the temperature errors. An alternative density history (blue, dashed) is determined from the self-emission X-ray images under the assumption of dominant Bremsstrahlung emission. **c)** Evolution of bulk in-flow speed (blue), sound speed (red) and turbulent velocity (purple) in the Thomson scattering volume. Errors are calculated in the same way as those for density and temperature.

also increased, to $\bar{n}_e \approx 8 \times 10^{19}\,\mathrm{cm}^{-3}$; in addition, a range of densities were observed, with $\Delta n_e \approx 2 \times 10^{19}\,\mathrm{cm}^{-3}$. For a measured characteristic in-flow velocity of $\bar{u}_{\mathrm{in}} \approx 220\,\mathrm{km/s}$, this range of densities gives rise to small-scale stochastic velocity $\Delta u \approx 55\,\mathrm{km/s}$. Assuming Kolmogorov scaling for the random small-scale motions – indeed, as is consistent with the spectral slope determined in Figure 4.7d – the characteristic velocity u_ℓ at scale ℓ satisfies $u_\ell \sim u_{rms}(\ell/L)^{1/3}$; thus, because the dominant contribution to Δu arises from stochastic motions with scale compara-

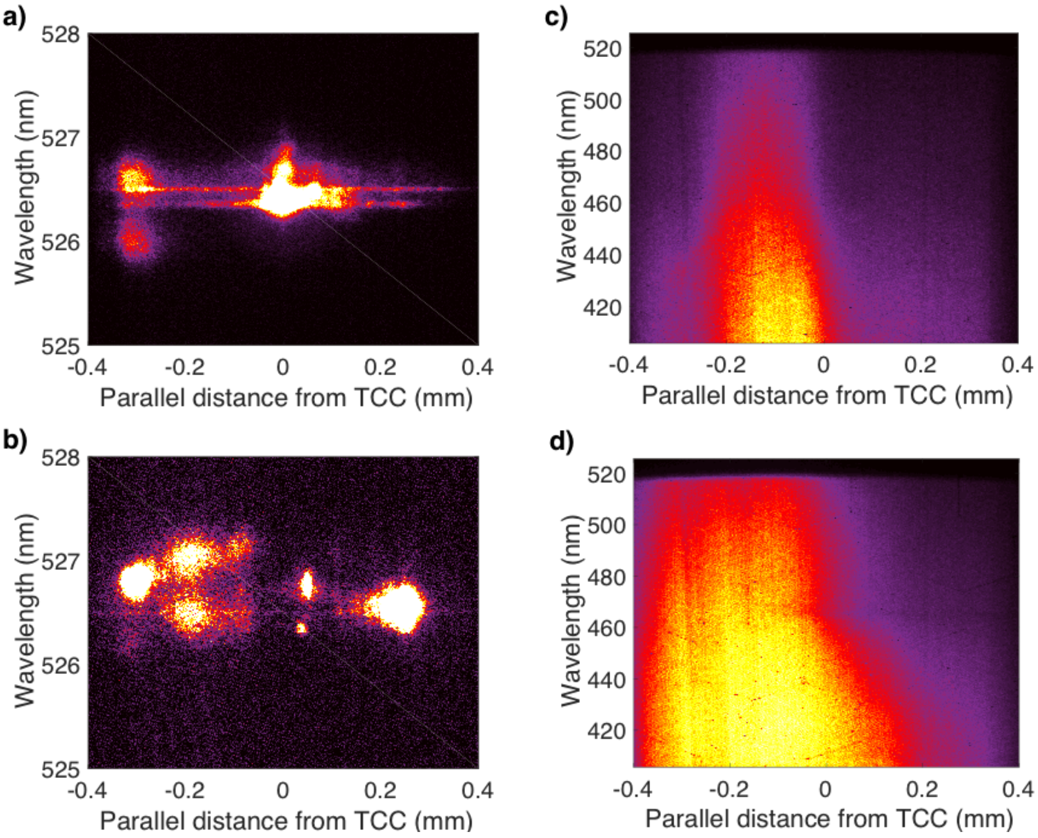

Figure 4.13: Experimental Thomson scattering spectra at later times. The low-frequency spectra (IAW features) are shown on the left (a-b) and the high-frequency spectra (EPW features) in the right column (c-d). The timings of the images are as follows: **a)**, **c)**, 30.0 ns; **b)**, **d)** 37.5 ns.

ble to the Thomson scattering cross-section width $l_{\mathrm{TS}} \approx 50\,\mu$m, we conclude that $u_{rms} \approx 110\,$km/s. In the 3 ns interval subsequent to collision, the ion temperature increased above the electron temperature ($T_i \approx 600\,$eV), before both fell to lower values ($T_e \approx T_i \approx 400\,$eV). The mean electron number density increased monotonically over the same interval, with a final measured mean electron number density of $\bar{n}_e \approx 1.8 \times 10^{20}\,\mathrm{cm}^{-3}$. The relative magnitude of density fluctuations remained consistent ($\Delta n_e/\bar{n}_e \approx 0.25$) over the interval.

For later times, no EPW feature was observed and the IAW feature manifested itself erratically (see Figure 4.13). We believe that this diagnostic failure was due to the increased density of the interaction region (as well as substantial density gradients) resulting in significant refraction of the Thomson scattering probe beam. We were therefore unable to measure $\bar{n}_e$ or Δn_e for times $\gtrsim 30\,$ns using the Thomson scattering diagnostic. A reasonable estimate of $\bar{n}_e$ can still be obtained, however, using the X-ray framing camera diagnostic. More specifically, (again) assuming that X-ray emission from the plasma is dominated by Bremsstrahlung, we can estimate the mean electron number density $\bar{n}_e(t_1)$ at time t_1 in terms of the mean electron number density $\bar{n}_e(t_2)$ at time t_2 via the following relationship: $\bar{n}_e(t_1) \approx \bar{n}_e(t_2)[I(t_1)/I(t_2)]^{1/2}$. Thus, assuming a reference value for $\bar{n}_e(t_2)$ at $t_2 = 29.0\,\mathrm{ns}$ (derived via linear interpolation from the Thomson scattering density measurements), we obtain the evolution profile shown in Figure 4.12b. The results imply that the density continues to rise for a ~ 2 ns interval after the final Thomson scattering measurement of density is obtained, reaching a peak value $\bar{n}_e \approx 2.4 \times 10^{20}\,\mathrm{cm}^{-3}$ at $t = 30\,\mathrm{ns}$, before subsequently falling slightly at later times.

We were still able to use the IAW feature to measure the bulk flow velocity, the electron temperature and the effective ion temperature in some spatial locations at later times. The bulk flow velocity was found to drop to around 100 km/s at 30 ns; at 37.5 ns, a similar value was obtained but with a reversed sign. The electron temperature as measured by the Thomson scattering diagnostic remained consistently around 400 eV. However, as was discussed at the end of Section 4.3, evidence from the X-ray framing camera diagnostic suggests that heating of the interaction-region plasma by the Thomson-scattering beam becomes significant at later times in the experiment, on account of the higher densities, reduced temperatures, and extended path-length of the beam through the plasma.

We can explain this effect theoretically via the following simple argument. The fraction of probe beam energy f_a absorbed by the plasma can be estimated as $f_a \approx 1 - \exp\left(-\kappa_a l_{\mathrm{beam}}\right)$, where κ_a is the the absorption coefficient of the beam in the plasma and l_{beam} the path-length of the beam through the interaction-region plasma (Colvin and Larsen 2013). The dominant absorption process affecting the beam is inverse

Bremsstrahlung and so

$$\begin{aligned}\kappa_a &= 3.6\left[\frac{Z_{\mathrm{eff}}}{5.3}\right]\left[\frac{\log\Lambda}{7}\right]\left[\frac{n_e(\mathrm{cm}^{-3})}{1.5\times10^{20}\,\mathrm{cm}^{-3}}\right]^2 \\ &\quad\times\left[\frac{T_e(\mathrm{eV})}{330\,\mathrm{eV}}\right]^{-3/2}\left[\frac{\omega_0(\mathrm{s}^{-1})}{3.6\times10^{15}\,\mathrm{s}^{-1}}\right]^{-2}\left[\frac{\epsilon_{\mathrm{D}}}{0.97}\right]^{-1/2}\mathrm{cm}^{-1}, \qquad (4.9)\end{aligned}$$

where $\epsilon_{\mathrm{D}} \equiv 1-\omega_{\mathrm{pe}}^2/\omega_0^2$ is the dielectric permittivity of the plasma. Estimating $l_{\mathrm{beam}} \approx 0.13\,\mathrm{cm}$ from the interaction-region-width X-ray measurements at 38.5 ns, we conclude that $\kappa_a l_{\mathrm{beam}} \approx 0.45$ and thus $f_a \approx 0.36$. We conclude that the total energy E_{heat} conferred to the Thomson scattering volume (neglecting conduction) is $E_{\mathrm{heat}} \approx 1.1\times10^8\,\mathrm{erg}$. Noting that the internal energy density $\varepsilon_{\mathrm{th}}$ of the plasma is $\varepsilon_{\mathrm{th}} \approx 3n_eT_e\left(1+\langle Z\rangle^{-1}\right)/2$ (assuming $T_i \approx T_e$), it follows that the total thermal energy E_{th} present in the Thomson scattering volume is given by

$$E_{\mathrm{th}} = 1.1\times10^8\left[\frac{\langle Z\rangle+1}{4.5}\right]\left[\frac{n_e(\mathrm{cm}^{-3})}{1.5\times10^{20}\,\mathrm{cm}^{-3}}\right]\left[\frac{T_e(\mathrm{eV})}{330\,\mathrm{eV}}\right]\left[\frac{\mathcal{V}_{\mathrm{T}}(\mathrm{cm}^3)}{7.5\times10^{-4}\,\mathrm{cm}^3}\right]\mathrm{erg}\,, \qquad (4.10)$$

where $\mathcal{V}_{\mathrm{T}}$ is the volume of the Thomson scattering collection volume. We conclude that at the prescribed density, $E_{\mathrm{heat}} \gtrsim E_{\mathrm{th}}$ for electron temperatures $T_e \lesssim 330\,\mathrm{eV}$. We therefore conclude that the electron temperature at later times could be significantly lower than the value measured by the Thomson scattering beam in the absence of the probe beam heating.

This heating effect can also now be investigated directly by combining the Thomson scattering results with those from the X-ray imaging diagnostic. We recall that the intensity I recorded on the CCD camera is dependent on temperature: $I \propto \int \mathrm{d}s\, n_e^2 \hat{f}(T_e)$, where $\hat{f}(T_e)$ is defined by equation (4.2) and plotted in Figure 4.6b. Thus, if the electron number density of the interaction-region plasma is known at two given times, any difference in total intensity evident in an X-ray image can be attributed to distinct temperatures. Applying this logic to unperturbed and perturbed X-ray images recorded at the same point in time (on different experimental shots) and presuming that at later times probe heating has a minimal effect on plasma density, we can use the differences in intensity calculated in Figure 4.8f to provide an estimate of the unperturbed electron temperature $(T_e)_{\mathrm{up}}$. More specifically, it follows that $(T_e)_{\mathrm{up}} \approx (T_e)_{\mathrm{p}} \hat{f}^{-1} \left(I_{\mathrm{up}}/I_{\mathrm{p}}\right) \approx 50\,\mathrm{eV}$, where $(T_e)_{\mathrm{p}}$ is the perturbed electron temperature, I_{p} the mean X-ray intensity in the unperturbed image, and I_{up} the mean X-ray intensity in the perturbed image. This inferred bound is significantly below the temperature measured by the Thomson scattering diagnostic, confirming the importance of probe-beam heating.

The absence of a direct measurement of Δn_e prohibits a specific measurement of the small-scale stochastic velocity for times $> 28.5\,\mathrm{ns}$. Instead, we obtain upper and lower bounds respectively on u_{rms} via two distinct methods. For the upper bound, we assume that $T_i = T_e$ (not an unreasonable assumption at later times in the experiment – see Section 4.6) and thus attribute the higher value of the effective ion temperature measured using the Thomson scattering as being solely due to small-scale stochastic motions. Such an approach does indeed provide an upper bound to the small-scale stochastic velocity, because compressive heating in the plasma preferentially affects the ion population (Shafranov 1957), and thus we would expect that $T_i \gtrsim T_e$ in the interaction-region plasma (as, indeed, is observed experimentally in the 3 ns interval after collision); assuming $T_i = T_e$ therefore minimises the contribution of thermal ion motions to the broadening of the IAW feature peaks. For the lower bound, we assume that $\Delta u \approx c_{\mathrm{s}} \min\left(\Delta n_e/\bar{n}_e\right)$, where the minimum is calculated over all Thomson scattering measurements of Δn_e subsequent to collision and c_{s} at later times is calculated assuming the previously discussed lower bound on the electron temperature. This bound is an underestimate of the turbulent velocity, because any cooling of the plasma at later times would result in an increased Mach number and thus increased density perturbations. Evaluating these bounds gives $40\,\mathrm{km/s} < u_{rms} < 120\,\mathrm{km/s}$ at later times: in other words, stochastic motions are maintained at later times, although those motions could be decaying in magnitude.

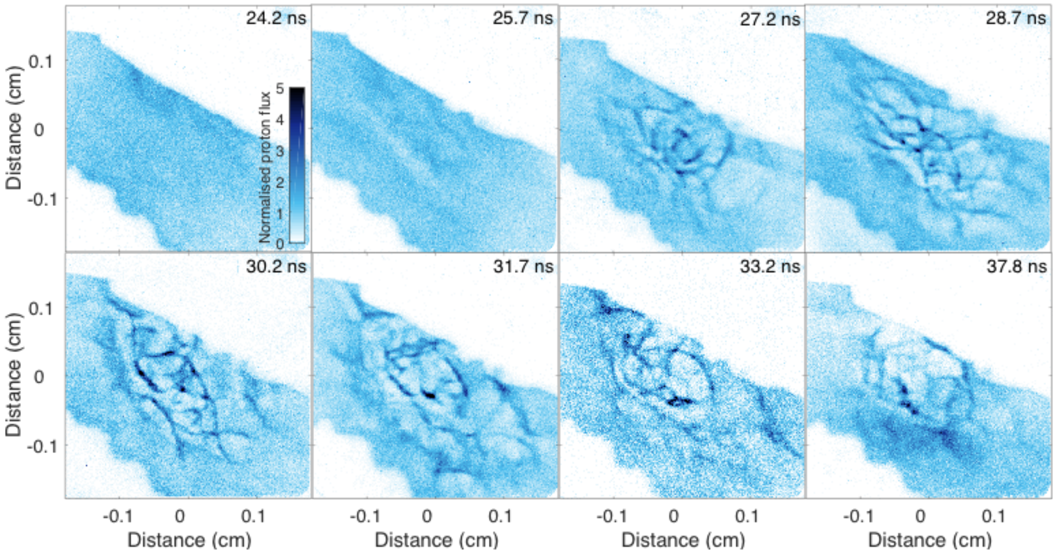

Figure 4.14: 15.0 MeV proton images of interaction-region plasma. Each image is approximately 300 × 300 pixels, with an effective pixel size of 12 μm; by comparison, the proton source size is $\sim$40 μm. The parameters of the imaging set-up are as follows: the distance r_i from the proton source to the centre of the target is $r_i = 1\,\text{cm}$, and the distance from the proton source to the detector is 28 cm. The magnification of the imaging set-up is thus ×28; all images are again presented with the magnification removed. The grid outline evident on the bottom left of each image is grid A and the top-right grid B. The mean proton flux Ψ_0 per pixel in these images is $\sim$ 50 protons per pixel; the signal-to-noise ratio is thus $\sim$ 14%.

4.5 Proton imaging diagnostic

The proton-imaging diagnostic was again implemented by imploding a D^{3}He capsule, whose specification was very similar to the previous OMEGA experiment, but with two key differences: the capsule was coated in a thin layer of aluminium and the laser-beam configuration altered so that each beam had a reduced energy of 270 J per beam but with a (shorter) 0.6 ns pulse length. The 15.0 MeV proton images for our experiment – presented in a time sequence – are shown in Figure 4.14. Proton images before the formation of the interaction-region plasma (Figure 4.14, top, far-left) show little in the way of structure at the centre of the grids, which is consistent with the absence of significant magnetic fields. Around the time at which the interaction region has formed, a moderate evacuation of proton flux is observed in a central region between the grids (Figure 4.14, top, mid-left), with characteristic magnitude Ψ similar to the mean proton flux Ψ_0: $|\Psi - \Psi_0| \lesssim 0.3\Psi_0$. By contrast, in all

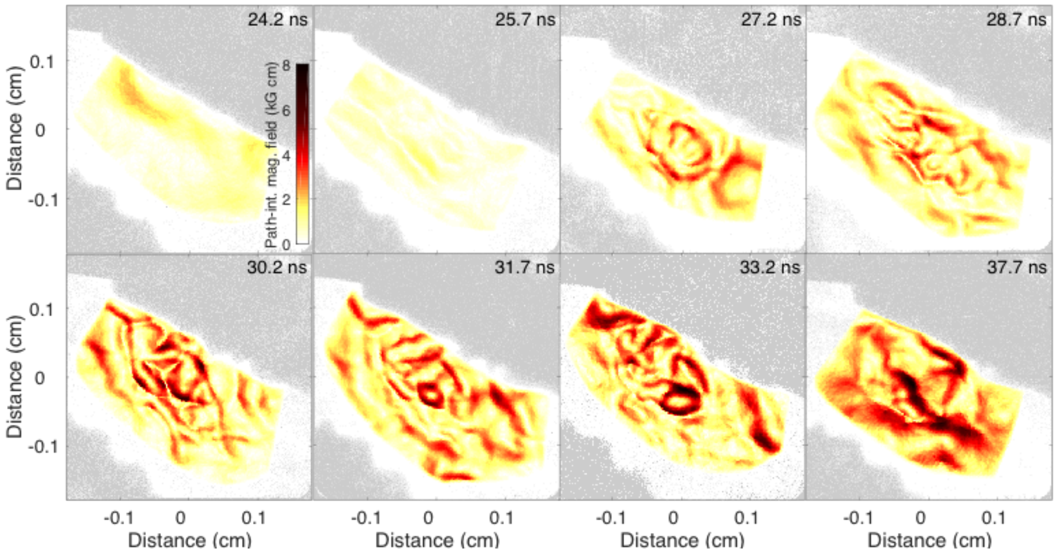

Figure 4.15: Path-integrated magnetic fields in interaction-region plasma. In each image, the magnitude of the path-integrated perpendicular magnetic field is shown; the output of the field-reconstruction algorithm is in fact two-dimensional. The method for applying the field-reconstruction algorithm is the same as described in Section 3.1.1.

subsequent proton images (beginning at times $t \gtrsim 27.2\,\mathrm{ns}$), order-unity variations in proton flux are measured ($|\Psi - \Psi_0| \gtrsim \Psi_0$) whose structure and position is highly stochastic – see Figure 4.14b for an example. Such a pronounced change is consistent with a significant alteration to the magnetic field's morphology.

Further analysis is again performed by reconstructing the path-integrated perpendicular magnetic field experienced by the imaging proton beam directly from the measured proton image using the field-reconstruction algorithm outlined in Chapter 2 (and 3). The results of the algorithm applied to the proton images shown in Figure 4.14 are presented in Figure 4.15. The strength and morphology of the reconstructed path-integrated fields after the collision are quite distinct from those at collision, with peak values in the latter case reaching $\sim$ 8 kG cm, and randomly orientated filamentary structures being evident.

Having determined the path-integrated magnetic field, the requisite approach for estimating the characteristic magnetic field strengths and structure sizes once again depends on the underlying nature of the magnetic field structure. The path-integrated field structures evident at earlier times (in particular, Figure 4.15, top, mid-left) are non-stochastic. Thus, the simplest way of estimating the average strength of magnetic fields in the interaction region is to repeat the approach taken in Section 3.1.1: calculate the mean value of the path-integrated perpendicular magnetic field and divide by the path length of the protons through the interaction region. We carry out this calculation for the data from this experiment by first evaluating $\langle | \int \mathrm{d}^2\mathbf{x}\, \mathbf{B}_\perp | \rangle$ in three square regions (see Figure 4.16a, and the caption for their precise dimensions), and determining the mean value (and errors) across the three regions. We then estimate l_z using our measurement of the average interaction-region width l_n derived from the X-ray imaging diagnostic (see Figure 4.7c), combined with the known angle $\theta_p = 55^\circ$ of the proton beam through the interaction region (as compared to the line-of-centres): it follows that $l_z \approx l_n / \sin(55^\circ) \approx 1.7 l_n$. Finally, we estimate $\langle B \rangle$ via $\langle B \rangle \approx \langle | \int \mathrm{d}^2\mathbf{x}\, \mathbf{B}_\perp | \rangle / l_z$; we obtain $\langle B \rangle \approx 5\,\mathrm{kG}$.

However, such an estimate implicitly makes several assumptions about the nature of the underlying structure of the (non-stochastic) magnetic field, which need to be checked. First, components of the magnetic field parallel to the path of the proton-imaging beam are assumed to be negligible compared to perpendicular components. Second, the estimate presupposes that the path-integrated field does not change sign along the path. To check these assumptions, we follow a standard method for analysing proton images of non-stochastic magnetic fields (Sarri et al. 2012, Kugland et al. 2013), and consider parametrised models of known three-dimensional magnetic field structures. To assist in finding such a model for our experimental data, we note that the largest component of the path-integrated field at 25.7 ns is predominantly orientated perpendicularly to the direction of the line-of-centres projected onto the proton image (Figures 4.16b and 4.16c show this component and its alternative respectively). As we show presently, the observed structure at the point of maximum path-integrated field strength – which is oscillatory in the parallel direction, and elongated in the perpendicular direction – can be shown to be consistent with the presence of two 'cocoon' structures with oppositely signed azimuthal magnetic fields, with symmetry axis parallel to the line-of-centres.

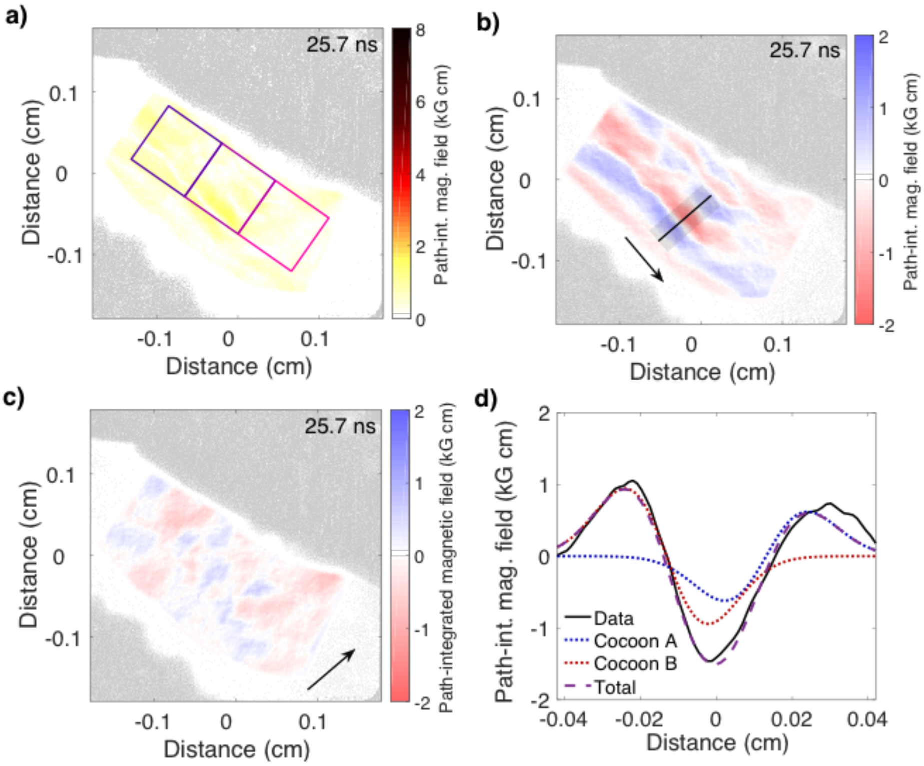

Figure 4.16: Path-integrated magnetic fields at interaction-region-plasma coalescence. **a)** Magnitude of path-integrated perpendicular magnetic field 25.7 ns after drive-beam pulse initiation. The three square regions in which the average path-integrated field is evaluated have an edge length of 800 μm, and are angled at 35° to the horizontal axis of the path-integrated field map. The centre of the middle square region corresponds to the centre of the proton image. **b)** Component of the path-integrated magnetic field in the direction perpendicular to the projected line-of-centres. The component is calculated from the full (two-dimensional) perpendicular path-integrated magnetic field. The arrow indicates the (positive) direction of the chosen path-integrated field component. **c)** Component of the path-integrated magnetic field in the direction parallel to the projected line-of-centres **d)** One-dimensional lineout of path-integrated field component given in b) (black, solid line) calculated by averaging the semi-transparent rectangular region denoted in a) across its width, along with model (4.18) using optimised parameters $B_0^+ b = -0.72\,\mathrm{kG}$ cm, $B_0^- b = 0.47\,\mathrm{kG}$ cm, $a = 270\,\mu$m, and $l_c = 131\,\mu$m. The total contribution is plotted (purple, dashed), as well as the individual contributions from the cocoon nearer grid A (blue, dotted), and nearer grid B (red, dotted).

A particularly simple model of a single cocoon structure is provided by (Kugland et al. 2012): in this model, the magnetic field $\mathbf{B}$ is given by

$$\mathbf{B} = B_0 \frac{r}{a} \exp\left(-\frac{r^2}{a^2} - \frac{z^2}{b^2}\right) \mathbf{e}_\phi\,, \tag{4.11}$$

where (r, ϕ, z) is a cylindrical coordinate system with symmetry axis z, B_0 is a characteristic magnetic field strength (related to the maximum field strength $B_{\max}$

via $B_0 = B_{\rm max}\sqrt{2}\exp{[1]}$), a the characteristic perpendicular size of the cocoon, b the characteristic parallel size of the cocoon, and $\mathbf{e}_\phi$ the azimuthal unit vector. Kugland et al. (2012) shows that the path-integrated magnetic field associated with such a structure when viewed at angle θ with respect to z axis is

$$\begin{aligned} \int \mathrm{d}s\, B_x &= \frac{B_0 a^2 b\sqrt{\pi}\cos\theta}{d^2}\frac{y}{d}\exp\left(-\frac{x^2}{a^2}-\frac{y^2}{d^2}\right), \qquad (4.12) \\ \int \mathrm{d}s\, B_y &= -\frac{B_0 a b\sqrt{\pi}\cos\theta}{d}\frac{x}{a}\exp\left(-\frac{x^2}{a^2}-\frac{y^2}{d^2}\right), \qquad (4.13) \end{aligned}$$

where

$$d \equiv \sqrt{a^2\cos^2\theta + b^2\sin^2\theta}\,. \qquad (4.14)$$

Here, the two-dimensional Cartesian coordinate system (x, y) is chosen to be perpendicular to the viewing direction, with basis vectors satisfying $\hat{\mathbf{x}}\cdot\hat{\mathbf{z}} = 0$, $\hat{\mathbf{y}}\cdot\hat{\mathbf{z}} \neq 0$. Motivated by the geometry of our experiment, we further assume that the perpendicular extent of the cocoon structures is much greater than the parallel extent i.e. $a \gg b$; then, it follows that for angles θ such that $\pi/2-\theta \gg b/a$, $d \approx a\cos\theta$. For our experiment, $\theta \approx 54^\circ$, and so $d \approx a/\sqrt{3}$. Under these assumptions, equations (4.12) and (4.13) become

$$\begin{aligned} \int \mathrm{d}s\, B_x &\approx 3B_0 b\sqrt{\pi}\frac{y}{a}\exp\left(-\frac{x^2}{a^2}-3\frac{y^2}{a^2}\right), \qquad (4.15) \\ \int \mathrm{d}s\, B_y &\approx -B_0 b\sqrt{\pi}\frac{x}{a}\exp\left(-\frac{x^2}{a^2}-3\frac{y^2}{a^2}\right). \qquad (4.16) \end{aligned}$$

We conclude that in such a model the path-integrated field is indeed elongated in the x direction (which by definition is precisely the direction perpendicular to the projected-line-of-centres), and for $x \lesssim y$ the path-integrated perpendicular magnetic field is also predominantly in the x direction.

The magnetic field associated with a double-cocoon configuration takes the form

$$\begin{aligned}\mathbf{B} &= \mathbf{B}^{+}+\mathbf{B}^{-} \\ &= \left[B_0^{+}\exp\left(-\frac{(z+\ell_c)^2}{b^2}\right)+B_0^{-}\exp\left(-\frac{(z-\ell_c)^2}{b^2}\right)\right]\frac{r}{a}\exp\left(-\frac{r^2}{a^2}\right)\mathbf{e}_{\phi}\,, \quad (4.17)\end{aligned}$$

where $\mathbf{B}^{+}$ is the magnetic field of the cocoon centred at $z=-\ell_c<0$ (and B_0^{+} its magnetic field strength), and $\mathbf{B}^{-}$ is the magnetic field of the cocoon centred at $z=\ell_c>0$ (and B_0^{-} its magnetic field strength). Under the assumptions previously discussed for a single cocoon, the x component of the path-integrated magnetic field associated with the double-cocoon configuration is

$$\begin{aligned}\int \mathrm{d}s\, B_x &\approx 3b\sqrt{\pi}\exp\left(-\frac{x^2}{a^2}\right) \\ &\quad\times\left[B_0^{+}\frac{y+\tilde{\ell}_c}{a}\exp\left(-3\frac{(y+\tilde{\ell}_c)^2}{a^2}\right)\right. \\ &\qquad\left.+B_0^{-}\frac{y-\tilde{\ell}_c}{a}\exp\left(-3\frac{(y-\tilde{\ell}_c)^2}{a^2}\right)\right], \quad (4.18)\end{aligned}$$

where $\tilde{\ell}_c \approx \sqrt{2}\ell_c/\sqrt{3}$. Having finally derived a model for the path-integrated magnetic field (with four free parameters: $B_0^{+}b$, $B_0^{-}b$, a and ℓ_c), we compare it with a lineout across the strongest path-integrated magnetic field structure (see Figure 4.16b). Figure 4.16d shows the lineout, as well as the model with an optimised fit: $B_0^{+}b = -0.72 \pm 0.05\,\mathrm{kG\ cm}$, $B_0^{-}b = 0.47 \pm 0.05\,\mathrm{kG\ cm}$, $a = 270 \pm 19\,\mu\mathrm{m}$, and $\ell_c = 131 \pm 9\,\mu\mathrm{m}$ (here, the errors in the model parameters correspond to the 95% confidence intervals for each parameter). The agreement of the model with these parameters is reasonable, with an adjusted R-squared value of 0.97. As a further reality check, we calculate the predicted one-dimensional profile of proton flux associated with our model, and compare the result to a one-dimensional lineout calculated directly from the relevant proton image in the same region as was used to determine the experimental path-integrated field profile (see Figure 4.17a and Figure 4.17b); we find that the predicted profile is a close match to the experimental data.

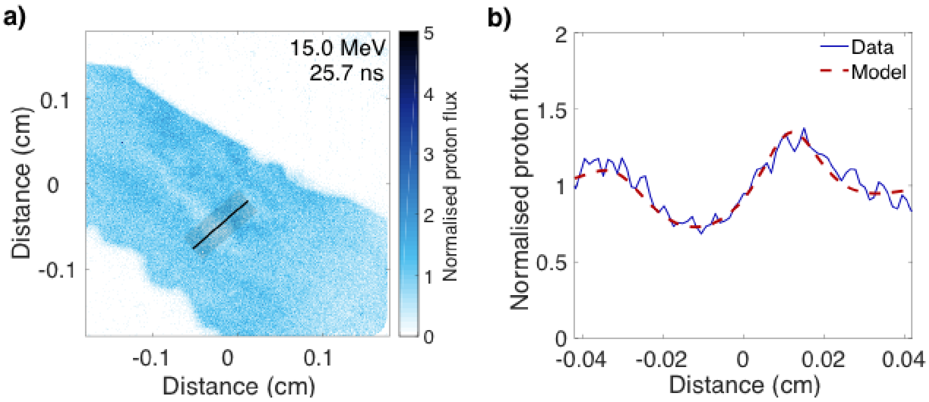

Figure 4.17: Validating double-cocoon model for magnetic field at interaction-region coalescence. a) 15.0 MeV proton image from which Figure 4.16a is calculated, portrayed with semi-transparent rectangular region. **b)** One-dimensional lineout normalised proton flux (blue, solid line) calculated by averaging semi-transparent rectangular region denoted in b) across its width, along with one-dimensional prediction from model (4.18) using the optimised parameters given in the caption of Figure 4.16.

Having obtained a satisfactory model for the magnetic field, we are now able to address the two assumptions implicitly made in the original estimate of the characteristic magnetic field strength at interaction-region coalescence. First, inside the rectangular region to which we have applied our model, the magnetic field is predominantly in the x direction, and so the component parallel to the protons' path is indeed small. Second, due to the particular angle of imaging, the B_x components of the opposing cocoon structures add constructively rather than destructively at all positions. Thus, we conclude that the assumptions we made were reasonable (at least, for the strongest path-integrated structure). We note that the mean magnetic field strength associated with the double-cocoon configuration is $\sim 7\,\mathrm{kG}$, which is consistent with our previous estimate.

Unfortunately, the full three-dimensional structure associated with the double-cocoon magnetic field configuration cannot be recovered from the path-integrated field alone: this is because the latter only determines the path-integrated field strengths $B_0^+ b$ and $B_0^- b$, rather than B_0^+, B_0^- and b separately. To overcome this underdetermination, we invoke the likely origin of the fields (the Biermann battery mechanism), and assume that $b \approx \lambda_{\mathrm{T}}/2$, where λ_{T} is the thermal precursor length (Graziani et al. 2015). This quantity denotes the typical length scale of elec-

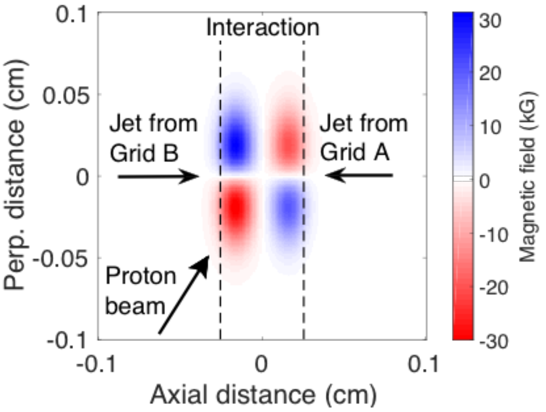

Figure 4.18: 3D structure of magnetic fields at interaction-region-plasma coalescence. a) Slice-plot (in plane characterised by basis vectors $\hat{\mathbf{y}}$ and $\hat{\mathbf{z}}$) of B_x component associated with three-dimensional double-cocoon magnetic-field configuration (4.17), with optimised model parameters $B_0^+ b = -0.72\,\mathrm{kG\ cm}$, $B_0^- b = 0.47\,\mathrm{kG\ cm}$, $a = 270\,\mu\mathrm{m}$, and $\ell_c = 131\,\mu\mathrm{m}$, and $b = 0.01\,\mathrm{cm}$. The width of the plotted interaction region is obtained from the X-ray image recorded at the equivalent time (c.f. Figure 4.3c).

tron temperature gradients at the shocks demarcating the interaction-region plasma (see Section 4.6); for our experimental parameters, we find $\lambda_{\mathrm{T}} \approx 200\,\mu\mathrm{m}$, and so $b \approx 100\,\mu\mathrm{m}$. We thereby obtain $B_0^+ \approx 72\,\mathrm{kG}$ and $B_0^- \approx 47\,\mathrm{kG}$. A slice plot of the resulting three-dimensional double-cocoon structure is shown in Figure 4.18. The maximum field strength of the configuration is $B_{\max} \approx 31\,\mathrm{kG}$. For reference, the position of the interaction region observed from the X-ray imaging diagnostic is plotted; our model is consistent with the measured fields being inside the interaction region. We note that the two critical assumptions initially made to estimate the magnetic field strength – weak magnetic fields parallel to the direction of the proton beam, and no cancellation of field along the proton's path – are self-evident from the three-dimensional structure of the magnetic field.

For the stochastic path-integrated magnetic fields which emerge subsequent to collision, a different approach is required: as in Section 3.1.1, we again assume isotropic, homogeneous statistics of the stochastic magnetic field in the interaction-region plasma, which in turn allows for the extraction of the RMS magnetic field strength B_{rms} directly from the path-integrated field spectrum E_{path} via

$$B_{rms} = \left[\frac{2}{\pi \ell_z} \int \mathrm{d}k \, k E_{\text{path}}(k)\right]^{1/2} . \tag{4.19}$$

This equation arises from substituting equation (3.4) for the magnetic-energy spectrum into (3.6) for the magnetic-energy density. We can subsequently calculate the characteristic correlation length ℓ_B of the stochastic magnetic field via equation (2.13), which can be rewritten in terms of the path-integrated perpendicular magnetic field as

$$\ell_B = \frac{1}{\ell_z B_{rms}^2} \left(\int \mathrm{d}^2\mathbf{x} \, \mathbf{B}_\perp\right)^2_{\text{rms}} . \tag{4.20}$$

We focus on measuring B_{rms} and ℓ_B rather than the magnetic-energy spectrum for the reasons discussed in Chapter 3: in particular, the likely presence of strong, small-scale magnetic fields leading to self-intersection of the imaging beam, in turn meaning that the magnetic-energy spectrum is not robustly measured by the proton-imaging diagnostic for this experiment.

To systematise our analysis of the data for this experiment, we consider the same three fixed regions of the path-integrated magnetic field images introduced in Figure 4.16a, and calculate B_{rms} and ℓ_B for those particular regions (see Figure 4.19a). Such an approach also allows us to test the assumption that the stochastic magnetic fields are both homogeneous and isotropic. Figure 4.19 shows the magnetic-energy spectra calculated using equation (3.4) for the three chosen regions in the case of path-integrated fields calculated at 27.2 ns. Apart from at the largest scales, we find that the three spectra match closely, supporting our original assumption. The isotropy assumption is tested in Figure 4.19c. In each box, we calculate the magnetic-energy spectra both for wavenumbers predominantly parallel to the projected line-of-centres, and for wavenumbers predominately perpendicular to the projected line-of-centres. The results are then combined to obtain averaged parallel and perpendicular spectra. We find that both spectra agree within the uncertainty of

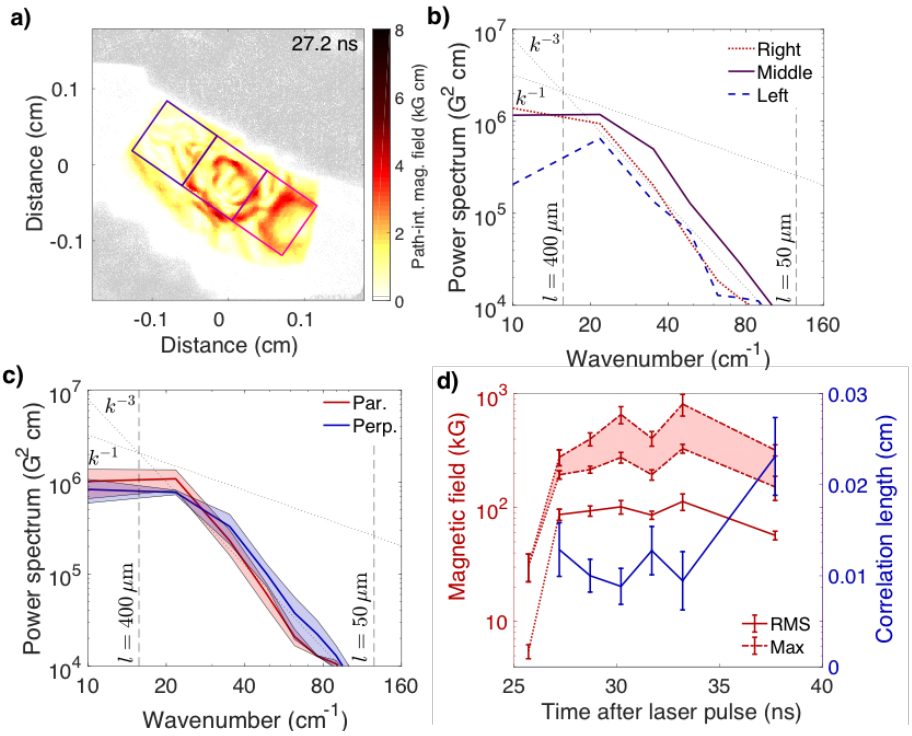

Figure 4.19: Magnetic fields subsequent to interaction-region-plasma coalescence. **a)** Path-integrated perpendicular magnetic field determined from the field-reconstruction algorithm applied to the 15.0 MeV proton image obtained at 27.2 ns, plotted with the boundaries of fixed square regions used for calculating B_{rms} and ℓ_B. The dimensions and positioning of these regions is the same as in Figure 4.16. **b)** Test of homogeneity of stochastic magnetic field statistics. The magnetic-energy spectra associated with the left, middle and right square regions are calculated using (3.4), along with the nominal resolution of the proton-imaging diagnostic, and the grid scale. The plotted k^{-3} is included for reference, but does not have physical significance. **c)** Test of isotropy of stochastic magnetic field statistics. For each square region, the magnetic-energy spectrum associated with predominantly parallel wavenumbers is calculated by determining the spectral slope from magnetic-field Fourier components with $k_{\|} > k_{\perp}$, and vice versa for the magnetic-energy spectrum associated with predominantly perpendicular wavenumbers. Mean parallel and perpendicular spectra are subsequently obtained by averaging the results from each region (the errors are determined similarly). **d)** RMS magnetic field strength (red, solid) and maximum magnetic field bounds (red, dashed), over time, with correlation length ℓ_B (blue). We emphasise that the mean and maximum field strengths at 25.7 ns (red, dotted) are calculated differently to the other times, on account of the non-stochastic field structure (see Figure 4.16a).

the measurement. This validates the isotropy assumption because, from the symmetry of our experiment, any anisotropy would manifest itself with respect to the line-of-centres and would therefore be evident in our images.

Having validated the assumptions underlying our method, we now calculate the mean values of B_{rms} and ℓ_B arising from each path-integrated field image, and the errors on those measurements. The results of this calculation applied to the full time-sequence of proton images Figure 4.15 are shown in Figure 4.19d. B_{rms} is found to jump significantly in a 1.5 ns interval subsequent to collision, reaching a peak value $\sim$ 120 kG, before decaying quite significantly, to around $\sim$ 70 kG. The correlation length ℓ_B obtains characteristic values $\ell_B \approx 0.01\,\mathrm{cm}$ for all measured times, save those at later times, where ℓ_B increases somewhat.

We can also calculate reasonable upper and lower bounds of the maximum magnetic field strength obtained in the stochastic field via two distinct methods. For the lower bound, we note that by the central limit theorem, the kurtosis of the path-integrated magnetic field will always be smaller than the actual magnetic field itself. Therefore, the ratio between the maximum path-integrated field and the RMS path-integrated field will always be smaller than the equivalent ratio for the magnetic field: in other words, a reasonable lower bound is $B_{\mathrm{max,l}} = B_{rms}(\int \mathrm{d}^2\mathbf{x}\,\mathbf{B}_\perp)_{\mathrm{max}}/(\int \mathrm{d}^2\mathbf{x}\,\mathbf{B}_\perp)_{\mathrm{rms}}$. The upper bound is derived using the approach previously employed in Section 3.5: we assume that the maximum measured path-integrated magnetic fields are obtained while associated imaging protons crossed just a single magnetic structure: $B_{\mathrm{max,u}} = (\int \mathrm{d}^2\mathbf{x}\,\mathbf{B}_\perp)_{\mathrm{max}}/\ell_B$. The results of these bounds are shown in Figure 4.19d, and at the time corresponding to maximal B_{rms}, we find $310\,\mathrm{kG} < B_{\mathrm{max}} < 810\,\mathrm{kG}$.

In addition to providing a time-resolved characterisation of the evolution of the stochastic magnetic fields in the plasma, the proton images from the experiment also demonstrate the degree of robustness of the key result: the amplification of magnetic fields to dynamically significant values. More specifically, the eddy turnover time on the scale $\tilde{\ell}_B$ of magnetic structures corresponding to the peak of the reconstructed magnetic-energy spectrum is $\sim$ 3 ns, which is greater than the 1.5 ns time interval between consecutive proton images; thus, the statistics of stochastic magnetic fields in the plasma should in principle not change significantly over the 1.5 ns time interval. It thereby follows that if the characteristic values of B_{rms} and ℓ_B obtained in the experiment are robust, then one would expect consistency between the results obtained from the analysis of proton images separated by 1.5 ns intervals. Employing

Figure 4.19d to assess this consistency (or lack of it), we see that in the time interval between 27.2 ns and 33.2 ns, the differences in RMS field strengths and correlation lengths between consecutive images are much smaller than the actual values themselves, although a ∼20% dip in the measured field strength at 31.7 ns (and a similar increase in the correlation length) demonstrates the degree of uncertainity in our key result.

4.6 Discussion

We conclude that similarly to the first OMEGA experiment, the new experiment does indeed result in a region of plasma which manifests stochastic motion on a range of scales, and quite possibly turbulent motion. In spite of some uncertainty about the late-time physical properties of the turbulent plasma, there exists a 5 ns time window starting from the formation of the interaction region during which the plasma state is throughly characterised. In this window, we find that the plasma is fairly well described as being classical and collisional ($\lambda_e \approx 10\,\mu$m, $\lambda_{\mathrm{CC}} \approx 0.6\,\mu$m, $\lambda_{\mathrm{HC}} \approx 16\,\mu$m), and so transport coefficients can be estimated (see Tables 4.1 and 4.2) using collisional transport theory (Braginskii 1965, Colvin and Larsen 2013, Cross et al. 2014, Huba 1994). More specifically, momentum transport in the plasma is dominated by hydrogen ions, on account of their long mean-free-path compared to carbon ions (Simakov and Molvig 2014, 2016), while heat transport is dominated by electrons. We assume the conventions given in Schekochihin et al. (2004c) for the resistive and viscous dissipation scales.

The time history of both the fluid Reynolds number Re and the magnetic Reynolds number Rm in the interaction-region plasma is shown in Figure 4.20a. Prior to the formation of the interaction-region plasma, Re $\approx 1,200$, which exceeds Rm ≈ 200. However, after the jets coalesce, the rapid collisional shock heating of both ions and electrons simultaneously decreases the resistivity and enhances the viscosity, leading to a switched ordering of dimensionless numbers: Re ≈ 200, and Rm $\lesssim 900$. Both

Quantity	Value
Carbon/hydrogen charges (M_{C},M_{H})	12, 1
Average atomic weight ($\langle M \rangle$)	6.5
Carbon/hydrogen charges (Z_{C},Z_{H})	6, 1
Mean ion charge ($\langle Z \rangle$)	3.5
Effective ion charge (Z_{eff})	5.3
Electron temperature (T_e)	460 eV
Ion temperature (T_i)	580 eV
Electron number density (n_e)	1.2×10^{20} cm^{-3}
Carbon number density (n_{C})	1.7×10^{19} cm^{-3}
Hydrogen number density (n_{H})	1.7×10^{19} cm^{-3}
Bulk velocity ($\bar{u}_{\mathrm{in}}$)	1.9 $\times 10^7$ cm/s
Turbulent velocity (u_{rms})	1.1 $\times 10^7$ cm/s
Outer scale (L)	0.04 cm
RMS magnetic field (B)	90 kG
Maximum magnetic field (B)	250 kG
Adiabatic index (γ_I)	5/3

Table 4.1: Summary of measured plasma parameters related to the experiment at ~ 27 ns after the drive-beam laser pulse is initiated. The effective ion charge (which appears in various physical parameters) is given by $Z_{\mathrm{eff}} = (Z_{\mathrm{C}}^2 + Z_{\mathrm{H}}^2)/(Z_{\mathrm{C}} + Z_{\mathrm{H}})$.

the viscosity and resistivity are sensitive functions of ion and electron temperature respectively ($\nu \propto T_i^{5/2}$, $\eta \propto T_e^{-3/2}$), and so even the moderate cooling observed in the 5 ns interval after peak temperatures are reached results in approximate equalisation of both parameters (Re $\approx$ Rm $\approx$ 500). At very late times, the potential heating effects associated with the external diagnostics lead to significant uncertainty as to the values of Re and Rm in the absence of any diagnostic perturbation. With temperatures matching those measured directly by the Thomson scattering diagnostic, Re $\approx$ 750, Rm $\approx$ 300; however, assuming instead temperatures close to the (previously discussed) lower bound $T_e \approx T_i \approx 50\,$eV, the fluid Reynolds number is over two orders of magnitude larger (Re $\approx 10^5$), while Rm $\approx$ 20.

We note that for times $\lesssim 30\,$ns, the characteristic velocity of stochastic motion is smaller than the in-flow velocity, and thus the fluid Reynolds number Re$_L$ and magnetic Reynolds number Rm$_L$ of the driving-scale stochastic motions are somewhat reduced in the interval of interest: Re$_L \approx 120-600$, and Rm$_L \approx 250-450$. Since the

Quantity	Formula	Value
Coulomb logarithm ($\log\Lambda$)	$23.5 - \log n_e^{1/2} T_e^{-5/4} - \sqrt{10^{-5} + \frac{(\log T_e - 2)^2}{16}}$	~ 7
Mass density (ρ)	$1.7 \times 10^{-24} \left(M_{\mathrm{C}} n_{\mathrm{C}} + M_{\mathrm{H}} n_{\mathrm{H}}\right)$	3.7×10^{-4} g cm^{-3}
Debye Length (λ_{D})	$7.4 \times 10^2 \frac{T_e^{1/2}}{n_e^{1/2}} \left[1 + \frac{T_e}{T_i} Z_{\mathrm{eff}}\right]^{-1/2}$	6.3×10^{-7} cm
Sound speed (c_{s})	$9.8 \times 10^5 \frac{[(\langle Z\rangle+1)\gamma_I T_e]^{1/2}}{\langle M\rangle^{1/2}}$	2.3×10^7 cm/s
Mach number	u_{rms}/c_{s}	0.5
Plasma β	$4.0 \times 10^{-11} \frac{n_{\mathrm{e}} T_{\mathrm{e}} + (n_{\mathrm{C}} + n_{\mathrm{H}}) T_i}{B^2}$	370
Carbon-carbon mean free path (λ_{CC})	$2.9 \times 10^{13} \frac{T_i^2}{Z_C^4 n_{\mathrm{C}} \log\Lambda}$	6.2×10^{-5} cm
Hydrogen-carbon mean free path (λ_{HC})	$2.1 \times 10^{13} \frac{T_i^2}{Z_H^2 Z_C^2 n_{\mathrm{C}} \log\Lambda}$	1.6×10^{-3} cm
Electron-ion mean free path (λ_e)	$2.1 \times 10^{13} \frac{T_e^2}{Z_{\mathrm{eff}} n_e \log\Lambda}$	1.0×10^{-3} cm
Electron-carbon equilibration time ($\tau^{\varepsilon}_{\mathrm{Ce}}$)	$3.2 \times 10^8 \frac{M_C T_e^{3/2}}{Z_C^2 n_{\mathrm{C}} \log\Lambda}$	8.6×10^{-9} s
Electron Larmor radius (ρ_e)	$2.4 \frac{T_e^{1/2}}{B}$	5.7×10^{-4} cm
Carbon Larmor radius (ρ_{C})	$1.0 \times 10^2 \frac{M_{\mathrm{C}}^{1/2} T_i^{1/2}}{Z_{\mathrm{C}} B}$	1.5×10^{-2} cm
Hydrogen Larmor radius (ρ_{H})	$1.0 \times 10^2 \frac{M_H^{1/2} T_i^{1/2}}{Z_{\mathrm{H}} B}$	2.6×10^{-2} cm
Thermal diffusivity (χ)	$3.0 \times 10^{21} \frac{T_e^{5/2}}{Z_{\mathrm{eff}} n_e \log\Lambda}$	3.0×10^6 cm^2 s^{-1}
Turbulent Peclet number (Pe_L)	$u_{rms} L/\chi$	0.15
Dynamic viscosity (ζ)	$3.7 \times 10^{-5} \frac{M_{\mathrm{H}}^{1/2} T_i^{5/2}}{Z_C^2 \log\Lambda}$	1.2×10^2 g cm^{-1} s^{-1}
Kinematic viscosity (ν)	ζ/ρ	3.1×10^3 cm^2 s^{-1}
Turbulent Reynolds number (Re_L)	$u_{rms} L/\nu$	140
Viscous dissipation scale (l_ν)	$L/\mathrm{Re}_L^{3/4}$	9.8×10^{-4} cm
Resistivity (η)	$3.1 \times 10^5 \frac{Z_{\mathrm{eff}} \log\Lambda}{T_e^{3/2}}$	1.0×10^3 cm^2 s^{-1}
Magnetic Reynolds number (Rm_L)	$u_{rms} L/\eta$	380
Magnetic Prandtl number (Pr)	$\mathrm{Rm}_L/\mathrm{Re}_L$	~ 1
Resistive scale (l_η)	$L/\mathrm{Pr}^{1/2}$	6.0×10^{-4} cm

Table 4.2: Summary of relevant theoretical plasma parameters for the experiment at ~ 27 ns after the drive-beam laser pulse is initiated. The units system used for all physical quantities in the above formulas is again Gaussian CGS, except temperature expressed in eV.

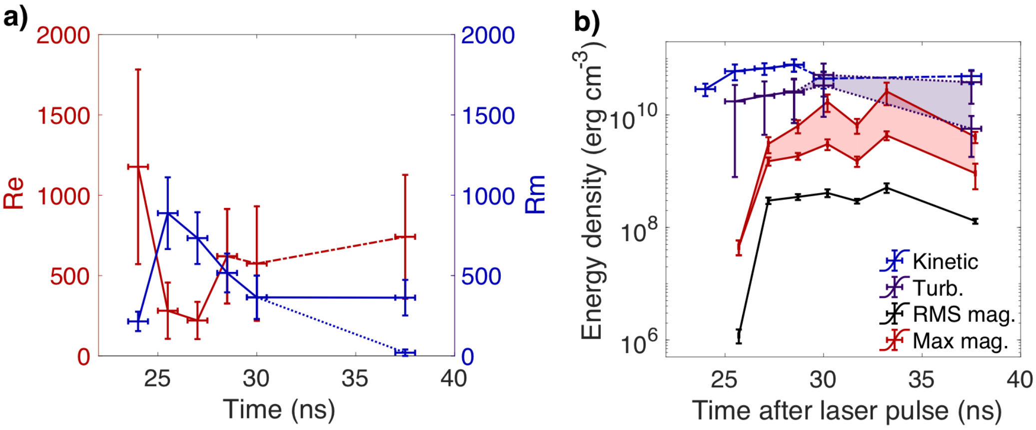

Figure 4.20: Evolution of theoretical plasma parameters. a) Evolution of the fluid Reynolds number Re (red, solid line) and magnetic Reynolds number Rm (blue, solid line) over time. Re and Rm are calculated using the formulae given in Table 4.2, though substituting u_{rms} with $\bar{u}_{\text{in}}$ in order to enable comparisons between the state of the plasma across the entire evolution of the experiment. The input plasma state variables are those measured by the Thomson scattering diagnostic; however, Re at later time (red, dash-dot) is instead calculated using an extrapolated density derived from the X-ray measurements. An estimate of Rm at later times assuming lower bound on electron temperature $T_e \approx 50\,\text{eV}$ is also shown (blue, dotted). **b)** Evolution of energy densities in the plasma-interaction region. For times $\leq 30\,\text{ns}$, the kinetic energy and turbulent kinetic energy are calculated using plasma state variables as derived from the Thomson scattering diagnostic; at later times, the density is determined using the X-ray imaging diagnostic. The bounds on the turbulent kinetic energy derive from the equivalent bounds on the turbulent velocity. The RMS and maximum magnetic energy derive from proton imaging diagnostic.

turnover time τ_L of the largest stochastic motions is $\tau_L = L/u_{rms} \approx 4\,\text{ns}$, we conclude that the experimental platform does indeed produce a region of plasma with Prandtl number Pr $\sim$ 1 which persists for the timescale over which the largest stochastic motions decorrelate. It should be emphasised that the fluid Reynolds number of the interaction-region plasma is sufficiently low that the flow will not be entirely chaotic; however, as was discussed in Section 1.1.4, fully developed turbulence is not necessary for the fluctuation dynamo to operate.

We have also measured magnetic fields over time in the interaction-region plasma, and found that stochastic magnetic fields emerge during the 5 ns time window. Having measured both the magnetic field and dynamical properties of the interaction-region plasma, we can now compare the time history of the turbulent and magnetic energy densities (see Figure 4.20b). When the interaction-region plasma initially coalesces, the turbulent kinetic energy density $\varepsilon_{\text{turb}} \equiv \rho u_{rms}^2/2 \approx 2 \times 10^{10}\,\text{erg/cm}^3$

is over four orders of magnitude larger than the average magnetic-energy density ($\varepsilon_B = B^2/8\pi \approx 1 \times 10^6\,\mathrm{erg/cm^3}$). However, 1.5 ns later, the relative magnitude of the magnetic energy is significantly larger: $\varepsilon_B/\varepsilon_{\mathrm{turb}} \approx 0.02$. As the density of the interaction-region plasma subsequently rises, both the turbulent kinetic energy and magnetic energy increase, maintaining a relative constant ratio. The upper bound on the magnetic energy at later times becomes (within error) a comparable order of magnitude to the average turbulent energy.

We attribute the origin of the initial magnetic fields to the Biermann battery mechanism acting on the jet plasma as it passes through the (just-formed) shocks demarcating the interaction region plasma; mis-aligned density and temperature gradients arise on account of this initial inhomogeneity of the jets perpendicular to the flow direction. The magnitude of this magnetic field can be estimated as

$$B \approx 10 \left[\frac{\delta n_e/n_e}{0.5}\right] \left[\frac{\delta T_e(\mathrm{eV})}{200\,\mathrm{eV}}\right] \left[\frac{L(\mathrm{cm})}{0.04\,\mathrm{cm}}\right]^{-1} \left[\frac{\bar{u}_{\mathrm{in}}(\mathrm{cm/s})}{2 \times 10^7\,\mathrm{cm/s}}\right]^{-1} \mathrm{kG}\,, \tag{4.21}$$

for δn_e the magnitude of the density profile inhomogeneity (which is assumed to be on the scale of the grid periodicity L), δT_e the temperature jump from the initial jet to the interaction region. This estimate agrees approximately with our experimentally observed initial field strengths. We note that the previous OMEGA experiment did not observe the Biermann battery field generated by the interaction-region-boundary shocks, on account of lacking time-resolved measurements of the magnetic field during collision. In the interaction-region itself, magnetic fields generated by the Biermann battery mechanism alone seem insufficient to explain the observed field strengths; this is because the turbulent Peclet number $\mathrm{Pe}_L \equiv u_{rms}L/\chi$ (for χ the thermal diffusivity) in the interaction-region plasma is small ($\mathrm{Pe}_L \approx 0.1$), and so electron temperature gradients in the interaction-region plasma are suppressed (as was also found for the previous OMEGA experiment). It therefore seems a plausible conclusion that turbulence is responsible for amplifying magnetic fields from their initial values up to dynamical strengths.

We can use the experimental data to provide a lower bound on the growth rate γ of the observed stochastic magnetic fields. Noting the field strength both at collision ($B_1 \approx 5\,\mathrm{kG}$) and 1.5 ns later ($B_2 \approx 87\,\mathrm{kG}$), we find $\gamma \gtrsim 6.7 \log{(B_2/B_1)} \times 10^8\,\mathrm{s}^{-1} \approx 1.9 \times 10^9\,\mathrm{s}^{-1} \approx 8\tau_L^{-1}$ (for τ_L the turnover time of the largest-scale stochastic motions). Thus, we conclude that the initial growth is significantly more rapid that would be expected were magnetic field amplification solely due to the largest-scale stochastic motions. Assuming Kolmogorov scaling for the velocity $u_\ell \sim u_{rms}(\ell/L)^{1/3}$ of stochastic motions at scale ℓ, it can be concluded that this rate of field growth is only consistent with stochastic motions whose characteristic scale satisfies $\ell \lesssim 20\,\mu\mathrm{m} \ll L$. Such a result validates a key prediction of fluctuation-dynamo theory that the most rapid initial growth is not caused by stochastic motions with the largest magnitude but instead those with the largest shear rate; for stochastic motions obeying Kolmogorov scalings, the most rapidly shearing motions are expected to be those at the viscous scale $\ell_\nu \approx 4\,\mu\mathrm{m}$, with growth rate $\gamma \approx \mathrm{Re}_L^{1/2}\tau_L^{-1} \approx 12\tau_L^{-1}$.

We note that the maximum measured ratio $\varepsilon_B/\varepsilon_{\mathrm{turb}} \approx 0.03$ of the magnetic energy ε_B to the turbulent kinetic energy $\varepsilon_{\mathrm{turb}}$ is somewhat smaller than that obtained for $\mathrm{Pr} \approx 1$ MHD simulations with comparable Reynolds numbers (Schekochihin et al. 2004c, Haugen et al. 2004); a similar phenomenon to that found for the previous OMEGA experiment. Simulations with $\mathrm{Pr} \approx 1$ typically find that $\varepsilon_B/\varepsilon_{\mathrm{turb}}$ is between 10% and 40% of the turbulent kinetic energy at saturation; complete equipartition of magnetic and kinetic energy is not obtained, because the magnetic field tends to have a higher degree of intermittency. In spite of this, the argument proposed in Section 3.5 attributing the discrepancy to poor effective resolution in the proton imaging diagnostic also applies here: indeed, since for the $\mathrm{Pr} \approx 1$ MHD dynamo it is anticipated that magnetic energy will be concentrated at scales closer to the resistive scale, this problem may be even more acute for this experiment. However, the time-resolved measurements from the second OMEGA experiment also reveals another potential explanation: soon after the emergence of strong, stochastic magnetic fields, the Hall parameter $\omega_H = \lambda_e/\rho_e$ attains order-unity values. It is well known that both magnetic field evolution and heat conduction is altered significantly in a plasma with magnetised electrons (Braginskii 1965); thus, we cannot rule out the possibility that the fluctuation dynamo's saturation mechanism is altered in our experiment compared to that of a bona fide MHD plasma.

In terms of how the experiments compares to astrophysically relevant plasma – in particular, the turbulent ICM – Schekochihin and Cowley (2006) provide typical parameters for both the cool cores of galaxy clusters (such as Hydra A), and surrounding hot cluster plasma. The length and time scales associated with the cluster plasma are greater than their laboratory equivalents by many orders of magnitude (for example, $L_{ICM} \approx 3 \times 10^{23}\,\mathrm{cm}$). However, it is well known that in the absence of dissipation two systems with different length and time scales can be modelled by the same governing equations (Cross et al. 2014); thus, provided the relevant dimensionless numbers which quantify dissipation in the laboratory plasma (in particular, Re_L, Pe_L and Rm_L) obey the same asymptotic hierachy as the astrophysical plasma of interest, then the results of the experiment are relevant to their astrophysical analogue. For the ICM, $\mathrm{Pe}_{L,ICM} \approx 1$, $\mathrm{Re}_{L,ICM} \approx 10 - 100$, and $\mathrm{Rm}_{L,ICM} \approx 10^{30}$. Comparing these to the experimental values, we see reasonable agreement for Re_L and Pe_L: both the laboratory and astrophysical systems are moderately turbulent (but not hugely so), and in both systems the isothermal approximation holds below the driving scale of the turbulence. The magnetic Reynolds number in the astrophysical case is much larger than the laboratory experiment; however, since the physical mechanism underpinning the $\mathrm{Pr} = \mathrm{Rm}_L/\mathrm{Re}_L > 1$ dynamo is expected to be similar to the $\mathrm{Pr} \gg 1$ dynamo (see Section 1.1.4), it might be hoped that the physics of the former would still be relevant to the latter. That being said, there do remain some significant differences between the experiment and astrophysical plasma. In particular, the underlying microphysics of the laboratory plasma places it arguably closer to a collisional MHD model than the astrophysical case; as discussed in Section 1.1.5, the strong magnetisation of both electrons and ions introduces new physics, the full ramifications of which are not understood for dynamo processes.

4.7 Conclusions

In summary, the second experiment at OMEGA facility broadly supports the results of the first: plasma undergoing stochastic motion is capable of amplifying magnetic fields up to dynamical strengths, provided the magnetic Reynolds number is large enough. The time-resolved characterisation provided by the second experiment has demonstrated that magnetic-field amplification occurs more rapidly than the turnover rate of the driving-scale stochastic motions, a result consistent with theoretical expectations. However, the experiment has also revealed two facets of the plasma's evolution hitherto not considered. First, the seed field in the interaction region is not simply magnetic field generated at the laser spots and then advected to the centre of the target; it is instead likely to be the result of the Biermann battery acting at the shocks demarcating the interaction region plasma itself. Second, the saturation of the fluctuation dynamo in our experiments may be affected by electron magnetisation effects: an effect not considered in conventional MHD fluctuation dynamo theory.

Chapter 5

Conclusions and future research

5.1 Summary of work undertaken

In this thesis we have been concerned with two laser-plasma experiments carried out on the OMEGA facility, which have investigated magnetic-field amplification in turbulent plasmas and in particular the fluctuation dynamo.

Chapter 1 details the first of the two experiments, which consisted of the collision of two rear-side-blowoff plasma jets with profiles pre-modified by misaligned grids: evidence for both the presence of turbulence and the necessary theoretical plasma conditions for the fluctuation dynamo to operate were presented. Key to demonstrating the actual existence and efficacy of the dynamo (and thus realise the scientific goals of the experiment) was the ability to measure accurately stochastic magnetic fields; yet with the analysis techniques available at the time when the experiment was initially conducted, such measurements could not be performed.

In order to overcome this deficiency, a new analysis technique for recovering the magnetic-energy spectrum of stochastic magnetic fields using a proton imaging diagnostic (a commonly employed diagnostic in laser-plasma experiments) was developed in Chapter 2 using both pen-and-paper theory, and numerical simulations with test stochastic magnetic fields. It was found that recovering the magnetic-energy spectrum is possible if the proton imaging set-up obeys certain constraints:

in particular, that gradients in deflections of the imaging proton beam must not be so large as to cause the beam to self-intersect prior to reaching the detector. Four 'contrast' regimes of proton imaging were defined – linear, non-linear injective, caustic and diffusive – in which the underlying relationship between the path-integrated stochastic magnetic field and the associated distributions of detected proton flux are qualitatively distinct; the magnetic-energy spectrum can only be recovered in the first two regimes. Further limits on the technique placed by both theoretical and experimental considerations were discussed in some depth, so that the technique's proper application could be understood.

In Chapter 3, the analysis technique was applied to proton-imaging data arising from the initially presented fluctuation-dynamo OMEGA experiment. Quantitative estimates of the initial magnetic field strengths at collision, and then after it, were obtained. The quality of these measurements was successfully verified using a range of appropriate tests. For the strong stochastic magnetic fields observed after collision the magnetic-energy spectrum was derived; however, subsequent validations using FLASH simulations as a test case illustrated that the high-wavenumber component of the spectrum was not robustly determined for these particular experiments. In spite of this limitation, the magnetic field strength determined by the analysis technique demonstrated that a fluctuation dynamo was indeed likely to be realised in the experiment: the first time this has been done in the laboratory.

Finally, a second experiment on the OMEGA facility was described in Chapter 4. This experiment attempted to provide a time-resolved characterisation of dynamo-generated magnetic fields using a slightly modified target to that employed to the first experiment. Imaging of self-emitted X-rays was used to provide information about the collision between the two jets, and the subsequent formation of a plasma undergoing stochastic motion. Analysis of Thomson-scattering data provided detailed information about the plasma state over the course of the experiment. Analysis of proton-imaging data – again using the previously developed technique – demonstrated that amplification of magnetic fields occurs much more rapidly than the timescale of the largest-scale stochastic motions in the plasma. This observation provided experimental evidence for the theoretical hypothesis that magnetic-field amplification via the fluctuation dynamo occurs most rapidly at small, rather than large, scales.

5.2 Future research paths

There are various ways in which the work carried out for this thesis could be extended. Firstly, the study of the proton imaging of stochastic magnetic fields conducted in Chapter 2 is by no means exhaustive. To start with, magnetic stochasticity is often not isotropic. Recent laser-plasma experiments investigating Weibel and filamentation instabilities (Fox et al. 2013, Huntington et al. 2015) observed elongated coherent magnetic structures with stochastic variation in the plane perpendicular to the colliding flows, but with approximate uniformity in the parallel direction. The assumption of three-dimensionally isotropic statistics is not appropriate for such experiments; however, adapting the analysis carried out in this chapter relating the deflection-field spectrum (obtained from proton images) to the magnetic-energy spectrum should be possible in principle, and would be of scientific interest. This would be an appropriate question to be addressed separately and would ideally include numerical tests with simulations of Weibel-like perturbations.

In Chapter 2, we focused on determining the magnetic-energy spectrum from proton images: but the spectrum is not the only statistical quantity of interest for non-Gaussian fields. Probing the helicity or intermittency of stochastic magnetic fields is likely to be possible with a proton imaging diagnostic; doing so could help to address questions about the detailed structure of fields generated by the small-scale fluctuation dynamo (Schekochihin et al. 2004c) or the saturated state of the Weibel instability (Huntington et al. 2015).

The techniques currently proposed for analysing caustic and diffusive regime images are significantly less comprehensive than other regimes. However, work carried out in the context of optics suggests that approaches such as statistical topology could be used to directly analyse caustic features more methodically, particularly with additional prescriptions for the sort of stochastic field being investigated (Berry and Upstill 1980). In the diffusive regime, investigating the inversion of a diffusive model of proton imaging in order to extract the diffusion coefficient also promises to be a fruitful avenue of research. It should be noted that there is a practical motivation for exploring these problems: recent laboratory-astrophysics experiments creating stochastic magnetic fields at the National Ignition Facility (USA) seem to result in proton images which fall squarely into the diffusive regime (work yet to be published, but see Rygg et al. 2015).

On the topic of fluctuation-dynamo experiments, there still remain a number of potential future experiments which would strengthen the claims outlined in this thesis. First of these would be an experiment which convincingly demonstrated that the saturated RMS field strengths found in these experiments does indeed correspond to dynamical significance. This could be realised by increasing the initial seed field strength in the experiment using, for example, a pulsed magnetic field generator (Fiksel et al. 2015). If the previously measured saturated states are indeed dynamically significant, the magnetic field strength measured in this state should be independent of the seed field strength. Another experiment could attempt to pin down the threshold value of $\mathrm{Rm_c}$ at which the fluctuation dynamo becomes operative by performing a parameter scan over different Rm. Finally, there exist a number of theoretical uncertainties concerning dynamo processes which future experiments could potentially address. One such example another would be the conclusive demonstration of dynamo action in a weakly collisional plasma. Several experiments addressing these questions are currently in the design or post-shot-day-analysis phases.

All being said and done, the theory of proton imaging of stochastic magnetic fields outlined in Chapter 2 provides a helpful conceptual framework for approaching analysis of stochastic magnetic fields using proton imaging, as well as enabling more information to be extracted from experimentally-obtained proton-flux images than was previously possible. Furthermore, the insights from this same chapter are useful for optimising the design of future experiments investigating magnetic stochasticity in plasma such that imaging regimes of maximal efficacy can be achieved. All of these aspects will hopefully allow for proton imaging to be increasingly comprehensive as a diagnostic tool for assessing stochastic magnetic fields in laser-plasma experiments. The successful experimental realisation of the fluctuation dynamo described in Chapters 3 and 4 renews confidence in the theoretical frameworks (outlined in Chapter 1) which attribute the origin and sustainment of dynamical magnetic fields in the ICM to the operation of dynamo processes. Future experiments based on those outlined here can only further improve our understanding of this fundamental physical process.

Bibliography

Adler, R. (1981). *The Geometry of Random Fields.* Classics in Applied Mathematics. Society for Industrial and Applied Mathematics (SIAM), Philadelphia. 1.1.2, I.2

Arévalo, P., Churazov, E., Zhuravleva, I., Hernández-Monteagudo, C., and Revnivtsev, M. (2012). A Mexican hat with holes: calculating low-resolution power spectra from data with gaps. *Mon. Not. R. Astron. Soc.*, 426(3):1793–1807. 2.3.5, 4.3, I.2

Backus, G. E. and Chandrasekhar, S. (1956). On Cowling's theorem on the impossibility of self-maintained axisymmetric homogeneous dynamos. *Proc. Natl. Acad. Sci. U.S.A.*, 42(3):105. 1.1.4

Batchelor, G. K. (1953). *The Theory of Homogeneous Turbulence.* Cambridge University Press, Cambridge. 1.1.3, 1.1.3, 1.1.3

Batchelor, G. K. and Taylor, G. I. (1950). On the spontaneous magnetic field in a conducting liquid in turbulent motion. *Proc. R. Soc. A.*, 201(1066):405–416. 1.1.1

Beresnyak, A. (2012). Universal nonlinear small-scale dynamo. *Phys. Rev. Lett.*, 108:035002. 1.1.1, 3.5

Berry, M. V. and Upstill, C. (1980). Catastrophe optics: morphologies of caustics and their diffraction patterns. *Prog. Optics.*, 18:257–346. 5.2

Biermann, L. and Schlüter, A. (1951). Cosmic radiation and cosmic magnetic fields. II. Origin of cosmic magnetic fields. *Phys. Rev.*, 82:863–868. 1.1.1

Birdsall, C. K. and Langdon, A. B. (1991). *Plasma physics via computer simulation.* Institute of Physics Publishing, Bristol and Philadelphia. I.1

Blandford, R. and Eichler, D. (1987). Particle acceleration at astrophysical shocks: a theory of cosmic ray origin. *Phys. Rep.*, 154(1):1–75. 2.3.4

Boehly, T. R., Brown, D. L., Craxton, R. S., Keck, R. L., Knauer, J. P., Kelly, J. H., Kessler, T. J., Kumpan, S. A., Loucks, S. J., Letzring, S. A., Marshall, F. J., McCrory, R. L., Morse, S. F. B., Seka, W., Soures, J. M., and Verdon, C. P. (1997). Initial performance results of the OMEGA laser system. *Optics Commun.*, 133(1):495–506. 1.2.2

Boldyrev, S. (2001). A solvable model for nonlinear mean field dynamo. *Astrophys. J.*, 562(2):1081–1085. 1.1.4

Borghesi, M., Campbell, D. H., Schiavi, A., Haines, M. G., Willi, O., MacKinnon, A. J., Patel, P., Gizzi, L. A., Galimberti, M., Clarke, R. J., Pegoraro, F., Ruhl, H., and Bulanov, S. (2002). Electric field detection in laser-plasma interaction experiments via the proton imaging technique. *Phys. Plasmas*, 9(5):2214–2220. 1.3

Borghesi, M., Fuchs, J., Bulanov, S., Mackinnon, A., Patel, P., and Roth, M. (2006). Fast ion generation by high-intensity laser irradiation of solid targets and applications. *Fusion Sci. Technol.*, 49(3):412–439. 1.3, 2.4.1

Borghesi, M., Kar, S., Romagnani, L., Toncian, T., Antici, P., Audebert, P., Brambrink, E., Ceccherini, F., Cecchetti, C. A., Fuchs, J., Galimberti, M., Gizzi, L. A., Grismayer, T., Lyseikina, T., Jung, R., Macchi, A., Mora, P., Osterholtz, J., Schiavi, A., and Willi, O. (2007). Impulsive electric fields driven by high-intensity laser matter interactions. *Laser Part. Beams.*, 25(1):161–167. 1.3

Bott, A. F. A., Graziani, C., Tzeferacos, P., White, T. G., Lamb, D. Q., Gregori, G., and Schekochihin, A. A. (2017). Proton imaging of stochastic magnetic fields. *J. Plasma Phys.*, 83(6):905830614. 2.1, 2.2.2, 2.2.2, 2.2.2, 2.2.2, 2.2.3, 2.3.2, 2.3.3, 2.3.3, 2.3.4, 2.3.4, 2.3.4, 2.4.3, 2.4.3, I.3

Bradley, D. K., Bell, P. M., Landen, O. L., Kilkenny, J. D., and Oertel, J. (1995). Development and characterization of a pair of 30–40 ps X-ray framing cameras. *Rev. Sci. Instrum.*, 66(1):716–718. 4.3

Braginskii, S. I. (1965). Transport processes in a plasma. *Rev. Plasma Phys.*, 1:205. 4.6, 4.6

Brenier, Y. (1991). Polar factorization and monotone rearrangement of vector-valued functions. *Comm. Pure Appl. Math.*, 44(4):375–417. 2.3.2, H

Carilli, C. L. and Taylor, G. B. (2002). Cluster magnetic fields. *Annu. Rev. Astron. Astrophys.*, 40(1):319–348. 1.1.1

Cattaneo, F. and Tobias, S. M. (2009). Dynamo properties of the turbulent velocity field of a saturated dynamo. *J. Fluid Mech.*, 621:205–214. 1.1.4

Childress, S. and Gilbert, A. (1995). *Stretch, Twist, Fold: The Fast Dynamo*. Lecture Notes in Physics Monographs. Springer, Berlin. 1.1.4

Cho, J. and Vishniac, E. T. (2000). The generation of magnetic fields through driven turbulence. *Astrophys. J.*, 538(1):217–225. 1.1.4

Churazov, E., Vikhlinin, A., Zhuravleva, I., Schekochihin, A., Parrish, I., Sunyaev, R., Forman, W., Böhringer, H., and Randall, S. (2012). X-ray surface brightness and gas density fluctuations in the coma cluster. *Mon. Not. R. Astron. Soc.*, 421(2):1123–1135. 1.2.3, 2.4.3

Colvin, J. and Larsen, J. (2013). *Extreme Physics: Properties and Behavior of Matter at Extreme Conditions*. Cambridge University Press, Cambridge. 4.4, 4.6

Cowling, T. G. (1933). The magnetic field of sunspots. *Mon. Not. R. Astron. Soc.*, 94(1):39–48. 1.1.4

Cowling, T. G. (1957). The dynamo maintenance of steady magnetic fields. *Quart. J. Mech. Appl. Math.*, 10(1):129–136. 1.1.4

Cowling, T. G. (1962). Magnetohydrodynamics. *Rep. Prog. Phys.*, 25(1):244–286. 1.1.4

Cross, J. E., Reville, B., and Gregori, G. (2014). Scaling of magneto-quantum-radiative hydrodynamic equations: from laser-produced plasmas to astrophysics. 795(1):59. 4.6, 4.6

Daido, H., Nishiuchi, M., and Pirozhkov, A. S. (2012). Review of laser-driven ion sources and their applications. *Rep. Prog. Phys.*, 75(5):056401. 2.4.1

Davidson, P. A. (2004). *Turbulence: an introduction for scientists and engineers.* Oxford University Press, Oxford. 1.1.2, 1.1.3, 1.1, 1.2, 1.3, G.3

Davidson, R. C. (1983). Kinetic waves and instabilities in a uniform plasma. In Galeev, A. A. and Sudan, R. N., editors, *Basic Plasma Physics: Selected Chapters, Handbook of Plasma Physics, Volume 1*, page 229. 1.1.2

Dean, E. J. and Glowinski, R. (2006). Numerical methods for fully nonlinear elliptic equations of the Monge–Ampère type. *Comput. Methods Appl. Mech. Engrg.*, 195(13):1344–1386. 2.3.2, H, I.4

Dolginov, A. Z. and Toptygin, I. (1967). Multiple scattering of particles in a magnetic field with random inhomogeneities. *Sov. Phys. JETP.*, 24:1195. 2.1, 2.3.4, 2.3.4

Dubey, A., Antypas, K., Calder, A. C., Daley, C., Fryxell, B., Gallagher, J. B., Lamb, D. Q., Lee, D., Olson, K., Reid, L. B., Rich, P., Ricker, P. M., Riley, K. M., Rosner, R., Siegel, A., Taylor, N. T., Weide, K., Timmes, F. X., Vladimirova, N., and ZuHone, J. (2013). Evolution of FLASH, a multi-physics scientific simulation code for high-performance computing. *Int. J. High Perform. Comput. App*, 28(2):225–237. 1.2.2

Ensslin, T. and Vogt, C. (2003). The magnetic power spectrum in Faraday rotation screens. *Astron. Astrophys.*, 401(3):835–848. 1.2.5, 2.4.2, C, C.1, C.1, C.1, C.4, D, F, I.2

Evans, D. E. and Katzenstein, J. (1969). Laser light scattering in laboratory plasmas. *Rep. Prog. Phys.*, 32(1):207–271. 1.2.3, 1.9, 4.4, 4.4

Fatenejad, M., Bell, A. R., Benuzzi-Mounaix, A., Crowston, R., Drake, R. P., Flocke, N., Gregori, G., Koenig, M., Krauland, C., Lamb, D., Lee, D., Marques, J. R., Meinecke, J., Miniati, F., Murphy, C. D., Park, H. S., Pelka, A., Ravasio, A., Remington, B., Reville, B., Scopatz, A., Tzeferacos, P., Weide, K., Woolsey, N., Young, R., and Yurchak, R. (2013). Modeling HEDLA magnetic field generation experiments on laser facilities. *High Energ. Dens. Phys.*, 9(1):172–177. 1.2.2

Fiksel, G., Agliata, A., Barnak, D., Brent, G., Chang, P. Y., Folnsbee, L., Gates, G., Hasset, D., Lonobile, D., Magoon, J., Mastrosimone, D., Shoup, M. J., and Betti, R. (2015). Note: Experimental platform for magnetized high-energy-density plasma studies at the OMEGA laser facility. *Rev. Sci. Instrum.*, 86(1):016105. 5.2

Fox, W., Fiksel, G., Bhattacharjee, A., Chang, P.-Y., Germaschewski, K., Hu, S. X., and Nilson, P. M. (2013). Filamentation instability of counterstreaming laser-driven plasmas. *Phys. Rev. Lett.*, 111:225002. 5.2

Fried, B. and Conte, S. (1961). *The Plasma Dispersion Function.* Academic Press, New York. 4.4

Fryxell, B., Olson, K., Ricker, P., Timmes, F. X., Zingale, M., Lamb, D. Q., MacNeice, P., Rosner, R., Truran, J. W., and Tufo, H. (2000). FLASH: An adaptive mesh hydrodynamics code for modeling astrophysical thermonuclear flashes. *Astrophys. J. Supp.*, 131(1):273–334. 1.2.2

Gailitis, A., Lielausis, O., Dement'ev, S., Platacis, E., Cifersons, A., Gerbeth, G., Gundrum, T., Stefani, F., Christen, M., Hänel, H., and Will, G. (2000). Detection of a flow induced magnetic field eigenmode in the riga dynamo facility. *Phys. Rev. Lett.*, 84:4365–4368. 1.2.1

Gailitis, A., Lielausis, O., Platacis, E., Dement'ev, S., Cifersons, A., Gerbeth, G., Gundrum, T., Stefani, F., Christen, M., and Will, G. (2001). Magnetic field saturation in the riga dynamo experiment. *Phys. Rev. Lett.*, 86:3024–3027. 1.2.1

Galloway, D. J. and Proctor, M. R. E. (1992). Numerical calculations of fast dynamos in smooth velocity fields with realistic diffusion. *Nature*, 356(6371):691–693. 1.1.4

Gangbo, W. and McCann, R. J. (1996). The geometry of optimal transportation. *Acta Math.*, 177(2):113–161. 2.3.2, 2.3.5, H

Golitsyn, G. S. (1960). Fluctuations of the magnetic field and current density in a turbulent flow of a weakly conducting fluid. *Soviet Phys. Doklady*, 5:536. 1.1.4, 2.3

Graziani, C., Tzeferacos, P., Lamb, D. Q., and Li, C. (2017). Inferring morphology and strength of magnetic fields from proton radiographs. *Rev. Sci. Instrum.*, 88(12):123507. 1.3, 2.1, 2.2.2, 2.2.3, 2.3.1, 2.3.1, 2.3.1, 2.3.1, E, F

Graziani, C., Tzeferacos, P., Lee, D., Lamb, D. Q., Weide, K., Fatenejad, M., and Miller, J. (2015). The Biermann catastrophe in numerical magnetohydrodynamics. *Astrophys. J.*, 802(1):43. 1.2.2, 4.5

Gregori, G., Reville, B., and Miniati, F. (2015). The generation and amplification of intergalactic magnetic fields in analogue laboratory experiments with high power lasers. *Phys. Reports.*, 601:1–34. 1.1.2, 1.1.5, 1.2.1, 1.4, 2.3, 2.3, 3.3.1

Hall, D. E. and Sturrock, P. A. (1967). Diffusion, scattering, and acceleration of particles by stochastic electromagnetic fields. *Phys. Fluids*, 10(12):2620–2628. 2.1, 2.3.4

Haugen, N. E. L., Brandenburg, A., and Dobler, W. (2003). Is nonhelical hydromagnetic turbulence peaked at small scales? *Astrophys. J.*, 597(2):L141–L144. 1.1.4

Haugen, N. E. L., Brandenburg, A., and Dobler, W. (2004). Simulations of nonhelical hydromagnetic turbulence. *Phys. Rev. E*, 70:016308. 1.1.4, 1.1.4, 1.1.4, 4.6

Helander, P. and Sigmar, D. (2005). *Collisional Transport in Magnetized Plasmas.* Cambridge Monographs on Plasma Physics. Cambridge University Press, Cambridge. 1.1.5

Helander, P., Strumik, M., and Schekochihin, A. A. (2016). Constraints on dynamo action in plasmas. *J. Plasma Phys.*, 82(6):905820601. 1.1.5

Hitomi Collaboration (2016). The quiescent intracluster medium in the core of the perseus cluster. *Nature*, 535:117. 1.1.5

Huba, J. D. (1994). *NRL Plasma Formulary.* Naval Research Laboratory, Washington DC. 1.4, 3.5, 4.6

Hughes, P. A. (1991). *Beams and Jets in Astrophysics.* Cambridge University Press, Cambridge. 1.2.2

Huntington, C. M., Fiuza, F., Ross, J. S., Zylstra, A. B., Drake, R. P., Froula, D. H., Gregori, G., Kugland, N. L., Kuranz, C. C., Levy, M. C., Li, C. K., Meinecke, J., Morita, T., Petrasso, R., Plechaty, C., Remington, B. A., Ryutov, D. D., Sakawa, Y., Spitkovsky, A., Takabe, H., and Park, H. S. (2015). Observation of magnetic field generation via the Weibel instability in interpenetrating plasma flows. *Nat. Phys.*, 11(2):173–176. 1.1.1, 1.3, 3.5, 5.2

Inogamov, N. A. and Sunyaev, R. A. (2003). Turbulence in clusters of galaxies and X–ray line profiles. *Astron. Lett.*, 29(12):791–824. 1.1.5, 1.2.3

Jokipii, J. R. (1972). Fokker-Planck equations for charged-particle transport in random fields. *Astrophys. J.*, 172:319. 2.1, 2.3.4

Kar, S., Borghesi, M., Audebert, P., Benuzzi-Mounaix, A., Boehly, T., Hicks, D., Koenig, M., Lancaster, K., Lepape, S., Mackinnon, A., Norreys, P., Patel, P., and Romagnani, L. (2008). Modeling of laser-driven proton radiography of dense matter. *High Energ. Dens. Phys.*, 4(1):26–40. 2.4.1

Kasim, M. F., Ceurvorst, L., Ratan, N., Sadler, J., Chen, N., Sävert, A., Trines, R., Bingham, R., Burrows, P. N., Kaluza, M. C., and Norreys, P. (2017). Quantitative shadowgraphy and proton radiography for large intensity modulations. *Phys. Rev. E*, 95:023306. 2.3.2, I.4

Kazantsev, A. P. (1968). Enhancement of a magnetic field by a conducting fluid. *JETP*, 26(5):1031. 1.1.4, 1.1.4

Kida, S., Yanase, S., and Mizushima, J. (1991). Statistical properties of MHD turbulence and turbulent dynamo. *Phys. Fluids A*, 3(3):457–465. 1.1.4

Kilkenny, J. D., Bell, P., Hanks, R., Power, G., Turner, R. E., and Wiedwald, J. (1988). High–speed gated X–ray imagers (invited). *Rev. Sci. Instrum.*, 59(8):1793–1796. 4.3

Kleeorin, N., Mond, M., and Rogachevskii, I. (1996). Magnetohydrodynamic turbulence in the solar convective zone as a source of oscillations and sunspots formation. *Astron. Astrophys.*, 307:293. 1.1.4, 1.1.4

Kleeorin, N. and Rogachevskii, I. (1994). Effective Ampère force in developed magnetohydrodynamic turbulence. *Phys. Rev. E*, 50:2716–2730. 1.1.4, 1.1.4

Kleva, R. G. and Drake, J. F. (1995). Nonlinear magnetohydrodynamic dynamo. *Phys. Plasmas*, 2(12):4455–4461. 1.1.4

Kolmogorov, A. N. (1941a). Dissipation of energy in the locally isotropic turbulence. *Dokl. Akad. Nauk. SSSR*, 19:31. 1.1.3, 1.1.3

Kolmogorov, A. N. (1941b). The local structure of turbulence in incompressible viscous fluid for very large Reynolds numbers. *Dokl. Akad. Nauk SSSR*, 30:301–305. 1.1.3

Krall, N. A. and Trivelpiece, A. W. (1973). *Principles of plasma physics.* McGraw-Hill. 1.1.2, B, B

Kugland, N. L., Ross, J. S., Chang, P. Y., Drake, R. P., Fiksel, G., Froula, D. H., Glenzer, S. H., Gregori, G., Grosskopf, M., Huntington, C., Koenig, M., Kuramitsu, Y., Kuranz, C., Levy, M. C., Liang, E., Martinez, D., Meinecke, J., Miniati, F., Morita, T., Pelka, A., Plechaty, C., Presura, R., Ravasio, A., Remington, B. A., Reville, B., Ryutov, D. D., Sakawa, Y., Spitkovsky, A., Takabe, H., and Park, H. S. (2013). Visualizing electromagnetic fields in laser-produced counter-streaming plasma experiments for collisionless shock laboratory astrophysics. *Phys. Plasmas*, 20(5):056313. 4.5

Kugland, N. L., Ryutov, D. D., Plechaty, C., Ross, J. S., and Park, H.-S. (2012). Invited article: Relation between electric and magnetic field structures and their proton-beam images. *Rev. Sci. Instrum.*, 83(10):101301. 1.3, 2.2.2, 2.2.2, 2.2.2, 2.2.2, 2.2.2, 2.2.3, 2.3.1, 2.3.3, 2.3.3, 2.4.1, 2.4.1, 3.3.1, 4.5, 4.5, B, G.3

Kulsrud, R. M. and Anderson, S. W. (1992). The spectrum of random magnetic fields in the mean field dynamo theory of the galactic magnetic field. *Astrophys. J.*, 396:606–630. 1.1.4

Kulsrud, R. M., Cen, R., Ostriker, J. P., and Ryu, D. (1997). The protogalactic origin for cosmic magnetic fields. *Astrophys. J.*, 480(2):481–491. 1.1.1

Kulsrud, R. M. and Zweibel, E. G. (2008). On the origin of cosmic magnetic fields. *Rep. Prog. Phys.*, 71(4):046901. 1.1.1

Kunz, M. W., Schekochihin, A. A., and Stone, J. M. (2014). Firehose and mirror instabilities in a collisionless shearing plasma. *Phys. Rev. Lett.*, 112:205003. 1.1.5

Landau, L. and Lifshitz, E. (1959). *Fluid Mechanics.* Pergamon Press, London. 1.1.3

Lee, D. (2013). A solution accurate, efficient and stable unsplit staggered mesh scheme for three dimensional magnetohydrodynamics. *J. Comput. Phys.*, 243:269–292. 1.2.2

Levy, M. C., Ryutov, D. D., Wilks, S. C., Ross, J. S., Huntington, C. M., Fiuza, F., Martinez, D. A., Kugland, N. L., Baring, M. G., and Park, H.-S. (2015). Development of an interpretive simulation tool for the proton radiography technique. *Rev. Sci. Instrum.*, 86(3):033302. 1.3

Li, C.-K. and Petrasso, R. D. (1993). Charged-particle stopping powers in inertial confinement fusion plasmas. *Phys. Rev. Lett.*, 70:3059–3062. 3.3.5

Li, C. K., Séguin, F. H., Frenje, J. A., Rygg, J. R., Petrasso, R. D., Town, R. P. J., Amendt, P. A., Hatchett, S. P., Landen, O. L., Mackinnon, A. J., Patel, P. K., Smalyuk, V. A., Knauer, J. P., Sangster, T. C., and Stoeckl, C. (2006a). Monoenergetic proton backlighter for measuring E and B fields and for radiographing implosions and high-energy density plasmas (invited). *Rev. Sci. Instrum.*, 77(10):10E725. 2.4.1

Li, C. K., Séguin, F. H., Frenje, J. A., Rygg, J. R., Petrasso, R. D., Town, R. P. J., Amendt, P. A., Hatchett, S. P., Landen, O. L., Mackinnon, A. J., Patel, P. K., Smalyuk, V. A., Sangster, T. C., and Knauer, J. P. (2006b). Measuring E and B fields in laser-produced plasmas with monoenergetic proton radiography. *Phys. Rev. Lett.*, 97:135003. 1.3, 1.4, 2.4.1, 2.4.1, 2.4.3, 3.1.1

Li, C. K., Tzeferacos, P., Lamb, D., Gregori, G., Norreys, P. A., Rosenberg, M. J., Follett, R. K., Froula, D. H., Koenig, M., Seguin, F. H., Frenje, J. A., Rinderknecht, H. G., Sio, H., Zylstra, A. B., Petrasso, R. D., Amendt, P. A., Park, H. S., Remington, B. A., Ryutov, D. D., Wilks, S. C., Betti, R., Frank, A., Hu, S. X., Sangster, T. C., Hartigan, P., Drake, R. P., Kuranz, C. C., Lebedev, S. V., and Woolsey, N. C. (2016). Scaled laboratory experiments explain the kink behaviour of the crab nebula jet. *Nat. Commun.*, 7:13081 EP –. 3.3.5

Lucy, L. B. (1974). An iterative technique for the rectification of observed distributions. *Astron. J.*, 79:745. 2.4.3, 3.1.1

Mackinnon, A. J., Patel, P. K., Borghesi, M., Clarke, R. C., Freeman, R. R., Habara, H., Hatchett, S. P., Hey, D., Hicks, D. G., Kar, S., Key, M. H., King, J. A., Lancaster, K., Neely, D., Nikkro, A., Norreys, P. A., Notley, M. M., Phillips, T. W., Romagnani, L., Snavely, R. A., Stephens, R. B., and Town, R. P. J. (2006). Proton radiography of a laser-driven implosion. *Phys. Rev. Lett.*, 97:045001. 1.3

Mackinnon, A. J., Patel, P. K., Town, R. P., Edwards, M. J., Phillips, T., Lerner, S. C., Price, D. W., Hicks, D., Key, M. H., Hatchett, S., Wilks, S. C., Borghesi, M., Romagnani, L., Kar, S., Toncian, T., Pretzler, G., Willi, O., Koenig, M., Martinolli, E., Lepape, S., Benuzzi-Mounaix, A., Audebert, P., Gauthier, J. C., King, J., Snavely, R., Freeman, R. R., and Boehlly, T. (2004). Proton radiography as an electromagnetic field and density perturbation diagnostic (invited). *Rev. Sci. Instrum.*, 75(10):3531–3536. 1.3

Manuel, M. J. E., Zylstra, A. B., Rinderknecht, H. G., Casey, D. T., Rosenberg, M. J., Sinenian, N., Li, C. K., Frenje, J. A., Séguin, F. H., and Petrasso, R. D. (2012). Source characterization and modeling development for monoenergetic-proton radiography experiments on OMEGA. *Rev. Sci. Instrum.*, 83(6):063506. 1.3, 1.4, 2.4.1, 2.4.1, 2.4.3, 2.4.3

Meinecke, J., Doyle, H. W., Miniati, F., Bell, A. R., Bingham, R., Crowston, R., Drake, R. P., Fatenejad, M., Koenig, M., Kuramitsu, Y., C. Kuranz, C., Lamb, D. Q., Lee, D., MacDonald, M. J., Murphy, C. D., Park, H.-S., Pelka, A., Ravasio, A., Sakawa, Y., Schekochihin, A. A., Scopatz, A., Tzeferacos, P., Wan, W. C., Woolsey, N. C., Yurchak, R., Reville, B., and Gregori, G. (2014). Turbulent amplification of magnetic fields in laboratory laser-produced shock waves. *Nat. Phys.*, 10:520. 1.2.1, 1.2.5

Meinecke, J., Tzeferacos, P., Bell, A., Bingham, R., Clarke, R., Churazov, E., Crowston, R., Doyle, H., Drake, R. P., Heathcote, R., Koenig, M., Kuramitsu, Y., Kuranz, C., Lee, D., MacDonald, M., Murphy, C., Notley, M., Park, H.-S., Pelka, A., Ravasio, A., Reville, B., Sakawa, Y., Wan, W., Woolsey, N., Yurchak, R., Miniati, F., Schekochihin, A., Lamb, D., and Gregori, G. (2015). Developed turbulence and nonlinear amplification of magnetic fields in laboratory and astrophysical plasmas. *Proc. Natl. Acad. Sci. U.S.A.*, 112(27):8211. 1.2.1, 1.2.2, 1.2.3

Meneguzzi, M., Frisch, U., and Pouquet, A. (1981). Helical and nonhelical turbulent dynamos. *Phys. Rev. Lett.*, 47:1060–1064. 1.1.4

Miller, R. S., Mashayek, F., Adumitroaie, V., and Givi, P. (1996). Structure of homogeneous nonhelical magnetohydrodynamic turbulence. *Phys. Plasmas*, 3(9):3304–3317. 1.1.4

Miniati, F. and Beresnyak, A. (2015). Self-similar energetics in large clusters of galaxies. *Nature*, 523:59. 1.1.1

Moffatt, K. (1961). The amplification of a weak applied magnetic field by turbulence in fluids of moderate conductivity. *J. Fluid Mech.*, 11(4):625–635. 1.1.4, 1.1.4, 2.3

Monchaux, R., Berhanu, M., Bourgoin, M., Moulin, M., Odier, P., Pinton, J.-F., Volk, R., Fauve, S., Mordant, N., Pétrélis, F., Chiffaudel, A., Daviaud, F., Dubrulle, B., Gasquet, C., Marié, L., and Ravelet, F. (2007). Generation of a magnetic field by dynamo action in a turbulent flow of liquid sodium. *Phys. Rev. Lett.*, 98:044502. 1.2.1

Mondal, S., Narayanan, V., Ding, W. J., Lad, A. D., Hao, B., Ahmad, S., Wang, W. M., Sheng, Z. M., Sengupta, S., Kaw, P., Das, A., and Kumar, G. R. (2012). Direct observation of turbulent magnetic fields in hot, dense laser produced plasmas. *Proc. Natl. Acad. Sci. U.S.A.*, 109(21):8011–8015. 2.4.1

Nürnberg, F., Schollmeier, M., Brambrink, E., Blažević, A., Carroll, D. C., Flippo, K., Gautier, D. C., Geißel, M., Harres, K., Hegelich, B. M., Lundh, O., Markey, K., McKenna, P., Neely, D., Schreiber, J., and Roth, M. (2009). Radiochromic film imaging spectroscopy of laser-accelerated proton beams. *Rev. Sci. Instrum.*, 80(3):033301. 2.4.1, 2.4.1

Parker, E. N. (1965). The passage of energetic charged particles through interplanetary space. *Planet. Space. Sci.*, 13(1):9–49. 2.1, 2.3.4

Ponomarenko, Y. B. (1973). Theory of the hydromagnetic generator. *J. Appl. Mech. Tech. Phys.*, 14(6):775–778. 1.1.4

Richardson, L. F. (1926). Atmospheric diffusion shown on a distance-neighbour graph. *Proc. R. Soc. Lond. A*, 110(756):709–737. 1.1.3

Richardson, W. H. (1972). Bayesian-based iterative method of image restoration. *JOSA*, 62(1):55–59. 2.4.3, 3.1.1

Rigby, A., Katz, J., Bott, A. F. A., White, T. G., Tzeferacos, P., Lamb, D. Q., Froula, D. H., and Gregori, G. (2018). Implementation of a Faraday rotation diagnostic at the OMEGA laser facility. *High Power Laser Sci. Eng.*, 6:49. 1.2.5, 4.2

Rincon, F., Califano, F., Schekochihin, A. A., and Valentini, F. (2016). Turbulent dynamo in a collisionless plasma. *Proc. Natl. Acad. Sci. U.S.A.*, 113(15):3950. 1.1.5

Roberts, G. and Bullard, E. C. (1972). Dynamo action of fluid motions with two-dimensional periodicity. *Phil. Trans. R. Soc. A*, 271(1216):411–454. 1.1.4

Rochau, G. A., Bailey, J. E., Chandler, G. A., Nash, T. J., Nielsen, D. S., Dunham, G. S., Garcia, O. F., Joseph, N. R., Keister, J. W., Madlener, M. J., Morgan, D. V., Moy, K. J., and Wu, M. (2006). Energy dependent sensitivity of microchannel plate detectors. *Rev. Sci. Instrum.*, 77(10):10E323. 4.3

Romagnani, L. (2005). *Laser-plasma investigations employing laser-driven proton probes.* PhD thesis, Queen's University Belfast. 1.3, 2.2.2, 2.2.2, 2.3.1, 2.3.1

Romagnani, L., Borghesi, M., Cecchetti, C. A., Kar, S., Antici, P., Audebert, P., Bandhoupadjay, S., Ceccherini, F., Cowan, T., Fuchs, J., Galimberti, M., Gizzi, L. A., Grismayer, T., Heathcote, R., Jung, R., Liseykina, T. V., Macchi, A., Mora, P., Neely, D., Notley, M., Osterholtz, J., Pipahl, C. A., Pretzler, G., Schiavi, A., Schurtz, G., Toncian, T., Wilson, P. A., and Willi, O. (2008). Proton probing measurement of electric and magnetic fields generated by ns and ps laser-matter interactions. *Laser Part. Beams.*, 26(2):241–248. 1.3

Romagnani, L., Fuchs, J., Borghesi, M., Antici, P., Audebert, P., Ceccherini, F., Cowan, T., Grismayer, T., Kar, S., Macchi, A., Mora, P., Pretzler, G., Schiavi, A., Toncian, T., and Willi, O. (2005). Dynamics of electric fields driving the laser acceleration of multi-MeV protons. *Phys. Rev. Lett.*, 95:195001. 1.3

Ruzmaikin, A. A. and Shukurov, A. M. (1982). Spectrum of the galactic magnetic fields. *Astrophys. Space Sci.*, 82:397–407. 1.1.4

Rybicki, G. B. and Lightman, A. P. (1979). *Radiative Processes in Astrophysics.* Wiley-Interscience, New York. 4.3

Rygg, J. R., Zylstra, A. B., Séguin, F. H., LePape, S., Bachmann, B., Craxton, R. S., Garcia, E. M., Kong, Y. Z., Gatu-Johnson, M., Khan, S. F., Lahmann, B. J., McKenty, P. W., Petrasso, R. D., Rinderknecht, H. G., Rosenberg, M. J., Sayre, D. B., and Sio, H. W. (2015). Note: a monoenergetic proton backlighter for the National Ignition Facility. *Rev. Sci. Instrum.*, 86(11):116104. 5.2

Ryu, D., Kang, H., Cho, J., and Das, S. (2008). Turbulence and magnetic fields in the large-scale structure of the universe. *Science*, 320(5878):909. 1.1.1

Ryutov, D. D., Fiuza, F., Huntington, C. M., Ross, J. S., and Park, H. S. (2014). Collisional effects in the ion Weibel instability for two counter-propagating plasma streams. *Phys. Plasmas*, 21(3):032701. 3.5, 3.5

Sarri, G., Macchi, A., Cecchetti, C. A., Kar, S., Liseykina, T. V., Yang, X. H., Dieckmann, M. E., Fuchs, J., Galimberti, M., Gizzi, L. A., Jung, R., Kourakis, I., Osterholz, J., Pegoraro, F., Robinson, A. P. L., Romagnani, L., Willi, O., and Borghesi, M. (2012). Dynamics of self-generated, large amplitude magnetic fields following high-intensity laser matter interaction. *Phys. Rev. Lett.*, 109:205002. 1.3, 4.5

Schekochihin, A. A., Boldyrev, S. A., and Kulsrud, R. M. (2002a). Spectra and growth rates of fluctuating magnetic fields in the kinematic dynamo theory with large magnetic Prandtl numbers. *Astrophys. J.*, 567(2):828–852. 1.1.4

Schekochihin, A. A. and Cowley, S. C. (2006). Turbulence, magnetic fields, and plasma physics in clusters of galaxies. *Phys. Plasmas*, 13(5):056501. 1.1.5, 4.6

Schekochihin, A. A., Cowley, S. C., Hammett, G. W., Maron, J. L., and McWilliams, J. C. (2002b). A model of nonlinear evolution and saturation of the turbulent mhd dynamo. *New J. Phys.*, 4:84–84. 1.1.4

Schekochihin, A. A., Cowley, S. C., Kulsrud, R. M., Hammett, G. W., and Sharma, P. (2005a). Plasma instabilities and magnetic field growth in clusters of galaxies. *Astrophys. J.*, 629(1):139. 1.1.5

Schekochihin, A. A., Cowley, S. C., Maron, J. L., and McWilliams, J. C. (2004a). Critical magnetic Prandtl number for small-scale dynamo. *Phys. Rev. Lett.*, 92:054502. 1.1.4

Schekochihin, A. A., Cowley, S. C., Taylor, S. F., Hammett, G. W., Maron, J. L., and McWilliams, J. C. (2004b). Saturated state of the nonlinear small-scale dynamo. *Phys. Rev. Lett.*, 92:084504. 1.1.4

Schekochihin, A. A., Cowley, S. C., Taylor, S. F., Maron, J. L., and McWilliams, J. C. (2004c). Simulations of the small-scale turbulent dynamo. *Astrophys. J.*, 612(1):276. 1.1.4, 1.1.4, 1.1.4, 1.1.4, 2.3, 3.5, 4.6, 4.6, 5.2, I.2

Schekochihin, A. A., Haugen, N. E. L., Brandenburg, A., Cowley, S. C., Maron, J. L., and McWilliams, J. C. (2005b). The onset of a small-scale turbulent dynamo at low magnetic Prandtl numbers. *Astrophys. J.*, 625(2):L115–L118. 1.1.4

Schekochihin, A. A., Iskakov, A. B., Cowley, S. C., McWilliams, J. C., Proctor, M. R. E., and Yousef, T. A. (2007). Fluctuation dynamo and turbulent induction at low magnetic Prandtl numbers. *New J. Phys.*, 9(8):300. 1.1.4, 1.4, 1.1.4, 1.5, 1.2.3, 2.3

Schekochihin, A. A., Maron, J. L., Cowley, S. C., and McWilliams, J. C. (2002c). The small-scale structure of magnetohydrodynamic turbulence with large magnetic Prandtl numbers. *Astrophys. J.*, 576(2):806–813. 1.1.4

Segre, S. E. (1999). A review of plasma polarimetry - theory and methods. *Plasma Phys. Controlled Fusion*, 41(2):R57–R100. 1.2.5

Séguin, F. H., DeCiantis, J. L., Frenje, J. A., Kurebayashi, S., Li, C. K., Rygg, J. R., Chen, C., Berube, V., Schwartz, B. E., Petrasso, R. D., Smalyuk, V. A., Marshall, F. J., Knauer, J. P., Delettrez, J. A., McKenty, P. W., Meyerhofer, D. D., Roberts, S., Sangster, T. C., Mikaelian, K., and Park, H. S. (2004). D3He-proton emission imaging for inertial-confinement-fusion experiments (invited). *Rev. Sci. Instrum.*, 75(10):3520–3525. 1.3, 2.4.1, 2.4.3, 3.1.1

Séguin, F. H., Frenje, J. A., Li, C. K., Hicks, D. G., Kurebayashi, S., Rygg, J. R., Schwartz, B. E., Petrasso, R. D., Roberts, S., Soures, J. M., Meyerhofer, D. D., Sangster, T. C., Knauer, J. P., Sorce, C., Glebov, V. Y., Stoeckl, C., Phillips, T. W., Leeper, R. J., Fletcher, K., and Padalino, S. (2003). Spectrometry of charged particles from inertial-confinement-fusion plasmas. *Rev. Sci. Instrum.*, 74(2):975–995. 1.4, 2.4.1, 3.3.5

Shafranov, V. D. (1957). The structure of a shock wave in a plasma. *JETP*, 5(6):1183. 4.4

Shinozuka, M. and Deodatis, G. (1996). Simulation of multi-dimensional Gaussian stochastic fields by spectral representation. *Appl. Mech. Rev.*, 49(1):29–53. I.2

Simakov, A. N. and Molvig, K. (2014). Electron transport in a collisional plasma with multiple ion species. *Phys. Plasmas*, 21(2):024503. 3.5, 4.6

Simakov, A. N. and Molvig, K. (2016). Hydrodynamic description of an unmagnetized plasma with multiple ion species. II. Two and three ion species plasmas. *Phys. Plasmas*, 23(3):032116. 4.6

St-Onge, D. A. and Kunz, M. W. (2018). Fluctuation dynamo in a collisionless, weakly magnetized plasma. *Astrophys. J. Lett.*, 863(2):L25. 1.1.5

Stamper, J. A., Papadopoulos, K., Sudan, R. N., Dean, S. O., McLean, E. A., and Dawson, J. M. (1971). Spontaneous magnetic fields in laser-produced plasmas. *Phys. Rev. Lett.*, 26:1012–1015. 1.2.4

Subramanian, K. (2003). Hyperdiffusion in nonlinear large- and small-scale turbulent dynamos. *Phys. Rev. Lett.*, 90:245003. 1.1.4

Subramanian, K., Shukurov, A., and Haugen, N. E. L. (2006). Evolving turbulence and magnetic fields in galaxy clusters. *Mon. Not. R. Astron. Soc.*, 366(4):1437–1454. 1.1.1

Sulman, M. M., Williams, J. F., and Russell, R. D. (2011). An efficient approach for the numerical solution of the Monge–Ampère equation. *Appl. Numer. Math.*, 61(3):298–307. 2.3.2, H, I.4

Tobias, S., Cattaneo, F., and Boldyrev, S. (2013). *Ten Chapters in Turbulence*, pages 351–404. Cambridge University Press, Cambridge. 1.1.4, 1.1.4, 3.5

Tzeferacos, P., Fatenejad, M., Flocke, N., Graziani, C., Gregori, G., Lamb, D. Q., Lee, D., Meinecke, J., Scopatz, A., and Weide, K. (2015). FLASH MHD simulations of experiments that study shock-generated magnetic fields. *High Energy Dens. Phys.*, 17:24–31. 1.2.2

Tzeferacos, P., Rigby, A., Bott, A., Bell, A. R., Bingham, R., Casner, A., Cattaneo, F., Churazov, E. M., Emig, J., Fiuza, F., Forest, C. B., Foster, J., Graziani, C., Katz, J., Koenig, M., Li, C.-K., Meinecke, J., Petrasso, R., Park, H.-S., Remington, B. A., Ross, J. S., Ryu, D., Ryutov, D., White, T. G., Reville, B., Miniati, F., Schekochihin, A. A., Lamb, D. Q., Froula, D. H., and Gregori, G. (2017). Numerical modeling of laser-driven experiments aiming to demonstrate magnetic field amplification via turbulent dynamo. *Phys. Plasmas*, 24(4):041404. 1.2.2, 1.2.3, 1.2.3, 2.4.1

Tzeferacos, P., Rigby, A., Bott, A. F. A., Bell, A. R., Bingham, R., Casner, A., Cattaneo, F., Churazov, E. M., Emig, J., Fiuza, F., Forest, C. B., Foster, J., Graziani, C., Katz, J., Koenig, M., Li, C. K., Meinecke, J., Petrasso, R., Park, H. S., Remington, B. A., Ross, J. S., Ryu, D., Ryutov, D., White, T. G., Reville, B., Miniati, F., Schekochihin, A. A., Lamb, D. Q., Froula, D. H., and Gregori, G. (2018). Laboratory evidence of dynamo amplification of magnetic fields in a turbulent plasma. *Nat. Commun.*, 9(1):591. 1.2.2, 1.6, 1.2.3, 1.8, 1.9, 1.10, 1.11, 2.4.1

Villani, C. (2008). *Optimal transport: old and new*, volume 338. Springer Verlag, Berlin. 2.3.2, H

Vishik, M. M. (1989). Magnetic field generation by the motion of a highly conducting fluid. *Geophys. Astrophys. Fluid Dyn.*, 48(1-3):151–167. 1.1.4

Weibel, E. S. (1959). Spontaneously growing transverse waves in a plasma due to an anisotropic velocity distribution. *Phys. Rev. Lett.*, 2:83. 1.1.1

Welch, D. R., Rose, D. V., Clark, R. E., Genoni, T. C., and Hughes, T. P. (2004). Implementation of an non-iterative implicit electromagnetic field solver for dense plasma simulation. *Comp. Phys. Comm.*, 164(1):183–188. I.1

Wilks, S. C., Langdon, A. B., Cowan, T. E., Roth, M., Singh, M., Hatchett, S., Key, M. H., Pennington, D., MacKinnon, A., and Snavely, R. A. (2001). Energetic proton generation in ultra-intense laser–solid interactions. *Phys. Plasmas*, 8(2):542–549. 1.3, 2.4.1, 2.4.1, 2.4.1, 2.4.3

Yamazaki, F. and Shinozuka, M. (1988). Digital generation of non-Gaussian stochastic fields. *J. Eng. Mech.*, 114(7):1183–1197. I.2

Zhuravleva, I., Churazov, E. M., Schekochihin, A. A., Lau, E. T., Nagai, D., Gaspari, M., Allen, S. W., Nelson, K., and Parrish, I. J. (2014). The relation between gas density and velocity power spectra in galaxy clusters: qualitative treatment and cosmological simulations. *Astrophys. J.*, 788(1):L13. 1.2.3, 4.3

Ziegler, J. F. (1999). Stopping of energetic light ions in elemental matter. *J. Appl. Phys / Rev. Appl. Phys.*, 85(3):1249–1272. 2.4.1, B

Appendix A

Glossary of notation and mathematical conventions

As an aid to reading, in this appendix we provide a glossary of notation commonly used throughout the thesis in Table A.1; in Table A.2, notation pertaining to the theory of proton imaging of stochastic fields described in Chapter 2 is summarised. The units system is Gaussian CGS.

We define the Fourier transform $\hat{f}$ of a function f and the inverse transform in n-dimensions according to the following convention:

$$\hat{f}(\mathbf{k}) = \frac{1}{(2\pi)^n} \int \mathrm{d}^n\mathbf{x} \, \exp\left[-i\mathbf{k}\cdot\mathbf{x}\right] f(\mathbf{x}) \, , \tag{A.1}$$

$$f(\mathbf{x}) = \int \mathrm{d}^n\mathbf{k} \, \exp\left[i\mathbf{k}\cdot\mathbf{x}\right] \hat{f}(\mathbf{k}) \, . \tag{A.2}$$

For isotropic functions $f = f(r)$ and $\hat{f} = \hat{f}(k)$ in three dimensions, this gives

$$f(r) = 4\pi \int_0^\infty \mathrm{d}k \, k^2 \hat{f}(k) \, \frac{\sin kr}{kr} \, , \tag{A.3}$$

which in turns implies that the value of f at the origin under this convention is

Notation	Quantity
e	Elementary charge
m_e, m_p	Electron/proton mass
c	Speed of light
$\mathbf{u}$	Total velocity field (1.1)
$\delta\mathbf{u}$	Fluctuating, stochastic velocity field (1.1)
$\bar{\mathbf{u}}$	Mean velocity field (1.1)
$E(k)$	Kinetic-energy spectrum (1.3)
u_{rms}	RMS stochastic velocity field strength (1.4)
ℓ_u	Velocity field correlation length (1.5)
$\mathbf{B}$	Total magnetic field (1.2)
$\delta\mathbf{B}$	Fluctuating, stochastic magnetic field (1.2)
$\bar{\mathbf{B}}$	Mean, regular magnetic field (1.2)
$E_B(k)$	Magnetic-energy spectrum (1.6)
B_{rms}	RMS stochastic magnetic field strength (1.7)
ℓ_B	Magnetic field correlation length (1.8)
$\tilde{\ell}_B$	Scale of magnetic-energy spectral peak
$(p_e)\ p$	(Electron) pressure
ρ	Mass density
ν	Kinematic viscosity
L	Outer scale of turbulent cascade
$(u_\ell)\ u_L$	Characteristic velocity at scale $(\ell)\ L$
τ_L	Turnover rate u_L/L
ℓ_ν	Viscous dissipation scale
η	Resistivity
ℓ_η	Resistive scale
$\mathbf{E}$	Electric field
$\mathbf{j}$	Current
T_e, T_i	Electron/ion temperature
n_e, n_i	Electron/ion density
$(l_{n\perp})\ l_n$	Interaction-region width (perp. extent)
l_{TS}	Thomson-scattering focal-spot scale
l_{path}	Thomson-scattering beam path-length
λ	Thomson-scattering beam wavelength

Table A.1: Glossary of commonly used notation

Notation	Quantity
V	Beam-proton speed
W	Beam-proton energy
r_i	Distance from beam source to magnetic field configuration/plasma
l_z	Parallel size of magnetic field configuration/plasma
$l_\perp$	Perpendicular size of magnetic field configuration/plasma
r_s	Distance from magnetic field configuration/plasma to detector
$\mathcal{M}$	image-magnification factor (2.18)
a	Finite proton-source radius
$\delta\theta$	Typical proton deflection angle (2.52)
$\delta\alpha$	Paraxial parameter (2.49)
$\delta\beta$	Point-projection parameter (2.50)
μ	Contrast parameter (2.17)
$(\mathbf{x}_{\perp 0})\ \mathbf{x}_0$	(Perpendicular) initial beam-proton position coordinate
$(\mathbf{x}_\perp)\ \mathbf{x}$	(Perpendicular) beam-proton position coordinate
$(\mathbf{x}_\perp^{(s)})\ \mathbf{x}^{(s)}$	(Perpendicular) beam-proton image position coordinate
$(\mathbf{r}_\perp)\ \mathbf{r}$	(Perpendicular) distance vector
$\mathbf{w}(\mathbf{x}_{\perp 0})$	Perpendicular-deflection field (2.8)
w_{rms}	RMS deflection-field strength
$E_W(k_\perp)$	Deflection-field spectrum (2.12)
$B_{rms,0}$	Effective RMS stochastic magnetic field strength (2.23)
$\varphi(\mathbf{x}_{\perp 0})$	Deflection-field potential (2.15)
$\Psi_0(\mathbf{x}_{\perp 0})$	Initial beam flux distribution
$\Psi\left(\mathbf{x}_\perp^{(s)}\right)$	Image-flux distribution function (2.9)
$\delta\Psi\left(\mathbf{x}_\perp^{(s)}\right)$	Image-flux deviation from mean proton flux
l_Ψ	Relative image-flux correlation length (F.27)
$\Psi_0^{(s)}\left(\mathbf{x}_\perp^{(s)}\right)$	Unperturbed image-flux distribution
D_w	(Isotropic) perp. stochastic magnetic diffusion coefficient (2.43)
τ_{pulse}	Temporal pulse-length of proton source
τ_{path}	Transit time of imaging protons across plasma
τ_{source}	Transit time of imaging protons to plasma

Table A.2: Glossary of notation for proton-imaging theory simply the integral of the 1D power spectrum of f:

$$f(0) = 4\pi \int_0^\infty \mathrm{d}k\, k^2 \hat{f}(k) \equiv \int_0^\infty \mathrm{d}k\, E_f(k) \ . \tag{A.4}$$

The integral of f over all radii (which for normalised correlation functions gives the correlation scale) is

$$\int_0^\infty \mathrm{d}r\, f(r) = 2\pi^2 \int_0^\infty \mathrm{d}k\, k\hat{f}(k) \ . \tag{A.5}$$

For two-dimensional isotropic functions,

$$f(r) = 2\pi \int_0^\infty \mathrm{d}k\, k\hat{f}(k)\, J_0(kr) \ , \tag{A.6}$$

where J_0 is the zeroth-order Bessel function of the first kind. Similarly to the three-dimensional case, we find

$$f(0) = 2\pi \int_0^\infty \mathrm{d}k\, k\hat{f}(k) \equiv \int_0^\infty \mathrm{d}k\, E_f(k) \ , \tag{A.7}$$

and

$$\int_0^\infty \mathrm{d}r\, f(r) = 2\pi \int_0^\infty \mathrm{d}k\, k\hat{f}(k) \ . \tag{A.8}$$

Appendix B

Negligible processes when deriving plasma-image mapping (2.7)

In deriving plasma-image mapping (2.7), perpendicular-deflection field (2.8), and RK image-flux relation (2.9), it was assumed that the evolution of the proton beam as it passes through the plasma is dominated by forces arising due to magnetic fields inherent in the plasma; in this appendix, we explain the justification for this simplification. In general, the interaction of a beam of protons with a plasma involves a broad range of physical processes. However, due to the large velocity of the beam protons, and their low density, the governing physics can be simplified considerably.

Firstly, self-interaction of the beam can be taken to be negligible, on account of the beam's initial number density n_{beam} taking values $n_{\mathrm{beam}} \sim 10^{10} - 10^{12}\,\mathrm{cm}^{-3}$. This can be demonstrated by considering space-charge effects in the beam: it can be shown that the electric potential energy in an un-neutralised proton cloud (assuming the above values for the beam density) drops to a small fraction of the beam's kinetic energy well before reaching the plasma (Kugland et al. 2012). Furthermore, once the protons reach the plasma, beam space charge is screened by plasma electrons.

Typically, a fast particle beam interacting with a plasma would be subject to collisionless kinetic effects, such as the beam-plasma instability. For initial beam velocity V, the maximum linear growth rate of the beam-plasma instability scales as

$$\gamma \sim \omega_{\mathrm{p}i} \frac{n_{\mathrm{beam}}}{n_i} \left(\frac{V}{\Delta V} \right)^2 , \tag{B.1}$$

where $\omega_{\mathrm{p}i}$ is the ion plasma frequency, n_i the density of ions in the plasma, and ΔV the initial velocity spread inherent in the proton beam (Krall and Trivelpiece 1973). For the beam-plasma instability to have a significant effect on the proton-flux image, we require that the transit time τ_{path} through the plasma be much shorter than the typical time scale on which the beam-plasma instability grows: viz.,

$$\gamma \sim \frac{1}{\tau_{\mathrm{path}}} \approx \frac{V}{l_z} , \tag{B.2}$$

which can be rearranged to give an estimate for the typical uncertainty in deflection angle $\Delta\theta_{kin}$ resulting from collisionless kinetic effects:

$$\Delta\theta_{kin} \leq \frac{\Delta V}{V} \sim \left(\frac{n_{\mathrm{beam}}}{n_i} \right)^{1/4} \left(\frac{Z}{A} \omega_{\mathrm{p,beam}} \tau_{\mathrm{path}} \right)^{1/2} , \tag{B.3}$$

where $\omega_{\mathrm{p,beam}}$ is the plasma frequency of beam protons in the beam, Z the charge of the plasma ions, and A their atomic mass. Substituting typical parameters in (for example) a carbon plasma, with $n_i \sim 10^{20}\,\mathrm{cm}^{-3}$, $n_{\mathrm{beam}} \sim 10^{10}\,\mathrm{cm}^{-3}$ and $l_z \sim 0.1\,\mathrm{cm}$, we have for 3.3 MeV protons that $\omega_{\mathrm{p,beam}} \sim 1.3 \times 10^8\,\mathrm{s}^{-1}$, and $\tau_{\mathrm{path}} \sim 4 \times 10^{-11}\,\mathrm{s}$, which gives

$$\Delta\theta_{kin} \sim 2 \times 10^{-4} , \tag{B.4}$$

a smaller effect than other asymptotic parameters.

Collisional effects are also negligible, on account of τ_{path} typically being larger than collisional relaxation times – in a plasma, for fast ions with energy W the stopping power is to a good approximation given by the Bohr formula

$$S(W) = -\frac{\mathrm{d}W}{\mathrm{d}z} = \frac{4\pi e^4 n_e}{m_p V^2} \log \left(\frac{V}{\omega_p b_{min}} \right) , \tag{B.5}$$

where b_{min} is the impact parameter, and z the distance travelled through the plasma (Ziegler

1999). For protons with energy $W \geq 3.3\,\mathrm{MeV}$ passing through a carbon plasma, $n_e \sim 3.5 \times 10^{20}\,\mathrm{cm}^{-3}$, this gives $S(W) = 6 \times 10^4\,\mathrm{eV/cm}$. Since $S(W) \ll W/l_z$, the energy ΔW lost by a typical proton crossing the plasma is approximately $\Delta W \approx -l_z S(W)$. For a $l_z \sim 1\,\mathrm{mm}$ plasma, this gives

$$\frac{\Delta W}{W} \leq 2 \times 10^{-3}\,, \tag{B.6}$$

The resulting deflection angles are even smaller: for a Maxwellian plasma, it can be shown that for a suprathermal beam the typical deflection time τ_D over which the proton beam distribution spreads perpendicularly to the direction of travel of the beam is given by

$$\tau_D = \frac{m_p^2}{16\pi e^4} \frac{V^3}{n_e \log \Lambda}\,, \tag{B.7}$$

where $\log \Lambda$ is the Coulomb logarithm (Krall and Trivelpiece 1973). An estimate for the typical spread in deflection angles $\Delta\theta_{\mathrm{coll}}$ resulting from collisions is then

$$\Delta\theta_{\mathrm{coll}} \sim \frac{l_z}{V \tau_D} \sim \frac{16\pi e^4}{m_p^2} \frac{l_z n_e \log \Lambda}{V^4}\,, \tag{B.8}$$

which has a strong beam-velocity dependence. Estimating $\Delta\theta_{\mathrm{coll}}$ for the same carbon plasma (and $\log \Lambda \approx 10$) described previously, we find

$$\Delta\theta_{\mathrm{coll}} \sim 1 \times 10^{-5}\,. \tag{B.9}$$

Appendix C

Further statistical characterisation of stochastic magnetic fields

This appendix extends the discussion of the statistical characterisation of stochastic magnetic fields provided in Section 2.2.1 by introducing the *magnetic autocorrelation function* (defined in Appendix C.1). For clarity of exposition, we do not directly refer to the magnetic autocorrelation function in the main text, because by the Wiener-Khinchin theorem it is equivalent to the magnetic-energy spectrum (2.2) for isotropic, homogeneous stochastic fields (Ensslin and Vogt 2003): and the magnetic-energy spectrum is generally of greater interest physically, for reasons discussed in Section 2.2.1. However, as we state in Section 2.2.1, we introduce the magnetic autocorrelation function in this appendix for two reasons. First, it provides the most natural definition of the correlation length ℓ_B of a stochastic magnetic field (Appendix C.2). We show in Appendix C.3 how the result (2.4) in the main text is derived from this definition. Second, using the magnetic autocorrelation function to derive deflection-field spectral relation (2.11) (Appendix D) and linear-regime flux spectral relation (2.35) (Appendix F) enables a simple quantification of asymptotic approximations made in doing so. In particular, in Appendix C.4 we state a result concerning the magnitude of the integrated tail of the magnetic autocorrelation function, a term whose neglect is necessary for the derivations of (2.11) and (2.35).

C.1 The magnetic autocorrelation function

The *magnetic autocorrelation tensor* $M_{nn'}(\mathbf{x}, \tilde{\mathbf{x}})$ of a general, zero-mean stochastic magnetic field ($\bar{\mathbf{B}} = 0$, $\mathbf{B} = \delta\mathbf{B}$) is defined by

$$M_{nn'}(\mathbf{x}, \tilde{\mathbf{x}}) \equiv \langle B_n(\mathbf{x})\, B_{n'}(\tilde{\mathbf{x}}) \rangle \ , \tag{C.1}$$

for arbitrary positions $\mathbf{x}$, $\tilde{\mathbf{x}}$ in the plasma. If the stochastic fields are isotropic and homogeneous, the autocorrelation tensor can be written as a function of displacement vector $\mathbf{r} = \tilde{\mathbf{x}} - \mathbf{x}$ only:

$$M_{nn'}(\mathbf{x}, \tilde{\mathbf{x}}) = M_{nn'}(\mathbf{r}) = M_N(r)\, \delta_{nn'} + (M_L(r) - M_N(r))\, \frac{r_n r_{n'}}{r^2} + M_H(r)\, \epsilon_{nn'l} r_l \ , \tag{C.2}$$

for longitudinal, normal and helical autocorrelation functions $M_L(r)$, $M_N(r)$ and $M_H(r)$, and distance coordinate $r = |\tilde{\mathbf{x}} - \mathbf{x}|$ (Ensslin and Vogt 2003). The solenoidal condition on the magnetic field $\nabla \cdot \mathbf{B} = 0$ gives corresponding relation

$$\frac{\partial}{\partial r_i} M_{ij}(r) = 0 \, , \tag{C.3}$$

which can be used to relate M_L to M_N (Ensslin and Vogt 2003) via a differential identity:

$$M_N(r) = \frac{1}{2r} \frac{\mathrm{d}}{\mathrm{d}r} \left[r^2 M_L(r) \right] \ . \tag{C.4}$$

For convenience, we derive this result explicitly in Appendix C.5. The magnetic autocorrelation function $M\,(r)$ is then defined as trace of the magnetic autocorrelation tensor:

$$M(r) = M_{ii}(r) \ . \tag{C.5}$$

Similarly to the magnetic-energy spectrum, the magnetic autocorrelation function provides information about typical magnetic field strengths. More specifically, the

RMS magnetic field strength is given in terms of $M(r)$ by

$$B_{rms}^2 = M(0) \ . \tag{C.6}$$

As discussed in Appendix C.2, the autocorrelation function can also be used to estimate typical structure sizes via the correlation length.

We now state the sense in which the magnetic-energy spectrum and magnetic autocorrelation function are equivalent: from the Wiener-Khinchin theorem (Ensslin and Vogt 2003), it follows that the (assumed isotropic) magnetic-energy spectrum $E_B(k)$ defined by (2.2) and autocorrelation function $M(r)$ are related by

$$E_B(k) = \frac{k^2}{2\,(2\pi)^3} \int \mathrm{d}^3\mathbf{r}\, \exp\left(-i\mathbf{k}\cdot\mathbf{r}\right) M(r) = \frac{1}{(2\pi)^2} \int_0^\infty \mathrm{d}r\, kr \sin kr\, M(r) \ , \tag{C.7}$$

where we have assumed Fourier-transform normalisation conventions as specified in Appendix A. The Fourier-inversion relations specified in the same appendix can be used to deduce the magnetic autocorrelation function from the magnetic-energy spectrum:

$$M(r) = 8\pi \int_0^\infty \mathrm{d}k\, E_B(k)\, \frac{\sin kr}{kr} \ . \tag{C.8}$$

Thus if the magnetic-energy spectrum is known, the magnetic autocorrelation function can be determined, and visa versa.

C.2 Formal definition of correlation length

The correlation length of a stochastic magnetic field ℓ_B is defined in terms of the magnetic autocorrelation function $M(r)$ introduced in the previous sub-appendix:

$$\ell_B \equiv \frac{1}{B_{rms}^2} \int_0^\infty \mathrm{d}r\, M(r) \ . \tag{C.9}$$

Thus, as the name suggests, the correlation length of a stochastic magnetic field is simply a measure of the typical distance over which that field decorrelates with itself.

C.3 Derivation of expression (2.4) for the correlation length in terms of the magnetic-energy spectrum

The inversion relation (C.8) enables a simple derivation of the expression (2.4) for the correlation length, that is

$$\ell_B = \frac{\pi}{2} \frac{\int_0^\infty \mathrm{d}k\, E_B(k)\,/k}{\int_0^\infty \mathrm{d}k\, E_B(k)}\,, \tag{C.10}$$

in terms of the magnetic-energy spectrum. Integrating (C.8) over the interval $r \in [0, \infty)$ gives

$$\int_0^\infty \mathrm{d}r\, M(r) = 8\pi \int_0^\infty \mathrm{d}r \int_0^\infty \mathrm{d}k\, E_B(k)\, \frac{\sin kr}{kr}\,. \tag{C.11}$$

Applying correlation-length definition (C.9) and switching the order of integration leads to

$$B_{rms}^2\, \ell_B = 8\pi \int_0^\infty \mathrm{d}k\, E_B(k) \int_0^\infty \mathrm{d}r \frac{\sin kr}{kr} = 4\pi^2 \int_0^\infty \mathrm{d}k\, \frac{E_B(k)}{k}\,, \tag{C.12}$$

which on rearrangement and use of equation (2.3), viz.

$$B_{rms}^2 = 8\pi \int_0^\infty \mathrm{d}k\, E_B(k)\;, \tag{C.13}$$

for the magnetic field strength RMS gives the desired result (C.10).

C.4 Bound on integrated tail of magnetic autocorrelation function

In this appendix we provide an estimate for integrated tail of the magnetic autocorrelation function, which will be used in subsequent derivations of the deflection-field spectral relations (2.11) and linear-regime flux spectral relation (2.35) given in Appendices D and F respectively.

It can be shown that in a finite magnetised volume, the autocorrelation function must satisfy (Ensslin and Vogt 2003)

$$\int_0^\infty \mathrm{d}r \, r^2 \, M(r) = 0 \, . \tag{C.14}$$

which implies that $M(r) = o\big[(r/\ell_B)^{-3}\big]$ as $r/\ell_B \to \infty$. It follows from this that for lengths $l \gg \ell_B$,

$$\frac{1}{B_{rms}^2 \ell_B} \int_l^\infty \mathrm{d}r \, M(r) = \mathcal{O}\left(\left(\frac{\ell_B}{l}\right)^2\right) \, . \tag{C.15}$$

Thus we conclude that for any magnetic autocorrelation function, the integral of its tail is algebraically small in ℓ_B/l. For some correlation functions (such as exponential or Gaussian), the tail of the integrated autocorrelation function is smaller still; for example, if

$$M(r) = B_{rms}^2 \, \exp\left[-r/\ell_B\right] , \tag{C.16}$$

then

$$\int_l^\infty \mathrm{d}r \, M(r) = B_{rms}^2 \, \ell_B \, \exp\left[-l/\ell_B\right] , \tag{C.17}$$

which is exponentially small in ℓ_B/l.

C.5 Derivation of relation (C.4) between normal and longitudinal autocorrelation functions

In this subsection, we show that the magnetic field's solenoidality imposes the condition (C.4) on the longitudinal and normal helical autocorrelation functions, by considering the autocorrelation tensor of the vector potential **A**.

Define vector-potential autocorrelation tensor $S_{ll'} = S_{ll'}(\mathbf{x}, \tilde{\mathbf{x}})$ by

$$S_{ll'}(\mathbf{x}, \tilde{\mathbf{x}}) \equiv \langle A_l(\mathbf{x})\, A_{l'}(\tilde{\mathbf{x}}) \rangle \ . \tag{C.18}$$

By definition, $\mathbf{B} = \nabla \times \mathbf{A}$, so the magnetic autocorrelation tensor $M_{nn'}$ is related to $S_{ll'}$ by

$$M_{ll'}(\mathbf{x}, \tilde{\mathbf{x}}) = \epsilon_{lmn} \epsilon_{l'm'n'} \frac{\partial^2}{\partial x_m \partial \tilde{x}_{m'}} S_{nn'}(\mathbf{x}, \tilde{\mathbf{x}}) \ . \tag{C.19}$$

Supposing that the stochastic vector potential is isotropic and homogeneous, we can rewrite $S_{ll'}$ in terms of the displacement vector $\mathbf{r}$, similarly to (C.1):

$$S_{ll'}(\mathbf{x}, \tilde{\mathbf{x}}) = S_{ll'}(\mathbf{r}) = S_N(r)\, \delta_{ll'} + [S_L(r) - S_N(r)]\, \frac{r_l r_{l'}}{r^2} + S_H(r)\, \epsilon_{ll's} r_s \, , \tag{C.20}$$

for longitudinal, normal and helical vector-potential autocorrelation functions $S_L(r)$, $S_N(r)$ and $S_H(r)$. We assume that these functions are unconstrained. Changing variables to

$$\mathbf{r} = \tilde{\mathbf{x}} - \mathbf{x} \, , \tag{C.21}$$

$$\bar{\mathbf{x}} = \mathbf{x} \qquad , \tag{C.22}$$

transforms partial derivatives with respect to $\tilde{\mathbf{x}}$, $\mathbf{x}$ by

$$\frac{\partial}{\partial \mathbf{x}} = \frac{\partial}{\partial \bar{\mathbf{x}}} - \frac{\partial}{\partial \mathbf{r}} \, , \tag{C.23}$$

$$\frac{\partial}{\partial \tilde{\mathbf{x}}} = \frac{\partial}{\partial \mathbf{r}} \qquad . \tag{C.24}$$

Since $S_{ll'} = S_{ll'}(\mathbf{r})$ is independent of $\bar{\mathbf{x}}$, we deduce

$$M_{ll'}(\mathbf{r}) = -\epsilon_{lmn}\epsilon_{l'm'n'}\frac{\partial^2}{\partial r_m \partial r_{m'}}\Big\{S_N(r)\,\delta_{nn'} + [S_L(r) - S_N(r)]\,\frac{r_n r_{n'}}{r^2} + S_H(r)\,\epsilon_{nn's}r_s\Big\}\ . \tag{C.25}$$

After some elementary but somewhat lengthy manipulations, it can be shown that

$$\begin{aligned}\epsilon_{lmn}\epsilon_{l'm'n'}\frac{\partial^2}{\partial r_m \partial r_{m'}}\left\{S_N(r)\,\delta_{nn'}\right\} &= \delta_{ll'}\left[S''_N(r) + \frac{1}{r}S'_N(r)\right] \\ &\quad - \frac{r_l r_{l'}}{r^2}\left[S''_N(r) - \frac{1}{r}S'_N(r)\right], \qquad \text{(C.26)} \\ \epsilon_{lmn}\epsilon_{l'm'n'}\frac{\partial^2}{\partial r_m \partial r_{m'}}\left\{[S_L(r) - S_N(r)]\,\frac{r_n r_{n'}}{r^2}\right\} &= -\delta_{ll'}\left[\frac{S'_L(r) - S'_N(r)}{r}\right] \\ &\quad + \frac{r_l r_{l'}}{r}\left[\frac{S_L(r) - S_N(r)}{r^2}\right]' \ . \qquad \text{(C.27)}\end{aligned}$$

Assuming that the magnetic autocorrelation tensor is of the form given by (C.1), it follows that

$$M_N(r) = S''_N(r) + \frac{2S'_N(r) - S'_L(r)}{r}\quad , \tag{C.28}$$

$$M_L(r) = \frac{S'_N(r)}{r} + \frac{2S_N(r) - 2S_L(r)}{r^2}\,. \tag{C.29}$$

Finally, we observe that $M_L(r)$, $M_N(r)$ satisfying these expressions implies

$$M'_L(r) + 2\frac{M_L(r) - M_N(r)}{r} = 0\,. \tag{C.30}$$

With some further algebraic rearrangement, (C.30) can be recast as (C.4), completing the proof.

Appendix D

Derivation of deflection-field spectral relation (2.11)

Section 2.2.2 claims that the magnetic-energy spectrum $E_B(k)$ of a zero-mean stochastic magnetic field ($\bar{\mathbf{B}} = 0$, $\mathbf{B} = \delta\mathbf{B}$) can be related to the one-dimensional spectrum $E_W(k_\perp)$ of the perpendicular-deflection field $\mathbf{w}(\mathbf{x}_{\perp 0})$ by spectral relation (2.11), that is

$$E_B(k) = \frac{m_p^2 c^2}{4\pi^2 l_z e^2} k E_W(k) \ . \tag{D.1}$$

We derive (D.1) in this appendix under the assumption that the correlation length ℓ_B of the stochastic magnetic field is much smaller than the path-length l_z of the proton beam through the magnetic field, as well as homogeneity and isotropy of magnetic field statistics. Our approach for doing so will be to first relate the magnetic autocorrelation function $M(r)$ defined by (C.2) in Appendix C.1 to an autocorrelation function of the perpendicular-deflection field, and then utilise the Wiener-Khinchin theorem.

We begin by defining the deflection-field autocorrelation tensor:

$$C_{ll'}(\mathbf{x}_{\perp 0}, \tilde{\mathbf{x}}_{\perp 0}) \equiv \langle w_l(\mathbf{x}_{\perp 0})\, w_{l'}(\tilde{\mathbf{x}}_{\perp 0}) \rangle \ . \tag{D.2}$$

Substituting the definition (2.8) of the perpendicular-deflection field into (D.2) gives

$$C_{ll'}(\mathbf{x}_{\perp 0}, \tilde{\mathbf{x}}_{\perp 0}) = \frac{e^2}{m_p^2 c^2} \epsilon_{lmn} \epsilon_{l'm'n'} \hat{z}_m \hat{z}_{m'} \int_0^{l_z} \mathrm{d}z \int_0^{l_z} \mathrm{d}z' \left\langle \delta B_n[\mathbf{x}_\perp(z)]\, \delta B_{n'}[\tilde{\mathbf{x}}_\perp(z')] \right\rangle \, , \tag{D.3}$$

where $\mathbf{x}_\perp(z)$ and $\tilde{\mathbf{x}}_\perp(z)$ denote the trajectories of protons with initial perpendicular positions $\mathbf{x}_{\perp 0}$ and $\tilde{\mathbf{x}}_{\perp 0}$ respectively. We then neglect the distinction between the integrated field along the undeflected trajectories and along paths parallel to the z-direction, because the resulting error is $\mathcal{O}\left(\delta\alpha, \delta\theta\right)$ under assumptions of statistical homogeneity and isotropy of magnetic field statistics. The autocorrelation tensor becomes

$$\begin{aligned} C_{ll'}(\mathbf{x}_{\perp 0}, \tilde{\mathbf{x}}_{\perp 0}) &= \frac{e^2}{m_p^2 c^2} \epsilon_{lmn} \epsilon_{l'm'n'} \hat{z}_m \hat{z}_{m'} \int_0^{l_z} \mathrm{d}z \int_0^{l_z} \mathrm{d}z' \left\langle \delta B_n(\mathbf{x}_{\perp 0}, z)\, \delta B_{n'}(\tilde{\mathbf{x}}_{\perp 0}, z') \right\rangle \\ &= \frac{e^2}{m_p^2 c^2} \epsilon_{lmn} \epsilon_{l'm'n'} \hat{z}_m \hat{z}_{m'} \\ &\qquad \times \int_0^{l_z} \mathrm{d}z \int_0^{l_z} \mathrm{d}z'\, M_{nn'}(\mathbf{x}_{\perp 0} + z\hat{\mathbf{z}}, \tilde{\mathbf{x}}_{\perp 0} + z'\hat{\mathbf{z}}) \, , \end{aligned} \tag{D.4}$$

where we have introduced the magnetic autocorrelation tensor defined by (C.1) in C. Anticipating a recourse to homogeneity and isotropy of the magnetic autocorrelation tensor, change variables in the double integral by

$$(\mathbf{r}_\perp, r_z) = (\tilde{\mathbf{x}}_{\perp 0} - \mathbf{x}_{\perp 0}, z' - z) \, , \tag{D.5}$$

$$\bar{z} = z \qquad\qquad\qquad , \tag{D.6}$$

which on explicitly assuming a homogeneous, isotropic magnetic autocorrelation tensor gives a homogeneous, isotropic deflection-field autocorrelation tensor

$$C_{ll'}(r_\perp) = \frac{e^2}{m_p^2 c^2} \epsilon_{lmn} \epsilon_{l'm'n'} \hat{z}_m \hat{z}_{m'} \int_0^{l_z} \mathrm{d}\bar{z} \int_{-\bar{z}}^{l_z - \bar{z}} \mathrm{d}r_z\, M_{nn'}\left(\sqrt{r_\perp^2 + r_z^2}\right) \, . \tag{D.7}$$

The small scale of the field ℓ_B allows for an extension of the integration limits to $(-\infty, \infty)$ via an intermediate scale $\ell_B \ll l \ll l_z$, producing an $\mathcal{O}(\ell_B/l)$ error from

(C.15) in Appendix C.4. The outer integral can then be evaluated independently, leaving

$$C_{ll'}(r_\perp) = \frac{l_z e^2}{m_p^2 c^2} \epsilon_{lmn} \epsilon_{l'm'n'} \hat{z}_m \hat{z}_{m'} \int_{-\infty}^{\infty} \mathrm{d}r_z \, M_{nn'}\left(\sqrt{r_\perp^2 + r_z^2}\right) . \tag{D.8}$$

Taking the trace of the deflection-field autocorrelation tensor gives the deflection-field autocorrelation function $C\left(r_\perp\right) \equiv C_{ll}(r_\perp)$ in terms of the magnetic autocorrelation function:

$$C(r_\perp) = \frac{l_z e^2}{m_p^2 c^2} \int_{-\infty}^{\infty} \mathrm{d}r_z \, \left[M\left(\sqrt{r_\perp^2 + r_z^2}\right) - M_{zz}\left(\sqrt{r_\perp^2 + r_z^2}\right)\right] . \tag{D.9}$$

We can then use the solenoidality of the magnetic field – in particular, relation (C.4) between the longitudinal and normal correlation functions – to show that

$$\begin{aligned} \int_{-\infty}^{\infty} \mathrm{d}r_z \, M_{zz}\left(\sqrt{r_\perp^2 + r_z^2}\right) &= \int_{-\infty}^{\infty} \mathrm{d}r_z \, \frac{r_z^2}{r^2} M_L\left(\sqrt{r_\perp^2 + r_z^2}\right) + \frac{r_\perp^2}{r^2} M_N\left(\sqrt{r_\perp^2 + r_z^2}\right) \\ &= \frac{1}{2} \int_{-\infty}^{\infty} \mathrm{d}r_z \, M\left(\sqrt{r_\perp^2 + r_z^2}\right) . \end{aligned} \tag{D.10}$$

Therefore,

$$C(r_\perp) = \frac{l_z e^2}{m_p^2 c^2} \int_{0}^{\infty} \mathrm{d}r_z \, M\left(\sqrt{r_\perp^2 + r_z^2}\right) . \tag{D.11}$$

This correlation measure has an essentially identical form to that for Faraday rotation autocorrelation function (see Ensslin and Vogt 2003), and so analogies can be made with results derived in that case. In particular, the correlation length of the magnetic field is related to $C(0)$ by

$$\ell_B = \frac{m_p^2 c^2}{l_z e^2} \frac{C(0)}{M(0)} , \tag{D.12}$$

which in turn can be rearranged to give the RMS perpendicular-deflection field:

$$w_{rms} = \frac{e \left\langle \delta \mathbf{B}^2 \right\rangle^{1/2}}{m_p c} \sqrt{l_z \ell_B} \, . \tag{D.13}$$

Deflection angle RMS (2.13) follows immediately.

The relation (D.1) between the magnetic-energy spectrum and the perpendicular-deflection field spectrum can be found by recourse to the Wiener-Khinchin theorem, which takes the following form for an isotropic deflection-field autocorrelation function:

$$E_W(k_\perp) = 2\pi k_\perp \hat{C}(k_\perp) \ , \tag{D.14}$$

where $\hat{C}(k_\perp)$ is the Fourier-transformed deflection-field autocorrelation function. Fourier-transforming (D.11) in the perpendicular direction gives

$$\hat{C}(k_\perp) = \frac{\pi l_z e^2}{m_p^2 c^2} \hat{M}(k_\perp, 0) \ . \tag{D.15}$$

However, since magnetic fluctuations are assumed isotropic, we note that

$$\hat{M}(k_\perp, 0) = \hat{M}(k_\perp) = 4\pi k_\perp^2 E_B(k_\perp) \ , \tag{D.16}$$

where the second equality follows from equation (C.7) in Appendix C.1. The desired result (D.1) is obtained by substituting (D.14) and (D.16) into (D.15), and rearranging.

In addition to the proof of (D.1), we provide one comment on its validity for compact configurations. The assumption of universal homogeneity and isotropic field statistics is technically an inconsistent one for inhomogeneous fields (as is inevitable for a compact magnetic field); however, autocorrelation-type analysis can be extended to include slow variation along path length. In particular, if geometrical statistics are preserved along the path length, but $\left\langle \delta \mathbf{B}^2 \right\rangle^{1/2}$ slowly varies, then we can describe magnetic autocorrelation tensors of the form

$$M_{nn'}(r) = \tilde{M}_{nn'}(r) \left\langle \delta \mathbf{B}^2 \right\rangle(z) \ . \tag{D.17}$$

The deflection-field autocorrelation function becomes

$$C(r_\perp) = \frac{e^2}{m_p^2 c^2} \int_0^{l_z} \mathrm{d}\bar{z} \left\langle \delta \mathbf{B}^2 \right\rangle(\bar{z}) \int_0^{\infty} \mathrm{d}r_z \, \tilde{M}\left(\sqrt{r_\perp^2 + r_z^2}\right) . \tag{D.18}$$

However, such a picture is only valid if there is a sufficient separation of scales between variation of $\langle \delta \mathbf{B}^2 \rangle(z)$ and stochastic fluctuations. In particular, if

$$\frac{l_z}{\ell_B} \sim \frac{\max_{z \in [0, l_z]} \{\delta \mathbf{B}(z)\}}{\left\langle \delta \mathbf{B}^2 \right\rangle^{1/2}} , \tag{D.19}$$

then the magnitude of deflections will deviate from (D.1).

Appendix E

Derivation of linear-regime image-flux relation (2.26) from small-deflection RK image-flux relation (2.9)

In Section 2.3.1, it was stated that in the linear regime, plasma-image mapping (2.7), and RK image-flux relation (2.9) reduce to simplified expressions (2.24) and (2.25), which for convenience we reproduce here:

$$\mathbf{x}_{\perp}^{(s)} = \frac{r_s + r_i}{r_i} \mathbf{x}_{\perp 0} \left[1 + \mathcal{O}(\mu)\right] \, , \tag{E.1}$$

and

$$\frac{\delta\Psi\left(\mathbf{x}_{\perp}^{(s)}\right)}{\Psi_0^{(s)}} = \frac{r_s r_i}{r_s + r_i} \frac{4\pi e}{m_p c^2 V} \int_0^{l_z} j_z\left(\mathbf{x}_{\perp 0}\left(1 + \frac{z'}{r_i}\right), z'\right) \mathrm{d}z' \, . \tag{E.2}$$

It was also claimed that the image-flux deviation $\delta\Psi(\mathbf{x}_{\perp 0})$ could be related to the deflection-field potential $\varphi(\mathbf{x}_{\perp 0})$ defined by (2.15) according to Poisson equation (2.30):

$$\nabla_{\perp 0}^2 \varphi(\mathbf{x}_{\perp 0}) = -\Xi(\mathbf{x}_{\perp 0}) \, , \tag{E.3}$$

where $\Xi(\mathbf{x}_{\perp 0})$ is a source function defined by (2.30),

$$\Xi(\mathbf{x}_{\perp 0}) = \frac{r_s + r_i}{r_i} \frac{V}{r_s} \frac{\delta\Psi\left(\mathbf{x}_\perp^{(s)}\right)}{\Psi_0^{(s)}} \,. \tag{E.4}$$

In this appendix we derive these results using the fact that in the linear regime, $\mu \ll 1$, allowing for asymptotic expansions of plasma-image mapping (2.7) and RK image-flux relation (2.9) in μ. It also examines the proper magnitude of terms neglected in the asymptotic expansion of RK image-flux relation (2.9) in μ – in particular, whether it is consistent to not expand the argument of the image-flux distribution in terms of its argument, the plasma-image mapping.

To derive the simplified plasma-image mapping (E.1), we start from full mapping (2.7), that is,

$$\mathbf{x}_\perp^{(s)}(\mathbf{x}_{\perp 0}) = \left(\frac{r_s + r_i}{r_i} \mathbf{x}_{\perp 0} + \frac{r_s}{V} \mathbf{w}(\mathbf{x}_{\perp 0}) \right) \left[1 + \mathcal{O}(\delta\alpha, \delta\theta) \right] \,, \tag{E.5}$$

and note that

$$\frac{r_s \left| \mathbf{w}(\mathbf{x}_{\perp 0}) \right| / V}{(r_s + r_i) \left| \mathbf{x}_{\perp 0} \right| / r_i} \sim \mu \,. \tag{E.6}$$

Thus, (E.5) can be re-written as the simplified linear mapping (E.1) to leading order in μ:

$$\mathbf{x}_\perp^{(s)} = \frac{r_s + r_i}{r_i} \mathbf{x}_{\perp 0} \left[1 + \mathcal{O}(\delta\alpha, \mu) \right] \,. \tag{E.7}$$

Note that the asymptotic expansion carried out in $\delta\theta$ in order to derive (E.5) is superceded by the expansion in μ, since by its definition μ is a larger parameter.

Now turning to the image-flux relation, we begin with (2.9):

$$\Psi\left(\mathbf{x}_\perp^{(s)}(\mathbf{x}_{\perp 0})\right) = \sum_{\mathbf{x}_\perp^{(s)} = \mathbf{x}_\perp^{(s)}(\mathbf{x}_{\perp 0})} \frac{\Psi_0}{\left| \det \nabla_{\perp 0} \left[\mathbf{x}_\perp^{(s)}(\mathbf{x}_{\perp 0}) \right] \right|} \,. \tag{E.8}$$

Evaluating the determinant in the denominator of image-flux relation (E.8) explicitly in terms of the full plasma-image mapping (E.5), we find

$$\begin{aligned}\det \frac{\partial \mathbf{x}_{\perp}^{(s)}}{\partial \mathbf{x}_{\perp 0}} &= \det \left(\frac{r_s + r_i}{r_i} \underline{\underline{\mathrm{I}}} + \frac{r_s}{V} \frac{\partial \mathbf{w}(\mathbf{x}_{\perp 0})}{\partial \mathbf{x}_{\perp 0}} \right) \\ &= \left(\frac{r_s + r_i}{r_i} \right)^2 \left\{ 1 + \frac{r_s r_i}{(r_s + r_i)\, V} \nabla_{\perp 0} \cdot \mathbf{w}(\mathbf{x}_{\perp 0}) \right. \\ &\qquad \left. + \left[\frac{r_s r_i}{(r_s + r_i)\, V} \right]^2 \det \frac{\partial \mathbf{w}(\mathbf{x}_{\perp 0})}{\partial \mathbf{x}_{\perp 0}} \right\} . \end{aligned} \tag{E.9}$$

Estimating the relative size of terms on the right hand side of (E.9), we have

$$\frac{r_s r_i}{(r_s + r_i)\, V} \nabla_{\perp 0} \cdot \mathbf{w}(\mathbf{x}_{\perp 0}) \sim \mu \, , \qquad \left(\frac{r_s r_i}{(r_s + r_i)\, V} \right)^2 \det \frac{\partial \mathbf{w}(\mathbf{x}_{\perp 0})}{\partial \mathbf{x}_{\perp 0}} \sim \mu^2 \, . \tag{E.10}$$

Assuming $\mu \ll 1$, the determinant can therefore be expanded in terms of μ as

$$\det \frac{\partial \mathbf{x}_{\perp}^{(s)}}{\partial \mathbf{x}_{\perp 0}} = \left(\frac{r_s + r_i}{r_i} \right)^2 \left[1 + \frac{r_s r_i}{(r_s + r_i)\, V} \nabla_{\perp 0} \cdot \mathbf{w}(\mathbf{x}_{\perp}) + \mathcal{O}\big(\mu^2\big) \right] . \tag{E.11}$$

Then expanding image-flux relation (E.8) in terms of μ leads to

$$\Psi\Big(\mathbf{x}_{\perp}^{(s)}\Big) \approx \left(\frac{r_i}{r_s + r_i} \right)^2 \Psi_0 \left[1 - \frac{r_s r_i}{(r_s + r_i)\, V} \nabla_{\perp 0} \cdot \mathbf{w}(\mathbf{x}_{\perp 0}) + \mathcal{O}\big(\mu^2\big) \right] , \tag{E.12}$$

which can be re-written in terms of the relative flux, normalised by the unperturbed image flux

$$\Psi_0^{(s)} \equiv \left(\frac{r_i}{r_s + r_i} \right)^2 \Psi_0 \, , \tag{E.13}$$

to give

$$\frac{\delta \Psi\Big(\mathbf{x}_{\perp}^{(s)}\Big)}{\Psi_0^{(s)}} = \frac{\Psi\Big(\mathbf{x}_{\perp}^{(s)}\Big) - \Psi_0^{(s)}}{\Psi_0^{(s)}} \approx - \frac{r_s r_i}{(r_s + r_i)\, V} \nabla_{\perp 0} \cdot \mathbf{w}(\mathbf{x}_{\perp 0}) \, . \tag{E.14}$$

The perpendicular-deflection field in this case is given by (2.16), that is

$$\mathbf{w}(\mathbf{x}_{\perp 0}) = \frac{e}{m_p c} \hat{\mathbf{z}} \times \int_0^{l_z} \mathrm{d}z' \, \mathbf{B}\bigg(\mathbf{x}_{\perp 0} \left(1 + \frac{z'}{r_i} \right) , z' \bigg) \left[1 + \mathcal{O}\bigg(\delta\alpha , \delta\theta \, \frac{l_z}{\ell_B} \bigg) \right] , \tag{E.15}$$

since for $\mu \ll 1$, $\delta\theta \, l_z/\ell_B \sim \mu \, \delta\alpha \, (r_s + r_i) / r_s \ll 1$. We recover the result that in the linear regime the image displays the undeflected path integrated z-component of the magnetic field curl:

$$\begin{aligned}
\frac{\delta\Psi\left(\mathbf{x}_\perp^{(s)}\right)}{\Psi_0^{(s)}} &= \frac{r_s r_i}{r_s+r_i}\frac{e}{m_p c V}\hat{\mathbf{z}}\cdot\int_0^{l_z}\nabla_{\perp 0}\times\mathbf{B}\left(\mathbf{x}_{\perp 0}\left(1+\frac{z'}{r_i}\right),z'\right)\mathrm{d}z'\left[1+\mathcal{O}(\delta\alpha,\mu)\right] \\
&= \frac{r_s r_i}{r_s+r_i}\frac{e}{m_p c V} \\
&\qquad \times\hat{\mathbf{z}}\cdot\int_0^{l_z}\nabla\times\mathbf{B}\left(\mathbf{x}_{\perp 0}\left(1+\frac{z'}{r_i}\right),z'\right)\mathrm{d}z'\left[1+\mathcal{O}(\delta\alpha,\mu)\right] \, . \qquad \text{(E.16)}
\end{aligned}$$

Applying Ampére's law (in the absence of the displacement current) gives the desired result (F.5).

To derive (2.30), we start from an expression for the perpendicular-deflection field in terms of the deflection-field potential:

$$\mathbf{w}(\mathbf{x}_{\perp 0}) = \frac{V}{r_s}\nabla_{\perp 0}\varphi(\mathbf{x}_{\perp 0})\left[1+\mathcal{O}\left(\delta\theta\,\frac{l_z}{\ell_B}\right)\right] \, , \qquad \text{(E.17)}$$

Substitution of (E.17) into (E.14) gives

$$\frac{\delta\Psi\left(\mathbf{x}_\perp^{(s)}\right)}{\Psi_0^{(s)}} = -\frac{r_i}{r_s+r_i}\nabla_{\perp 0}^2\varphi(\mathbf{x}_{\perp 0}) \, , \qquad \text{(E.18)}$$

which on rearrangement gives the expected result (2.30).

A potential subtlety in the derivations of (F.5) and (2.30) (noticed by Graziani et al. (2017)) arises from the observation that the image-flux distribution is evaluated in the image-coordinate system. More specifically, we need to check whether using (E.5) for calculating the argument for the image-flux distribution does not result in the systematic neglect of any $\mathcal{O}(\mu)$ terms in the expansion of (E.8) in μ. We do this by first assuming sufficiently small image-flux gradients, then Taylor expanding (E.12):

$$\Psi\left(\mathbf{x}_\perp^{(s)}\right) = \Psi\left(\frac{r_s+r_i}{r_i}\mathbf{x}_{\perp 0}\right) + \frac{r_s}{V}\mathbf{w}\cdot\nabla_\perp^{(s)}\Psi\left(\frac{r_s+r_i}{r_i}\mathbf{x}_{\perp 0}\right)\left[1+\mathcal{O}\left(\frac{r_s\,\delta\theta}{l_\Psi}\right)\right] \, , \quad \text{(E.19)}$$

where $\nabla_{\perp}^{(s)} \equiv \partial/\partial \mathbf{x}_{\perp}^{(s)}$, and $l_{\Psi} \gg r_s \delta\theta$ is a typical scale on which image-flux deviations occur. If we further assume that image-flux deviations occur with the same length scale as magnetic field fluctuations including the image-magnification factor $\mathcal{M} = \left(r_s + r_i\right)/r_i$, that is $l_{\Psi} \sim \tilde{l}_B = \mathcal{M}\ell_B$, the size of the discrepancy in the image-flux distribution resulting from using (E.5) as the image-flux distribution function's argument is

$$\Psi\left(\mathbf{x}_{\perp}^{(s)}\right) - \Psi\left(\frac{r_s + r_i}{r_i}\mathbf{x}_{\perp 0}\right) = \frac{r_s}{V}\mathbf{w} \cdot \nabla_{\perp}^{(s)}\Psi\left(\frac{r_s + r_i}{r_i}\mathbf{x}_{\perp 0}\right) \sim \mu\,\delta\Psi \ll \delta\Psi\,. \qquad \text{(E.20)}$$

a quadratic term in μ. Thus we see that using (E.5) as the argument for the image-flux distribution is consistent to the asymptotic order of the expansion provided the perpendicular-deflection field and its derivatives vary on similar scales to the magnetic field (taking into account the image-magnification factor). That being said, this term could become important if image-flux gradients occur on smaller scales than gradients of the magnetic field.

Appendix F

Derivation of linear-regime flux RMS relation (2.26) and spectral relation (2.35)

Section 2.3.1 claims that provided $\mu \ll 1$, the RMS of relative image-flux deviations can be related to the RMS magnetic field strength via equation (2.26), which is

$$\left\langle \frac{\delta\Psi}{\Psi_0^{(s)}}^{2} \right\rangle^{1/2} = \sqrt{\frac{\pi}{2}} \frac{r_i r_s}{r_s + r_i} \frac{e B_{rms}}{mcV} \sqrt{\frac{l_z}{l_\Psi}} = \frac{\mu}{\mu_0}\,, \tag{F.1}$$

where μ_0 is defined by $\mu_0 = \sqrt{2 l_\Psi / \ell_B \pi}$ – l_Ψ is the relative-image flux correlation length defined subsequently in equation (F.27) – and satisfies lower bound $\mu_0 \leq 2/\pi$.

Furthermore, under the same assumption $\mu \ll 1$ the magnetic-energy spectrum $E_B(k)$ is related to the 2D spectrum of image-flux deviations $\hat{\eta}(k)$ for homogeneous and isotropic magnetic field statistics satisfying $\ell_B \ll l_z$ by equation (2.35):

$$E_B(k) = \frac{1}{2\pi} \frac{m_p^2 c^2 V^2}{e^2 r_s^2 l_z} \hat{\eta}\left(\frac{r_i}{r_s + r_i} k \right) . \tag{F.2}$$

where $\hat{\eta}(k)$ is defined by

$$\hat{\eta}(k_\perp) \equiv \frac{1}{2\pi}\int \mathrm{d}\theta \left(\frac{1}{\Psi_0^{(s)}}\right)^2 \left\langle \left|\delta\hat{\Psi}(\mathbf{k}_\perp)\right|^2 \right\rangle , \tag{F.3}$$

and $\delta\hat{\Psi}(\mathbf{k}_\perp)$ is the Fourier-transformed relative image-flux deviation. In this appendix we prove both results using a similar approach to that adopted in Appendix D: we first define an autocorrelation function of the relative image-flux distribution function and then writing the magnetic autocorrelation function in terms of it. Evaluating this at the origin will give (F.1). We shall then use the Wiener-Khinchin theorem to relate the respective spectra of the relative-image flux and magnetic field.

Adopting a uniform initial flux distribution $\Psi_0(\mathbf{x}_{\perp 0}) = \Psi_0$, define the image-flux autocorrelation function by

$$\eta\left(\mathbf{x}_\perp^{(s)}, \tilde{\mathbf{x}}_\perp^{(s)}\right) = \left\langle \frac{\delta\Psi\left(\mathbf{x}_\perp^{(s)}\right)}{\Psi_0^{(s)}} \frac{\delta\Psi\left(\tilde{\mathbf{x}}_\perp^{(s)}\right)}{\Psi_0^{(s)}} \right\rangle . \tag{F.4}$$

This correlation function can then be related to the magnetic autocorrelation function by substituting for the relative image-flux distribution using the linear-regime image-flux relation (2.25), which can be written as

$$\frac{\delta\Psi\left(\mathbf{x}_\perp^{(s)}\right)}{\Psi_0^{(s)}} \approx \frac{r_s r_i}{r_s + r_i}\frac{e}{m_p c V}\hat{\mathbf{z}} \cdot \int_0^{l_z} \nabla \times \delta\mathbf{B}\left(\mathbf{x}_{\perp 0}\left(1 + \frac{z}{r_i}\right), z\right) \mathrm{d}z \left[1 + \mathcal{O}(\delta\alpha, \mu)\right] . \tag{F.5}$$

The substitution gives

$$\begin{aligned} \eta\left(\mathbf{x}_\perp^{(s)}, \tilde{\mathbf{x}}_\perp^{(s)}\right) &= \left\langle \frac{e^2 r_i^2 r_s^2}{m_p^2 c^2 V^2 \left(r_s + r_i\right)^2} \epsilon_{lmn}\epsilon_{l'm'n'}\hat{z}_l \hat{z}_{l'} \int_0^{l_z} \mathrm{d}z \int_0^{l_z} \mathrm{d}\tilde{z}\, \frac{\partial\, \delta B_n(\mathbf{x})}{\partial x_m} \frac{\partial\, \delta B_{n'}(\tilde{\mathbf{x}})}{\partial \tilde{x}_{m'}} \right\rangle \\ &= \frac{e^2 r_i^2 r_s^2}{m_p^2 c^2 V^2 \left(r_s + r_i\right)^2} \epsilon_{lmn}\epsilon_{l'm'n'}\hat{z}_l \hat{z}_{l'} \int_0^{l_z} \mathrm{d}z \int_0^{l_z} \mathrm{d}\tilde{z}\, \frac{\partial^2 M_{nn'}(\mathbf{x}, \tilde{\mathbf{x}})}{\partial x_m \partial \tilde{x}_{m'}} , \end{aligned} \tag{F.6}$$

where $M_{nn'}(\mathbf{x}, \tilde{\mathbf{x}})$ is again the magnetic autocorrelation tensor, and its arguments are the plasma coordinates

$$\mathbf{x} = \left[\mathbf{x}_{\perp 0}\left(1 + \frac{z}{r_i}\right), z\right], \tag{F.7}$$

$$\tilde{\mathbf{x}} = \left[\mathbf{x}_{\perp 0}\left(1 + \frac{\tilde{z}}{r_i}\right), \tilde{z}\right]. \tag{F.8}$$

As when calculating the deflection-field correlation function, we expand the argument of the autocorrelation function in (F.6) along the z-projection of unperturbed trajectories – neglecting small, $\mathcal{O}(\delta\alpha, \delta\theta)$ terms – to give simplified expressions for the plasma coordinates, the perpendicular components of which can then be written in terms of the perpendicular image-coordinate using linear-regime plasma-image mapping (2.24):

$$\mathbf{x} = \left[\frac{r_i}{r_i + r_s}\mathbf{x}_\perp^{(s)}, z\right], \tag{F.9}$$

$$\tilde{\mathbf{x}} = \left[\frac{r_i}{r_i + r_s}\tilde{\mathbf{x}}_\perp^{(s)}, \tilde{z}\right]. \tag{F.10}$$

Again we change integration variables to

$$(\mathbf{r}_\perp, r_z) = (\tilde{\mathbf{x}}_\perp - \mathbf{x}_\perp, \tilde{z} - z), \tag{F.11}$$

$$\bar{\mathbf{x}} = \mathbf{x} \qquad , \tag{F.12}$$

which transforms partial derivatives by

$$\frac{\partial}{\partial \mathbf{x}} = \frac{\partial}{\partial \bar{\mathbf{x}}} - \frac{\partial}{\partial \mathbf{r}}, \tag{F.13}$$

$$\frac{\partial}{\partial \tilde{\mathbf{x}}} = \frac{\partial}{\partial \mathbf{r}} \qquad . \tag{F.14}$$

Thus,

$$\begin{aligned}\eta\left(\mathbf{x}_\perp^{(s)},\tilde{\mathbf{x}}_\perp^{(s)}\right) &= \frac{e^2 r_i^2 r_s^2}{m_p^2 c^2 V^2 \left(r_s+r_i\right)^2}\epsilon_{lmn}\epsilon_{l'm'n'}\hat{z}_l\hat{z}_{l'} \\ &\quad\times\int_0^{l_z}\mathrm{d}\bar{z}\int_{-\bar{z}}^{l_z-\bar{z}}\mathrm{d}r_z\left(\frac{\partial^2}{\partial\bar{x}_m\partial r_{m'}}-\frac{\partial^2}{\partial r_m\partial r_{m'}}\right)M_{nn'}(\bar{\mathbf{x}},\mathbf{r})\ . \quad \text{(F.15)}\end{aligned}$$

Under the same assumption that $\ell_B \ll l_z$, we extend the limits of the inner integral to $(-\infty,\infty)$, invoking at worst an $\mathcal{O}(\ell_B/l_z)$ error. If we then assume the turbulence to be locally homogeneous, the magnetic autocorrelation function is again a function of $\mathbf{r}$ alone, eliminating the first term in the integrand (F.15). The outer integral can be evaluated independently, leaving

$$\eta\left(\mathbf{r}_\perp^{(s)}\right) = -\frac{e^2 r_i^2 r_s^2 l_z}{m_p^2 c^2 V^2 \left(r_s+r_i\right)^2}\epsilon_{lmn}\epsilon_{l'm'n'}\hat{z}_l\hat{z}_{l'}\int_{-\infty}^{\infty}\mathrm{d}r_z\,\frac{\partial^2 M_{nn'}(\mathbf{r})}{\partial r_m\partial r_{m'}}\,. \quad \text{(F.16)}$$

Alternatively writing entirely in terms of variables on the scale of the interaction region, define rescaled relative image-flux autocorrelation function

$$\eta^{(0)}(\mathbf{r}_\perp) = \eta\left(\mathbf{r}_\perp^{(s)}\right)\ , \quad \text{(F.17)}$$

which gives

$$\eta^{(0)}(\mathbf{r}_\perp) = -\frac{e^2 r_i^2 r_s^2 l_z}{m_p^2 c^2 V^2 \left(r_s+r_i\right)^2}\epsilon_{lmn}\epsilon_{l'm'n'}\hat{z}_l\hat{z}_{l'}\int_{-\infty}^{\infty}\mathrm{d}r_z\,\frac{\partial^2 M_{nn'}(\mathbf{r})}{\partial r_m\partial r_{m'}}\,. \quad \text{(F.18)}$$

If we further assume isotropy, the magnetic correlation tensor takes the form given by (C.2). In this case, it can be shown (after quite a bit of tedious but elementary manipulation) that the image flux correlation function is directly related to the magnetic autocorrelation function by

$$\eta\left(r_\perp^{(s)}\right) = \eta^{(0)}(r_\perp) = -\frac{e^2 r_i^2 r_s^2 l_z}{m_p^2 c^2 V^2 \left(r_s+r_i\right)^2}\frac{1}{r_\perp}\frac{\mathrm{d}}{\mathrm{d}r_\perp}\left(r_\perp\frac{\mathrm{d}}{\mathrm{d}r_\perp}\left[\frac{1}{2}\int_{-\infty}^{\infty}\mathrm{d}r_z\,M(r)\right]\right)\,. \quad \text{(F.19)}$$

Now, by appropriate integration of (F.19) to invert the 2D Laplacian operator, we obtain an equation with exactly the same form as the deflection autocorrelation function (D.11), but substituting an integrated form of the autocorrelation function:

$$\zeta(r_\perp) \equiv \int_{r_\perp}^{\infty} \frac{\mathrm{d}\tilde{r}_\perp}{\tilde{r}_\perp} \int_{\tilde{r}_\perp}^{\infty} \mathrm{d}r'_\perp \, r'_\perp \, \eta^{(0)}(r'_\perp) = -\frac{e^2 r_i^2 r_s^2 l_z}{m_p^2 c^2 V^2 \left(r_s + r_i\right)^2} \frac{1}{2} \int_{-\infty}^{\infty} \mathrm{d}r_z \, M(r) \ . \tag{F.20}$$

We can re-express $\zeta(r_\perp)$ as a single integral of $\eta(r_\perp)$ by swapping the order of integration:

$$\zeta(r_\perp) = \int_{r_\perp}^{\infty} \mathrm{d}r'_\perp \, r'_\perp \, \eta^{(0)}(r'_\perp) \int_{r_\perp}^{r'_\perp} \frac{\mathrm{d}\tilde{r}_\perp}{\tilde{r}_\perp} = \int_{r_\perp}^{\infty} \mathrm{d}r'_\perp \, r'_\perp \, \eta^{(0)}(r'_\perp) \log \frac{r'_\perp}{r_\perp} \, . \tag{F.21}$$

We can then derive an expression for the magnetic autocorrelation function in terms of $\zeta(r)$ by noting (F.20) is an Abel integral equation which can be inverted (Ensslin and Vogt 2003). The magnetic autocorrelation function is given by

$$M(r) = \frac{2}{\pi} \frac{m_p^2 c^2 V^2 \left(r_s + r_i\right)^2}{e^2 r_i^2 r_s^2 l_z} \int_r^{\infty} \mathrm{d}y \, \frac{\zeta'(y)}{\sqrt{y^2 - r^2}} \, . \tag{F.22}$$

We can rewrite this in terms of the relative image-flux autocorrelation function using

$$\zeta'(y) = -\frac{1}{y} \int_y^{\infty} \mathrm{d}r' \, r' \, \eta^{(0)}(r') \ , \tag{F.23}$$

and so

$$M(r) = -\frac{2}{\pi} \frac{m_p^2 c^2 V^2 \left(r_s + r_i\right)^2}{e^2 r_i^2 r_s^2 l_z} \int_r^{\infty} \frac{\mathrm{d}y}{y\sqrt{y^2 - r^2}} \int_{r'}^{\infty} \mathrm{d}r' \, r' \, \eta^{(0)}(r') \ . \tag{F.24}$$

Swapping the order of integration again, obtain

$$M(r) = -\frac{2}{\pi} \frac{m_p^2 c^2 V^2 \left(r_s + r_i\right)^2}{e^2 r_i^2 r_s^2 l_z} \int_r^{\infty} \mathrm{d}r' \, r' \, \eta^{(0)}(r') \int_r^{r'} \frac{\mathrm{d}y}{y\sqrt{y^2 - r^2}} \, . \tag{F.25}$$

This is the desired relation for the magnetic autocorrelation function in terms of the relative image-flux autocorrelation function.

To recover (F.1), we take the limit as $r \to 0$ in (F.25) and using the regularity condition, deducing

$$\begin{aligned} \frac{B_{rms}^2}{8\pi} &= \frac{1}{(2\pi)^2} \frac{m_p^2 c^2 V^2 (r_s + r_i)^2}{e^2 r_i^2 r_s^2 l_z} \int_0^\infty \mathrm{d}r \, \eta^{(0)}(r) \\ &= \frac{1}{(2\pi)^2} \frac{m_p^2 c^2 V^2 (r_s + r_i)}{e^2 r_i r_s^2 l_z} \int_0^\infty \mathrm{d}r \, \eta(r) \ . \end{aligned} \tag{F.26}$$

Now, defining relative image-flux correlation length l_Ψ by

$$l_\Psi = \int_0^\infty \mathrm{d}r \, \frac{\eta^{(0)}(r)}{\eta^{(0)}(0)} = \left\langle \left(\frac{\delta\Psi}{\Psi_0^{(s)}} \right)^2 \right\rangle^{-1/2} \int_0^\infty \mathrm{d}r \, \eta^{(0)}(r) \ , \tag{F.27}$$

we see by substituting (F.27) into (F.26) that the RMS of relative image-flux deviations is related to the magnetic field RMS by

$$\left\langle \left(\frac{\delta\Psi}{\Psi_0^{(s)}} \right)^2 \right\rangle^{1/2} = \sqrt{\frac{\pi}{2}} \frac{r_i r_s}{r_s + r_i} \frac{e B_{rms}}{m_p c V} \sqrt{\frac{l_z}{l_\Psi}} = \frac{\mu}{\mu_0} \, , \tag{F.28}$$

in agreement with (F.1).

The relation (F.2) between the magnetic-energy spectrum and two-dimensional spectrum of the relative image-flux in the linear regime can be determined by rewriting (F.19) in the following form:

$$\eta^{(0)}(r_\perp) = -\frac{e^2 r_s^2 r_i^2 l_z}{m_p^2 c^2 V^2 (r_s + r_i)^2} \nabla_\perp^2 \left[\frac{1}{2} \int_{-\infty}^\infty \mathrm{d}r_z \, M(r) \right] \, , \tag{F.29}$$

where $\nabla_\perp = \partial/\partial \mathbf{r}_\perp$. Now Fourier transforming with respect to $r_\perp$, (F.29) becomes

$$\hat{\eta}^{(0)}(k_\perp) = \frac{e^2 r_s^2 r_i^2 l_z}{2 m_p^2 c^2 V^2 (r_s + r_i)^2} k_\perp^2 \hat{M}(k_\perp, 0) \ . \tag{F.30}$$

Then, we note that the Fourier transform of the rescaled relative image-flux autocorrelation function is related to the Fourier transform of the relative image-flux autocorrelation function by

$$\hat{\eta}^{(0)}(k_\perp) = \hat{\eta}(k_\perp)\left(\frac{r_i}{r_s + r_i}\right)^2 . \tag{F.31}$$

Again invoking isotropic magnetic field statistics and the Wiener-Khinchin theorem, we deduce

$$\hat{\eta}(k) = \frac{2\pi e^2 r_s^2 r_i^2 l_z}{m_p^2 c^2 V^2 \left(r_s + r_i\right)^2} E_B(k) . \tag{F.32}$$

This can be rearranged to give (F.2) as claimed. The derived result agrees with previous work by Graziani et al. (2017).

Finally, to demonstrate that $\mu_0 \leq 2/\pi$, we note the following result:

$$\left\langle \left(\frac{\delta\Psi}{\Psi_0^{(s)}}\right)^2 \right\rangle = 2\pi \int_0^\infty \mathrm{d}k\, k\hat{\eta}(k) = \frac{r_s^2 r_i^2}{\left(r_i + r_s\right)^2} \frac{4\pi^2 e^2 l_z}{m_p^2 c^2 V^2} \int_0^\infty \mathrm{d}k\, k E_B(k) . \tag{F.33}$$

Substituting for the mean of squared relative image-flux using (F.28), this can be used to find the relative image-flux correlation length l_Ψ in terms of the magnetic-energy spectrum:

$$l_\Psi = \frac{\int_0^\infty \mathrm{d}k\, E_B(k)}{\int_0^\infty \mathrm{d}k\, k E_B(k)} . \tag{F.34}$$

Recalling that the magnetic correlation length is given by

$$\ell_B = \frac{\pi}{2} \frac{\int_0^\infty \mathrm{d}k\, E_B(k)/k}{\int_0^\infty \mathrm{d}k\, E_B(k)} , \tag{F.35}$$

we conclude that

$$\mu_0 = \sqrt{\frac{2 l_\Psi}{\pi \ell_B}} = \frac{2}{\pi} \frac{\int_0^\infty \mathrm{d}k\, E_B(k)}{\left[\int_0^\infty \mathrm{d}k\, k E_B(k)\right]^{1/2} \left[\int_0^\infty \mathrm{d}k\, E_B(k)/k\right]^{1/2}} \leq \frac{2}{\pi} , \tag{F.36}$$

where the final step results from the Cauchy-Schwarz inequality applied to the (positive) integrands in the denominator.

To investigate the accuracy of (F.1) as μ is increased, we consider a particular stochastic field configuration and then vary the effective μ of a proton-imaging set-up

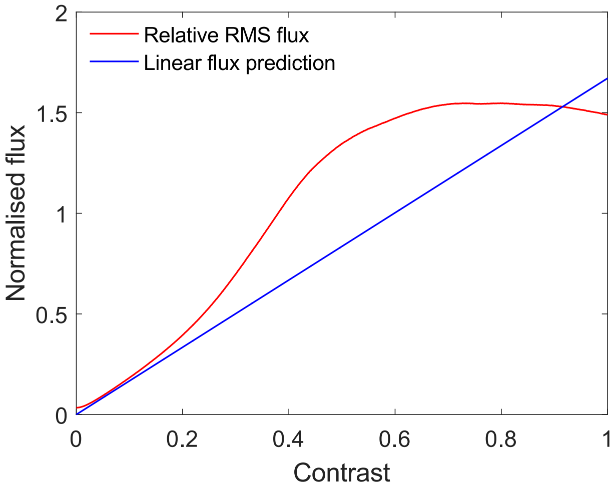

Figure F.1: Validity of linear-regime prediction (F.28) of RMS relative image-flux variations for general μ. For a particular stochastic magnetic field specified on a 201^3 array in interaction region, side length $l_i = l_\perp = l_z = 0.1\,\mathrm{cm}$ (grid spacing $\delta x = l_i/201$), the RMS of magnetic field strength B_{rms} is varied; for each different value of B_{rms}, the same proton-imaging set-up outlined in Figure 2.1 is carried out, and the associated RMS of relative image-flux deviations is calculated. This is compared to linear-regime prediction (F.1), with $\mu_0 = 3/2\sqrt{2\pi} \approx 0.6$. The field has a magnetic-energy spectrum of the form (F.37), $B_{rms} = 10\,\mathrm{kG}$, and $\ell_B = 30\,\mu\mathrm{m}$.

applied to it. In particular, we consider a random collection of 'cocoon' magnetic fields (see Appendix G.3), which has the following magnetic-energy spectrum:

$$E_B(k) = \frac{\langle \mathbf{B}^2 \rangle \, \ell_e}{12\sqrt{2}\pi^{3/2}} \ell_e^4 k^4 \exp\left(-\ell_e^2 k^2/2\right) , \tag{F.37}$$

for ℓ_e the typical size of a cocoon. It can be shown for this form of magnetic-energy spectrum that normalisation constant μ_0 is given by $\mu_0 = 3/2\sqrt{2\pi} \approx 0.6$ – derived in Appendix G. Figure F.1 plots this prediction for a range of normalised μ, along with the measured RMS for a particular numerical numerical instantiation of a Gaussian cocoon field.

We observe that (F.1) is very accurate for small μ; however, this no longer holds as μ increases. For $0.25 < \mu < 0.9$, the RMS of relative image-flux variations is under-predicted, with

$$\left\langle \left(\frac{\delta\Psi}{\Psi_0^{(s)}} \right)^2 \right\rangle \sim 1 \implies \mu \approx 0.35 \approx 0.6\mu_0 \,. \tag{F.38}$$

For $\mu > 0.7$, the RMS of relative image-flux deviations begins to decrease with μ, with the consequence that for large values of μ, it becomes much larger than the RMS of relative image-flux deviations. In short, the condition of order-unity image-flux variations does not imply that μ as defined by (2.17) in the main text is of the same order.

Appendix G

Calculation of spectra/correlation scales for model stochastic fields

In this chapter, we consider three particular examples of magnetic energy spectra: the power law spectra (2.21) and (2.55) specified in the main text, and the 'cocoon' spectrum (first given in (F.37)). For each of these fields, this appendix provides a more detailed summary of the properties of magnetic fields with this spectra and associated image-flux distributions: more specifically, the magnetic correlation length ℓ_B given by (2.4), the RMS of the perpendicular-deflection field w_{rms}, the relative image-flux correlation length l_Ψ given by (F.27), the RMS of relative image-flux deviations in the linear regime, and μ normalisation constant μ_0.

G.1 Power law spectrum (2.21)

For this chapter we consider the simplest possible power law of the form (for $p \neq 1$)

$$E_B(k) = \frac{B_{rms}^2}{8\pi}\,(p-1)\,\frac{k^{-p}}{k_l^{-p+1} - k_u^{-p+1}}\,, \tag{G.1}$$

where $k_l = 2\pi/l_c$ and k_u are lower and upper spectral wavenumber cutoffs. Calculating the correlation length ℓ_B with (2.4) gives

$$\ell_B = \frac{l_c}{4}\frac{p-1}{p}\frac{1-(k_l/k_u)^p}{1-(k_l/k_u)^{p-1}} \approx \frac{p-1}{p}\frac{l_c}{4}\,, \tag{G.2}$$

where the approximate expression is valid is $(k_l/k_u)^{p-1} \ll 1$. Note that the correlation length is approximately four times smaller than the wavelength associated with the lower wavenumber cutoff, even if the spectrum is very steep ($p \gg 1$). The RMS of the perpendicular deflections is then given by

$$w_{rms}^2 = \frac{l_c}{4}\frac{p-1}{p}\frac{1-(k_l/k_u)^p}{1-(k_l/k_u)^{p-1}}\frac{e^2\left\langle \mathbf{B}^2\right\rangle l_z}{m_p^2c^2}\,. \tag{G.3}$$

The relative image-flux correlation length – calculated using (F.34) – is related to the upper and lower spectral wavenumber cutoffs by

$$l_\Psi = \frac{2}{\pi}\frac{p\,(p-2)}{(p-1)^2}\frac{\left(1-(k_l/k_u)^{p-1}\right)^2}{\left(1-(k_l/k_u)^p\right)\left(1-(k_l/k_u)^{p-2}\right)}\ell_B\,. \tag{G.4}$$

Substituting this result into RMS of relative image-flux deviations (2.26) gives

$$\begin{aligned}\left\langle\left(\frac{\delta\Psi}{\Psi_0^{(s)}}\right)^2\right\rangle &= \frac{\pi}{2}\frac{r_s^2r_i^2}{(r_i+r_s)^2}\frac{e^2\left\langle\mathbf{B}^2\right\rangle}{m_p^2c^2V^2}\frac{p-1}{p-2}\frac{k_l^{-p+2}-k_u^{-p+2}}{k_l^{-p+1}-k_u^{-p+1}}\\ &= \frac{\pi^2}{4}\frac{(p-1)^2}{p\,(p-2)}\frac{\left(1-(k_l/k_u)^p\right)\left(1-(k_l/k_u)^{p-2}\right)}{\left(1-(k_l/k_u)^{p-1}\right)^2}\mu^2\,. \end{aligned}\tag{G.5}$$

In the limit of $(k_l/k_u)^{p-2} \ll 1$ (a condition which requires $p > 2$), this gives μ normalisation constant

$$\mu_0 \approx \frac{2}{\pi}\frac{\sqrt{p\,(p-2)}}{p-1}\,. \tag{G.6}$$

For $1 < p < 2$, the μ normalisation constant becomes a function of the wavenumber range, decreasing as k_u/k_l increases – specifically

$$\mu_0 \approx \frac{2}{\pi} \frac{\sqrt{p\,(2-p)}}{p-1} \left(\frac{k_l}{k_u} \right)^{2-p} . \tag{G.7}$$

This is unsurprising, since heuristically we would expect that for spectral indices in this range the dominant wavemodes in terms of image-flux in the linear regime are at the smallest scales, on account of the image-flux distribution being closely related to projections of MHD current structure in the linear regime.

G.2 Power law spectrum (2.55)

The special case of $p = 1$ gives power law

$$E_B(k) = \frac{\langle \mathbf{B}^2 \rangle}{8\pi} \frac{1}{k \log k_u/k_l} . \tag{G.8}$$

The correlation length is

$$\ell_B = \frac{l_c}{4} \left(1 - \frac{k_l}{k_u} \right) \frac{1}{\log k_u/k_l} , \tag{G.9}$$

and so

$$w_{rms}^2 = \frac{l_c}{4} \left(1 - \frac{k_l}{k_u} \right) \frac{1}{\log k_u/k_l} \frac{e^2 B_{rms}^2 l_z}{m_p^2 c^2} . \tag{G.10}$$

Unlike the case $p > 1$, the correlation length decreases (albeit logarithmically) with the wavenumber range of the power law. The relative image-flux correlation length is

$$l_\Psi = \frac{l_c}{2\pi} \frac{1}{k_u/k_l - 1} \log k_u/k_l . \tag{G.11}$$

This is inversely proportional to the wavenumber range if $k_l \ll k_u$, so is much smaller than the correlation length. The RMS of relative image-flux deviations is

$$\left\langle \left(\frac{\delta\Psi}{\Psi_0^{(s)}} \right)^2 \right\rangle = \frac{\pi^2}{4} \frac{r_s^2 r_i^2}{(r_i + r_s)^2} \frac{e^2 B_{rms}^2}{m_p^2 c^2 V^2} \frac{l_z}{\ell_B} \frac{k_u}{k_l} \frac{1}{[\log k_u/k_l]^2} \,, \tag{G.12}$$

which gives μ normalisation constant

$$\mu_0 = \frac{2}{\pi} \sqrt{\frac{k_l}{k_u}} \log \frac{k_u}{k_l} \,. \tag{G.13}$$

Thus for a spectrum as shallow as a k^{-1} power law, order-unity variations in image flux will occur at $\mu \sim \mu_0 \sqrt{k_l/k_u}$. This can be interpreted as being due to the smallest structures having the highest μ for such shallow spectra – discussed in Section 2.4.2.

G.3 Cocoon field

The magnetic cocoon field is formed from spherical blobs of size ℓ_e defined precisely by

$$\mathbf{B} = B_0 \frac{r}{\ell_e} \exp\left(-\frac{r^2}{\ell_e^2} \right) \mathbf{e}_\phi \,. \tag{G.14}$$

for azimuthal basis vector $\mathbf{e}_\phi$. As demonstrated elsewhere (see Kugland et al. 2012), when imaged in the $\mathbf{e}_z$ direction such a field can lead to either a defocusing or focusing ring of image flux, depending on its orientation; however, when imaged from the side, symmetry implies that no overall deflections can be seen. It can be shown that the spectrum of a field of randomly orientated and positioned magnetic cocoons with field energy $B_{rms}^2/8\pi$ has magnetic-energy spectrum (Davidson 2004)

$$E_B(k) = \frac{B_{rms} \ell_e}{12\sqrt{2}\pi^{3/2}} \ell_e^4 k^4 \exp\left(-\ell_e^2 k^2 / 2 \right) . \tag{G.15}$$

The magnetic correlation length is

$$\ell_B = \frac{\sqrt{2\pi}}{3}\ell_e \,, \tag{G.16}$$

and the RMS deflection-field strength

$$w_{rms}^2 = \frac{\sqrt{2\pi}}{3}\frac{e^2 B_{rms}^2 l_z \ell_e}{m_p^2 c^2} \,. \tag{G.17}$$

The relative image-flux correlation length becomes

$$l_\Psi = \frac{9}{16}\ell_B . \tag{G.18}$$

Now calculating the RMS of relative image-flux deviations for the linear regime using (2.26), we find

$$\left\langle \left(\frac{\delta\Psi}{\Psi_0^{(s)}} \right)^2 \right\rangle = \frac{8\pi}{9}\frac{r_s^2 r_i^2}{(r_i + r_s)^2}\frac{e^2 B_{rms}^2}{m_p^2 c^2 V^2}\frac{l_z}{\ell_B} = \frac{8\pi}{9}\mu^2 \,. \tag{G.19}$$

This implies that for a cocoon field, the appropriate normalisation μ_0 for the spectra is given by $\mu_0 = 2\sqrt{2\pi}/3 \approx 1.65$.

Appendix H

Derivation of lower bound (2.47) for magnetic field RMS by analogy to the Monge-Kantorovich problem

In this appendix we show that inverting the Monge-Ampère equation to solve for the path-integrated field is equivalent to the L_2 *Monge-Kantorovich problem*. Due to the coordinate perturbation itself being the argument of the image-flux distribution, it is clear that in general treating (2.39) analytically is challenging. However, relating the Monge-Ampère equation to the L_2 Monge-Kantorovich problem enables an explicit reference to be given to a proof of the existence of a solution. We subsequently demonstrate the validity of lower-bound for the RMS magnetic field strength (2.47) in terms of the predicted deflection-field potential resulting from the application of the field reconstruction algorithm descrived in the main text.

We state again the image-flux relation (2.39) in the case when the plasma-image mapping is injective:

$$\Psi(\nabla_{\perp 0}\phi(\mathbf{x}_{\perp 0})) = \frac{\Psi_0(\mathbf{x}_{\perp 0})}{\det \nabla_{\perp 0}\nabla_{\perp 0}\phi(\mathbf{x}_{\perp 0})} \, . \tag{H.1}$$

For convenience, we renormalise the image-coordinates by

$$\mathbf{x}_{\perp 0}^{(s)} = \frac{r_i}{r_i + r_s} \mathbf{x}_{\perp}^{(s)} \,, \tag{H.2}$$

to give modified plasma-image mapping (written in terms of the deflection-field potential)

$$\tilde{\phi} = \frac{1}{2} \mathbf{x}_{\perp 0}^2 + \frac{r_i r_s}{r_s + r_i} \frac{\varphi(\mathbf{x}_{\perp 0})}{V} \,. \tag{H.3}$$

The renormalised image-flux relation is then

$$\Psi\Big(\nabla_{\perp 0} \tilde{\phi}(\mathbf{x}_{\perp 0})\Big) = \frac{\Psi_0(\mathbf{x}_{\perp 0})}{\det \nabla_{\perp 0} \nabla_{\perp 0} \tilde{\phi}(\mathbf{x}_{\perp 0})} \,. \tag{H.4}$$

A necessary (but not sufficient) condition for the problem of determining $\nabla_{\perp 0} \tilde{\phi}$ from the image-flux distribution to be well posed is a suitable boundary condition. In the main text, we state this boundary condition in Neumann form, that is

$$\nabla_{\perp 0} \tilde{\phi}(\Omega_I) = \Omega_S \,. \tag{H.5}$$

For a finite region, it can be shown that (H.5) is equivalent to a global flux conservation condition of the form

$$\int_{\Omega_I} \Psi_0(\mathbf{x}_{\perp 0}) \, \mathrm{d}^2 \mathbf{x}_{\perp 0} = \int_{\Omega_S} \Psi\Big(\mathbf{x}_{\perp 0}^{(s)}\Big) \, \mathrm{d}^2 \mathbf{x}_{\perp 0}^{(s)} \,. \tag{H.6}$$

where the mapping sends image region Ω_I to Ω_S: that is $\nabla_{\perp 0} \phi(\Omega_I) = \Omega_S$. This is known as a *second boundary condition.*

The L_2 Monge-Kantorovich problem in the context of proton flux mapping is as follows: given two positive flux distributions functions $\Psi_0(\mathbf{x}_{\perp 0})$ and $\Psi\Big(\mathbf{x}_{\perp 0}^{(s)}\Big)$ defined on regions Ω_I and Ω_S with equal total mass, find the mapping $\mathbf{x}_{\perp 0}^{(s)} = \mathbf{x}_{\perp 0}^{(s)}(\mathbf{x}_{\perp 0})$ which minimises the cost functional

$$\mathcal{C}\left(\mathbf{x}_{\perp 0}^{(s)}\right) = \int \mathrm{d}^2\mathbf{x}_{\perp 0} \left|\mathbf{x}_{\perp 0}^{(s)}(\mathbf{x}_{\perp 0}) - \mathbf{x}_{\perp 0}\right|^2 \Psi_0(\mathbf{x}_{\perp 0}) \ , \tag{H.7}$$

where global flux conservation condition (H.6) holds (Gangbo and McCann 1996, Villani 2008).

The equivalence with the Monge-Ampère equation follows by introducing $\mathbf{x}_{\perp 0}^{(s)} = \mathbf{x}_{\perp 0}^{(s)}(\mathbf{x}_{\perp 0})$ explicitly into the right hand side of (H.6), to give local condition

$$\det \frac{\partial \mathbf{x}_{\perp 0}^{(s)}}{\partial \mathbf{x}_{\perp 0}} = \frac{\Psi_0(\mathbf{x}_{\perp 0})}{\Psi\left(\mathbf{x}_{\perp 0}^{(s)}(\mathbf{x}_{\perp 0})\right)} \, . \tag{H.8}$$

A theorem (due to Brenier (1991)) shows that the solution to the Monge-Kantorovich problem is unique, and characterised as the gradient of a convex potential mapping (Sulman et al. 2011). Since $\nabla_{\perp 0}\tilde{\phi}$ in the case of proton mapping is convex if and only if the plasma-image mapping is injective, this solution is precisely the Monge-Kantorovich potential.

Thus, with boundary condition (H.5) or (H.6), the inversion problem associated with is well-posed. As mentioned in the main text, a variety of numerical schemes have been suggested to implement this (see for example Dean and Glowinski 2006, Sulman et al. 2011).

Explicitly calculating the cost functional in terms of physical quantities for our problem, we see that for an initially uniform flux,

$$\mathcal{C}\left(\mathbf{x}_{\perp 0}^{(s)}\right) = \Psi_0 \frac{r_s^2 r_i^2}{\left(r_s + r_i\right)^2 V^2} \int \mathrm{d}^2\mathbf{x}_{\perp 0} \, \left|\mathbf{w}(\mathbf{x}_{\perp 0})\right|^2 \propto w_{rms}^2 \, . \tag{H.9}$$

Thus, the reconstructed Monge-Kantorovich potential minimises the RMS of all possible perpendicular-deflection fields:

$$w_{rms}^2 \geq \left\langle (\nabla_{\perp 0}\varphi)^2 \right\rangle \, . \tag{H.10}$$

This rigorously demonstrated lower bound can in turn be used to find a lower bound on predicted field strengths. Supposing we have a field configuration $\mathbf{B}$ in a compact volume V, with size l_z in the z direction. Then, it follows from the Cauchy-Schwarz inequality that

$$\int_V \mathbf{B}^2 \mathrm{d}V \geq \int_V \mathbf{B}_\perp^2 \mathrm{d}V \geq \frac{1}{l_z} \int \mathrm{d}^2\mathbf{x}_\perp \left| \int_0^{l_z} \mathrm{d}z\, \mathbf{B}_\perp(\mathbf{x}_\perp, z) \right|^2 . \tag{H.11}$$

Thus,

$$B_{rms}^2 \geq \frac{1}{l_z^2} \left\langle \left| \int_0^{l_z} \mathrm{d}z\, \mathbf{B}_\perp(\mathbf{x}_\perp, z) \right|^2 \right\rangle , \tag{H.12}$$

with equality if and only if $\mathbf{B} = \mathbf{B}_\perp$, and $\mathbf{B}_\perp = \mathbf{B}(\mathbf{x}_\perp)$. Since

$$\int_0^{l_z} \mathrm{d}z\, \mathbf{B}_\perp(\mathbf{x}_\perp, z) = -\frac{m_p c}{e} \hat{\mathbf{z}} \times \mathbf{w} , \tag{H.13}$$

it follows that

$$\left\langle \left| \int_0^{l_z} \mathrm{d}z\, \mathbf{B}_\perp(\mathbf{x}_\perp, z) \right|^2 \right\rangle = \frac{m_p^2 c^2}{e^2} w_{rms}^2 . \tag{H.14}$$

Therefore, the magnetic field is bounded below by

$$B_{rms}^2 \geq \frac{m_p^2 c^2}{e^2 l_z^2} w_{rms}^2 . \tag{H.15}$$

The final lower bound is given by the deflection-field potential from (H.10):

$$B_{rms}^2 \geq \frac{m_p^2 c^2}{e^2 l_z^2} \left\langle (\nabla_{\perp 0} \varphi)^2 \right\rangle . \tag{H.16}$$

Operationally, we conclude that applying a field reconstruction algorithm to a particular proton-flux image to obtain the perpendicular-deflection field associated with the Monge-Kantorovich potential, then calculating the RMS deflection-field strength, provides a technique for determining a lower bound for the RMS magnetic field strength.

The accuracy of the bound is another matter; Figure H.1 shows the RMS deflection-

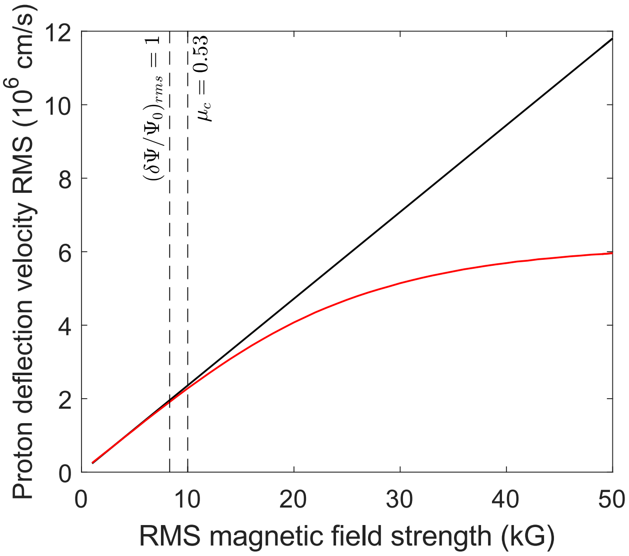

Figure H.1: Accuracy of lower bound (H.10) for RMS deflection-field strength over increasing RMS magnetic field strengths. Left: actual RMS deflection-field strength (black) associated with Golitsyn magnetic field configuration defined in Figure 2.1 for a range of RMS magnetic field strengths compared to predicted RMS deflection-field strength calculated from the perpendicular-deflection field reconstructed from numerically-generated proton-flux images (red). The imaging parameters of the proton beam were identical to those used to create proton-flux images in Figure 2.2, as was the implementation.

field strength w_{rms} for the Golitsyn field defined in Figure 2.1 for a range of RMS magnetic field strengths. For values of μ not much bigger that μ_c, the estimate of the perpendicular-deflection field RMS obtained is not that different from the true value. However, the discrepancy grows increasingly fast if μ is raised further, diminishing the usefulness of the bound.

Appendix I

Numerical algorithms

I.1 Generating proton-flux images numerically

In the main text and other appendices, we carry out various numerical experiments, for which artificial proton-flux images of magnetic fields are generated. In this appendix, we briefly explain how such images are created.

For a proton point-source, the following procedure is followed. An artificial proton is generated at a position with Cartesian coordinate $(0, 0, -r_i)$, and is assigned a random velocity, with speed fixed at V. The direction vector is chosen from a uniform distribution on a constrained surface region of the unit sphere; more specifically, defining a spherical polar coordinate system around the z-axis, the polar angle θ is restricted to the interval $\theta \in [0, \arctan{(l_\perp/r_i)}]$. The proton is then mapped to the plane $z = 0$, assuming its motion is free. If the initial perpendicular coordinate $\mathbf{x}_{\perp 0}$ of the proton on intersection with the $z = 0$ plane has either $|x_{\perp 0}| > l_\perp/2$ or $|y_{\perp 0}| > l_\perp/2$ – that is, it does not pass through the cuboid containing the simulated magnetic field ('interaction region') – then the artificial proton is discarded. The procedure is repeated until the specified number of imaging protons is reached.

Once inside the interaction region, the proton's position and velocity are evolved using a Boris algorithm combined with magnetic field interpolation (Birdsall and Langdon 1991, Welch et al. 2004). When a given proton leaves the interaction region, it is then mapped to the plane $z = r_s + l_z$ (if its z-velocity is negative, it is discarded), again assuming free motion. To create synthetic proton-flux images, protons with perpendicular image-coordinates $\mathbf{x}_\perp^{(s)}$ satisfying $\left|x_\perp^{(s)}\right| < \mathcal{M} l_\perp/2$ or $\left|y_\perp^{(s)}\right| < \mathcal{M} l_\perp/2$ – for $\mathcal{M}$ the image-magnification factor – are binned into pixels.

For a proton source with finite spatial extent – a sphere, radius a – emitting protons isotropically, a similar process is carried out to the point source, with one modification. Each artificial proton is assigned a random position drawn from uniform distribution defined on the unit ball, which is then scaled by the radius a.

I.2 Generating stochastic Gaussian fields

The creation of artificial stochastic magnetic fields, and then undertaking numerical experiments simulating proton-flux images, is a useful way of testing the various analytic theories of proton imaging derived in the chapter. Of the many possibilities, Gaussian stochastic magnetic fields are particularly convenient, since they are entirely characterised statistically by their magnetic-energy spectrum (Adler 1981). As mentioned in the main text, it is well known that stochastic magnetic fields in many situations of interest are not Gaussian (Schekochihin et al. 2004c); nevertheless, for the purposes of testing spectral extraction methods, assuming Gaussian statistics is perfectly adequate.

The technique used in the main text to generate stochastic Gaussian fields is a spectral method based on an approach due to Yamazaki and Shinozuka (1988). For a scalar stochastic field, it consists of the following steps:

1. Create an array of random uncorrelated Gaussian noise with zero mean, and transform into Fourier space with a fast Fourier transform (FFT).
2. Calculate the moduli of the Fourier wavemodes, and ‘colour’ these with a term proportional to $[E(k_{nm})]^{1/2}$, where $E(k)$ is the desired spectrum, and k_{nm} is a centralised array of wavevectors. This must be done in a way to preserve the

symmetries of the discrete Fourier transform associated with a real field.

3. Applying the inverse FFT gives a Gaussian, zero-mean field with that spectrum.

Generating random field with other types of statistics can be done in a similar manner (Shinozuka and Deodatis 1996).

For a stochastic magnetic field, we need three such components, but also have the further requirement that $\nabla \cdot \mathbf{B} = 0$. We enforce this solenoidality condition by generating three uncorrelated components of a vector potential $\mathbf{A}$, then calculating $\mathbf{B} = \nabla \times \mathbf{A}$. To obtain the desired spectrum, we note that for a vector potential with Fourier-transformed autocorrelation tensor

$$\hat{M}_{ij}^{(A)}(\mathbf{k}) = \frac{\hat{M}^{(A)}(k)}{2} \delta_{ij} \,, \tag{I.1}$$

the relation $\hat{B}_n = i\epsilon_{lmn} k_m \hat{A}_n$ implies that

$$\hat{M}_{ij}^{(B)}(\mathbf{k}) = \frac{1}{V} \left\langle \hat{B}_i(\mathbf{k}) \, \hat{B}_j^*(\mathbf{k}) \right\rangle = \frac{k^2 \hat{M}^{(A)}(k)}{2} \left(\delta_{ij} - \frac{k_i k_j}{k^2} \right) \,. \tag{I.2}$$

Since this is proportional to the general form of an isotropic Fourier-transformed autocorrelation tensor for a solenoidal vector field (Ensslin and Vogt 2003), we conclude that taking

$$\hat{M}^{(A)}(k) = \frac{\hat{M}^{(B)}(k)}{k^2} \tag{I.3}$$

will give a stochastic magnetic field with the desired properties. When calculating the curl of the vector potential $\mathbf{A}$ for this procedure numerically, it is best done spectrally, since naive application of a discrete finite-difference operator in real space without respecting periodic boundary conditions will result in significant spectral distortion under the curl operation. The desired field-strength normalisation for a generated magnetic field can be found simply by re-scaling. Similar approaches can be undertaken to generate two-dimensional perpendicular-deflection fields from random 2D Gaussian noise slices in terms of an assumed spectral form for the Monge-Kantorovich potential.

In many situations, a periodic cube (side length $l_i = l_\perp = l_z$) of homogeneous stochastic magnetic field is not sufficient: including some general variation in the RMS of a magnetic field gives for a more realistic configuration. This can be achieved by multiplying the vector potential used to generate the magnetic field by the desired smooth envelope function $f(\mathbf{x})$ which only varies over $\mathcal{O}(l_i)$ length scales:

$$\tilde{\mathbf{A}}(\mathbf{x}) = f(\mathbf{x})\,\mathbf{A}(\mathbf{x}) \ . \tag{I.4}$$

Then,

$$\tilde{\mathbf{B}}(\mathbf{x}) = \nabla \times \tilde{\mathbf{A}}(\mathbf{x}) = f(\mathbf{x})\,\nabla \times \mathbf{A}(\mathbf{x}) + \nabla f \times \mathbf{A}(\mathbf{x}) \approx f(\mathbf{x})\,\mathbf{B}(\mathbf{x}) \ , \tag{I.5}$$

where the second term is smaller than the first for $\mathbf{x} < l_i$. Over larger scales, for appropriately decaying f the second term can often also be ignored for scales $\mathbf{x} \sim l_i$: for example, with a Gaussian envelope

$$f(\mathbf{x}) = \exp\left(-\frac{4\sigma\mathbf{x}^2}{l_i^2}\right) , \tag{I.6}$$

it follows that even for $\mathbf{x} \sim l_i$

$$\frac{\nabla f \times \mathbf{A}(\mathbf{x})}{f(\mathbf{x})\,\nabla \times \mathbf{A}(\mathbf{x})} \sim \frac{\ell_B}{l_i} \ll 1 \, . \tag{I.7}$$

Since the strength of the field is much reduced at the edges anyway (where field strengths are weak), the approximation is a good one. In terms of affecting the spectrum, the impact of multiplying by a envelope function in real space is to apply a convolution in Fourier space, with the subsequent result of slight resolution loss. For $l_i \gg \ell_B$ this effect on spectral shape is very small; however, the overall normalisation of the field is altered. In particular, the RMS field strengths of the two fields are related by

$$\left\langle \tilde{\mathbf{B}}^2 \right\rangle = \frac{1}{V} \int \mathrm{d}V f(\mathbf{x})^2 \left|\mathbf{B}\right|^2 . \tag{I.8}$$

Again invoking separation of scales, we find $\left\langle \tilde{\mathbf{B}}^2 \right\rangle \approx \langle \mathbf{B}^2 \rangle \langle f^2 \rangle$. For a Gaussian envelope of the form (I.6), this gives

$$\frac{\left\langle \tilde{\mathbf{B}}^2 \right\rangle}{B_{rms}^2} \approx \frac{1}{16}\sqrt{\frac{\pi^3}{2\sigma^3}} \left[\mathrm{erf}\left(\sqrt{2\sigma}\right)\right]^3 . \tag{I.9}$$

If the RMS magnetic field strength of the enveloped field $\tilde{\mathbf{B}}$ is renormalised to match that of its parent field $\mathbf{B}$, this gives a 'maximum' RMS $\langle \mathbf{B}^2 \rangle_{max}$ (localised at the centre of the envelope) with value

$$\left\langle \mathbf{B}^2 \right\rangle_{max} = B_{rms}^2 \left\{ \frac{1}{16}\sqrt{\frac{\pi^3}{2\sigma^3}} \left[\mathrm{erf}\left(\sqrt{2\sigma}\right)\right] \right\}^{-1} . \tag{I.10}$$

However, from the perspective of an imaging proton beam, this is not the effective increase in the RMS magnetic field strength observed – since the proton beam experiences a path-integrated magnetic field along the z-coordinate direction. Denoting the effective RMS magnetic field strength along the perperpendicular origin $\mathbf{x}_{\perp 0} = (0, 0)$ resulting from a enveloping procedure combined with renormalisation by $B_{rms,0}$, we find

$$B_{rms,0} = B_{rms} \left[\frac{1}{l_i^2} \int \mathrm{d}^2\mathbf{x}_{\perp 0}\, f(\mathbf{x}_{\perp 0})^2\right]^{-1/2} = B_{rms} \left[\frac{\pi}{8\sigma} \mathrm{erf}\left(\sqrt{2\sigma}\right)\right]^{-1/2} , \tag{I.11}$$

which is equation (2.23) in the main text. Substituting $\sigma = 3$ gives

$$B_{rms,0} \approx 2.7 B_{rms} . \tag{I.12}$$

The validity of such estimates can be checked numerically with simulated fields, and estimate (I.11) is usually accurate for $\sigma > 1$.

Applying an envelope to numerically generated stochastic fields is also a convenient way of avoiding edges effects when performing analysis on flux samples in testing. One such example is the loss of periodicity of flux samples generated from a periodic magnetic field sample as μ increases from small to moderate; another comes when applying a field reconstruction algorithm to a sample whose edges do not strictly satisfy the required boundary conditions due to loss of proton flux from the detector. The latter results in a loss of accuracy in the field reconstruction algorithm in an edge region of size similar to screen displacement magnitude; the former can lead to global spectral distortion if sufficiently strong. For the purposes of analysis of actual samples (where non-periodic boundaries cannot be avoided), additional techniques have to be applied, such as sample windowing or Δ-variance methods (Arévalo et al. 2012).

I.3 Generating proton-flux images from perpendicular-deflection fields

For general EM particle configurations, synthetic proton-flux images can be created as just described in Appendix I.1. However, for three-dimensional magnetic fields defined on a refined grid, this can quickly become quite computationally expensive – for example, the (non-optimised) MATLAB ray-tracing code used to create synthetic images for this work on a 32 processor parallelised system took 8 hours to propagate two million particles through a 201^3 grid. This can be improved by a more efficient implementation; however, various alternatives based on the analytic theory of proton imaging derived in Appendix D of Bott et al. (2017) can be used to achieve order of magnitude improvements.

As a first step, perpendicular-deflection fields can be used numerically to create proton images. This process involves assigning a random collection of proton positions on the imaging side of the array containing the desired magnetic field configuration, and then calculating the perpendicular-deflection field for that configuration.

This latter procedure can be carried out without making any asymptotic approximations at all by sending a selection of test protons though the field configuration, then using a scattered interpolation algorithm to determine the perpendicular-deflection field. Provided the correlation length of the perpendicular-deflection field is much greater than the pixel size, this numerically determined perpendicular-deflection field will accurately represent the actual perpendicular deflection experienced by protons. Once this perpendicular-deflection field is obtained, the full collection of protons positioned on the initial coordinate grid can be allocated perpendicular velocities according to the perpendicular-deflection field, and then the resulting proton-flux image created. Since only $\mathcal{O}(N^2)$ particles need to propagated through a N^3 array to give a reasonable description of the perpendicular-deflection field, and the process of random particle position allocation is typically much less demanding, this enables the same number of particle (indeed, far more) to be used in a fraction $\mathcal{O}(1/N)$ of the time for a full ray-tracing set-up. This whole process removes a redundancy implicit in a full ray-tracing implementation associated with randomly generated protons travelling along similar trajectories.

A further extension of this technique allows for the generation of extremely high resolution proton-flux images. Noting that the spectrum of the perpendicular-deflection field has the simple relation (2.11) to the magnetic-energy spectrum – and by the central limit theorem, is likely to be Gaussian at small-scales – a good approximation to an actual perpendicular-deflection field can be obtained simply by generating a Gaussian perpendicular-deflection field with an appropriate spectral curve. Since this latter quantity is two-dimensional, the computational difficulty of the problem is greatly reduced. For large grids ($N \geq 1000$), this enables proton-flux images to be created on a single processor which otherwise could only be conceivably attempted with hundreds. The only exception to this rule arises when proton trajectories cross inside the plasma – which occurs if and only if the diffusive regime is reached. In this case, a full ray-tracing scheme is needed to obtain a truly accurate proton-flux image.

I.4 Nonlinear field reconstruction algorithm for perpendicular-deflection field

There are various approaches for solving the Monge-Ampère equation numerically, using finite-element methods, or converting the problem to its Monge-Kantorovich equivalent and implementing an optimatisation (Dean and Glowinski 2006). Indeed, the latter approach has recently been used in the very context of proton imaging (Kasim et al. 2017). However, for this chapter, we use a particularly simple alternative based on the treating the deflection-field potential as the steady-state solution of the logarithmic parabolic Monge-Ampère equation:

$$\frac{\partial \Phi}{\partial t} = \log \frac{\Psi[\nabla_{\perp 0}\Phi(\mathbf{x}_{\perp})] \det \nabla_{\perp 0}\nabla_{\perp 0}\Phi(\mathbf{x}_{\perp 0})}{\Psi_0(\mathbf{x}_{\perp 0})} \, . \tag{I.13}$$

This in turn is solved on a square grid using a finite-difference scheme (first order in time, second order in space) combined with interpolation methods. The imposed boundary conditions are the same Neumann condition we wish to impose for the Monge-Ampère equation:

$$\nabla_{\perp 0}\Phi(\mathbf{x}_{\perp 0}) \cdot \hat{\mathbf{n}} = \mathbf{x}_{\perp} \cdot \hat{\mathbf{n}} \, . \tag{I.14}$$

A more detailed outline of this field reconstruction algorithm is given by Sulman et al. (2011), where existence and uniqueness of the solution of the parabolic Monge-Ampère equation (along with its convergence to the solution to the Monge-Ampère equation) is proven.

The field reconstruction algorithm seems to be faster than previous approaches – a single processor can usually reconstruct a perpendicular-deflection field for a 201^2 proton-flux image in under an hour. The nonlinear field reconstruction algorithm is publicly available in the Python code ‘PROBLEM’. PROBLEM is open source software and is hosted on GitHub at https://github.com/flash-center/PROBLEM.

Further modifications can be made to deal with non-rectangular boundaries. First, any given image-flux distribution can be embedded in a image-flux distribution defined on a larger rectangular region, with the exterior region filled with a small ‘shadow’ image-flux. The field reconstruction algorithm can then be applied using the initial flux distribution embedded in the same larger rectangular region, but also with the exterior region filled with a shadow initial flux whose sum is equal to that of the shadow image-flux. The calculated perpendicular-deflection field in the interior region should be a close match to the true perpendicular-deflection field, by conservation of particle number in the interior and exterior regions respectively. Alternatively, the image-flux distribution can be extended to a boundary, and then a window function used. Since the field reconstruction algorithm becomes linear (and local) for small image-flux deviations, the external flux region will not distort calculated internal perpendicular-deflection fields significantly. In both cases, the result can be tested by forward-propagating particles with the desired perpendicular-deflection field. It is acknowledged that both approaches are approximate.